Centrifuge Modelling of Monopiles in Sand Subject to Lateral Loading

Steven M. Bayton

A thesis submitted in partial fulfilment of the requirement for
Doctor of Philosophy

Department of Civil and Structural Engineering
University of Sheffield
January, 2020

Declaration

I hereby declare that the contents of this thesis are original and have not been submitted in whole, or in part, for consideration for any other qualification at this, or any other, university or institution. The work done as part of this thesis is the result of my own work, except where specific reference is made to the work of others.

Steven M. Bayton
January, 2020

Acknowledgements

Firstly, I would like to thank my supervisor, Dr Jonathan A. Black, for his invaluable guidance and selfless support throughout the entire PhD process. I thoroughly enjoyed our regular technical and social meetings over coffee, of which provided the stimulus for many interesting conversations. I am also very grateful to Dr Colin Smith for the thought provoking discussions both related and unrelated to this topic.

To the technical staff at the Department of Civil and Structural Engineering, in particular Alex Cargill and Paul Blackbourn, without whose assistance and support throughout the centrifuge testing periods, and beyond, this PhD work would not have been a success.

A special mention to the former Tuesday night track, carvery and quiz club, David, Martin and Will, with whom I shared many fond memories outside of the PhD during my time in Sheffied, both on the athletics track and in the Crosspool Tavern.

Finally, I cannot thank my family enough for their endless love and support, and continual source of inspiration.

This PhD research would not have been possible without the financial support from the Engineering and Physical Sciences Research Council (EPSRC).

Abstract

At present, the monopile is the leading foundation of choice in the offshore wind industry, with over four-fifths of all offshore wind turbines founded on this solution. In a drive towards greater efficiency and power production from the harnessing of more reliable, stronger winds, larger diameter rotor and blade systems are being deployed in deeper waters further from the shore. With this, the support foundation is subject to greater magnitude cyclic lateral loads and overturning moments at the seabed which need to be managed. Current design for laterally loaded monopiles follows the philosophy adopted in the offshore oil and gas industry, of which the piles are slender and present significantly different failure mechanisms to the now larger diameter monopile counterparts. As a result, current design methodology is no longer considered to be suitable.

This thesis presents the in-depth analysis of the results from a series of physical model experiments performed in the geotechnical centrifuge at The University of Sheffield. The behaviour of the monopile subject to both monotonic ultimate limit and long-term cyclic serviceability limit loading scenarios is explored, with the aim to build upon the growing knowledge of monopile performance. Comprehensive instrumentation is located on the extremity of the model pile allowing for the capture of interesting local soil-pile interaction behaviour, as well as the traditional global monopile characteristics.

The test programme is divided into two parts. Firstly, a suite of monotonic pushover tests are performed, which reveal a progressive change in pile failure mechanism with increasing load magnitude. At low load, pile deformation and soil mobilisation are restricted to the region close to the mudline, which is synonymous of a flexible type failure. As the applied load increases, a transition towards a rigid, rotational failure is observed, with the onset of a ‘toe-kick’ and associated additional base soil mobilisation, moment and shear resistance. In an attempt to address the shortcomings of current design methodologies, an analytical multi-spring framework model is developed to incorporate the additional soil resistance mechanisms and is validated against experimental results.

Following from this, a series of cyclic lateral loading experiments are performed which explore a range of loading scenarios, including long-term low magnitude, short-term high magnitude, and several different varying magnitude load packages. Observations show contrasting accumulation trends for high and low magnitude cyclic loading, with a power- and logarithmic-law model respectively providing the best prediction of the accumulation behaviour. Local soil-pile interaction behaviour reveals a transition of representative failure behaviour from a flexible to rigid type, which corresponds to the observed change in the selected accumulation trend model. Locked-in stresses within the soil are seen to progressively develop on unload with the application of cycles and the a distribution of these is dependant on the magnitude of the applied load.

With the application of more realistic cyclic load packages of varying magnitude, interesting interaction behaviour between the successive load packages, both at a global and local level, is seen to take place. The nature of this interaction is dependant on the magnitude and cycle count of the previous load history. A newly proposed cyclic rotation accumulation contour design model is able to predict the progression of the permanent rotation at the mudline, a critical design parameter, with the applied cyclic varying load packages.

Table of Contents

List of Figures

List of Tables

Nomenclature

Latin alphabet

a	Centrifugal acceleration	$[\mathrm{LT^{-2}}]$
A	Monotonic adjustment factor on p_{ult}	[-]
A_{cyc}	Cyclic adjustment factor on p_{ult}	[-]
A_{b}	Blade sweep area	$[\mathrm{L^{2}}]$
A_{N}	Pile normal area to current flow	$[\mathrm{L^{2}}]$
A_{p}	Pile cross-sectional area	$[\mathrm{L^{2}}]$
A_{s}	Soil column area	$[\mathrm{L^{2}}]$
C_1, C_2, C_3	Coefficients for calculation of p_{ult}	[-]
C_{D}	Coefficient of thrust (water)	[-]
C_{T}	Coefficient of thrust (air)	[-]
D, D_{o}	Pile outer diameter	[L]
D_{i}	Pile inner diameter	[L]
d_{10}, d_{50}, d_{90}	Particle size at 10%, 50% and 90% passing	[L]
E	Young's modulus	$[\mathrm{ML^{-1}T^{-2}}]$
E_{s}	Soil elastic modulus	$[\mathrm{ML^{-1}T^{-2}}]$
e	Void ratio	[-]
e_{cc}	Load eccentricity	[L]
e_{max}	Maximum void ratio	[-]
e_{min}	Minimum void ratio	[-]
F_{a}	Axial force	$[\mathrm{MLT^{-2}}]$
F_{D}	Current drag force	$[\mathrm{MLT^{-2}}]$
F_{s}	Wave force	$[\mathrm{MLT^{-2}}]$
F_{w}	Wind force	$[\mathrm{MLT^{-2}}]$
g	Acceleration due to Earth's gravity	$[\mathrm{LT^{-2}}]$
G	Shear modulus	$[\mathrm{ML^{-1}T^{-2}}]$
G_0	Initial shear modulus	$[\mathrm{ML^{-1}T^{-2}}]$
G_{s}	Specific gravity	[-]
H	Horizontal applied force	$[\mathrm{MLT^{-2}}]$
I	Second moment of area	$[\mathrm{L^{4}}]$
k_{h}	Modulus of subgrade reaction	$[\mathrm{ML^{-2}T^{-2}}]$
k_{s}	Pile horizontal coefficient of reaction	$[\mathrm{ML^{-2}T^{-2}}]$
K	Coefficient of earth pressure	[-]
K_{a}	Coefficient of active earth pressure	[-]
K_0	Coefficient of earth pressure at rest	[-]
K_{p}	Coefficient of passive earth pressure	[-]
K_{py}	Initial stiffness of p – y curve	$[\mathrm{ML^{-1}T^{-2}}]$
K_{r}	Relative pile-soil stiffness	[-]

k_θ	Global moment-rotation stiffness	[ML^{2}T^{-2}]
$K_{\theta,\mathrm{b}}$	Base moment spring stiffness	[ML^{2}T^{-2}]
$K_{\theta,\mathrm{s}}$	Vertical side-shear moment spring stiffness	[ML^{2}T^{-2}]
$K_{\tau,\mathrm{b}}$	Base shear spring stiffness	[ML^{-1}T^{-2}]
L	Embedment length	[L]
M	Moment	[ML^{2}T^{-2}]
$M_{\theta,\mathrm{b}}$	Base moment	[ML^{2}T^{-2}]
$M_{\theta,\mathrm{s}}$	Vertical side-shear moment	[ML^{2}T^{-2}]
N	Number of cycles	[-]
N^*	Transition number of cycles	[-]
N_q	Bearing capacity factor	[-]
p	Soil reaction force	[ML^{-1}T^{-2}]
p'	Mean effective stress	[ML^{-2}T^{-2}]
p_a	Atmospheric pressure	[ML^{-2}T^{-2}]
p_ult	Ultimate soil reaction force	[ML^{-1}T^{-2}]
Q	Shear force	[MLT^{-2}]
$Q_{\tau,\mathrm{b}}$	Base shear force	[MLT^{-2}]
r	Radius	[L]
R_d	Relative soil density	[-]
R_t	Pile roughness	[L]
s'	MIT stress path abscissa	[ML^{-2}T^{-2}]
t	Pile wall thickness	[L]
t'	MIT stress path ordinate	[ML^{-2}T^{-2}]
u	Incident current velocity	[LT^{-1}]
v_1	Upstream wind velocity	[LT^{-1}]
$V,\ V_\mathrm{o}$	Sensor output voltage	[ML^{2}T^{-3}A^{-1}]
y	Pile displacement	[L]
z	Depth	[L]

Greek alphabet

α, β	Coefficient of rotation accumulation	[-]
γ'	Effective unit weight	[ML^{-2}T^{-2}]
δ	Pile-soil interface friction coefficient	[-]
ϵ	Strain	[-]
ζ	Adjustment factor on pile normal resistance	[-]
$\zeta_{b,c}$	Cyclic load characteristics	[-]
η	Adjustment factor on pile normal resistance	[-]
θ	Rotation	[$^{\circ}$]
$\theta_{\mathrm{Ed,SLS}}$	Rotation at serviceability limit state	[$^{\circ}$]
θ_{max}	Rotation at maximum load	[$^{\circ}$]
θ_{min}	Rotation at minimum load	[$^{\circ}$]
κ	Timoshenko shear coefficient	[-]
κ_{θ}	Coefficient of global stiffness accumulation	[-]
μ	Mean value	[-]
ν	Poisson's ratio	[-]
ρ_{a}	Density of air	[ML^{-3}]
ρ_{w}	Density of water	[ML^{-3}]
σ	Stress	[ML^{-1}T^{-2}]
σ'_{1}	Major principal effective stress	[ML^{-1}T^{-2}]
σ'_{3}	Minor principal effective stress	[ML^{-1}T^{-2}]
σ'_{h}	Effective horizontal soil stress	[ML^{-1}T^{-2}]
σ'_{v}	Effective vertical soil stress	[ML^{-1}T^{-2}]
τ	Shear stress	[ML^{-1}T^{-2}]
ϕ'_{crit}	Effective critical angle of internal friction	[$^{\circ}$]
ϕ'_{peak}	Effective peak angle of internal friction	[$^{\circ}$]
χ	Coefficient of locked-in bending accumulation	[-]
ω	Angular velocity	[LT^{-1}]

Dimensionless parameters

$\tilde{H} = \frac{H}{\gamma' D^3}$	Horizontal applied load
$\tilde{k} = \frac{k}{\gamma' D^4}$	Global moment-rotation stiffness
$\tilde{M} = \frac{M}{\gamma' D^4}$	Moment
$\tilde{p} = \frac{p}{\gamma' z D}$	Soil reaction force
$\tilde{Q} = \frac{Q}{\gamma' D^3}$	Shear force
$\tilde{y} = \frac{y}{D}$	Pile displacement
$\tilde{z} = \frac{z}{D}$	Depth

1. Introduction

1.1 The future of energy

The climate is complex and dynamic system. Throughout the history of the Earth, there have been numerous changes to the global climate in response to the many natural processes that govern it; one such being the greenhouse effect – a natural process which reduces the cooling effect allowing for a climate that is habitable for life (UK Met Office, 2009). Historical natural variation in global temperature due to the greenhouse effect has been well documented (UCSD, 2018), and is closely linked to the natural fluctuations in concentration of greenhouse gases in the atmosphere at that time (British Antarctic Survey, 2014). It is now widely accepted, however, that human activity – namely the burning of fossil fuels for energy provision – has contributed to an enhanced greenhouse effect (West and Gawith, 2005) and the resulting increased global temperature is referred to as global warming. The rate of warming is such that 17 of the 18 warmest years in 136 years of records have occurred since 2001 (NASA, 2018).

In recognition of this global epidemic, the international Paris Climate Agreement (European Commission, 2015) was signed by 195 countries across the world in December 2015, outlining the first-ever universal, legally binding global climate deal to limit global warming to *well below* 2°C above pre-industrial levels. This, coupled with the Climate Change Act 2008 (UK Government, 2008), calling for a transitional plan to become a low-carbon economy by 2050, presents a significant challenge for the United Kingdom (UK) to strategically depart from traditional fossil fuel energy sources towards zero carbon electricity generation. In fact, it is the intention to fully decarbonise the energy supply sector in the UK by the year 2030 (DECC, 2009).

1.2 Wind energy

Wind energy presents a major opportunity to decarbonise the energy sector. Across the world, the deployment of turbines for wind energy harnessing is growing, of which offshore is a major contributor. The cumulative installed global capacity of offshore wind energy has risen from 67 MW in 2000 to around 20,000 MW in 2017, and this growth is expected to continue to 521 GW by 2050 (IRENA, 2018). In the UK alone, the proportion of electrical energy from wind has increased to 20 per cent in the third quarter of 2019 (Carbon Brief, 2019), making up around half of the total electricity production from renewable sources. Furthermore, the combined renewable sector generated more electricity in this same quarter than power stations fired by coal, oil and gas, representing a major milestone for the UK power sector. The offshore market makes up one third of this and is increasing year on year at a rapid rate. Interestingly, it has been shown that offshore wind has the potential to meet the UK's demands for electrical energy three times over (Oswald et al., 2008).

Nevertheless, the industry is not expanding as rapidly as planned or required, due to a number of factors, none more so than the high initial capital expenditure of the complex engineering solutions. Despite the UK Government's pledge of £177 million of investment in renewables in the recent Clean Growth Strategy (UK Government, 2017), challenging engineering obstacles are still delaying offshore wind growth. As an illustration, of the nine RenewableUK Round 3 offshore wind farms licensed in 2010 (The Crown Estate, 2010), two schemes have been withdrawn at the design phase due to the expense of the foundation solution required as a result of "*challenging and adverse ground conditions*" (Wind Power Offshore, 2013). A further scheme has also been refused consent on the grounds of damage to local tourism.

It has been estimated that over the lifetime of a typical offshore wind farm, total foundation costs can make up between 25 to 34 per cent of the complete capital expenditure (Bhattacharya et al., 2014). Figure 1.1 illustrates a typical cost breakdown over the entire life of an offshore wind turbine. Economies, by means of innovative research and development, made in the design, fabrication and installation of the foundation is one solution that would lead to increased feasibility and potential greater offshore deployment in the future.

1.3 The offshore monopile

To date, the monopile (Figure 1.2) remains the foundation of choice with 87 per cent of all offshore wind turbines founded on this type of structure (Wind Europe, 2018). This is thanks to a number of reasons including its simplicity, suitability to mass-production and historic success. Owing to the need to harness greater, more predictable wind speeds further from the shoreline, upscaled wind turbines (in the region of 12 MW power turbines) are now being deployed in much deeper waters, presenting new challenges for geotechnical engineers. The foundation is now subject to much greater magnitude cyclic lateral loads from both stronger winds and waves striking larger turbine blades and support structures, resulting in greater overturning moments at the mudline. This drives the requirement for larger pile diameters and wall thicknesses,

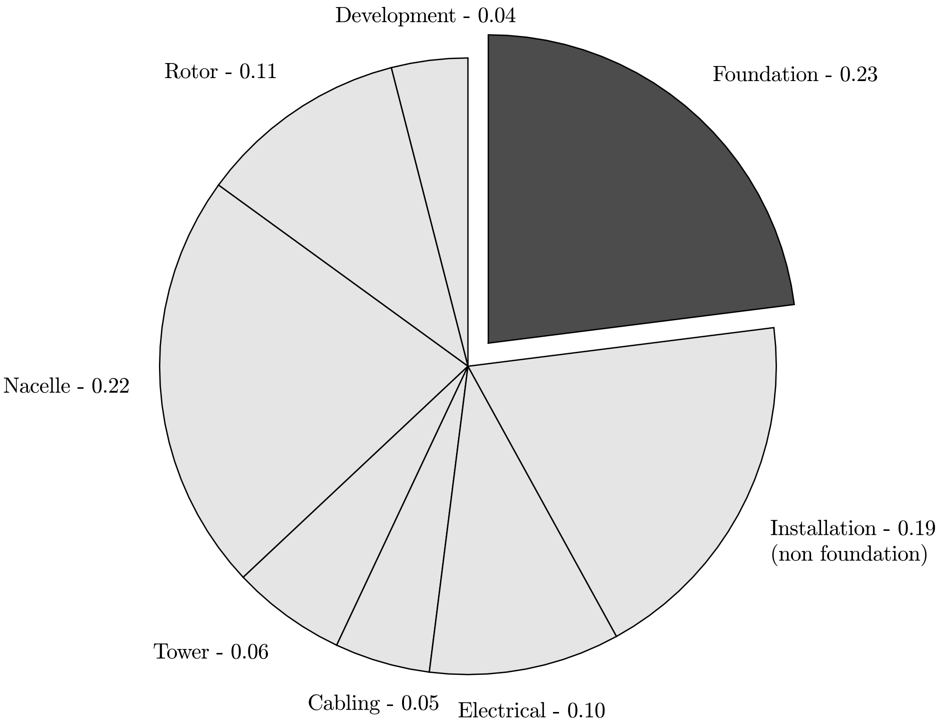

Figure 1.1: Cost breakdown of typical offshore wind turbine (Renewables Advisory Board, 2010)

associated reduced embedment ratios and as a consequence increased pile-soil stiffness. These combined lead to a potential change in pile failure mechanisms, cyclic behaviour and natural frequency measurements.

Current monopile design follows the recommendations set out in DNV GL (2016) and API (2011) design codes, where lateral soil resistance is based on an adaptation of the Winkler-on-a-beam model (Reese et al., 1974). Here, the soil is modelled as a series of empirically derived, non-linear springs, also known as $p - y$ springs, with characteristics calibrated from a series of experimental results of small diameter, slender piles destined for the offshore oil and gas (O&G) industry. With the diameter of modern day offshore wind turbine monopiles now of an order of magnitude greater, there is considerable concern over the direct translation of this empirical model to allow for the accurate design of a monopile foundation which meets the strict pile serviceability rotation requirements.

Equally pressing challenges arise surrounding the prediction of monopile behaviour subject to long-term cyclic lateral loading from the wind and waves. Over the course

Figure 1.2: Image of monopile leaving production. Credit: Ørsted

of its working life, the foundation is subject to 10's of millions of load cycles, and the resulting mudline rotation accumulation as well as foundation stiffness response changes which take place need to be considered.

1.4 Scope of research

In the light of the above, it is the aim of this thesis to build upon and improve the current understanding of monopile performance subject to lateral loads both under ultimate limit state (ULS) and serviceability limit state (SLS) design cases. An outline of the specific objectives of this thesis are presented below:

1. To explore the understanding of fundamental modelling effects in centrifuge testing of laterally loaded monopiles in sand. Implications of model preparation and experimental setup characteristics will be analysed;

2. To develop a greater comprehension of the soil-pile interaction for large diameter, rigid monopiles at ultimate limit state (ULS). Monotonic pushover experiments will allow for observations of pile failure mechanisms as well as the generation of alternative $p - y$ curves with depth along the monopile. These will be compared with existing design recommendations as well as previously published literature proposed alternatives;

3. To derive a new analytical spring framework to model the behaviour of large diameter, rigid monopile foundations which may present substantially different mechanisms of failure not captured by current design recommendations. This will

be validated against a number of experimental pile pushover results exemplifying a range of pile geometries;

4. To undertake long-term cyclic lateral loading experiments to go above and beyond currently available datasets at representative stress levels in order to develop a greater understanding of the serviceability limit state (SLS) of monopiles subject to a representative number of cycles of loading. Packages of varying lateral load will also be applied to gain knowledge of soil-pile interaction subject to more random loading events similar to realistic storm conditions;
5. To develop a new model for predicting the accumulation of monopile rotation subject to long-term cyclic lateral loads. The model will provide a preliminary design tool for cyclic packages of both constant and varying load magnitudes specific to the monopile design scenario.

1.5 Layout of thesis

The layout of the thesis is as follows:

1. Chapter 2 provides a background into the geotechnical challenges faced in the offshore wind energy sector and in particular regarding offshore wind. A comprehensive review of specific ULS and SLS literature is not outlined here, however will be found later in the thesis, in their respective chapters (Chapters 4 and 5);
2. Chapter 3 presents the principles of centrifuge modelling for monopile model experimentation as well as an overview of the centrifuge platform at The University of Sheffield (UoS50gT). The specific experimental apparatus, model preparation methodology and test matrix are thoroughly explained. In addition, initial exploratory results from a model preparation point of view are presented;
3. Chapter 4 commences with an in depth review of the specific literature surrounding ULS monopile design and previous experimental results. From here, centrifuge generated results are presented observing the progression of monopile failure, with a comparison between observed experimental $p - y$ and proposed alternatives across literature made. A new multi-spring analytical model is also introduced to incorporate additional soil-pile mechanisms that are not captured by current design;
4. Chapter 5 introduces the current extent of monopile cyclic knowledge as well as any existing predictive accumulation models. A new dataset of cyclic results is subsequently presented and global rotation and stiffness accumulation behaviour

is analysed. The cyclic results are then used to populate a monopile accumulation model concept. Instrumentation reveals information on monopile stiffness changes with cycles and the concept of ‘locked-in’ stresses with depth;

5. Chapter 6 summarises the key findings from the work conducted and outlines the future work that is required to continue the progression of monopile knowledge.

2. Offshore wind foundations

2.1 Background

The offshore industry is well established, at least from an oil and gas (O&G) perspective. Since the the first offshore drilling operations well over a century ago, the sector has developed massively with many thousands of platforms positioned offshore across the globe (Statista, 2018). The very nature of the O&G sector requires highly reliable and safe foundations, and as such large amounts of investment, typically made available from wealthy O&G associations, has resulted in over 70 years of valuable research and development.

When it comes to the design of offshore wind turbine foundations, however, important differences and specific challenges present themselves to necessitate further research in this area, such as the large diameter soil-pile interaction and long-term cyclic behaviour. That said, there remains considerable crossover between the two to warrant it unreasonable to disregard previous valuable lessons learnt from the O&G sector. A brief summary of the range of offshore foundation concepts that are either currently deployed or under consideration for offshore wind projects is first presented, alongside knowledge and experience gained from the O&G industry which should be taken into consideration. Figure 2.1 illustrates a selection of these foundation design choices.

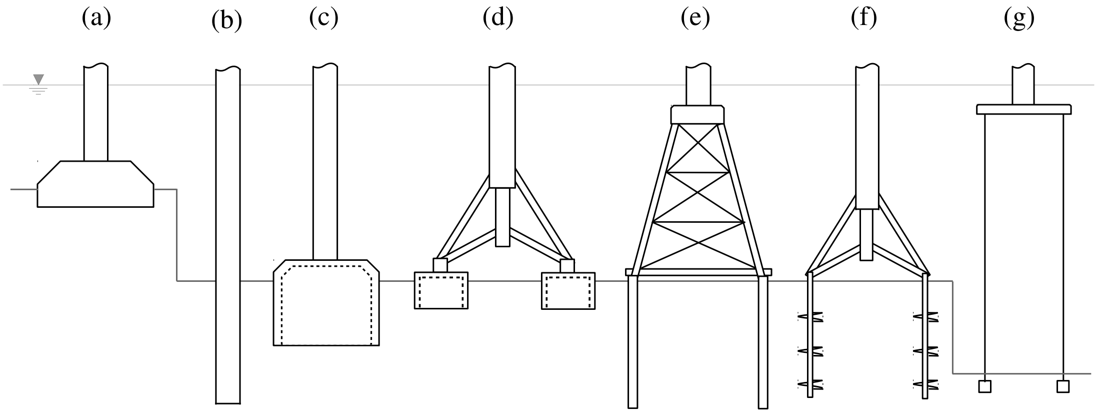

Figure 2.1: Typical foundation concepts: (a) gravity-based; (b) monopile; (c) suction caisson; (d) multi-suction; (e) jacket structure; (f) helical screw pile; (g) floating

The selection of foundation type depends on a number of site specific parameters such as ground conditions, water depth and, more often than not, the wind farm developer's experience and confidence in one particular foundation solution. A brief summary of a selection of the offshore solutions is outlined herein:

***(i) Gravity-based foundations*:** the first ever offshore wind turbine was founded on a gravity-based foundation (Vølund, 2005) and has since been deployed on numerous projects predominantly in shallow waters. Their main advantage is the ease of installation, as the base can simply be prefabricated on land and lowered into position. Their relatively large self-weight coupled with the bearing capacity of the underlying soil strata resist the large overturning moments from lateral loading. Lateral performance can also be enhanced with the addition of ballast. Despite very large gravity-based solutions in operation for many O&G projects, for deep water wind turbines they can be considered too large and cost-ineffective, given the vast material required to generate the necessary self-weight to resist the large overturning moments;

***(ii) Piled foundations*:** these are the most commonly adopted solution, given the typically soft nature of the upper deposits. Historically, research into the performance of offshore pile foundations has concentrated on the ultimate vertical capacity of the foundation system due to the great vertical load component of O&G structures. Resulting widely accepted design methods (ICP, Jardine et al. (2005); NGI Clausen et al. (2005); UWA Lehane et al. (2007) have proven to be reliable and accurate predictive tools for axial design of piles of different properties and methods of installation, founded in varying soil types and layering sequences. It should be noted, however, that the lateral behaviour of piles is not considered in these. That is not to say that piled foundations do not lend themselves well for this application – their high moment resistance capacity through the mobilisation of horizontal earth pressures, and their compatibility with the turbine tower present favourable characteristics;

***(iii) Suction caissons*:** these have been deployed extensively in the offshore O&G sector, from the use as anchors for floating systems to more recently as foundations for fixed platforms. In addition to their high axial performance in low-permeability soils, these offer an advantageous, relatively disturbance free installation and decommissioning. Recent research (Houlsby et al., 2005; Cotter et al., 2010; Bienen et al., 2018a,b) outlines the potential for suction caisson deployment for offshore wind, particularly in a 'multipod' arrangement. Axial cyclic load experiments reveal tight hysteretic curves for simple positive downward cyclic load packages, with little soil stiffness degradation. However, upon switching to a more realistic positive-negative loading sequence, large displacements are experienced in the form of open, out-of-control hysteresis loops, which are not acceptable for wind turbine design;

***(iv) Floating structures*:** these take many forms in both the method of achieving buoyancy and mooring to the seabed. The offshore O&G industry boasts great experience in anchors for floating platforms with methods including gravity mass, suction caisson and custom-designed offshore mooring anchors. The technology of floating wind turbines is still in its infancy and the commercial viability remains uncertain, but with two thirds of the North Sea between 50 and 220 metres deep (Carrington, 2015), exploitation of these seabed regions with floating wind turbines could prove very profitable;

***(v) Helical screw pile*:** it would not be completely novel to consider helical screw pile foundations in the offshore environment. The concept was first deployed for numerous offshore lighthouse structures (Mitchell, 1848), a small proportion of which have survived until today. More recently, the use of screw piles in an offshore environment has been limited and, in particular, there are no new offshore structures designed to rest on this foundation type. Nevertheless, large diameter helical screws offer an interesting opportunity for the offshore wind industry given their high resistive capacity to tensile forces (Byrne and Houlsby, 2015). Several issues, however, need to be addressed – *e.g.* installation upscale, pile-plate connection and cyclic performance – to ensure their feasibility for large-scale offshore deployment.

The different foundations solutions, presented above, show that there is a lot of potential for novelty, which may considerably reduce the substructure costs of an offshore wind turbine in the future. However, owing to its simple and robust design, suitability to mass-production, and track record over the past two decades, the monopile is most likely to remain the leading foundation choice for designers and contractors alike for the near future. With further optimisation and continued use in future projects, the design, fabrication and installation of the monopile will mature, providing numerous benefits to the offshore wind industry.

2.2 The offshore wind sector

When it comes to offshore wind, the UK is now considered to be the market leader. As of 2019, the 8.4 GW of installed capacity represents 34 per cent of the global installed capacity (Renewable UK, 2019), the largest proportion of any country in the world. Beyond the UK, Asian markets are starting to rapidly develop with a potential for 100 GW of installed capacity by the year 2030 (Offshore Wind Journal, 2018). In order to reach these ambitious targets, there will be a requirement for larger wind farm developments, greater optimisation of asset life and a reduction of operational maintenance.

In order to generate the most cost-effective, high power output offshore wind energy, the optimal selection of future wind farm location is vital. Staying closer to home, Figure 2.2 illustrates the variation of sea depth and average wind speeds around the British Isles. As shown, average wind speeds as well as the depth from water surface to sea floor are typically greater the further offshore. There are, however, locations at significant distances from the shore where average wind speeds remain high but the seabed is raised, presenting ideal locations for offshore wind farm developments. Dogger Bank Wind Farm, off the east coast of Yorkshire, planned as part of the RenewableUK Round 3 development, exemplifies this. The locations of the remaining developments are also presented in Figure 2.2 for interest.

If the offshore wind energy industry is to reach its full potential, developers will be required to deploy wind farms beyond these favourable locations and push towards deeper seas in order to harness the higher wind speeds and maximise overall efficiency. This will present extensive engineering challenges to deliver economical solutions. One such solution is through the greater efficiency of existing wind turbine technology, or equally through the implementation of innovative, low-cost solutions. Both of these will increase the economic feasibility of future offshore wind projects and will hopefully result in greater deployment.

2.2.1 Ground conditions in the North Sea

Of the remaining six RenewableUK Round 3 wind farm developments around the British Isles, five are located in the North Sea. According to Thomas (1990), soil profiles encountered at the upper surface of the North Sea can be divided into four separate groups as follows:

(a) stiff to very stiff overconsolidated clays and silty clays, overlain by a thin layer of fine sand;

(b) very soft to soft normally consolidated clays and silty clays overlying heavily overconsolidated deposits, these are overlain by a thin layer of fine sand;

(c) interbedded sand and clay strata. The uppermost layer is generally a fine sand;

(d) sands of varying degrees of sorting from fine sand at the surface to fine to coarse strata with clay laminations, seams and beds at depth.

It would appear that sand deposits at various thicknesses are a predominant feature in the North Sea, either overlying clays of varying degrees of consolidation or forming dense deposits and banks. Figure 2.3 presents the proposed wind farm schemes in

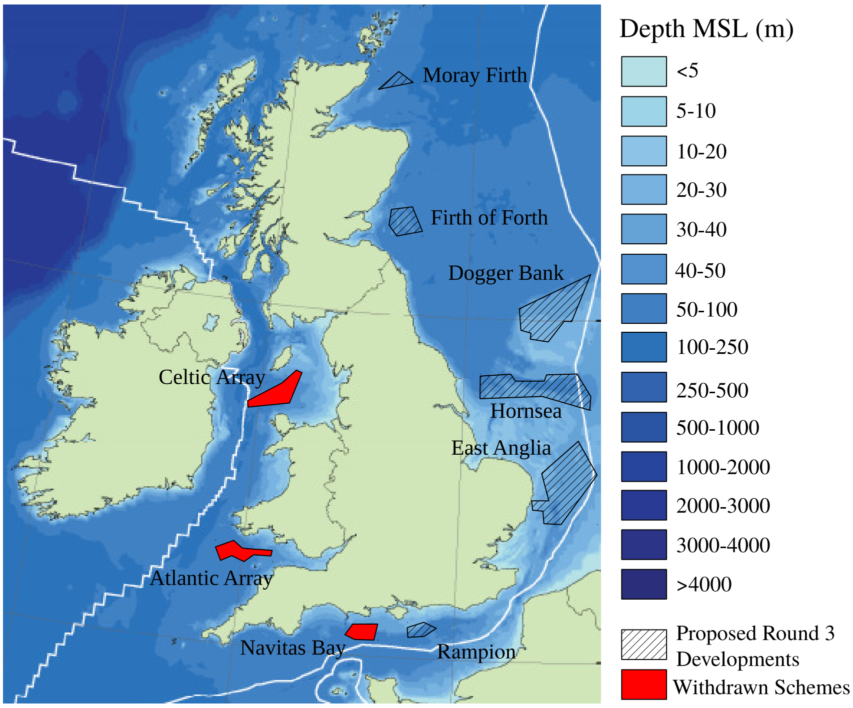

(a) Sea Depths

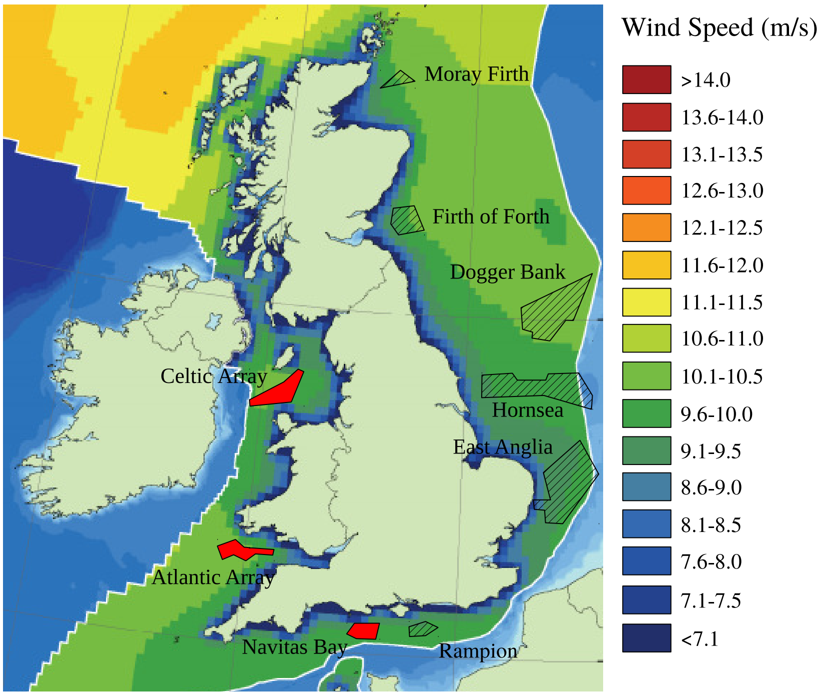

(b) Average Wind Speeds

Figure 2.2: Proposed RenewableUK Round 3 developments, sea depths and average wind speeds around United Kingdom (BERR, 2008)

relation to the upper layer soil deposits, which can be seen to be predominantly fine sand. It is for this reason that has driven the selection of sand as the soil type for testing throughout this current scope of research.

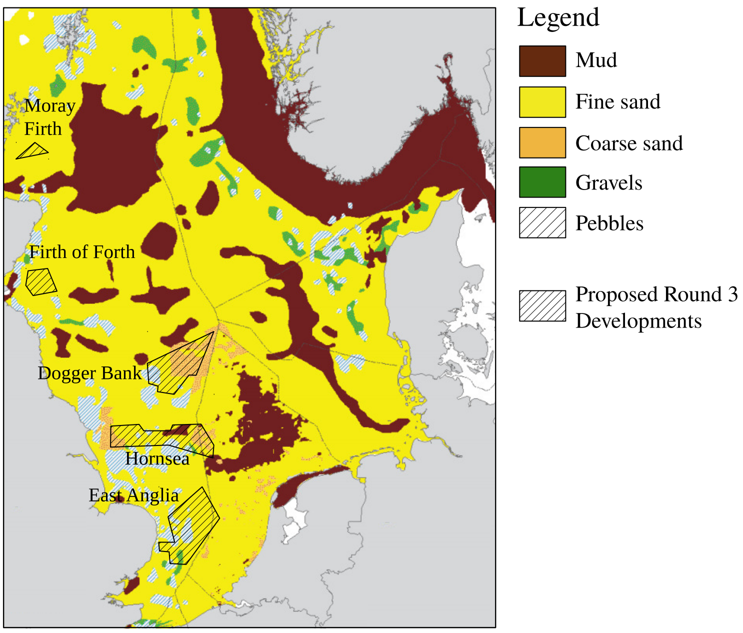

Figure 2.3: Soil deposits at RenewableUK Round 3 developments (Paramor et al., 2009)

2.3 Loads on offshore wind turbines

The offshore wind turbine foundation needs to be able to withstand the most severe weather conditions and the resulting horizontal forces from the wind and sea. The consequence of these loads is a very large design overturning moment at the seabed in relation to the relatively low vertical load. Specialised software packages, such as SESAM (DNV GL, 2016) and ROSAP (Ramboll, [no date]), are capable of calculating these, however forces can also be estimated with confidence using first principle calculations. Here, total overturning moment is determined as the sum of the combination of wind, current and wave forces, acting at a specified lever arm from the seabed.

(i) Wind force, F_w: during a complete blade sweep, F_{w} can be estimated using the actuator disc method (Burton et al., 2001). By applying the laws of conservation of energy and momentum from the upstream wind source; the magnitude of F_{w} is calculated by:

$$F_w = \frac{1}{2}(\rho_a \, A_b \, v_1^2 \, C_T) \tag{2.1}$$

where ρ_a is the density of air, A_b is the blade sweep area, v_1 is the upstream wind velocity and C_T is the coefficient of thrust. This force is at its maximum when maximum turbine power is being generated and thus the coefficient C_T takes a value of 8/9 (Betz, 1926).

***(ii) Current drag force, F_D*:** the chart of peak mean flow velocities around the British Isles stipulates that tidal velocities of up to 1.5 m/s can be encountered in the regions of the proposed wind farm developments (BERR, 2008). The British Standard for Maritime Structures, BS 6349 British Standards Institute, 2000), outlines a method for the calculation of F_D exerted by the sea current as follows:

$$F_D = \frac{1}{2}(\rho_w \, A_N \, u^2 \, C_D) \tag{2.2}$$

where ρ_w is the density of water, A_N is the pile area normal to flow, u is the incident water current velocity and C_D is the coefficient of thrust taking a value of 0.7 (for a smooth pile with a high Reynold's number (BS 6349)).

***(iii) Wave force, F_s*:** the magnitude of F_s depends on a number of factors, including the prevailing wind speed, the area over which it blows and the length of travel, or fetch. Guidelines in BS 6349 (2000) specify Morison's equation (Morison et al., 1950) should be applied to estimate the total design non-breaking wave force normal to the pile axis and can be expressed as the sum of the drag and inertial force components. For a breaking wave, slamming forces are also generated and guidance on the calculation of these can be found in literature such as (Lesny and Wiemann, 2005).

As a summary, Table 2.1 outlines the typical magnitude of the maximum loads applied to the foundation for different sized turbines with Figure 2.4 illustrating their position with respect to the seabed.

Table 2.1: Typical unfactored loads on wind turbine structures of different sizes (based on maximum operational wind velocities and typical ultimate current in relatively deep water $v = 12\text{ms}^{-1}$, $u_1 = 1.5\text{ms}^{-1}$, water depth = 40 m)

Rated Power (MW)	Pile Dia. (m)	Hub Height (m)	Wind Force, F_w (MN)	Drag Force, F_D (MN)	Wave Force, F_s (MN)	Axial Force, F_a (MN)	Resultant Moment, M (MNm)
2.0	4.0	70	0.50	0.08	2.50	4.0	162
3.6	5.0	80	0.72	0.16	3.67	6.0	245
5.0	6.0	85	0.79	0.20	4.81	10.0	313
8.0	8.0	110	1.35	0.32	6.09	12.0	461

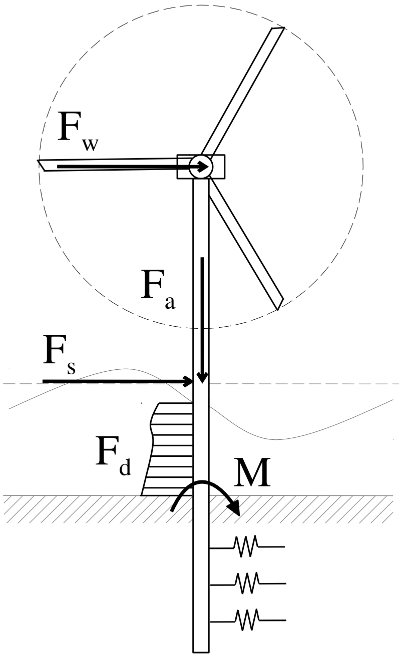

Figure 2.4: Schematic illustration of applied loads on a wind turbine structure

2.4 Challenges facing geotechnical engineers

As previously mentioned, current offshore design methods (for example DNV GL, 2016; API, 2011) for lateral pile design are based on the empirically derived, non-linear $p - y$ springs calibrated from small diameter, slender piles for offshore O&G deployment. Despite the similar harsh marine environments, the design loads are significantly different. The foundations for O&G platforms are required to resist greatly superior vertical loads and therefore critical foundation response is to provide sufficient vertical bearing capacity. As such, the piles are very long in order to reach the deeper, firm layers of sediment. Given the historic affluence of this industry, a wealth of research has been carried out with this in mind (Jardine and Chow, 1996; Jardine et al., 2005; Fleming et al., 2009). On the other hand, for an offshore wind turbine the horizontal loads are noticeably large in comparison to the relatively low vertical load, and the critical foundation response is to resist large resulting overturning moments for relatively short pile embedments (see Figure 2.5).

The current industry codes for lateral pile design adopt the recommendations of O'Neill and Murchison (1984) who derive empirical expressions for the $p - y$ springs from a database of 14 full-scale lateral load experimental results. Of these, the largest recorded pile diameter was 1.22 metres with an embedment length to diameter stiffness

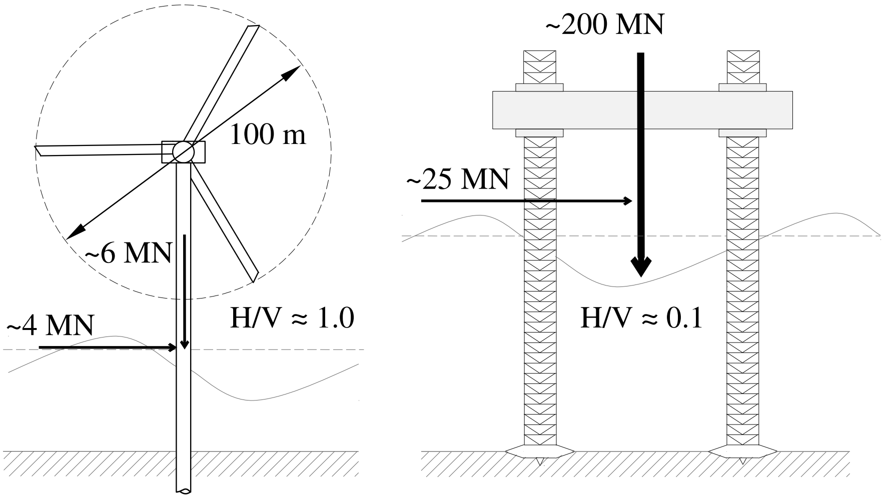

Figure 2.5: Schematic illustration of a 3.5 MW offshore wind turbine and a jack-up platform and externally applied forces (after Byrne and Houlsby, 2003)

ratio, L/D, upwards of 50. Modern day offshore wind turbine monopiles are now already at 6 metres in diameter (BVG Associates, 2019), with L/D ratios as low as 5, prompting the question of the model's empirical validity upon extrapolation to such opposing extremes. They present considerably different mechanisms of failure and have been widely recognised as no longer appropriate for monopile design (Byrne et al., 2015; Zdravkovic et al., 2015; Beuckelaers et al., 2017). Granted, this issue is acknowledged in the latest version of the design code, with recommendations for computationally expensive finite element modelling (FEM) to be carried out at detailed design stage so as to be fully confident of the monopile performance – though no guidance on this process is offered.

Likewise, design recommendations for cyclic loading cases are also widely accepted as no longer adequate given the criticality of an offshore wind turbine foundation's cyclic performance (LeBlanc et al., 2010b; Klinkvort, 2012; Abadie et al., 2018). Over the course of the design working life of a wind turbine, the foundation is subject to millions of cycles of load, and the method of prediction for monopile permanent rotations that incur is unsatisfactory. Current practice is to apply a blanket reduction factor (with up to three times lower magnitude strength compared to the static counterpart) on $p - y$ curve ultimate capacity, no matter of the number of cycles, in order to provide an estimation of the ultimate deformation expected. This is unacceptable in the wind industry given the stringent serviceability tolerances on mudline rotation. To illustrate this, a monopile experiencing a permanent rotation angle of just 0.5° at the mudline is widely considered to have reached industry serviceability failure (Rosbjerg and Gravesen, 2009). Given the 0.25° of error allowed at installation (DNV GL, 2016) this reduces the permissible cumulative permanent rotation to just 0.25° in worst cases. It is clear therefore that a more accurate cyclic accumulation model is required.

Concern is also raised over a change in the foundation stiffness over the lifetime of the wind turbine structure. Upon cycles of load, soils can experience either a hardening or softening of system stiffness depending on a number of factors, including soil type, initial void ratio and loading characteristics (Atkinson, 2009). With this change in stiffness comes a shift in natural frequency of the entire structure – typically designed to lie within the zone termed soft-stiff region (LeBlanc, 2009). Figure 2.6 presents a typical frequency spectrum, with wave and wind turbulence excitation frequencies. The wave energy-frequency spectrum has been estimated using the JONSWAP spectrum (Hasselmann et al., 1973). As the soil characteristics surrounding the foundation change with cycles, the natural frequency may shift from the safe soft-stiff region towards one of the critical harmonic frequencies of the rotating blades (1Ω or 3Ω), thus causing uncontrollable oscillations, and result in turbine downtime.

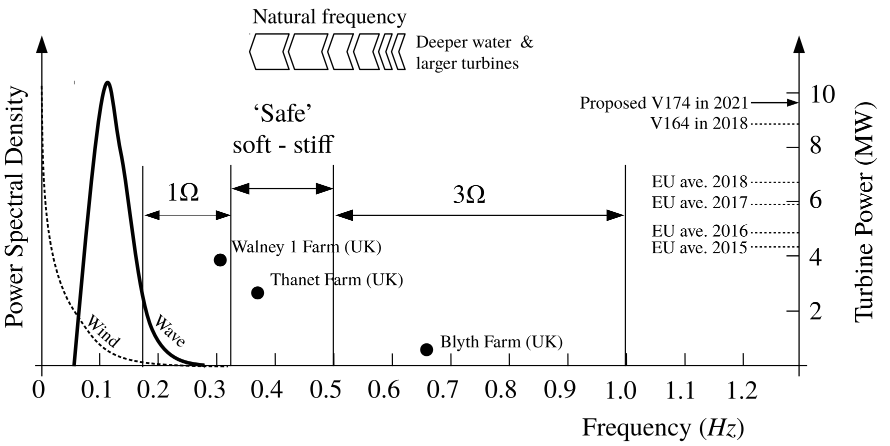

Figure 2.6: Frequency spectrum (including case study measured natural frequencies, adapted from Bhattacharya, 2014)

2.4.1 Outlook

This section has outlined a brief summary of some of the key issues and challenges faced in monopile design. Specific ULS and SLS critical reviews of previous literature and design methodologies are to be found in the individual chapters that follow (Chapter 4 - Monotonic Lateral Load Behaviour, and Chapter 5 - Cyclic Lateral Load Behaviour), to allow for a more fluid transition through the thesis.

3. Experimental Methodology

3.1 Scope of chapter

In this chapter, detailed outline of the physical modelling experimental methodologies adopted throughout the period of research is presented. The platform for testing was through the use of the UoS50gT geotechnical centrifuge facility at the University of Sheffield. Centrifuge principles, individual test setups, experimental procedures and data processing are each outlined in detail. In addition, results from preliminary tests are presented which offer insight into the affects of selected centrifuge modelling procedures and techniques which have not previously been documented.

3.2 Principle of physical modelling

Physical modelling is used extensively across almost all domains of geotechnical engineering; proposed hypotheses and new theories are typically validated and gain their authority by means of comparison with observed physical behaviour. Full (or field) scale testing provides the best representation of the prototype condition given its direct comparison of scale, and therefore carries high credibility if uncertainties such as the complete understanding of *in situ* soil conditions can be overcome. Testing of a full-scale structure is, however, not only highly costly, but also time-consuming and often impractical. It is for this reason that physical models are normally limited to small-scale representations of the prototype problem.

Small-scale physical models conducted on the laboratory floor, under the conditions of normal gravity ($1g$), are relatively straight forward to setup, test and acquire data from. They are also significantly less expensive than their full-scale representation. Indeed, Leblanc et al. (2010a; 2010b), Peralta et al. (2010) and Abadie et al. (2018) each conducted a number of physical model tests at $1g$ on the cyclic behaviour of laterally loading monopiles. Using the stress-dilatancy relationships outlined in Bolton (1986), the authors propose that sands of very low densities can be replicative of full scale much denser prototype conditions since they exemplify similar dilation adjusted angle of internal friction, and therefore generate quantifiable non-dimensional results. However, the stress levels acting in the soil here are not representative, and some fundamental soil characteristics which go hand in hand with overburden stress are not replicated, such as the correct representation of stiffness and stress development.

It is therefore not sufficient to simply upscale the model results here to prototype dimensions.

To overcome the problems associated with $1g$ model tests, the experimental setup can be placed in a geotechnical centrifuge where centrifugal accelerations generate an increased acceleration field throughout the model. With the correct centrifugal acceleration, a function of the angular velocity (Equation 3.1), the stress at homologous locations in the model are theoretically the same as those at prototype scale.

$$a = \omega^2 r \tag{3.1}$$

where a is the centrifugal acceleration, ω is angular velocity and r the radius from the centre of rotation (CoR) to the point of interest. Typically, the centrifugal acceleration is defined as a ratio of Earth's gravity, and expressed in the form of Ng, where N is the scaling factor and g takes a value of 9.81 m/s^2.

The complexity associated with the centrifuge modelling process is much greater than that at $1g$ due to the increased stresses all experimental components are subject to. However, with the scaling laws associated with the centrifuge modelling process, direct prototype behaviour can be derived from model scale results, presenting a great return on the invested time. Table 3.1 presents a selection of the relevant scaling relationships associated with the centrifuge modelling process. Further detail of these can be found in Garnier et al. (2007).

Table 3.1: Centrifuge modelling scaling laws

Parameter	Dimension	Scaling relationship (prototype/model)
Acceleration	LT^{-2}	$1/N$
Stress	ML^{-1}T^{-2}	1
Strain	-	1
Length	L	$1/N$
Mass	M	$1/N^3$
Force	MLT^{-2}	$1/N^2$
Bending moment	ML^{2}T^{-2}	$1/N^3$
Time (inertial)	T	$1/N$

Like with any representative physical model of a prototype problem, there are errors associated with the centrifuge modelling process. These include, though not limited to, soil scaling issues and stress variation across the model. In relation to the former, it is relatively simple to scale a foundation, for example, to suit the model size desired in the centrifuge. However, complications can arise when scaling the actual soil itself. Let's assume that the prototype problem is in a fine-grained sand, if the d_{50} of the sand is to be scaled exactly according to the length scale factor $(1/N)$, the chosen material particle size will now be N times smaller in diameter and may no longer exhibit the correct constitutive behaviour of sand (since this may now behave as a silt or even a clay). On the other hand, if the original prototype sand is used with no consideration for scaling, the sand particle size may now influence the foundation-soil interaction mechanics. With this in mind, a compromise is allowed such that effects of grain size can be avoided. For the case of laterally loaded 'flexible' and 'rigid' piles, values of $D/d_{50} > 40$ and $D/d_{50} > 88$ respectively have been proposed as necessary to achieve this (Remaud et al., 1998; Klinkvort, 2012).

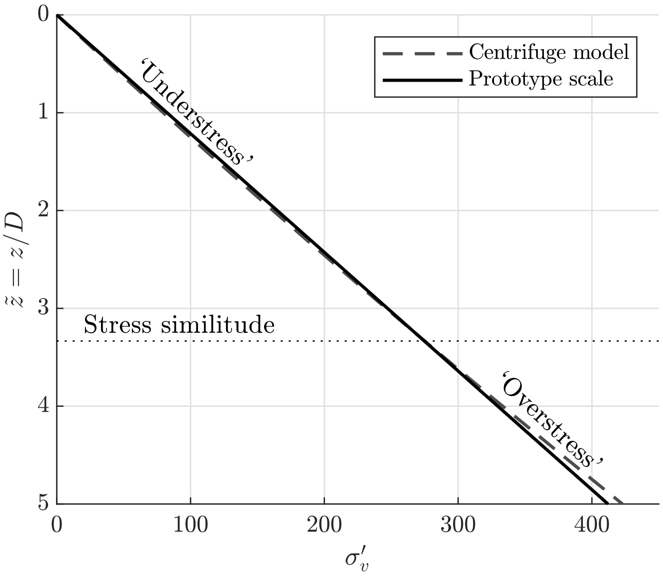

Figure 3.1: Model stress error with depth (for 2.0 m radius centrifuge and distance from CoR to model soil surface of 1.65 m)

Given that centrifugal acceleration at any given point of interest is proportional to the radius to this point, there is inherently a variation in acceleration across the model from the top to the base. The underlying result of this is an understress condition in the upper layers, a point of stress similitude and overstress at depth (for UoS50gT centrifuge, see Figure 3.1). In an attempt to minimise this, vertical stress similitude is taken at 2/3rd depth of the model. For a pile scenario, this is at 2/3rd embedment depth. In the model setup described herein, the maximum under and over stress errors are -4.8 % and 2.6 % (representing an absolute difference of -5 kPa and +11 kPa) respectively and can therefore be considered negligible. A difference in acceleration in the radial plane also exists, however this is very small. Additional information on the principles of centrifuge modelling can be found in Madabhushi (2014), for example.

3.3 UoS50gT centrifuge

All physical model experiments were performed on the 50g-tonne geotechnical research centrifuge (UoS50gT) located in the Centre for Energy and Infrastructure Ground Research (CEIGR), at the Department of Civil & Structural Engineering (Figure 3.2). As a brief summary, the 2 metre radius centrifuge is capable of accelerating a 500 kg payload to 100g. Signals, electrical power and fluid services are transferred on and off the beam by means of rotary stack assemblies fitted to the bottom and top of the centrifuge shaft. During flight, the on-board computer is controlled by remote desktop connection allowing in-flight control of the data acquisition software. The mass of the swing and payload are counterbalanced by a large counterweight, the position of which can be adjusted relative the centre of rotation depending on the payload mass and its respective centre of gravity. The centrifuge has also in-flight autobalance

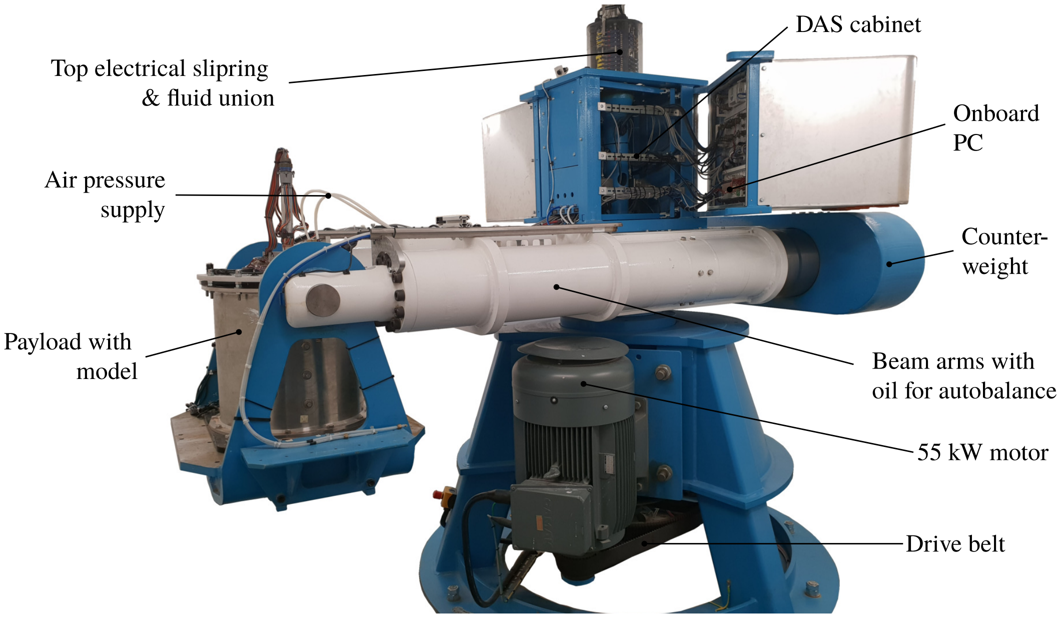

Figure 3.2: UoS50gT geotechnical research centrifuge

capabilities in the beam arms by way of oil which can be directed to one extremity or the other to allow for fine-tune system balance. Table 3.2 presents a brief summary of the centrifuge's performance specification. Further, more in depth, information on the UoS50gT can be found in Black et al. (2014).

Table 3.2: UoS50gT centrifuge specifications

Description	Specification
Platform radius	2.0 m
Payload size	W = 0.8 m (circumferential)
	L = 0.8 m (vertical in flight)
	H = 0.9 m (radial in flight)
Maximum acceleration	100g at 500kg payload; or 150g at 330kg payload

3.4 Experimental setup

The following section outlines in detail the physical model setup for monopile tests performed in dry dense sand alongside the implications of different model setup procedures on fundamental monopile performance. During this research project, a total of 44 centrifuge experiments were individually prepared and tested. The results from some of these are not presented in this thesis since these were purely for calibration and setup verification purposes. Across the test matrix, there was some variation in terms of model preparation methods as the equipment in the relatively young laboratory matured and these are well documented throughout. All tests were performed in a stainless steel cylindrical strong box of internal diameter 495 mm and height 500 mm which provided a rigid boundary condition.

3.4.1 Sand preparation

Across the test matrix, each test was prepared and conducted in dry sand. It is appreciated that in an offshore environment, saturated conditions exist, though experimental studies have traditionally assumed fully drained conditions which are implemented here. Recent FEM studies have, however, suggested that with the significant increase in pile diameter and associated longer pore fluid dissipation flow paths, there is a potential for excess pore pressures to develop with cycles at the load rate of a typical wave frequency (Klinkvort and Page, 2014). With this, it is possible that partial drainage conditions are developed which may alter the soil strength and monopile capacity. An appropriately scaled pore fluid would need to be taken into consideration to allow the partial drainage condition to be captured in the elevated gravity environment. Previous centrifuge physical model attempts with this in mind have yet to find any evidence of this behaviour (Klinkvort, 2012; Kirkwood, 2015). The above hypothesis is duly recognised and requires further research, however, there remain considerable pressing challenges for a fully drained scenario alone that it was decided to proceed in this manner.

Table 3.3: HST95 sand properties

Property	Value
Particle size, d_{10}	0.08 mm
Particle size, d_{50}	0.16 mm
Particle size, d_{90}	0.23 mm
Coefficient of uniformity	2.1
Specific gravity, G_s	2.65
Maximum void ratio, e_max	0.827
Minimum void ratio, e_min	0.514
Critical angle of shear, ϕ'_crit	30.5°
Peak angle of shear, ϕ'_peak	37.5° (1)
Elastic modulus, E_s	110 MPa (1)

(1)at R_d = 80% and p' = 100 kPa

The sand in question was a fine grained yellow sand commercially known as HST95. Prior to any centrifuge modelling, the sand was tested at an element level, by means of maximum and minimum density verification, particle sieving and triaxial testing, to gain an appreciation of its fundamental properties. Figure 3.3 illustrates stress path results from triaxial testing programme (presented in MIT $s' - t$ format) for a range of applied confining stresses. A target relative density of 80 % was achieved by dry pluviation. A breakdown of the HST95 sand properties are provided in Table 3.3.

In order to maintain a consistent model ground, not just with depth for each individual test but across the full test matrix, an accurate and repeatable method of sand preparation was important. In early tests, hand pluviation was performed (see Figure 3.5a). This was later superseded by automatic pluviation upon commission of the new three degree of freedom (3DOF) automatic pluviator at CEIGR (see Figure 3.5b).

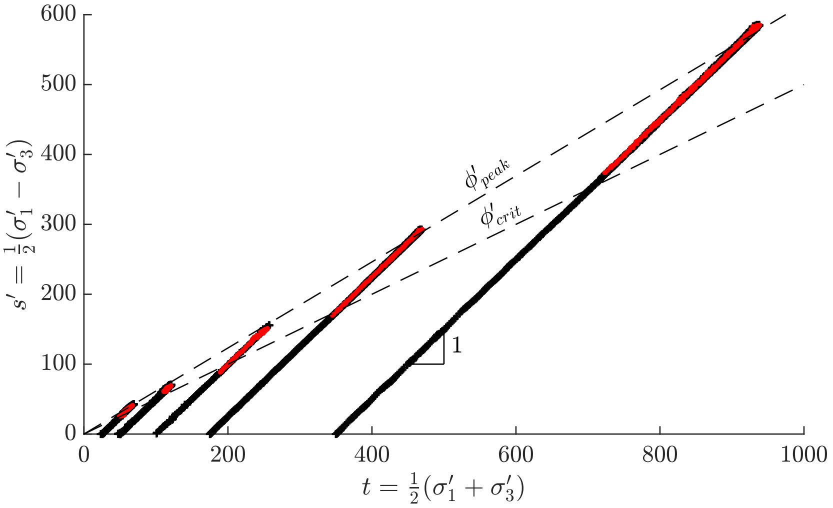

Figure 3.3: Stress path results from triaxial testing (red markers post peak)

Prior to any pluviation of actual test model sand beds, a suite of calibration studies were performed to determine the relationship between sieve aperture size and spacing, drop height and the placed relative density, R_{d}. As a summary, to achieve relative densities of 30 and 80 per cent (later defined as 'loose' and 'dense' respectively in future test descriptions) by hand pluviation, sieve combinations of S_{30} = [6,5] mm and S_{80} = [6,1.5] mm, at drop heights of 500 and 900 mm respectively. The sand flowing from the hopper first met the 6 mm aperture sieve which generated a broken, constant flow, which then fell through the smaller flow rate controlling aperture sieve below. A very consistent flow pattern was achieved in this manner. Individual test values of R_{d} can be found in the test matrix in Table 3.5. The average dense sample density across test matrix prepared by this method was 81.1 % with a standard deviation of 1.85 %.

Following the first suite of experiments prepared by hand, an automatic 3DOF pluviator was designed and fully commissioned. The system is a point pluviation device, with exit nozzle diameter 50 mm, and has a user interface allowing for the selection of programmable pluviation paths in each of the x, y and z directions. The full travel ranges for each of these are 595, 730 and 540 mm respectively, with maximum travel speeds of 108, 108 and 10 mm/s. A travel speed of 85 mm/s was selected here for each preparation as this was comparable to the travel speed adopted by hand. Typical pluviation paths were set to extend beyond the internal diameter of the bucket, where any sand falling outside the desired area was deflected away by a cylindrical collar. This was a preventative measure to avoid the gathering of sand at the edges of the sample. As an illustration, Figure 3.4 presents the surface topology across the cross section of a typical automatic test setup, with manual dipper locations and measured values from hand pluviation also marked for comparison.

The cylindrical hopper has a volumetric capacity of 20 L and is capable of delivering approximately 30 kg of sand in one refill, although across all pluviation events the hopper was never allowed to fully empty as variations in flow patterns were seen to occur at very low capacities. Binary flow or no-flow (open or closed) condition was controlled by an air pressure regulated pinch valve at the hopper base. The exiting sand passed through a series of meshes to control flow rate and pattern, and ultimately soil placed density of which was calibrated by the same methodology as the hand pluviation. Each layer density was calculated following the measurement of sand mass by means of a 1000 kg (± 0.1 kg) capacity scale, and layer height by a Keyence IL-600 laser (± 0.25% within range of 200 – 600 mm) placed on the base of the z axis actuator. Average placed relative density across all layer placements for this method was 80.2 % with a standard deviation of 0.88 %. Figure 3.6 illustrates the greater repeatability capability of the automatic system over that by hand, exemplified by the narrower 25^{th} and 75^{th} percentiles and lack of outliners.

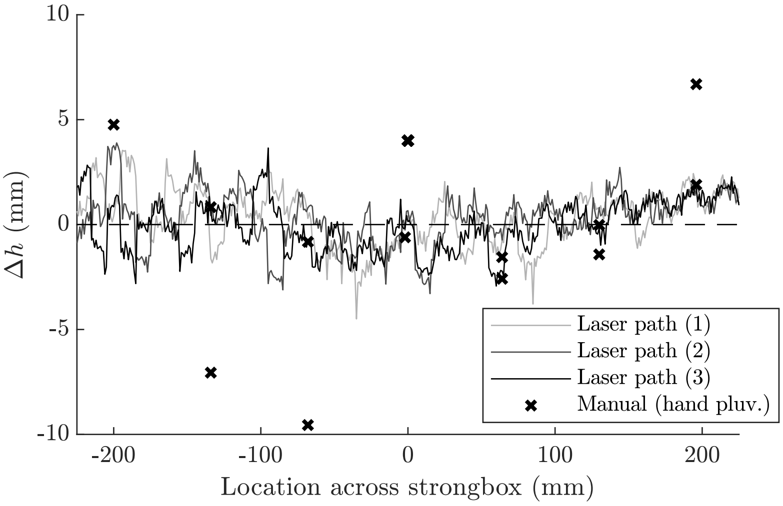

Figure 3.4: Surface topology across cross section of typical automatically pluviated test bed

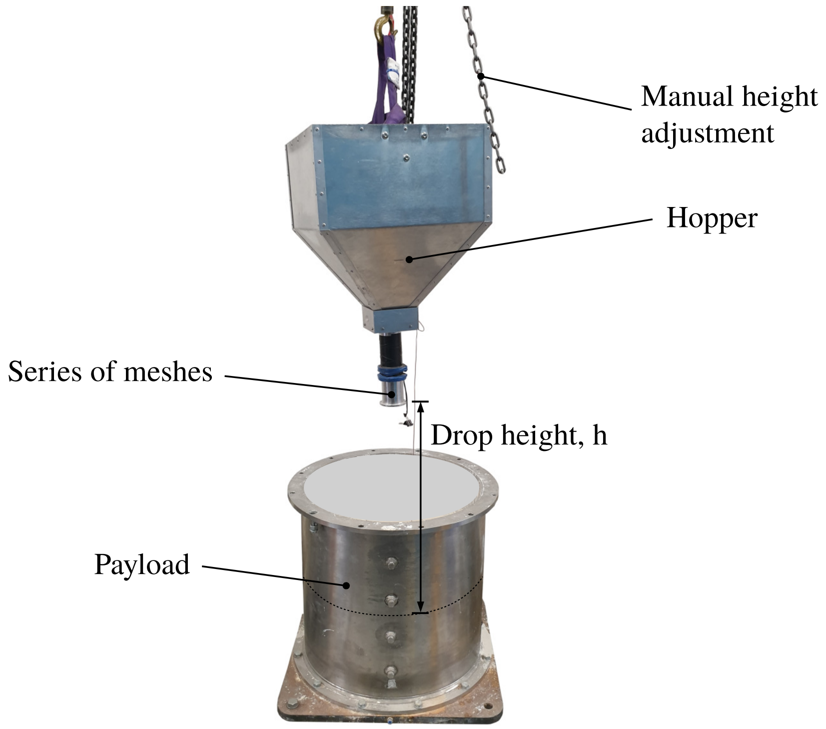

(a) Hand pluviation

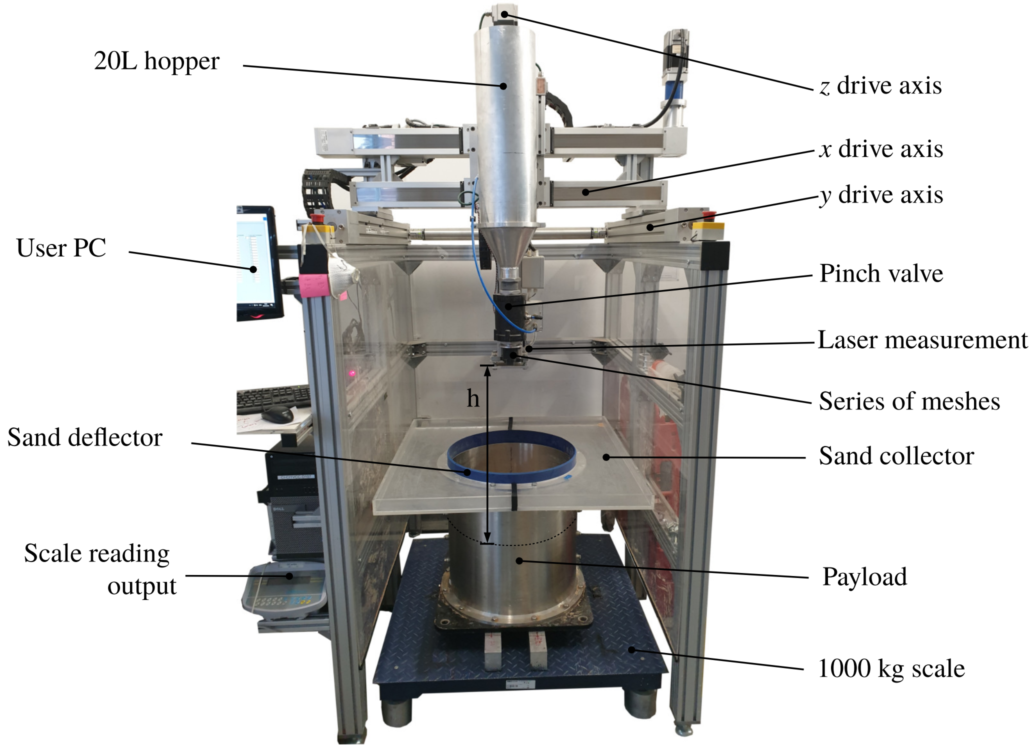

(b) Automatic three degree of freedom (3DOF) pluviation

Figure 3.5: Pluviation devices

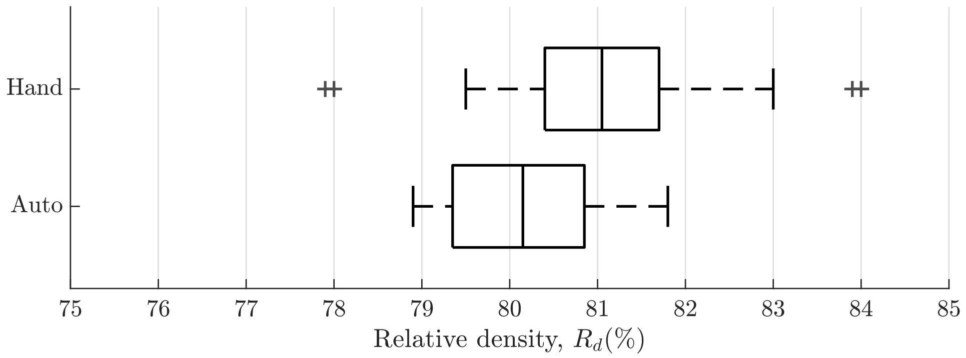

Figure 3.6: Variation in sand pluviation relative density across all tests (μ_{hand}=81.1 %, μ_{auto}=80.2 %)

The benefits of the automatic pluviation process over preparation by hand are numerous. Firstly the time and effort saved by the user is a great advantage since the sand hopper can be simply filled at the start of each desired layer and the system left to complete its path. With one refill, a model layer height of approximately 40 mm at $R_\mathrm{d} \approx 80$ % for the 495 mm diameter strong box can be placed (this includes any sand that was deflected beyond the boundary limits). If this was process was to be completed by hand, it would take around 25–30 minutes, plus the additional time for height measurement using the manual dipper and tape.

Secondly, there are clear repeatability advantages, given the exact same programmable path that the automatic pluviation process can follow with each placement. With hand pluviation, the direction and sequencing of pluviation can be considered almost random and is ultimately driven by the individuality of the user; the only conscious decision in this process being to target the areas that appear lower in elevation to ensure the bed remains visually flat across each layer. Of course, it could be argued that this would generate a more random sand bed, which could be more replicative of prototype conditions, however given this randomness the repeatability across a full test matrix is compromised. As an illustration of the precise repeatability of each method, Figure 3.7 shows the differences in monotonic pushover moment-rotation response that are seen across the two preparation methods. The sequencing selected for the automatic pluviation here is a criss-cross pattern (described in more detail below). With repeat experiments for each, the results from the automatic pluviation process are in much closer agreement.

Aside from sample to sample repeatability, another advantage of programmable automatic pluviation path is the ability to design user specific paths of interest. With this in mind, a series of exploratory experiments observing the effects of pluviation di-

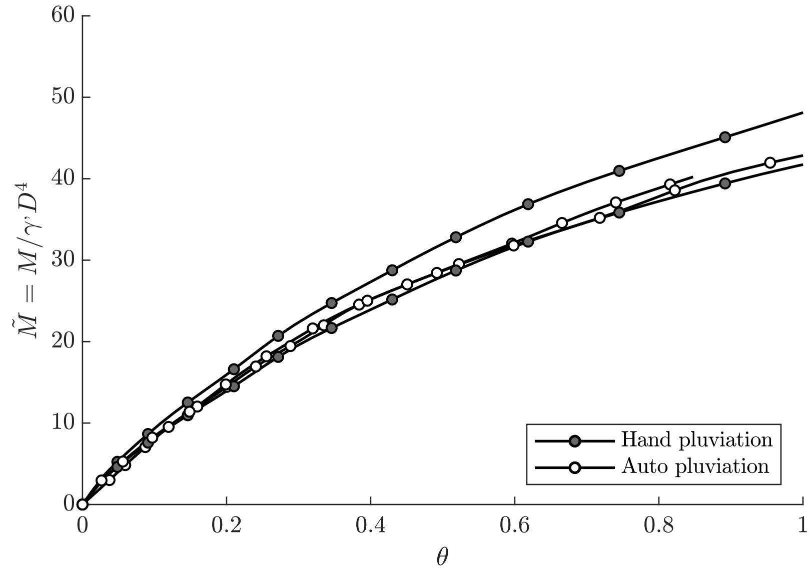

Figure 3.7: Global $\tilde{M} - \theta$ response depending on pluviation method (tests no. M21 to M24)

rection in relation to monopile lateral load orientation were performed (tests no. M13 to M17). Load orientations, α, from 0° to 90° in relation to the direction of a one-way pluviation path were explored (see Figure 3.8a). These were compared with an interlocking criss-cross pluviation pattern (see Figure 3.8b). The model un-instrumented piles were wished-in-place (WIP) to prevent any disturbance of the pluviation pattern during driving and maximise the observation of orientation effects. For each experimental setup, pluviation drop height was maintained constant across a full x and y pluviation pass (equating to approximately 11 mm of bed height gain). Upon raising, the pluviator path was then offset by the half spacing to ‘fill’ the previously avoided gaps and the process repeated (represented by dashed lines). This minimised sand ribbing across the surface of the bed.

Figure 3.9 compares the global moment-rotation response, of which a clear increase in stiffness can be observed for an increase in load angle. For the case of loading parallel to the direction of the one-way pluviation path (*i.e.* $\alpha = 0^{\circ}$), the initial stiffness as well as ultimate lateral capacity are greatly reduced which could be explained by the potential presence of bands of higher and lower density sands inherent of the pluviation path. This would cause preferential planes of shearing between these adjacent lines of pluviation. As the pluviation orientation increases in relation to load direction (*i.e.* $\alpha > 0^{\circ}$), both the stiffness and ultimate lateral capacity increase. With the change in angle, an increase in normal stress is now present at the shear interface allowing for

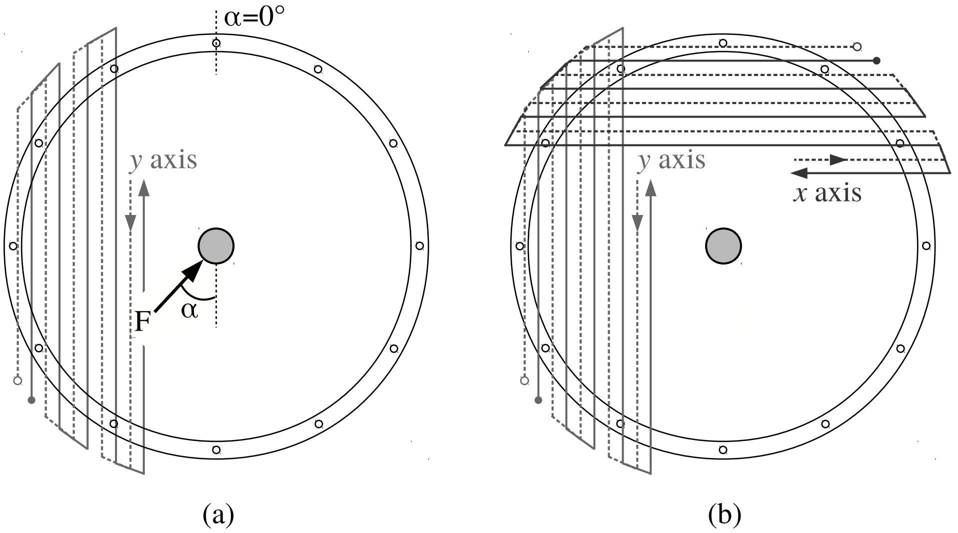

Figure 3.8: Schematic illustration of programmable paths of pluviation: (a) one-way pluviation; (b) interlocking criss-cross pattern (solid and dotted lines represent overlap pattern to minimise ribbing with pluviation)

greater mobilisation of shear strength. The increase in lateral resistance continues up to perpendicular load (*i.e.* $\alpha = 90^{o}$). Interestingly the criss-cross pluviation pattern presents a stiffness and strength sufficiently greater than $\alpha = 0^{o}$, however less than the other angle configurations. This is likely due to the interlocking pluviation path resulting in an alternating switch in load orientation from layer to layer across the full pile depth.

This is an interesting aspect of physical modelling which has not been previously reported, and needs to be considered in the design and interpretation of model monopile centrifuge tests.

3.4.2 Model monopiles

A number of model monopiles were deployed throughout the experimental series. Two of these were instrumented (MP1 and MP2) and their geometry, level of instrumentation and calibration of are presented herein. Four further piles were left uninstrumented and used in initial preliminary investigative studies. Details of these can be found in their respective sections.

The selection of model pile size was ultimately driven by the desire to represent the largest possible diameter pile within the capabilities of the underlying geometry of the

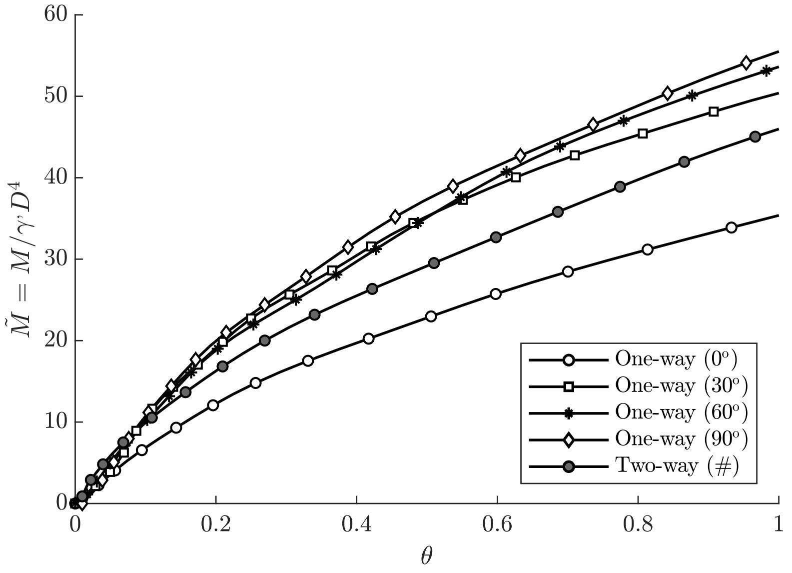

Figure 3.9: Global $\tilde{M} - \theta$ response depending on pluviation orientation (tests no. M13–M17)

payload strongbox. In order to not induce any unwanted boundary effects which would affect the pile–soil interaction, it was decided to deploy a monopile no bigger than 50 mm at model scale (representing 5.0 m prototype diameter at $100g$). This resulted in a distance from the outer pile diameter to internal face of the strong box of $4.5D$, given the internal cylindrical strong box diameter of 495 mm. The second instrumented model pile with diameter 38.1 mm (4.0 m prototype diameter at $105g$) gave a more preferential boundary distance of $6.0D$. It has been previously recommended that a separation distance of $\geq 10D$ be adopted for the case of vertical pile driving at Ng (Gui et al., 1998), however previous laterally loaded pile literature has neither adhered to this and nor observed any clear boundary effects with lower values (values of $5.4D$ and $6D$ in Klinkvort (2012) and Kirkwood (2015) respectively). Indeed, pure Rankine failure predicts a failure wedge at an angle of $\pi/4 + \phi'/2$ from the centre of rotation (taken at roughly $0.7D$ depth), equating to approximately $6.0D$ from the outer diameter of the pile. This assumption is based on a full body rotational failure mechanism, whereas in reality the model pile is experiencing a degree of bending as well as soil flow around the pile which reduces the extent of the failure. Concentric circle surface flocking (by means of laying modellers grass through a stencil, see Figure 3.16c) to track surface displacements was positioned to reveal the extent of surface movement, which did not reach the outer boundary condition, offering additional confidence of minimal boundary interaction.

Table 3.4: Model monopile geometries

Model monopile MP1 (D_{m} = 50 mm, tested at N = 100)		
Parameter	Model dimension	Prototype dimension
Diameter, D	50 mm	5.0 m
Thickness, t	2.8 mm	84 mm
Material	Aluminium	Steel
Young's Modulus, E	69 GPa	210 GPa
Flexural stiffness, EI	8.01x10^{3} Nm^{2}	8.01x10^{11} Nm^{2}
Bending resistance, M_{Ed}	920 Nm	560 MNm
Model monopile MP2 (D_{m} = 38.1 mm, tested at N = 105)		
Parameter	Model dimension	Prototype dimension
Diameter, D	38.1 mm	4.0 m
Thickness, t	3.0 mm	84 mm
Material	Aluminium	Steel
Young's Modulus, E	69 GPa	210 GPa
Flexural stiffness, EI	3.36x10^{3} Nm^{2}	4.06x10^{11} Nm^{2}
Bending resistance, M_{Ed}	510 Nm	350 MNm

At prototype scale, the appropriate wall thickness of the monopile is necessary to provide sufficient flexural stiffness as well as to prevent pile buckling and fatigue during driving. API (2011) design recommendation is for a minimum pile thickness of:

$$t_{min} \geq 6.35 + \frac{D}{100} \tag{3.2}$$

with D and t_{min} specified in mm. Table 3.4 presents the ultimate selected pile geometries for the two instrumented piles, each fabricated from aluminium. To maintain the flexural stiffness relationship with scaling, since prototype counterparts are made from steel, the wall thickness was increased accordingly,such that $E_{\mathrm{a}}I_{\mathrm{a}} = E_{\mathrm{s}}I_{\mathrm{s}}$.

Individually milled flat spots (with maximum depth from outer pile diameter to flattened area equal to 0.3 mm) for strain gauge placement, and channels for wire conveyance ensured the preservation of the original pile cylindrical profile. At the point of greatest material removal for gauge and wire management, the bending inertia, *EI*, in the major plane was reduced locally by 4.0 %. A fine layer of epoxy was then positioned around these for protection and electrical insulation and any protruding epoxy was made flush with the curvature of the pile using fine sandpaper. Model pile MP1

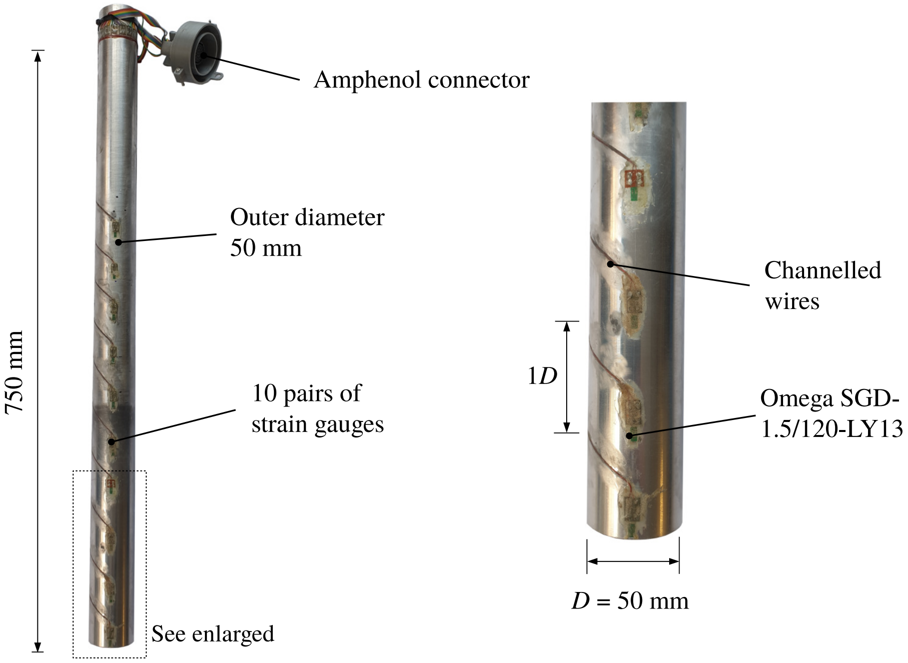

(a) MP1 (D=50 mm)

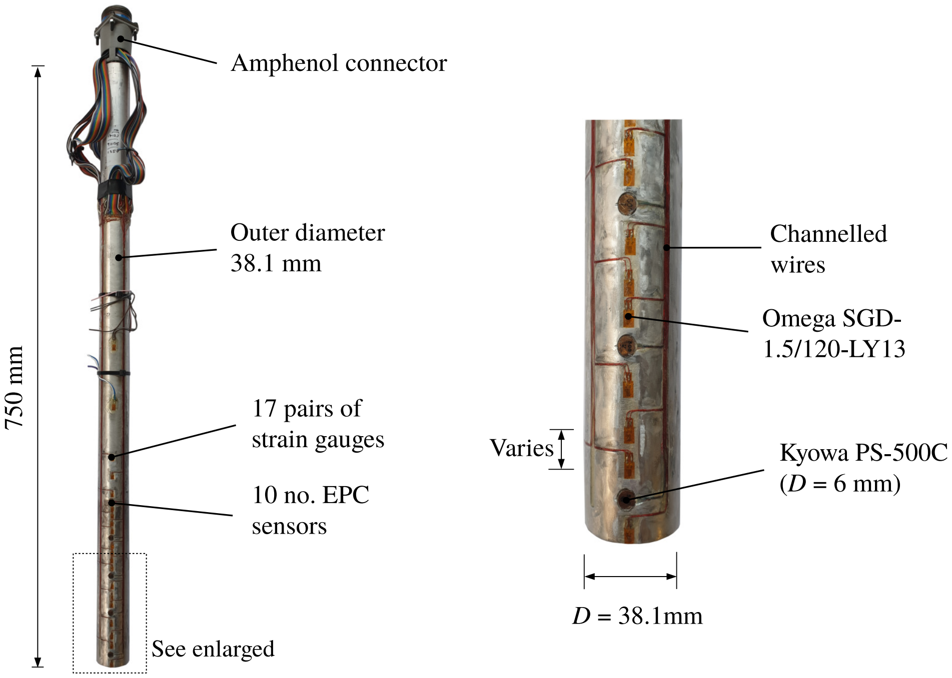

(b) MP2 (D=38.1 mm)

Figure 3.10: Instrumented model monopiles

(Figure 3.10a) was instrumented with 10 pairs of strain gauges (Omega SGD-1.5/120-LY13, gauge resistance = 120 Ω, grid length and width = 1.5 and 1.2 mm respectively, factor ≈ 2.1) at an equal spacing of the pile diameter in half Wheatstone bridge configurations. Signal wires were channelled up the side of the pile and connected to a 48-way amphenol connector to ease pile transport and installation. The electrical connection was then made when the temporarily restrained pile was in position in the strongbox.

The level of instrumentation complexion on model pile MP2 (see Figures 3.10b) was significantly greater. Here, 17 pairs of strain gauges (same model gauges as MP1) were located on the major plane, with a concentration close to the mudline given the greater precision of bending moment behaviour required here. A further 3 pairs were positioned on the minor plane to monitor the out-of-plane bending. In addition to this, 10 individual miniature earth pressure cell (EPC) sensors (Kyowa PS-500C, D = 6 mm, $P_{\max}$ = 500 kPa) measuring direct applied normal stress were located at regular intervals beneath the mudline in milled counter sunk holes and made flush with the pile outer diameter. All signal wires for MP2 were again directed in milled channels to the pile head and connected to a 128-way amphenol connector.

As an investigation of the effect of instrumentation and associated epoxy protection on pile surface roughness, the behaviour of MP2 was compared against two model

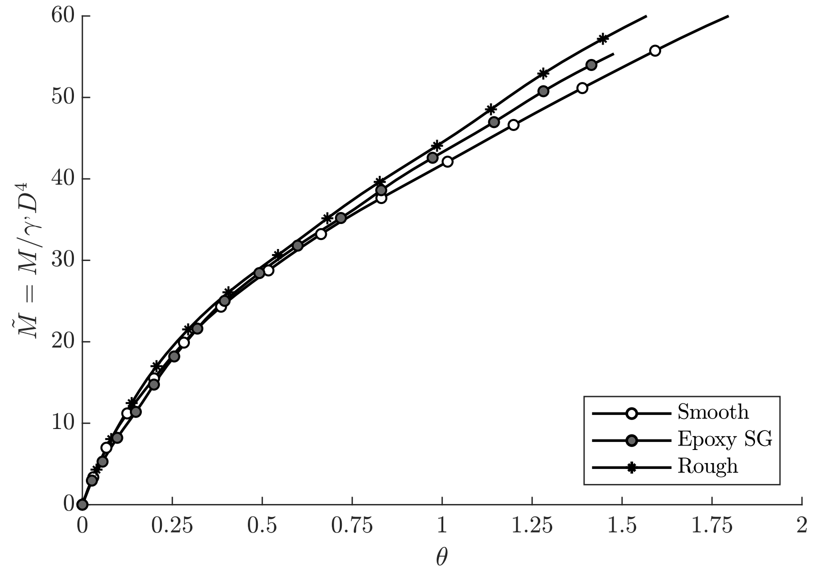

Figure 3.11: Global $\tilde{M} - \theta$ response depending on pile roughness (tests no. M18–M19 & M23)

uninstrumented piles, of the same geometry – one polished with very fine sand paper to ensure as smooth finish as possible, one upon which the sand (HST95) was glued to generate a rough interface. This resulted in relative roughness values, R_{t}/d_{50}, ≈ 0 & 1 for the smooth and rough respectively. It would be expected that the instrumented model pile presents a relative roughness value somewhere in between the smooth and rough limits. Each pile setup was jacked into position at $1g$, however little to no increase in jacking force was observed across the three configurations.

Global moment–rotation observations are presented in Figure 3.11. The model monopile with rough interface exhibits a very slight increase in ultimate lateral capacity with negligible differences to initial stiffness. Rosquoët et al. (2010) and Klinkvort (2012) observed similar behaviour. The monontonic response for MP2 lies in between the full rough and smooth responses. This provides confidence that the addition of instrumentation does not significantly affect pile performance, not just in terms of changes in surface roughness but also due to material losses.

3.4.3 Instrumentation calibration

The correct and accurate calibration of the instrumentation located on the model monopiles is vital since this drives the calculation of bending moment, and ultimately shear force and soil reaction force profiles. A small error here develops into a much larger discrepancy after several differentials. Strain gauge bridge configurations were calibrated in bending as well as the EPC sensors under direct soil stress. Any additional voltage output recorded by the EPC sensors during the bending calibration was also checked and taken into consideration during data analysis. In addition, verification of the model pile Young's Modulus was carried out by means of a circular ring compression test of a number of separate cross sectional areas. This was found to be 69.0 GPa (± 0.1%).

(i) Strain gauge calibration: strain gauge output voltage behaviour was calibrated using a simple 3-point bending test (typical calibration setup for an uninstrumented pile yield test illustrated in Figure 3.12). This was selected ahead of a 2-point cantilever setup due to the the greater similarities between the developed moment profile and that expected in the experiments. Through curiosity, two different free end support geometries were selected for comparison across the calibration process: a flat support sitting directly on the external diameter (SC1), a distance of 19.05 mm ($0.5D$) from the neutral axis (NA); and a V-notch section at an angle of 45 degrees (SC2), supporting the pile on the angle at a distance of 13.47 mm ($0.35D$) from the NA. Loading at two separate locations (distances l_{A} from the support) was performed for each 90^{o} angle around the circumference of the pile (*i.e.* both positive and negative bending on the

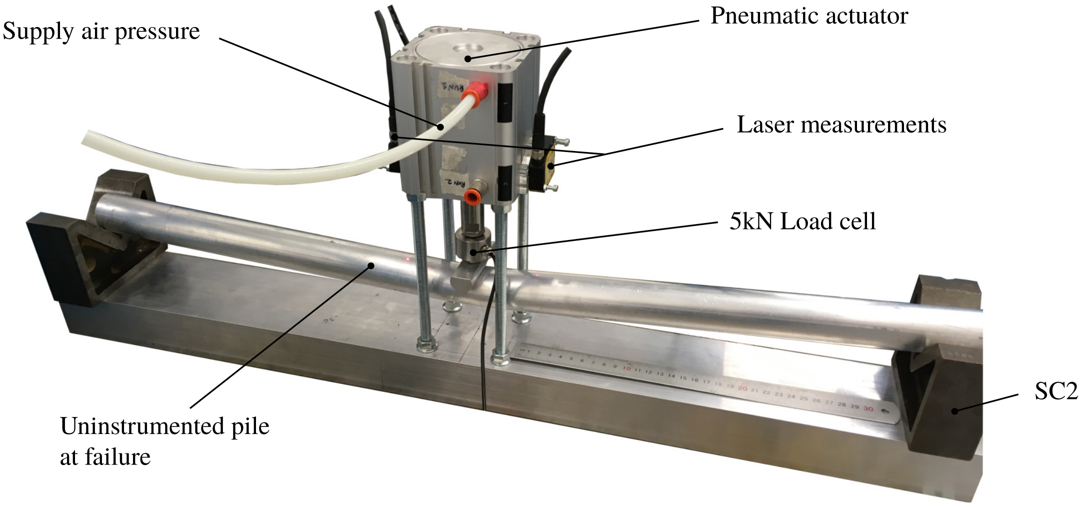

Figure 3.12: Model pile strain gauge calibration setup and support conditions

major and minor planes). These were then calibrated against theoretically predicted bending moments using classical mechanics theory calculated at the centroid location of each strain gauge pair.

The raw output voltage (mV) for both support conditions were explored for the same applied load conditions and calibration setup geometries. Any differences in output voltage measured prove that the nature of support condition affects the bending behaviour and needs to be considered. From Figure 3.13a, there is a distinct variation – output strain for SC1 is noticeably greater than that for SC2 for the same applied load at the same distance from the support. Results from a complimentary FEM study are in agreement and show an absolute shift in bending profile as the support condition's distance relative to the NA changes (see Figure 3.13b). The observed offset is synonymous of a reduction in beam length. In the light of this, it is recommended that the support condition for any monopile calibration should be noted and where possible be selected as per support condition SC1 since this appears to provide the most appropriate strain behaviour.

***(ii) EPC sensor calibration*:** these were ultimately calibrated by direct measurement of the change in raw voltage output from the horizontal stress increase during the incremental spin-up of the centrifuge (where $\sigma_\mathrm{h} = K_0\sigma_\mathrm{v}$, with the value of K_0 taken as $1 - \sin\phi'$ for WIP cases). The effects of over and under stress from the centrifuge methodology were taken into account. It was also assumed that there was no pile vertical movement during spin-up. Prior to this decision, calibration had been made in

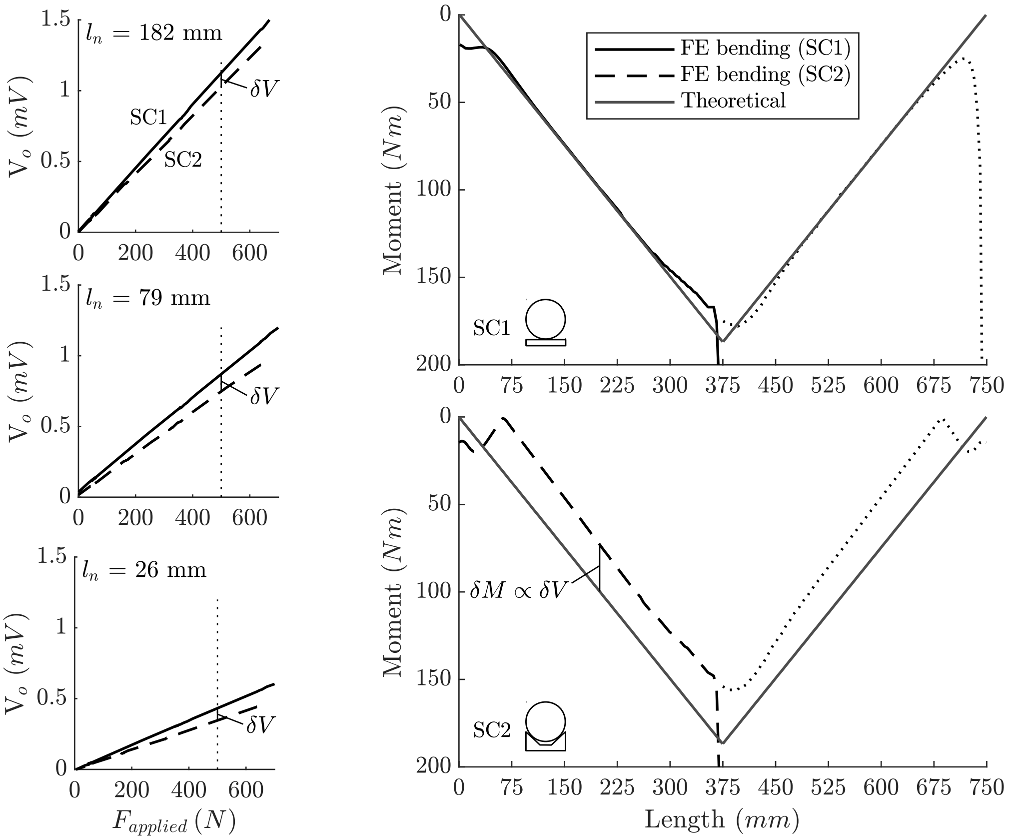

(a) (b)

Figure 3.13: (a) Raw output voltages from strain gauges for free support conditions SC1 and SC2; (b) comparison with FEM parametric study. Note l_n represents distance from support to gauge of interest

both an air chamber as well as in a shear box under direct stress. However, these did not provide a good representation of the contact stresses expected for the centrifuge application – air did not represent the finite number of grains which are in contact with sensor diaphragm and gave a unrepresentatively large output, and the arching characteristics observed in the shear box gave an output that became progressively too low at high normal stresses. It was also not anticipated that individual sand particle contact points would provide false, high output readings given the sensor diameter, d_{EPC}, to particle d_{50} ratio was quite large ($d_{\mathrm{EPC}}/d_{50} = 35$).

For each EPC used, the manufacturer supplied mmV/V calibration factor for direct pressure was stipulated as the same, 0.902 mmV/V, equating to 555 kPa/mV at 1V excitation. This of course means that each EPC sensor theoretically should present the same output for the same applied soil pressure. With this in mind, final calibration

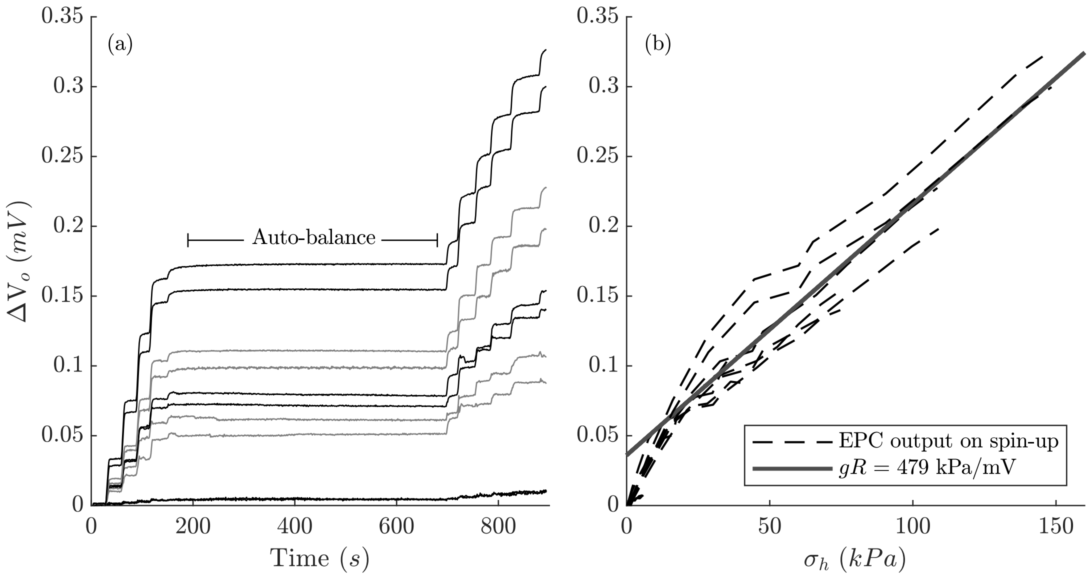

Figure 3.14: Typical EPC output voltages during calibration: (a) centrifuge spin-up; (b) comparison with theoretical horizontal stress

factors were adopted for the direct applied pressure from HST95 sand based on the mean of all individual EPC calculated relationships across all centrifuge incremental spin ups. This totalled 120 individual calibrations. Factors from each of the 120 individual calibrations are presented in Figure 3.15. As shown, the inclusion of EPC sensors 1 and 6 (which lie at 10 mm beneath the mudline at model scale) presents a much wider scatter in data, since the calibration here was only performed over a stress range of 0–15 kPa, less than 5 % of the range of those at depth. It was therefore decided to remove S1 and S6 from the calibration dataset mean and the calibration factor was chosen to take a value of 479 kPa/mV at 1V excitation.

3.4.4 Monopile installation

Both wished-in-place (WIP) and jacked monopile installation methods were explored across the test matrix. For the WIP condition, a base layer of sand was pluviated to the height of the proposed base of the monopile plus a nominal 10 mm to allow for settlement of the model pile under its self-weight at 1g. A series of perspex guides cut according to the geometry of the strong box provide clear holes to ensure the pile was located centrally and in the correct plane according to the loading direction (Figure 3.16a). Fine support wiring (diameter 0.2 mm), as shown in Figure 3.16b, was lassoed around the pile and attached to the strong box to restrain the pile from lateral movements during the pluviation process. The perspex guides were then subsequently removed and the pluviation process continued, allowing the sand to fall around the pile

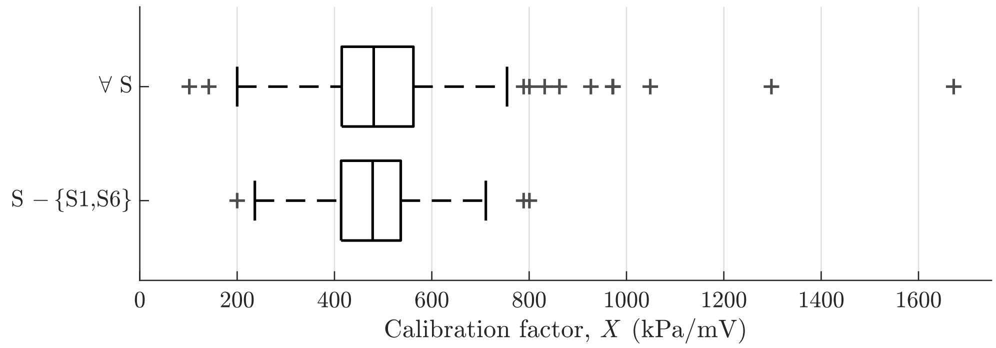

Figure 3.15: Variation in EPC calibration factors across individual sensors ($\mu_{\forall S}$=514 kPa/mV, $\mu_{S-\{S1,S6\}}$=479 kPa/mV)

until the desired embedment depth was achieved. This provided a K_0 initial condition. A calculated amount of sand representative of the depth of an unplugged scenario was placed inside the pile so that the internal soil column overburden stress at the base of the pile was maintained.

For the case of the jacked pile at $1g$, a full bed of sand to the desired height was pluviated. A bespoke attachment system was then positioned to the base of the z-direction actuator of the 3DOF pluviator, which allowed for a perfectly vertical jacking process (vertical alignment was adjusted using a four screw levelling system, with spirit level and plumb line, see Figure 3.17). The pile was then jacked at a rate of 2 mm/s to the desired embedment depth. Figure 3.18 presents the jacking force, and associated pile tip resistance, for each installation. A minor plug was observed for 12 out of the 17 jacked installations ranging from 2 to 14 mm, which appears to start at a penetration of around $1D$.

After installation, the pile was temporarily restrained above the mudline to prevent any unwanted disturbances before the model could be placed on the centrifuge beam. As previously mentioned, a texture was positioned on the surface of the sand in a series of concentric circles at a spacing of $0.5D$ from the extremity of the pile (see Figure 3.16c). The purpose of this was to track surface movements from both the monotonic pushover and cyclic tests.

A simple review of pile installation method on global moment-rotation response is made in Figure 3.19 (tests no. M17 & M18), where a greater stiffness and ultimate lateral capacity for a pile jacked at $1g$ is compared to a WIP condition, albeit to a small degree. This increase in stiffness can be attributed to the dilation of the dense sand that takes place under large strain shearing (Houlsby, 1991). From previous literature,

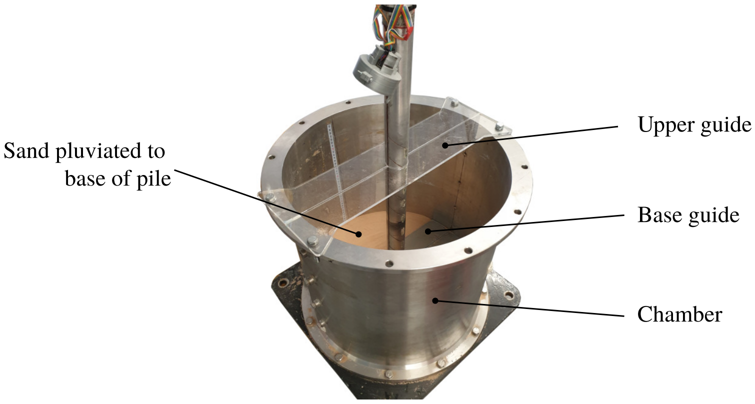

(a) Placement of laser cut guides

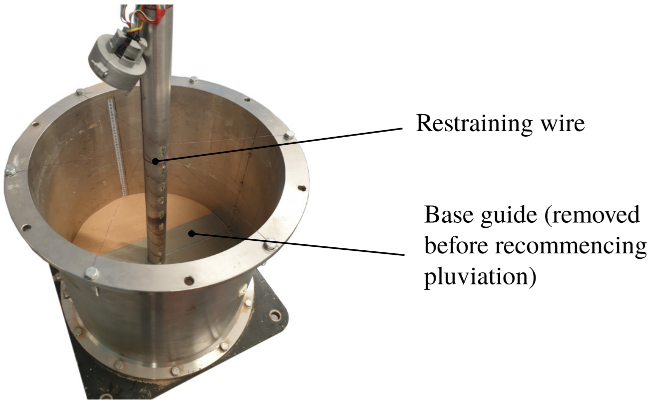

(b) Model pile restrained by fine wire

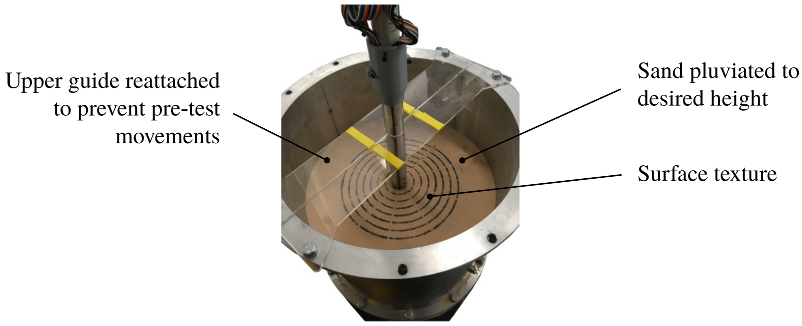

(c) Final setup pre-placement on centrifuge beam

Figure 3.16: Installation of WIP monopile

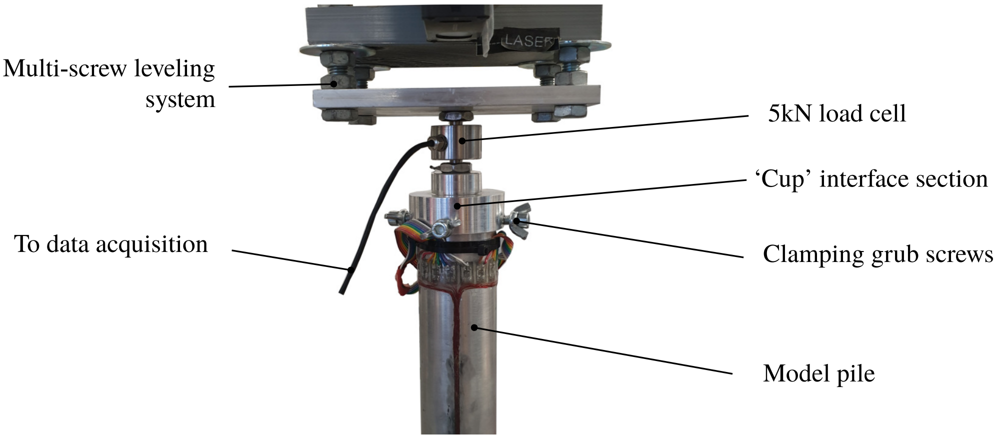

Figure 3.17: Monopile jacking using 3DOF actuator

the effect of driving is more noticeable at Ng (Dyson and Randolph, 2001; Klinkvort, 2012) given the greater initial confinement from the higher overburden stresses which allows for greater dilation induced pile confining stresses.

3.4.5 Lateral loading setup

Lateral loads, for both monotonic and cyclic experimental setups, were applied to the model monopile by means of stress based actuation systems. For the case of monotonic load, an 80 mm diameter bore compact double action pneumatic cylinder actuator (model no.: SMC CD55B80–80M) was deployed (see Figure 3.20a). With a safe operating pressure of 10 Bar, this was theoretically capable of applying a maximum load of approximately 5.0 kN. A load cell calibrated over the same range of 5.0 kN was attached between the end of the actuator piston and a T-shaped loading arm which interfaced with the pile, however did not attach or restrain the pile. Gradually increasing load was supplied by increasing actuator back pressure at a rate of 15 kPa/min, equating to an increase in force of approximately 75 N/min. Load was subsequently removed by increasing pressure to the front of the actuator at the same rate, whilst maintaining the back pressure constant. In this geometric arrangement, it was possible to reach load eccentricities of up to 8D for a typical sand bed height above the mudline.

Continuous cyclic loading was provided using a dual acting SMC low friction 25 mm diameter bore piston (model no.: SMC MQMLB25H–30D) together with two opposing +24V input solenoid valves (see Figure 3.20b). This generated a load capacity of 375 N at 7 Bar of input air pressure at a maximum frequency of 8 Hz. Individual test load magnitude and frequency were controlled by the piston input pressure and user-

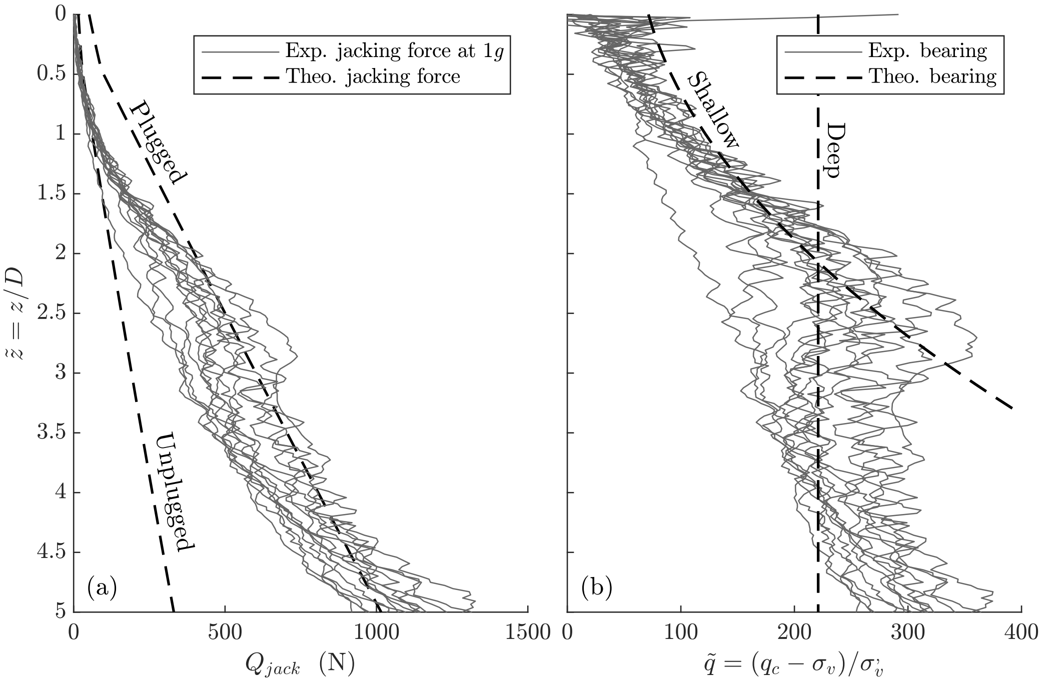

Figure 3.18: (a) Jacking force at $1g$ for model monopile installation; (b) normalised end bearing resistance

defined solenoid digital square wave frequency and phase respectively. The option of additional vertical load was controlled by the placement of static lead shot mass within a 3D-printed plastic collar at the top of the pile.

Two Baumer (OADM 12 type) laser sensors were directed perpendicular to the pile at two different positions to measure pile deflection (the location relative to load application of which varied from test to test depending on the geometry). These had the advantage over traditional linear-variable displacement transducers (LVDT) given the non-contact measurement and the capability of setting a specific measuring range specific to individual experiments to maximise signal to noise ratio across the test matrix. Figures 3.21 and 3.22 illustrate the complete setups both schematically and as taken by camera.

3.4.6 Data acquisition

The UoS50gT centrifuge cabinet is equipped with a National Instruments (NI) PXIe-8135 on-board computer, where a number of different NI modular hardware options can be found within the 18 slot chassis (see Figure 3.24). Of these, the NI PXI-6229 (32 AI, 48 DIO and 4AO) provides the +5V digital output (DO) square wave signal to control a user-designed relay switch board driving the amplified +24V solenoid valves

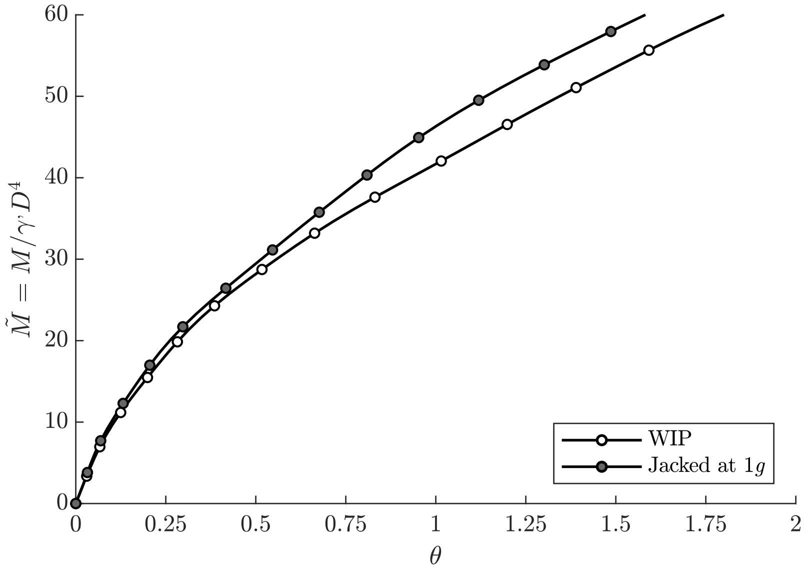

Figure 3.19: Global $\tilde{M} - \theta$ response depending on installation method (tests no. M17–M18)

for air pressure control (both for monotonic and cyclic load applications). Two NI cDAQ-9188XT 8 slot modules are positioned on the beam wings (see Figure 3.23), and communicate directly with the NI PXIe-1085 via ethernet connection. Within these, multiple NI-9237 C series strain/bridge input modules are located to directly measure millivolt (mV) output voltages from individual strain gauge and EPC sensors, without the need for signal amplification. In addition, one NI-9205 C series voltage input module records directly the 0–10V output voltage from the laser displacement sensors.

Two sampling frequencies were designated for the acquisition of data, the rate of which depended on the level of desired detail in pile behaviour at the given time in the test. For the monotonic test setup, the rate was set at a constant 100 Hz given the slow rate of loading and therefore all aspects of the load-unload response were captured to great precision. As for the cyclic experiments, which were run at approximately 5-6 Hz loading frequency, an increased data capture rate of 2000 Hz was selected for periods of particular interest (*e.g.* the first 100 cycles of every decade gain in cycle count). This allowed for a very high level capture of the pile behaviour at these times, however with this the raw data files gathered were very large in size. So as not to result in data overload, data was captured at a reduced rate of 100 Hz in the interim. With these, the general trends of pile behaviour at the maxima and minima of the load cycle were still able to be tracked, but the high level individual load cycle response was not captured.

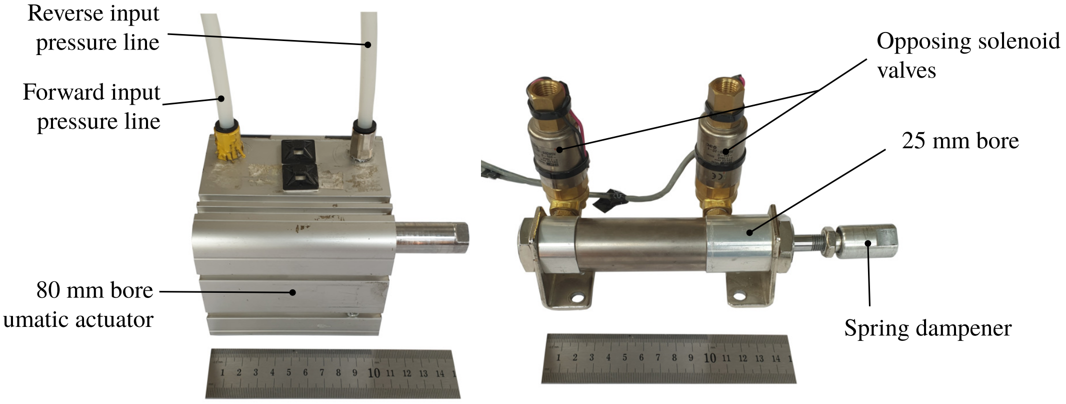

(a) (b)

Figure 3.20: (a) Double action pneumatic cylinder actuator for application of monotonic loads; (b) low friction pneumatic cylinder actuator for application of cyclic loads

3.4.7 Analysis of pile performance

To allow for a complete understanding of pile performance, it was necessary to perform a number of data processing steps to transfer the raw output voltage data into a manageable format for analysis and presentation. A flow diagram of the step process is illustrated in Figure 3.25, with description of the key stages outlined below.

***(i) Raw data packaging*:** all experimental data from each centrifuge test were imported and analysed using MATLAB (v2018b) software. Raw data packages were decomposed into individual sensor vectors and subsequently multiplied by respective calibration factors. Any non-zero data points at the start of the test (after centrifuge spin-up) were offset to zero as a way of data cleaning (*N.B* EPC readings were offset to the theoretical value of σ_h at the respective depth). Figure 3.26 presents an example raw voltage dataset alongside its respective ‘clean’ output for a typical monotonic load experiment.

***(ii) Filtering*:** for each calibrated data package, signal processing was implemented by means of a low pass filter, with the frequency threshold selected after scrutiny of the Fast Fourier Transform (FFT) distribution. Typical lower band frequencies for 100 Hz and 2000Hz sampling frequencies were in the region of 0.5 & 10 Hz and 12 & 50 Hz for monotonic and cyclic loading respectively. Figure 3.27 illustrates the impact of processing of the output data for a high frequency cyclic load sequence sampled at a rate of 2000 Hz.

***(iii) Interpolation*:** with data now in a manageable format of engineering units and much reduced electrical signal noise, post-processing was able to commence. Firstly,

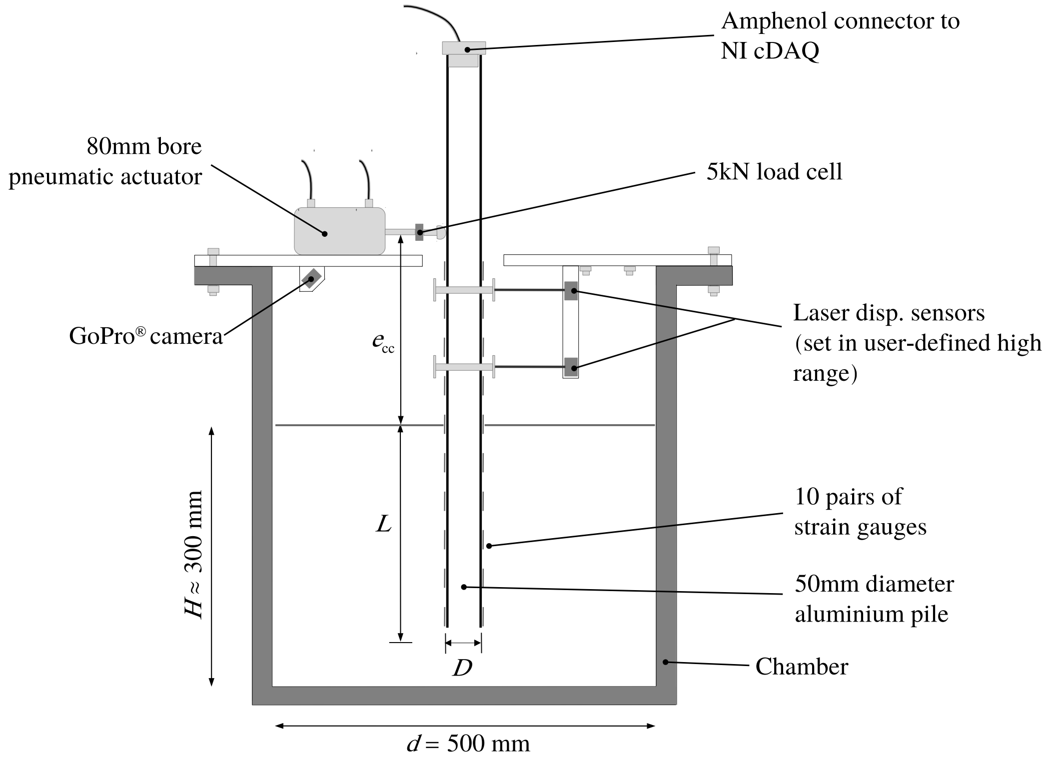

(a) Monotonic loading

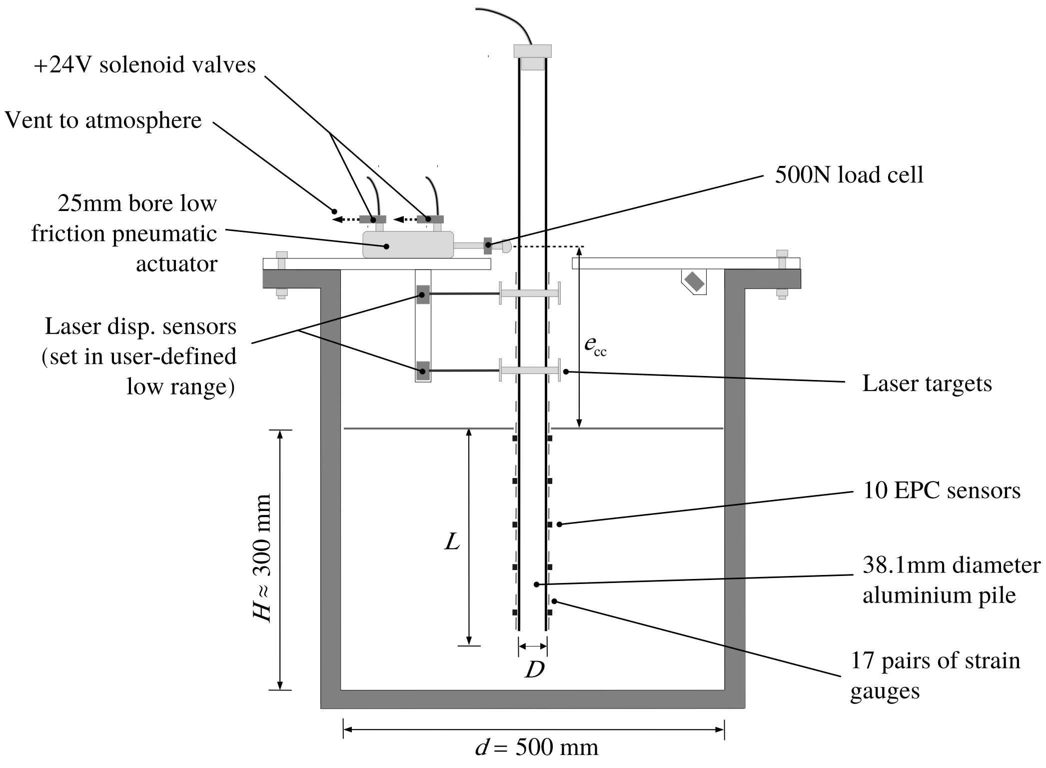

(b) Cyclic loading

Figure 3.21: Schematic illustration of experimental setup

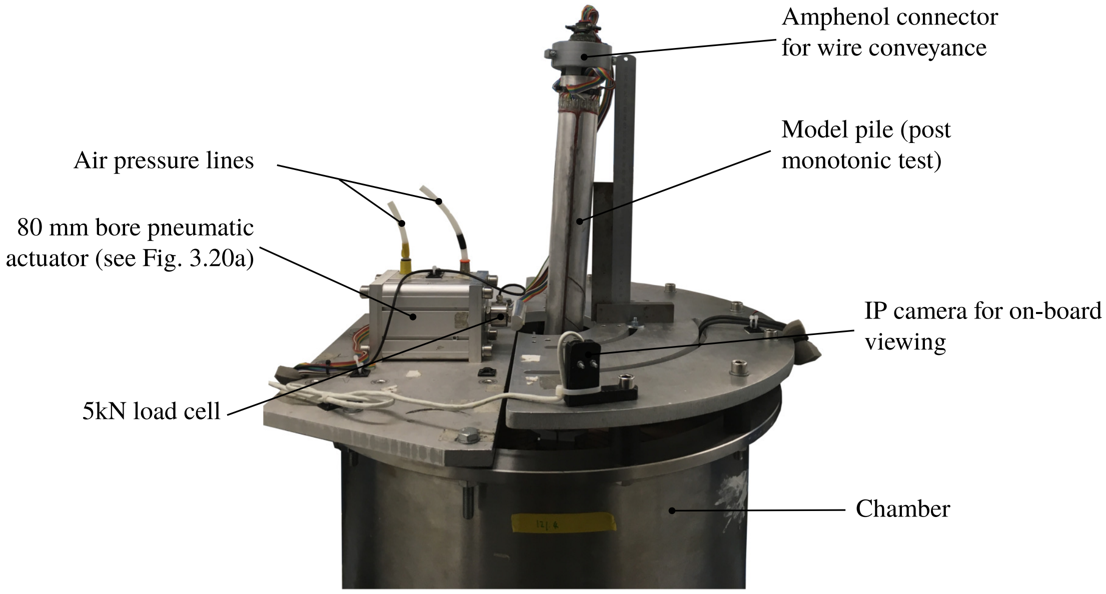

(a) Monotonic loading

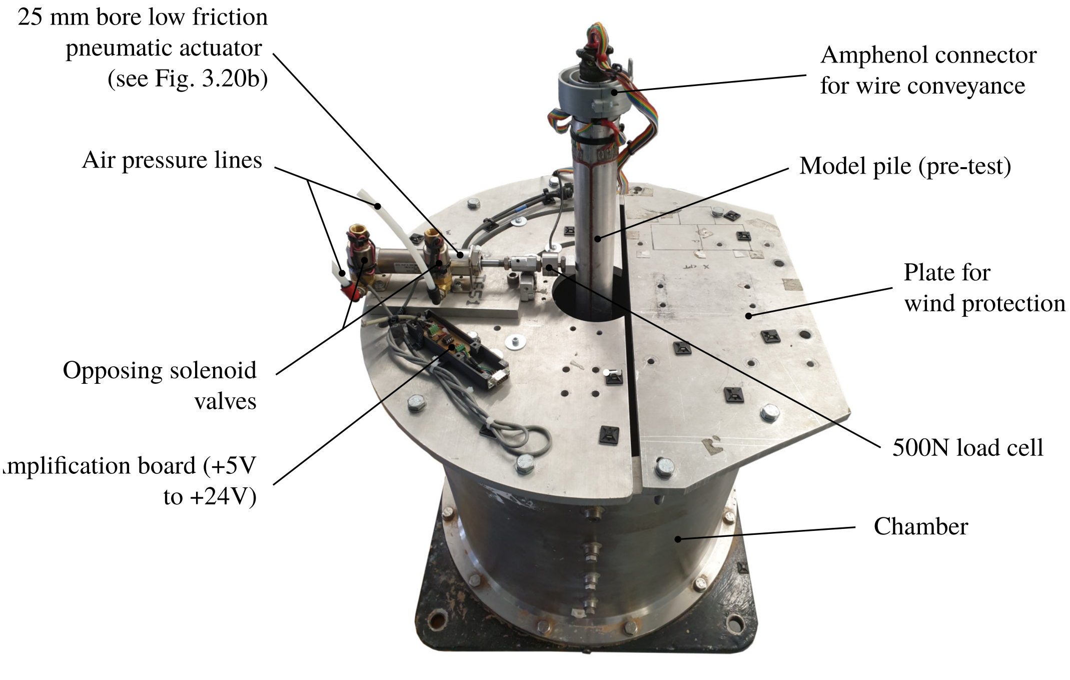

(b) Cyclic loading

Figure 3.22: Images of experimental setup

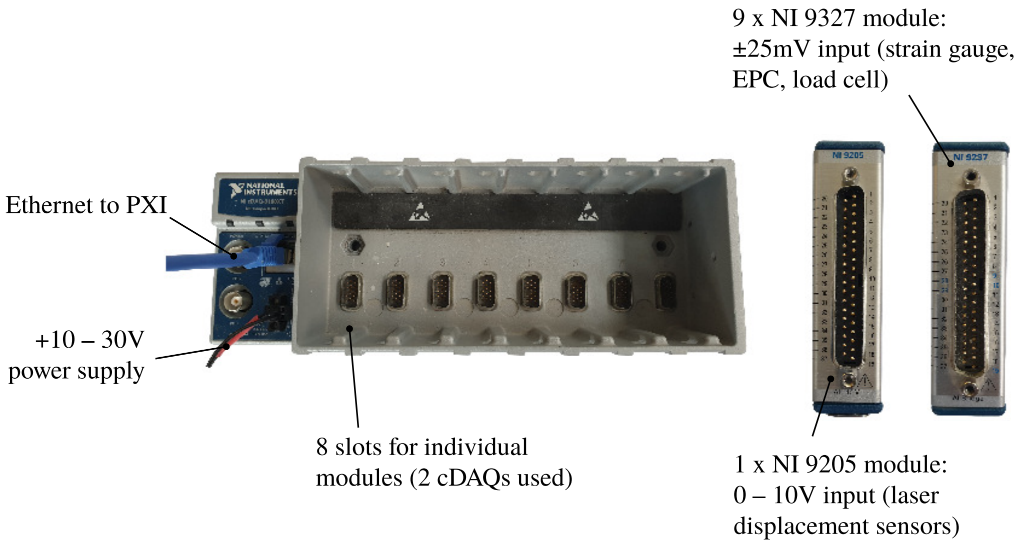

Figure 3.23: NI cDAQ-9188XT data acquisition chassis with C series modules

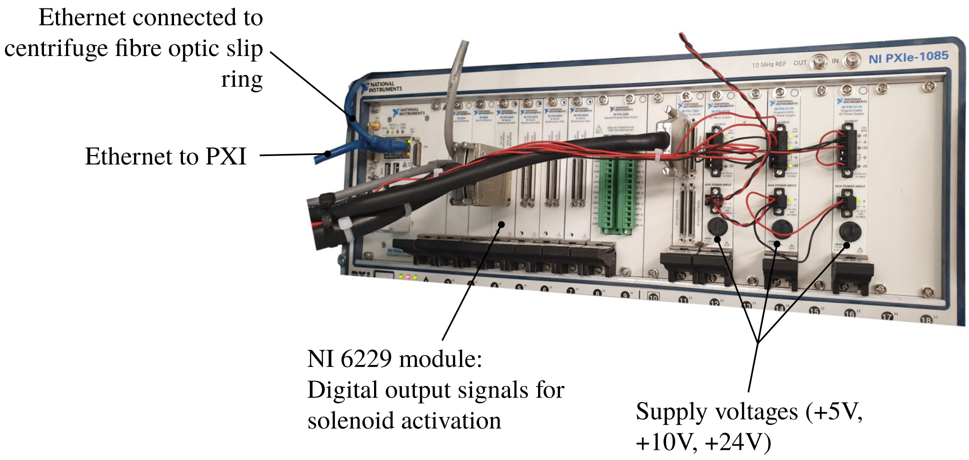

Figure 3.24: NI PXIe-1085 on-board computer

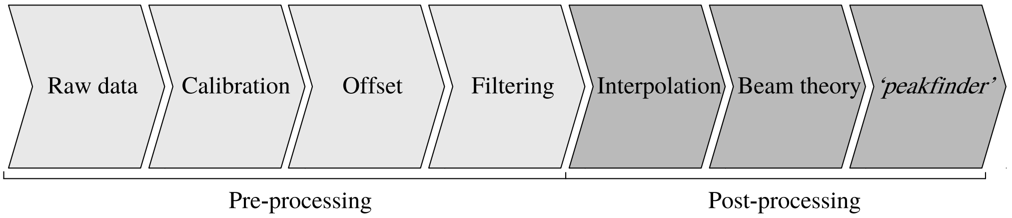

Figure 3.25: Flow chart from raw voltage output to analysed results

given the discrete locations of strain gauge sensors and therefore acquired bending moment with pile depth, it was necessary to apply a method of curve fitting to describe the behaviour between these points. This would facilitate the accurate estimation of bending moment dependant variables with depth, *i.e.* deflection, internal shear and

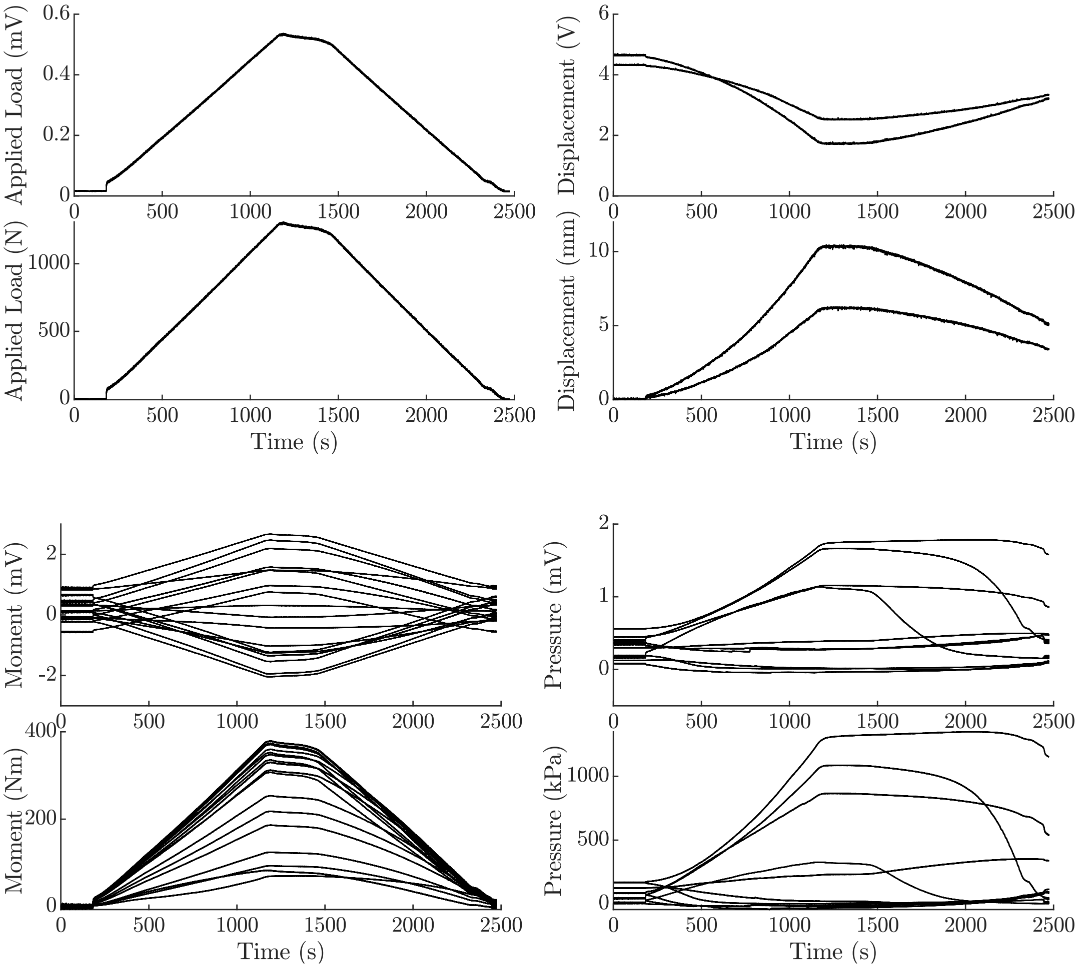

Figure 3.26: Example raw data set from monotonic load experiment

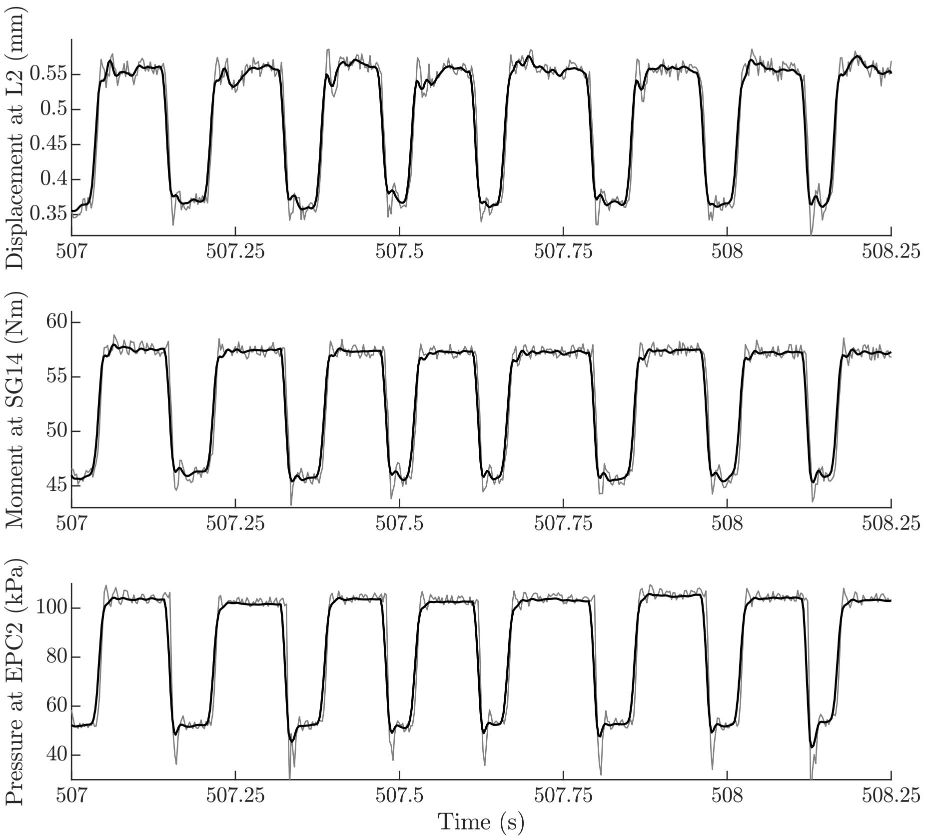

Figure 3.27: Example low-pass filtering of high frequency dataset using FFT

soil reaction force. Across literature, a selection of weighted splines (Haigh, 2014) and high-order polynomials (Kirkwood, 2015) has been made depending on the author's experience and observed outcomes. In this study, it was decided to adopt the piecewise polynomial *spline* function from MATLAB *cftool* toolbox.

Figure 3.28 presents an example of how an inappropriate curve fitting process can affect the higher order differentials. It can be seen that while apparent bending moment shapes remain relatively unaffected, with each order differential, the errors that ensue become greater and greater. Despite the general trends being captured across each, significant variations, particularly close to the pile toe, can be clearly observed.

***(iv) Beam theory*:** pile rotation and deflected shape was extracted from the fitted bending moment, M, profiles by means of the Timoshenko beam theory (Timoshenko, 1953). Timoshenko beam theory follows the same principles as Euler-Bernoulli elastic beam theory (Timoshenko, 1921), with the addition of shear deformation and rotational bending effects that may be present for particularly large diameter piles, such

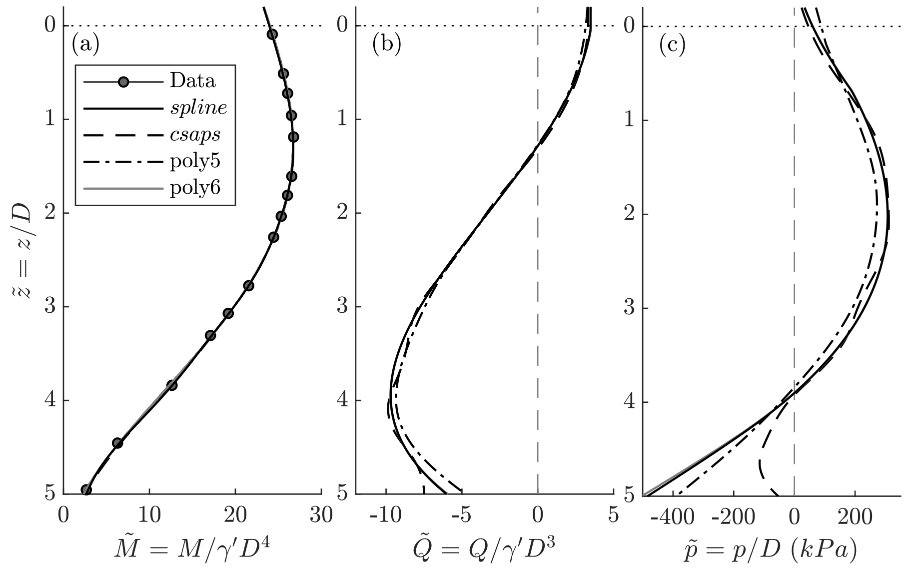

Figure 3.28: Effect of interpolation curve selection between discrete bending moment points: (a) bending moment; (b) shear force; (c) soil reaction force

that:

$$M = -EI\frac{\partial^2 y}{\partial z^2} \quad \text{and;} \tag{3.3}$$

$$\frac{\mathrm{d}y}{\mathrm{d}z} = \theta - \frac{1}{\kappa AG}\frac{\mathrm{d}}{\mathrm{d}z}\left(EI\frac{\mathrm{d}\theta}{\mathrm{d}z}\right) \tag{3.4}$$

where y is the pile deflection at a depth z, θ is the angle of pile rotation relative to its centreline, κ the Timoshenko shear coefficient taken as ≈ 0.6 for a hollow circular cross section (Hutchison, 2001), A is the cross sectional area and G the material shear modulus.

The above were numerically computed by the finite difference (FD) approximation method, with the laser measured displacements at two locations above the mudline as constants of integration, giving deflection at any point along the pile depth. Pile head and base boundary conditions were computed as free ends (however not assumed zero moment and shear). Internal pile shear and soil reaction force were subsequently calculated by numerically differentiating the bending moment profile both once and twice respectively. From here, any level of data analysis can be presented, *e.g.* global monopile moment-rotation or individual soil $p - y$ springs.

(v) 'peakfinder': a number of cyclic experiments reached cycle counts in the order of magnitude of 10^5, and therefore presented very large data file sizes. In order to accelerate the process of locating individual cycle number peaks and troughs within

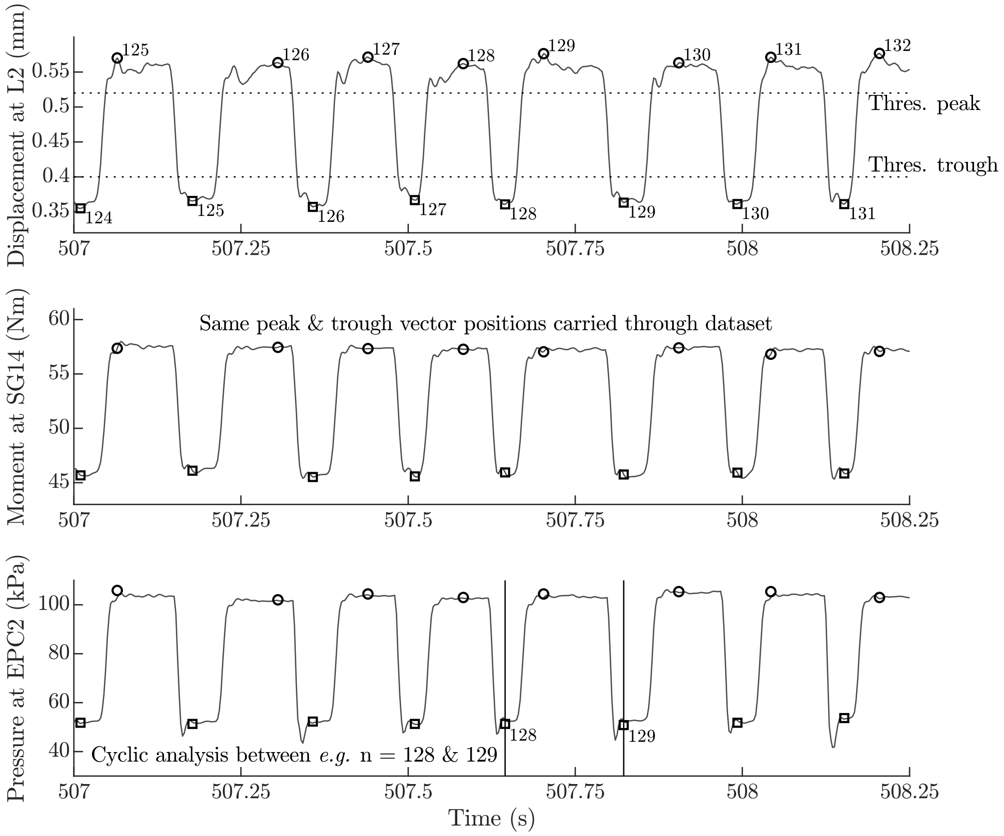

Figure 3.29: Illustration of the *peakfinder* threshold function

these, a bespoke *peakfinder* MATLAB script was written. The *peakfinder* function was able to locate the individual cycle peak and trough array position, provided a threshold maximum was specified. This allows only the one data maximum above that threshold to be counted, preventing one cycle from being counted twice if two spikes in data were seen, for example. Armed with the locations of the peaks and troughs, analysis of individual cycle behaviour can be easily made by selecting all data points in between adjacent cycle trough vector positions. Figure 3.29 illustrates the graphical output from an example high frequency cyclic load test.

3.5 Test matrix

A total of 44 centrifuge experiments were carried out. These can be separated into monotonic pushover and long-term cyclic tests, with the monotonic test results providing the backbone for cyclic normalisation. Tables 3.5 and 3.6 present the complete test matrix of all the experiments performed, with any additional specific test information of interest also stipulated. See Section 5.2.1 for definition of cyclic load parameters outlined in Table 3.6.

Table 3.5: Monotonic pushover test matrix

Test no.	Model pile	g level	D_{proto} (m)	L/D	R_d (%)	Installation method	Specific test information
M1*	UI	100	5.0	5	79.5	WIP (hand)	
M2*	UI	100	5.0	5	81.1	WIP (hand)	
M3*	MP1	100	5.0	4	80.2	WIP (hand)	
M4	MP1	100	5.0	5	80.4	WIP (hand)	
M5*	MP1	100	5.0	6	78.0	WIP (hand)	
M6*	MP1	100	5.0	8	81.5	WIP (hand)	
M7*	MP1	100	5.0	6	31.2	WIP (hand)	
M8	MP1	100	5.0	5	80.4	Driven (auto#$^{(1)}$)	
M9	MP1	40	2.0	5	79.0	Driven (auto#)	
M10	MP1	40	2.0	5	79.2	Driven (auto#)	
M11*	UI	100	5.0	5	84.0	WIP (hand)	Solid steel pile ($\approx 10EI$)
M12*	UI	100	5.0	5	81.3	WIP (hand)	Plastic pile ($\approx 0.1EI$)
M13	UI$^{(2)}$	105	4.0	5	80.1	WIP (auto)	Pluviation path orientation 0°
M14	UI	105	4.0	5	80.7	WIP (auto)	Pluviation path orientation 30°

Table 3.5: Monotonic pushover test matrix (cont.)

Test no.	Model pile	g level	D_{proto} (m)	L/D	R_d (%)	Installation method	Specific test information
M15	UI	105	4.0	5	81.2	WIP (auto)	Pluviation path orientation 60^{o}
M16	UI	105	4.0	5	81.5	WIP (auto)	Pluviation path orientation 90^{o}
M17	UI	105	4.0	5	80.5	WIP (auto#)	Pluviation path orientation #
M18	UI	105	4.0	5	79.8	Driven (auto#)	Smooth pile
M19	UI	105	4.0	5	81.8	Driven (auto#)	Rough pile
M20	MP3	105	4.0	5	81.1	WIP (hand)	
M21	MP3	105	4.0	5	77.9	Driven (hand)	
M22	MP3	105	4.0	5	81.2	Driven (hand)	
M23	MP3	105	4.0	5	80.2	Driven (auto#)	
M24	MP3	105	4.0	5	80.6	Driven (auto#)	

*supplementary tests; results not presented in thesis

(1) # = criss-cross pluviation pattern

(2) UI = uninstrumented pile

Table 3.6: Cyclic test matrix

Test no.	Model pile	g level	D_{proto} (m)	L/D	$\mathrm{R_d}$ (%)	Installation method	$\zeta_{\mathrm{b}=M_{\max}/M_{\mathrm{Ed}}}$	$\zeta_{\mathrm{c}=M_{\min}/M_{\max}}$	Cycle no.
C31	MP1	100	5.0	5	81.0	WIP (hand)	0.67	0.0	71
C32	MP1	100	5.0	5	79.5	WIP (hand)	0.49	0.0	1,229
C33	MP1	100	5.0	5	83.0	WIP (hand)	0.23	0.0	62,940
C34	MP1	100	5.0	5	80.4	WIP (hand)	0.16	0.0	100,698
							0.23		45,910
C35	MP1	100	5.0	5	81.7	WIP (hand)	0.09	0.0	100,290
							0.16		47,337
							0.09		17,763
C36	MP1	100	5.0	5	82.6	WIP (hand)	0.04	0.0	5,036
							0.07		5,519
							0.11		4,787
							0.14		4,951
							0.18		4,770
							0.21		4,919
							0.24		4,751
							0.26		1,119

Table 3.6: Cyclic test matrix (cont.)

Test no.	Model pile	g level	D_{proto} (m)	L/D	R_d (%)	Installation method	$\zeta_\text{b}{=}M_\text{max}/M_\text{Ed}$	$\zeta_\text{c}{=}M_\text{min}/M_\text{max}$	Cycle no.
C37	MP2	105	4.0	5	79.9	Driven (auto#)	0.08– 1.58	0.0	1 per ζ_b 14 total
C38	MP2	105	4.0	5	79.8	Driven (auto#)	1.55	0.0	22
C39	MP2	105	4.0	5	81.0	Driven (auto#)	1.23	0.0	100
C40	MP2	105	4.0	5	81.2	Driven (auto#)	0.99	0.0	250
C41	MP2	105	4.0	5	79.5	Driven (auto#)	0.68	0.0	10,012
C42	MP2	105	4.0	5	80.4	Driven (auto#)	0.71	0.0	52
C43	MP2	105	4.0	5	78.9	Driven (auto#)	0.23	0.0	10,074
							0.45		5,071
							0.60		2,774
							0.68		1,070
							0.61		2,748
							0.44		5,014
							0.24		10,044
C44	MP2	105	4.0	5	79.0	Driven (auto#)	0.33	0.0	10,029
							Random		1,220
							0.33		10,059

4. Monotonic Lateral Behaviour

4.1 Statement of intent

It is the aim of this chapter to explore the monotonic behaviour of the monopile. Concerns associated with the translation of current lateral pile design methodologies from across literature are first recognised and key design challenges are identified. Results from a series of lateral pushover experiments performed in the UoS50gT centrifuge are then presented and compared against current design recommendations and proposed alternatives. In light of observations, an updated analytically derived multi-spring model is presented which takes into consideration additional resistances associated with rigid pile failure that are not currently captured. This is validated against a number of tested geometric configurations to evaluate the range of its capabilities.

4.2 Background

4.2.1 Lateral pile design

The design of a laterally loaded pile can be achieved by one of a number approaches, each offering its own distinct advantage; be it the ease/speed of the solution derivation, or the desired design outcome, *e.g.* a more accurate prediction of performance at ultimate limit or serviceability limit state. The following section briefly outlines the general concept behind a selection of the key design philosophies found across literature.

(*i*) *Limit state approximation*: this method assumes full mobilisation of Rankine active and passive earth pressures (Rankine, 1857) such that an ultimate lateral pressure distribution with depth is established. This can then be used to determine the ultimate lateral capacity of the pile by means of horizontal force or overturning moment equilibrium assuming fully rigid body rotation. Across literature, a range in ultimate lateral pressure approximations with depth for the rigid monopile case can be seen (*e.g.* Brinch Hansen, 1961, Meyerhof *et al.*, 1981). This is in part due to the individual selection of empirical shape factor accounting for the circular geometry of the pile applied to the horizontal earth coefficient, K, as well as the choice of soil pressure distribution shape with depth. Figure 4.1 presents a selection of recommendations from various authors.

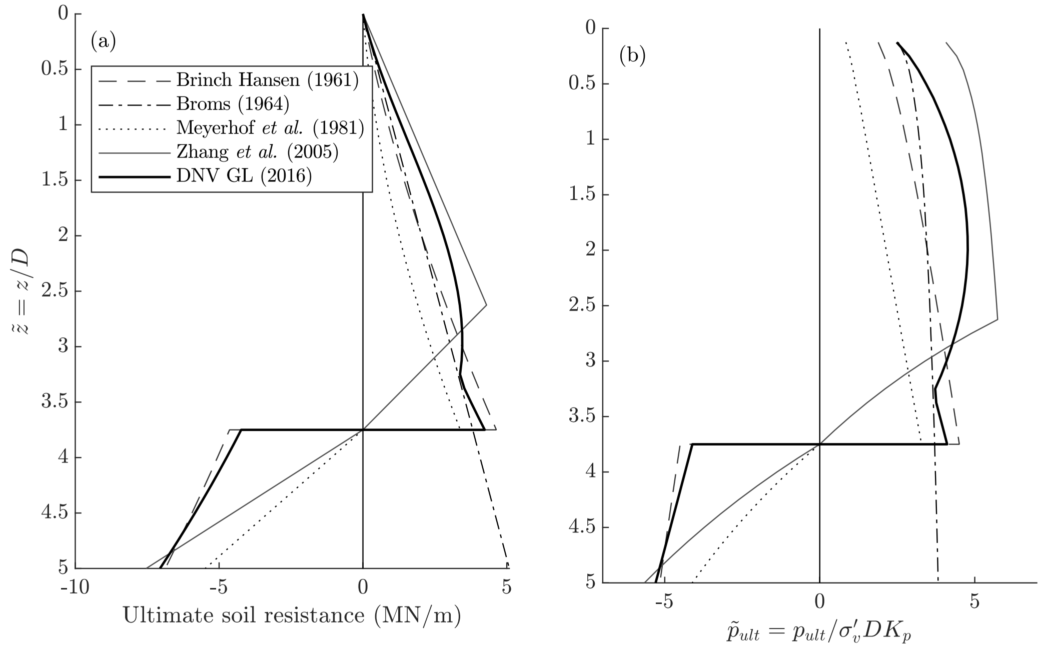

Figure 4.1: Illustration of ultimate soil resistance ($\gamma' = 16.5$ kN/m^3, $D_\mathrm{p} = 4$ m, $\phi' = 38^\mathrm{o}$)

While the limit state approach allows for the relatively straightforward calculation of pile ultimate lateral capacity, it does not permit the calculation of deflections, and as such pile head rotations, at working loads. Additionally, its validity is limited to fully rigid piles, whereas monopiles today present both rigid and flexible characteristics. The calculated ultimate soil resistance at discretised locations along the pile can however be used as a guide for the upper bound limit for future subgrade reaction spring approximations, outlined later.

***(ii) Elasticity theory*:** here the soil is simplified as a continuous, elastic, homogeneous medium (Douglas and Davis, 1964; Poulos, 1971). The elasticity method is capable of calculating exact lateral displacements based on the elastic interaction between the pile and soil. This has led to the development of a series of design equations for the prediction of pile head deformation and rotation subject to applied lateral load and overturning moment. Further to these, design charts incorporating influence factors based on the relative stiffness between the pile and soil are introduced for ease of calculation. Budhu and Davies (1988) later extended the model to a more realistic elastic perfectly plastic idealisation. Given the elastic simplification of soil deformation until plastic failure, the method is, however, restricted to only very small strain behaviour since the accurate representation of large strain is not captured. As such is rarely adopted in design.

(iii) Subgrade reaction theory**:** this method develops its roots from the early Winkler elastic spring model (Winkler, 1867), the underlying theory behind which idealises the support soil as a series of identical, independent, linearly elastic springs. Here, deformation, y, is assumed directly proportional to the applied reaction force per unit length, p, on each individually discretised spring (see Figure 4.2a) with a coefficient of proportionality for a soil defined as the modulus of subgrade reaction, k_{h}, such that:

$$p(y) = k_h y \tag{4.1}$$

To address the lack of continuity between adjacent individual soil springs, Hetenyi (1946) proposed the beam-on-Winkler foundation model where an elastic member, in this case the pile, is placed in contact with the subgrade reaction springs to allow for a degree of neighbouring soil interaction. The soil reaction force at any depth can then be directly related to pile deformation at that depth, and is calculated by means of the Euler-Bernoulli elastic beam theory (Timoshenko, 1953), outlined below:

$$EI\frac{d^4y}{dz^4} - p(y) = 0 \tag{4.2}$$

where y is the pile deformation, z the depth, EI the pile flexural stiffness, and $p(y)$ the subgrade reaction from the adjacent soil.

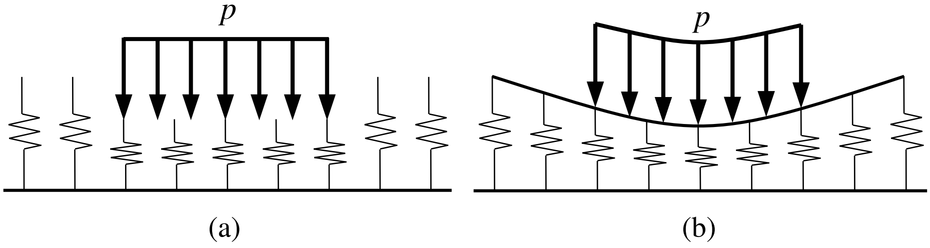

Figure 4.2: (a) Original Winkler model; and (b) beam-on-Winkler foundation

(iv) Finite element modelling**:** numerical approximations, which can represent the soil by a number of different constitutive models, are quickly establishing themselves as useful tools for monopile design. Indeed, finite element modelling (FEM) is encouraged by DNV GL design (2016) for the validation of large diameter monopile behaviour. Many 3D FEM studies (Achmus et al., 2009; Hamre et al., 2011; Haiderali et al., 2014) have been implemented across a range of monopile design scenarios and these offer a range of design charts for the prediction of pile lateral displacement based on dimensionless parameters of pile diameter, length and horizontal load. With the advancements in computer processing power, the scope for FEM to form the basis of monopile design in the future is growing, however, observational or experimental validation will always be necessary for full confidence in this approach.

4.2.2 The $p - y$ model

Of the design methods outlined above, it is an upgraded form of the subgrade reaction theory that remains the preferred choice for engineers. The application of original beam-on-Winkler foundation model theory, coupled with non-linear soil properties, was first applied to the laterally loaded pile problem during the 1950s (Reese and Matlock, 1956; McClelland, 1956). The non-linearity of the derived pile-soil interaction relationships coined the term '$p - y$ curve', and its fundamental nature is illustrated in Figure 4.3. It is worth noting that the historical progression and development of the $p - y$ curve for the laterally loaded pile translation has been documented in great detail on numerous occasions across literature (*c.f.* Brøbæk et al., 2009; Rosquoët et al., 2010; Klinkvort, 2012), and therefore only key milestones are outlined here.

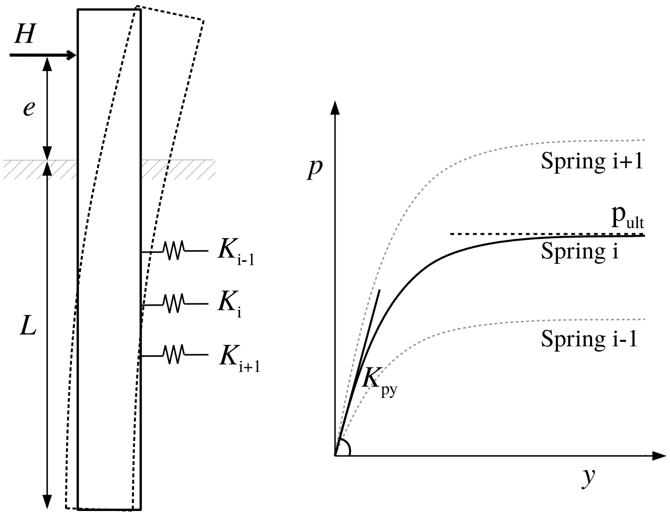

Figure 4.3: Nature of a $p - y$ curve

In the original studies of Reese and Matlock (1956) and McClelland (1956), the first non-linear $p - y$ curves were back-analysed using strain gauge measurements from a series of lateral load field tests on long, slender piles. The developments at this time coincided with two major advancements – the offshore O&G industry and the digital computer, the latter essential for the accurate calculation of the non-linear fourth order differential equation used to derive the $p - y$ relationship. Many alternatives have subsequently been proposed, each building upon previous observations, to accurately describe the behaviour of slender piles under monotonic lateral loading conditions (*e.g.* Reese and Matlock, 1956; Alizadeh and Davisson, 1970; Reese et al., 1974). Ultimately, it is the model of O'Neill and Murchison (1984) that is adopted in the current DNV GL (2016) and API (2011) design code recommendations, and is used for both slender and rigid lateral pile design today. Here, O'Neill and Murchison (1984) propose a semi-empirical expression for $p - y$ curve initial stiffness, $K_{\mathrm{py}} = k_{\mathrm{s}}z$, as well as for ultimate soil resistance, p_{ult}, with depth based on a database of previous field experiment results. Maximum pile diameters of up to 1.22 m installed in loose to dense sands were used to derive the hyperbolic tangent function, which takes the form as follows:

$$p(y) = Ap_{ult} \tanh\left(\frac{k_s z}{Ap_{ult}} y\right) \tag{4.3}$$

The magnitude of p_{ult} depends on the soil failure mechanism at depth, z, and takes the value:

$$p_{ult} = \begin{cases} (C_1 z + C_2 D)\gamma' z & \text{for} \quad z \leq z_r \\ C_3 D \gamma' z & \text{for} \quad z > z_r \end{cases} \tag{4.4}$$

where z_{r} is the transitional depth from shallow to deep mechanisms of failure. Coefficients C_1, C_2 and C_3 are calculated from Reese et al. (1974), based on the sand's specific angle of internal friction. Coefficient of subgrade modulus, k_{s}, is also defined as a function of the angle of internal friction. The empirical constant, A, adjusts the ultimate soil resistance with depth based on the loading conditions:

$$A = \begin{cases} 3 - 0.8\frac{z}{D} \geq 0.9 & \text{for static load conditions} \\ 0.9 & \text{for cyclic load conditions} \end{cases} \tag{4.5}$$

The model's simple formulation and graphical selection of coefficients C_1, C_2 and C_3, based solely on the soil's angle of internal friction, present a simple design tool for the end user.

4.2.3 Concerns with p – y extrapolation

The O'Neill and Murchison (1984) $p - y$ model forms the backbone of the DNV GL (2016) and API (2011) design code recommendations, and has been proven in industry to produce reliable predictions of laterally loaded long, slender piles deployed in the O&G industry. This is exemplified by the very low failure rate for O&G structures (Schneider and Senders, 2010). Currently, the model formulation is also recommended for the design of rigid, large diameter monopile foundations despite widespread concerns over its suitability for this distinctly different design problem (Byrne et al., 2015; Zdravkovic et al., 2015; Beuckelaers et al., 2017).

One of the most important issues is that the fundamental $p - y$ curves are heavily founded on empirically derived adjustment factors in both the formulation of initial stiffness and ultimate soil resistance. The calibration process for these is based on a database of just 14 piles with diameters ranging from 0.60 to 1.22 m. Modern day monopiles are already at $6 - 8$ m in diameter and are expected to reach 10 m and beyond (Kallehave et al., 2015). They present significantly more rigid failure behaviour, prompting the question of the method's validity upon extrapolation to such size of monopile.

According to Reece and Van Impe (2001), the accurate depiction of the $p - y$ curve is of greatest importance in the prediction of laterally loaded monopile performance, with the factors that most affect the nature of the curves being pile stiffness, geometry, installation method and head restraint condition. That being said, of these only pile diameter is considered in the design calculation of ultimate soil resistance. It is unclear whether the remaining characteristics are inherently taken into consideration within the empirical adjustment parameters, and if so, they are likely to be specific to the one particular pile condition and not suitable for wider design scenarios. Indeed, Georgiadis et al. (1992) and Klinkvort (2012) recognise this and propose alternative adjustment factors which ultimately govern the magnitude of p_{ult}, though these remain empirical in nature and are only applicable for the design range upon which they are calibrated. The following section outlines the key design concerns requiring careful consideration so as to be suitable for today's monopile design.

***(i) Initial stiffness of the $p - y$ curve*:** given the sensitivity of wind turbine performance to small mudline rotations, the correct representation of the small-strain stiffness in the $p - y$ curve formulation is key. As seen, DNV GL (2016) takes the initial stiffness, K_{py}, to be independent of all pile characteristics and vary linearly with depth such that $K_{\mathrm{py}} = k_{\mathrm{s}}z$, where k_{s} is an approximation for the modulus of subgrade reaction, a function of the soil's angle of friction.

The translation of design code $p - y$ curves from long, slender to 'short', rigid monopiles has given rise to numerous concerns over the validity of proposed initial stiffness relationships, particularly concerning its independence from pile characteristics. Contradictory findings on this matter are present across literature, as outlined below. Terzaghi (1955), Vesic (1961) and Fan & Long (2005) indeed agree with DNV GL (2016) whereby the modulus of subgrade reaction is independent of pile diameter. On the other hand, the model of Carter (1984), later verified by Ling (1988), establishes that pile diameter is in fact linearly dependant to initial stiffness of the $p - y$ curve. Recent FEM studies reflect this with the initial stiffness found to be of varying degrees of dependency on diameter (Wiemann et al., 2004; Sørensen et al., 2010; Sørensen, 2012; Kallehave et al., 2012). That said, in all previous studies the increase in diameter has directly coincided with an increase in pile-soil stiffness, a parameter which may be more influential on pile-soil interaction behaviour, which is explained in more detail later (point (*iii*)).

***(ii) Ultimate soil resistance*:** the different idealisations for ultimate soil resistance, based on individual empiricisms, present a large variation in magnitude with depth, making it difficult to confidently select an appropriate model. As seen, DNV GL (2016) recommends the O'Neill and Murchison (1984) semi-empirical approach, derived from the original Reese et al. (1974) formulation. This takes into account a wedge type failure near the ground surface and plane-strain failure at a considerable depth, with the transitional point based on the pile geometry. As with many of the aspects of the O'Neill and Murchison (1984) model, this may no longer be appropriate for the representation of offshore wind monopile ultimate capacity. More recent research specifically targeted at rigid piles has decomposed the lateral soil resistance into two analytically derived components – frontal normal soil reaction, σ_h, and side shear friction, τ – in order to gain a greater appreciation of the individual component resistance (see Figure 4.4, Briaud and Smith, 1983; Smith, 1987). Ultimate lateral resistance here is expressed as the sum of these:

$$p_u = (\eta\sigma_{h,max} + \zeta\tau_{max})D \tag{4.6}$$

where η and ζ are empirical adjustment factors based on pile shape.

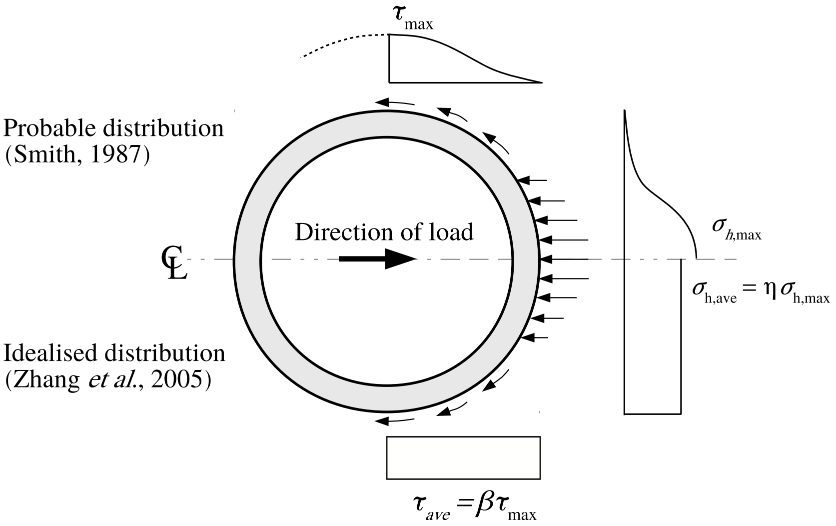

Figure 4.4: Distribution of soil pressures along pile

Measured normal pressure distribution using direct soil pressure transducers (Meyerhof and Sastry, 1985; Prasad and Chari, 1999) reveals an underestimation in the DNV GL (2016) approach for rigid piles, with a value of $\sigma_{\mathrm{h,max}}$ equal to $K_p^2\gamma' z$ (outlined in Fleming, 2009) presenting the best representation (Zhang et al., 2005). Comparison of obtained and proposed measurements was however restricted to close to the mudline since full mobilisation of soil resistance at depth was not achieved. $\tau_{\max}$ in Equation 4.6 is not measured, and is therefore proposed to take a value the same as the pile vertical shear resistance where $\tau_{\max} = K\gamma' z \tan\delta$. Details of K and δ can be found in Kulhawy (1991) or Randolph et al. (1994) for example.

(iii) Global pile-soil stiffness: this parameter is ultimately a more elaborate designation of the widely recognised pile L/D ratio, with additional consideration made for the relative stiffness between the pile and the soil. From a design perspective, the magnitude of global pile-soil stiffness dictates the pile's mechanism of failure; be it flexible or rigid (see Figure 4.5). A pile described as perfectly flexible fails by excessive bending and deflection at the pile head, whereas perfect rigid failure involves the entire pile rotating as one unit about a single point at depth and developing a 'toe-kick' at the base.

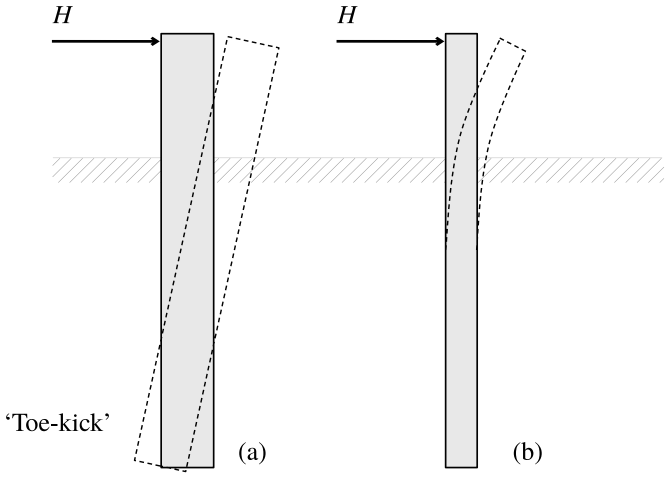

Figure 4.5: (a) Rigid; and (b) flexible failure mechanisms of a laterally loaded pile

Numerous criteria for the classification of global stiffness have been proposed (Dobry et al., 1982; Budhu and Davies, 1988; Carter and Kulhawy, 1988), though the method outlined by Poulos and Hull (1989) is more widely accepted. The global pile-soil stiffness coefficient, K_{r}, is described as follows:

$$K_r = \frac{E_s L^4}{EI} = \begin{cases} < 4.8 & \text{for perfectly rigid behaviour} \\ > 388.6 & \text{for perfectly flexible behaviour} \end{cases} \tag{4.7}$$

where E_{s} is taken as the average modulus of elasticity with depth of the soil. Traditional offshore piles for O&G platforms typically lie at K_{r} >10^4 and are classified as very flexible. Offshore wind monopiles, on the other hand, tend to fall towards the lower end of the transitional range outlined in Equation 4.7, with K_{r} <10^2 (as an example, a 5 m diameter monopile ($EI \approx 7.7$ x 10^{11} Nm^2), embedded to a depth of 25 m in dense sand presents $K_{\mathrm{r}} \approx 45$). At this magnitude of relative stiffness, the monopile experiences a combination of bending and rotational failure mechanisms, adding complexity to the pile design – a rotating rigid monopile mobilises several additional failure mechanisms that are not considered in the current design p – y spring model approximation. In addition to the traditional lateral translational soil reaction force, p, it is proposed that resistance is also derived from base shear, $Q_{\tau,\mathrm{b}}$, base moment, $M_{\theta,\mathrm{b}}$, and vertical side-shear moment, $M_{\theta,\mathrm{s}}$. Figure 4.6 illustrates the philosophy behind the multi-spring soil model formulation, first adopted by Davidson (1982) for the design of onshore drilled piers, which encapsulates these additional mechanisms.

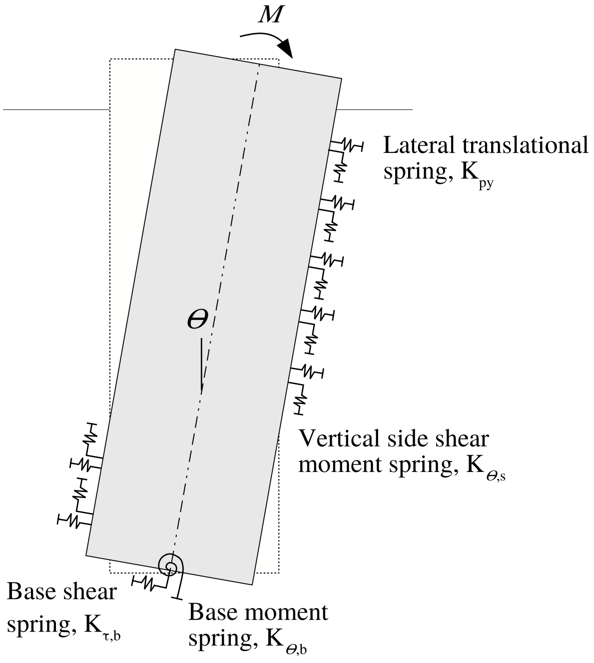

Figure 4.6: Multi-spring soil framework proposed by Davidson (1982), later adopted by PISA (Byrne et al., 2015)

The progressive increase in monopile relative stiffness provided the stimulus for the recent industry funded Pile Soil Analysis (PISA) project (Byrne et al., 2015; Zdravkovic et al., 2015). The aim here was to tailor the original Davidson (1982) model towards the offshore wind turbine monopile geometry. Parametric numerical analyses and medium scale field testing resulted in proposed new $p - y$ curves as well as the formulation of additional soil springs. Although the exact upgraded models and full experimental results are not publicly available at the time of writing, the authors propose that these can be introduced into classical finite difference (FD) approximation methods in the same way as traditional design methods.

4.3 ULS aims and objectives

It has been shown that there remain many concerns surrounding the effects of increased pile diameter and associated increased global stiffnesses on ULS design for offshore wind turbine monopile foundations. Proposed new methods of analysis have been outlined across literature to manage the effects of these however little experimental evidence is available for validation. With this in mind, it is the aim of this chapter to present the results from monotonic pushover centrifuge experiments to validate and address a number of these concerns, with specific aims and objectives outlined below:

1. Observation of the backbone failure and associated pile-soil interaction behaviour for a typical offshore wind turbine monopile geometry to allow for the comparison and validation against previous literature observations and proposed $p - y$ curve alternatives;

2. Development of a multi-spring soil analytical model for the accurate prediction of rigid monopile behaviour;

3. Validation of proposed alternative multi-spring model approach against the results from a range of different pile-soil global stiffness (K_{r}) scenarios.

4.4 Experimental monotonic response

Across the experimental test matrix, a total of 24 monotonic lateral pushover tests were performed, encompassing a number of different pile setups with varying degrees of pile instrumentation. Non-instrumented pile experiments specifically aimed at exploring the aspects of the centrifuge modelling setup procedure have already been documented in Chapter 3 and will not be included here. Only the results from instrumented pile tests will therefore be presented forthwith as these will allow for the most detailed analysis of the pile-soil interaction behaviour.

Firstly, by way of verification of the experimental results obtained from this current study, the dimensionless backbone monotonic failure curves from both instrumented piles (MP1 and MP2) are presented side by side. Dimensionless properties are outlined in detail in Klinkvort (2012). The prototype pile diameters ranging from 2 to 5 m present strong repeatability across the test matrix (Figure 4.7a). Comparison against previous results from literature also shows good agreement (Figure 4.7b), providing a high level of confidence in the validity of the results obtained. As a matter of interest, prototype typical ultimate design applied loads outlined previously in Table 2.1 represent dimensionless overturning moments, $\tilde{M}$, between 25 and 35 which here leads to mudline rotations in the region of 0.5^{o} to 0.7^{o}.

N.B. graphical markers to distinguish individual experimental results remain the same across all subsequent figures in this section and are therefore only shown once (see legend in Figure 4.7).

4.4.1 Analyses methods

The placement of strain gauges on the major axis of the two model monopiles (MP1 and MP2) presents the direct experimental bending moment at a number of finite locations along the pile depth. Selected weighted splines are used to interpolate between the finite points to give estimated values of bending moment at all depths, details of the spline selection can be found in Section 3.4.7. The back calculation of moment then allows for the derivation of shear force and subsequently the interactional $p - y$ behaviour along the length of the embedded portion of the pile. Figures 4.9 & 4.13 present the calculated dimensionless results for these.

In addition to strain measurements, MP2 was instrumented with 10 miniature direct earth pressure cell (EPC) sensors at strategic depths on both the front and rear of the monopile in the plane of loading. In depth information on the selection, location

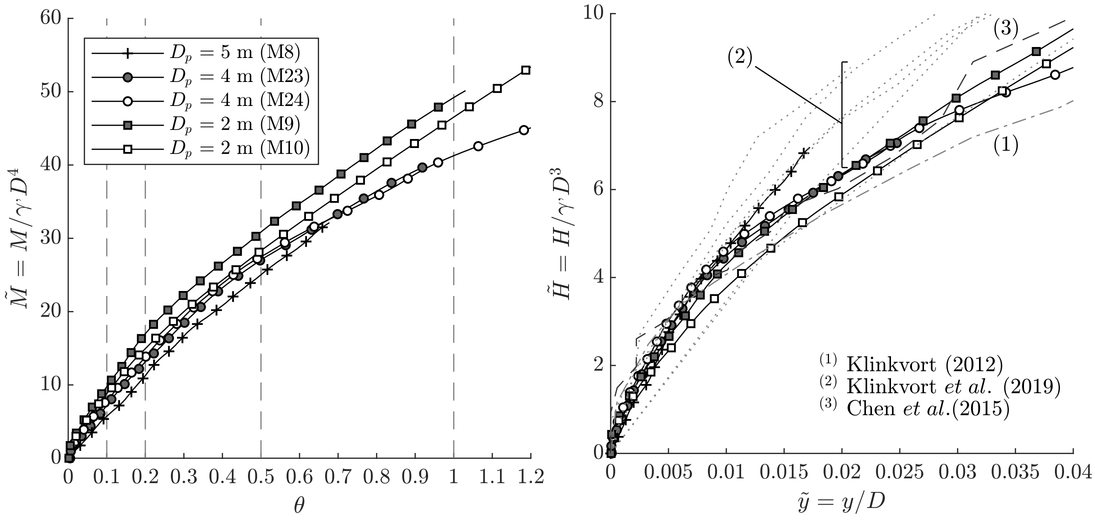

Figure 4.7: Experimental monotonic response overlaying results from previous literature

and calibration of each of these has previously been presented in Section 3.4.3. The output from these sensors offers the opportunity to identify a number of direct pile-soil interaction changes within the soil with applied load which have not been presented before.

Firstly, the individual EPC sensor readings allow for the direct analysis of horizontal stress behaviour, both in front and behind the pile, at each specific location with depth. The ratio with the vertical overburden stresses, and therefore coefficient of horizontal earth pressure, can then be calculated at these locations:

$$K = \frac{\sigma'_h}{\sigma'_v} \tag{4.8}$$

where σ'_v is the calculated theoretical overburden pressure at the depth of EPC sensor and σ'_h is the direct calibrated sensor output. The progression of these, and their comparison with theoretical passive and active horizontal earth coefficients is presented in Figures 4.10 and 4.11. In the same vain, stress path analyses at each individual EPC sensor location can be evaluated and these are presented in Figure 4.12. Given only vertical and horizontal stresses in the plane of loading are known, it was decided to adopt the MIT s'-t stress path representation where:

$$s' = \frac{1}{2}\Big(\sigma'_v + \sigma'_h\Big) \qquad \text{and} \qquad t = t' = \frac{1}{2}\Big(\sigma'_v - \sigma'_h\Big) \tag{4.9}$$

Figure 4.8 schematically illustrates the stress path development both in terms of passive and active failure in front and behind the pile respectively, which is reversed below the point of rotation. Here the initial coefficient of horizontal earth pressure is taken at unity (in an attempt to capture the affects of pile jacking at $1g$), and therefore the starting position in the s' space is at σ'_{v}. Stress paths at the passive and active EPC locations are directly comparable to expected triaxial lateral compression and lateral extension test behaviours respectively (see Head, 1986). It is assumed here that any potential sensor measurement from side friction (and associated shear stresses) from pile rotation is neglected – the additional dilation induced normal stresses are considered minimal in comparison to the active and passive earth pressure changes.

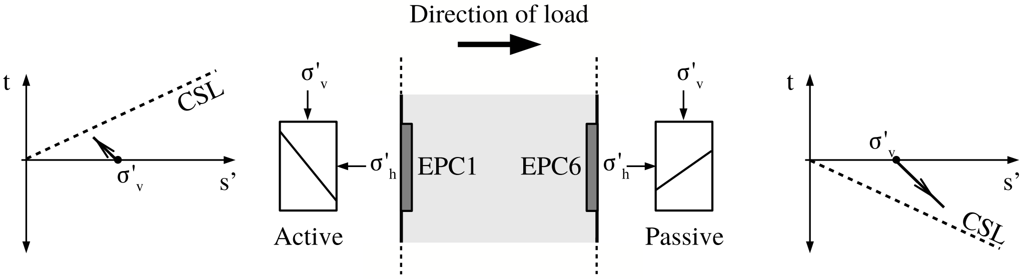

Figure 4.8: Stress path analysis of soil from direct pressure sensor readings

In addition to the individual analysis of the front and rear sensor outputs, taking the difference in these at each specific pile depth allows for the calculation of normal soil pressure $\sigma'_h - y$ behaviour. This is much like the traditional $p - y$ formulation, however in terms of normal reaction only. As a reminder, Zhang et al. (2005), proposed the following expression for total soil reaction force, $p = (\sigma_{h,ave} + \tau_{ave})D$, which represents soil reaction as a combination of normal ($\sigma_{h,ave} = \eta\sigma_{h,max}$) and shear ($\tau_{ave} = \zeta\tau_{max}$) components. ζ and η take the values of 1.0 and 0.8 respectively for a circular pile (Zhang et al., 2005). Since the magnitude of $\sigma_{h,max}$ has already been derived from direct EPC sensor readings, the individual shear reaction component can experimentally be determined as the difference between calculated average soil reaction stress across the full pile diameter, p/D, and the measured normal stress, such that:

$$\tau_{ave} = p/D - \eta\sigma_{h,max} \tag{4.10}$$

Normal and shear individual components are shown alongside calculated $p - y$ curve response at sensor depths later in this section in Figure 4.13.

4.4.2 Pile-soil interaction

The detailed examination of each of the above analyses is outlined below for the progressive monopile failure subject to increasing overturning moment. Behaviour at selected points of mudline rotation ($\theta = 0.1^{o}$, 0.2^{o}, 0.5^{o} and 1.0^{o}), are presented to show the onset of different failure mechanisms at different stages of load. For full appreciation of the complete pile interaction with the surrounding soil, it is advised to review the results in Figures 4.9 – 4.12 together. It is also to be noted that the selected results for illustration here have comparable experimental setup characteristics, *e.g.* similar relative stiffness parameters ($52 < K_{\mathrm{r}} < 73$), pile embedment ratio ($L/D = 5$) and load eccentricity ($5.0 < e/D < 7.5$), which allows for the most appropriate comparison.

On first inspection of Figures 4.9 – 4.12, it can be seen that there is a strong agreement in monopile behaviour with depth across the three tests presented (M23, M24 & M8). This demonstrates confidence in the observed mechanisms for the relative stiffness of monopile tested, representative of a prototype geometry (D_{p} = 4–5m, L/D = 5). The following section now evaluates changes in behaviour seen from low to high degrees of mudline deformation. Observed trends with increasing load are concurrent across each analysis method.

(i) Small deformation (0.1-0.2^{o}): at low magnitude overturning moment, the behaviour of the monopile presents mechanisms synonymous of a flexible failure; this being visible displacement and rotation close to the mudline, whereas at the pile toe these remaining close to zero (Figure 4.9a & c). As seen in the individual direct pressure readings (Figures 4.10 & 4.11) and stress path analyses (Figure 4.12), there is a noticeable mobilisation of soil reaction close to the surface compared to little response at depth at this load. In fact, these show a near full mobilisation of passive and active earth pressures at EPC sensor locations 1 & 6 (uppermost sensors) even with such low magnitude of load. By contrast, at depth there is little to no mobilisation of either active and passive horizontal earth pressures.

Base moment and shear observations at this low magnitude of load also reveal negligible mobilisation of additional resistance at depth (Figures 4.9e & f), which is due to the lack of ‘toe-tick’ at this stage.

‘

(ii) Medium deformation ($\sim$ 0.5^{o}): as the magnitude of overturning moment increases, the progressive mobilisation of soil reaction with depth begins to take place.

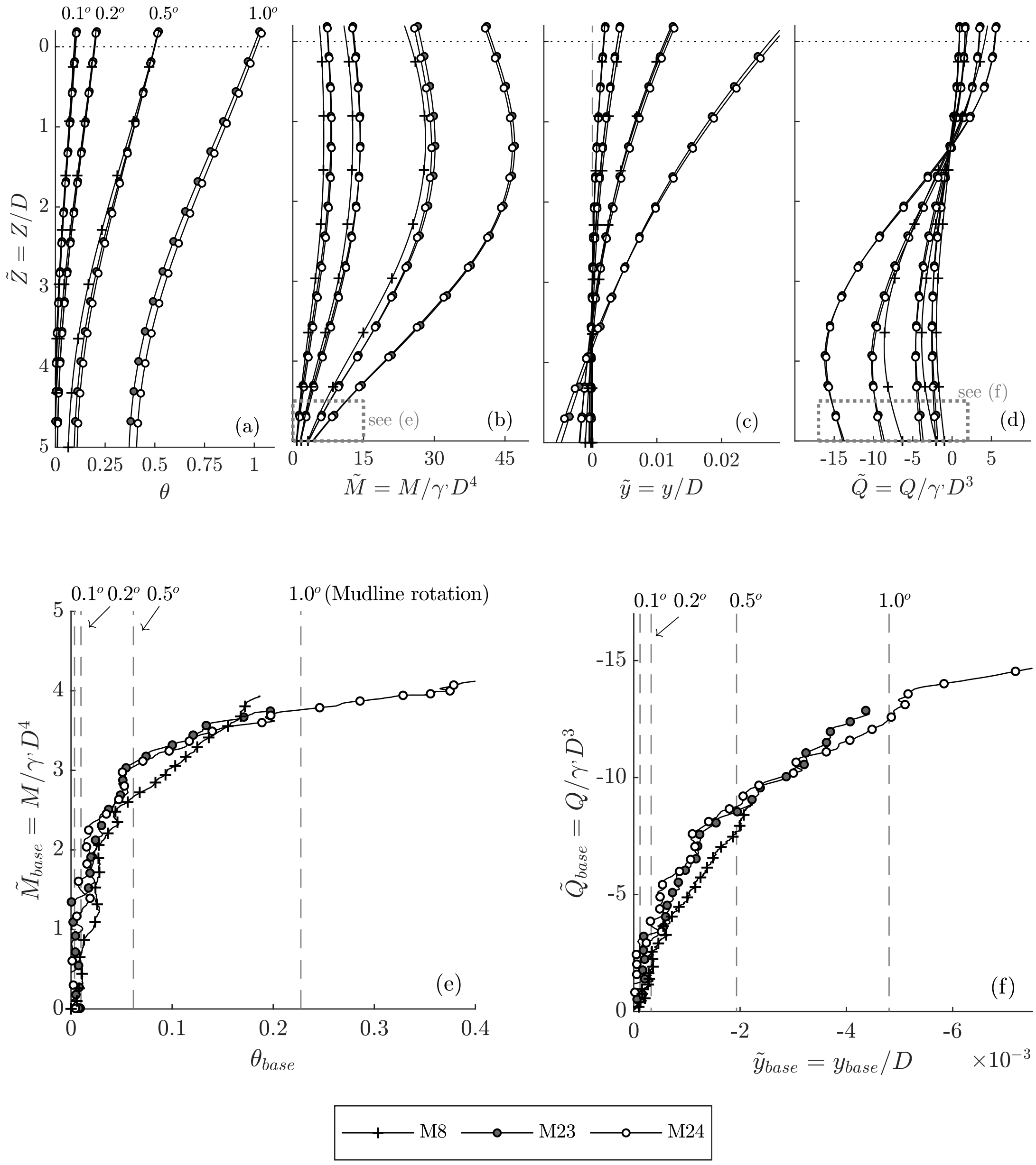

Figure 4.9: Monotonic pushover experimental results: (a) pile rotation with depth; (b) bending moment with depth; (c) deflection with depth; (d) shear with depth; (e) base moment variation with base rotation; (f) base shear variation with base displacement

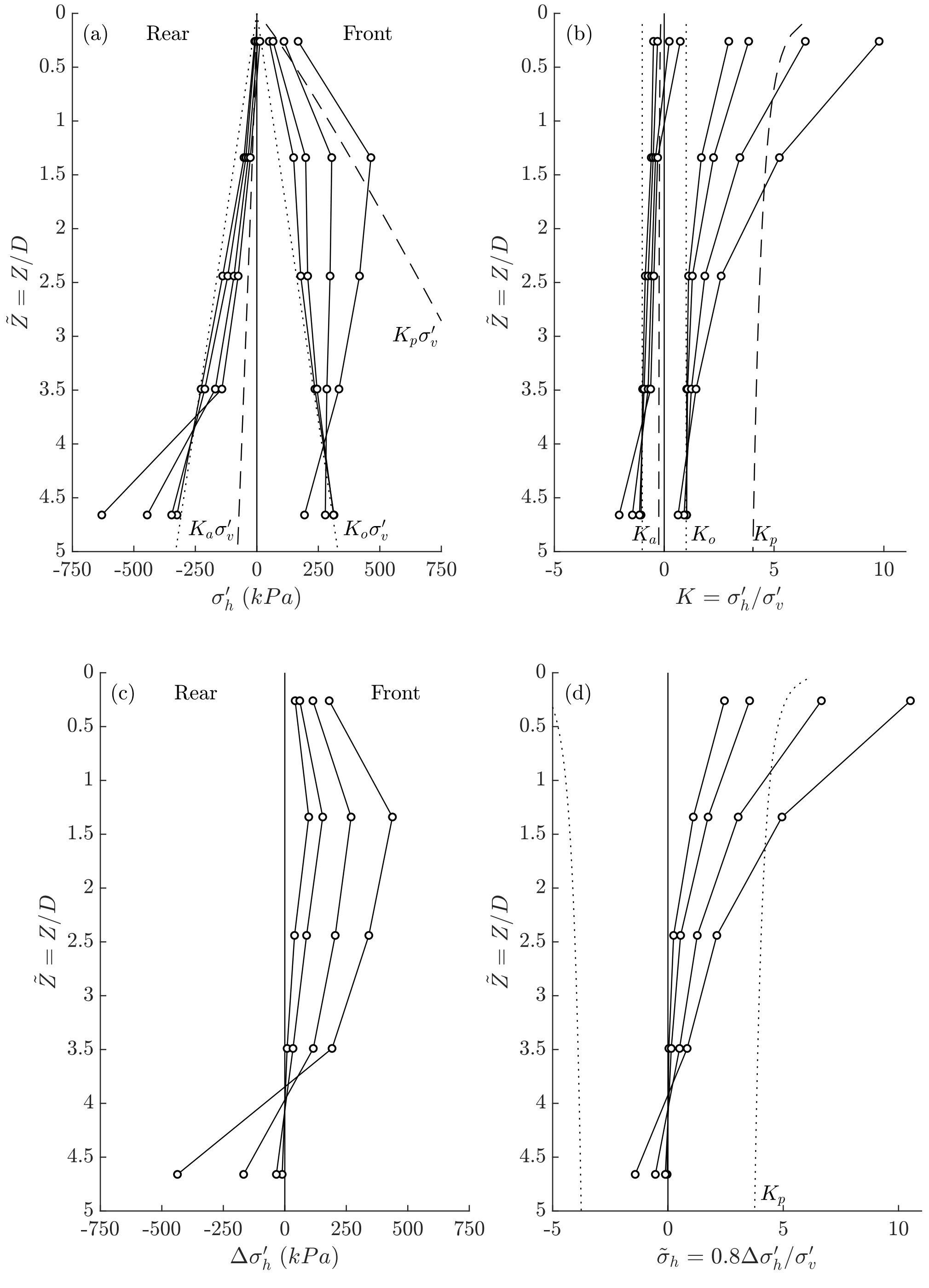

Figure 4.10: Monotonic pushover experimental results, horizontal stress distribution a the front and rear: (a) absolute magnitude; and (b) dimensionless magnitude. Difference between front and rear: (c) absolute magnitude; and (d) dimensionless magnitude

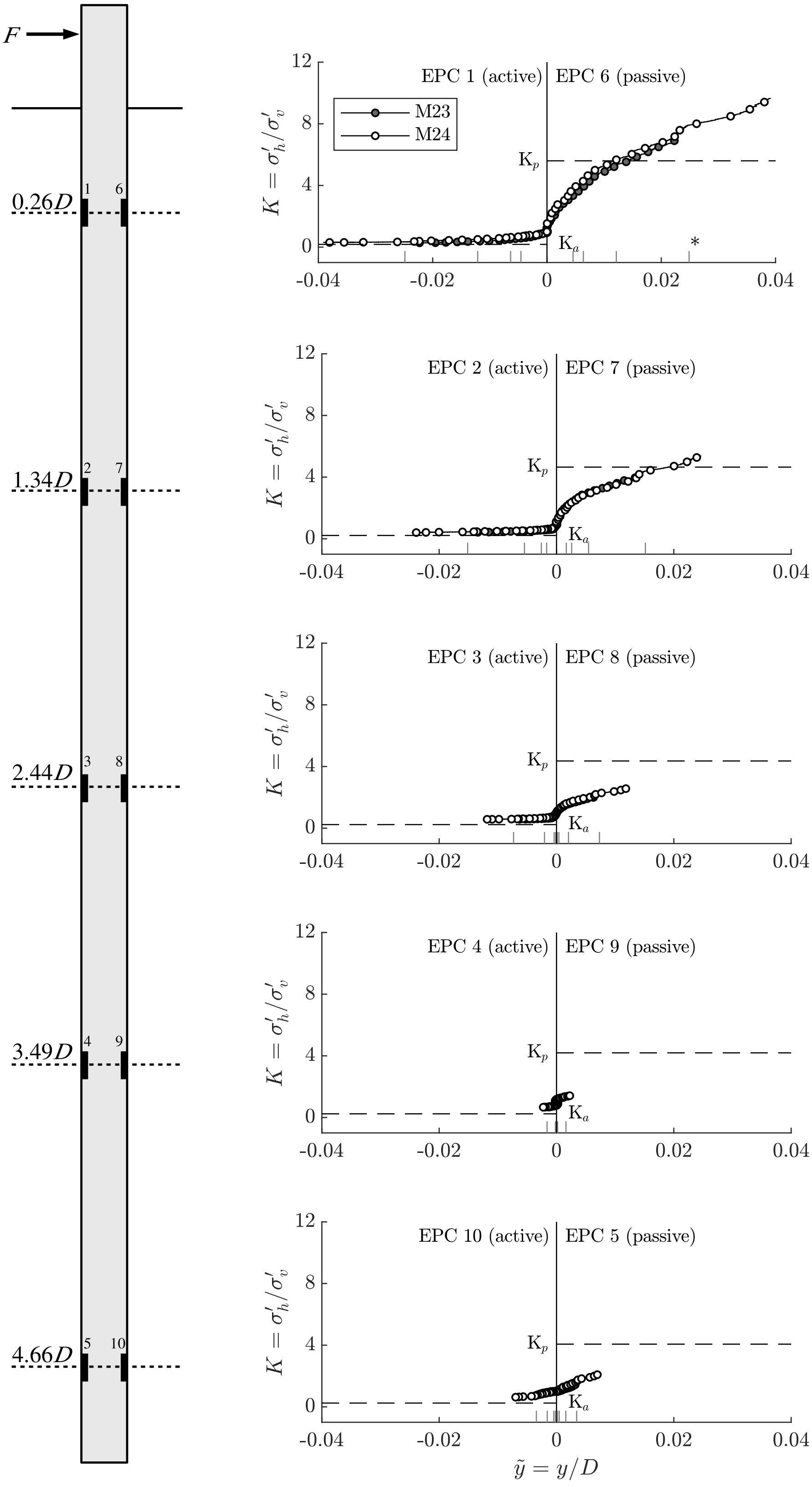

Figure 4.11: Calculated coefficient of horizontal earth pressure with depth, (*average mudline rotations at θ = 0.1, 0.2, 0.5 & 1.0°)

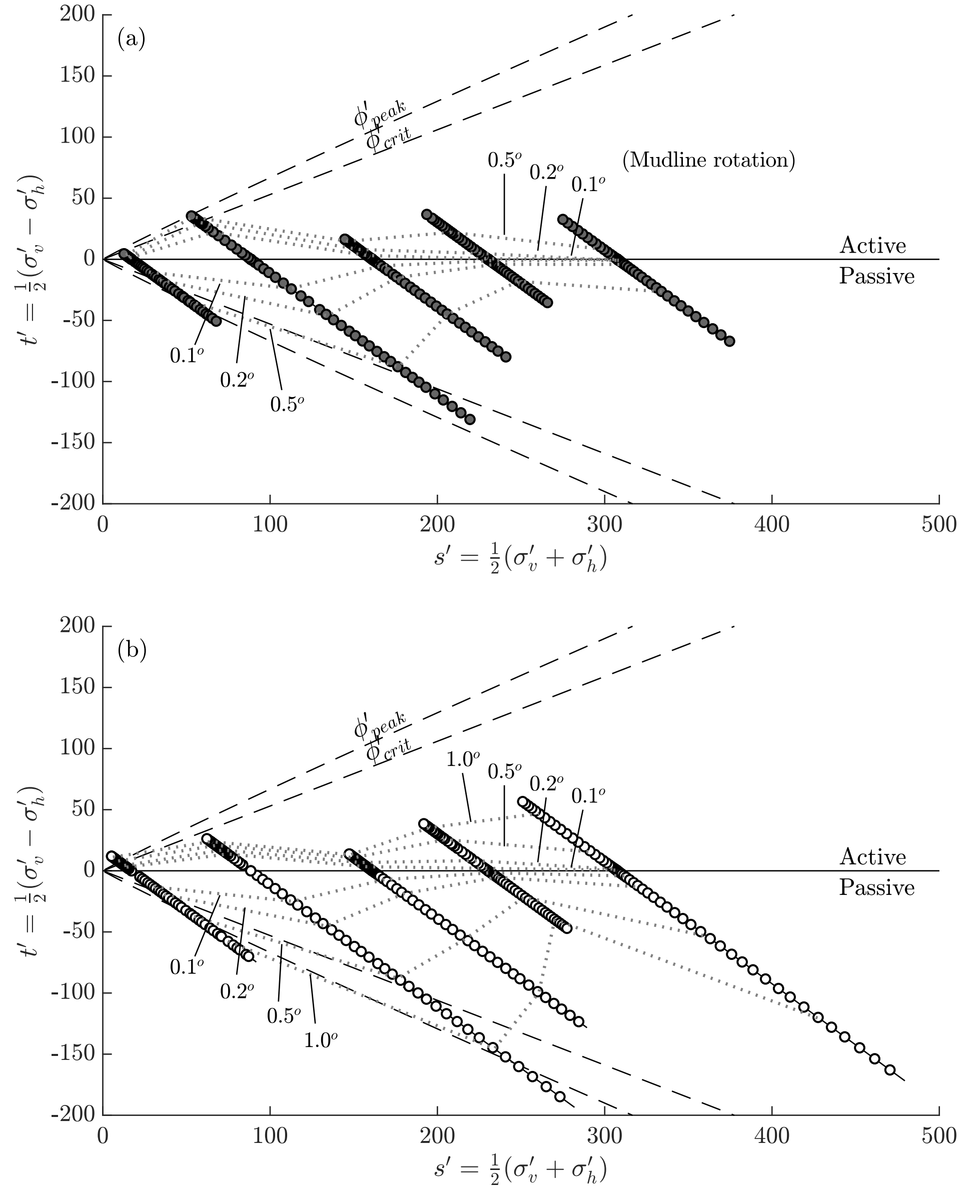

Figure 4.12: s'–t stress path analysis from direct soil pressure measurements along pile depth: (a) test M23; (b) test M24

Given the already almost fully mobilised passive resistance at shallow soil depths, horizontal resistance is now derived from deeper along the monopile. This is evidenced in stress path analyses which now reveal significant mobilisation of active and passive horizontal earth pressures at the subsequent deeper EPC sensor readings (EPC locations 2 & 7). Further load increases must result in soil resistance being developed from deeper mechanisms in order to continue to gain lateral resistance.

At the base of the pile, there is a clear change in horizontal active and passive earth pressures at sensor readings EPC5 & EPC10 (Figures 4.10 to 4.12) which illustrates the onset of rotation at the base. This is also seen in Figures 4.9a & c where the positive monopile rotation now progresses from the mudline to the toe and a visible 'toe-kick' is present. In conjunction with these, base moment and shear resistances begin to present deep resistance against these lateral deformations. From the above observations, it is clear a transition from the apparent flexible failure (at the low magnitude of load) to a rigid rotational failure has been made.

(iii) Large deformation ($\geq$1.0^o): upon reaching the large magnitude of overturning moment, there is a very clear rotational failure mechanism now which is evidenced across all data. Figures 4.9a & c show large rotation at the pile toe as well as a very distinct 'toe-kick'. Figures 4.9b & d show associated large base moment and shear, which provide significant deep resistance. In fact, it is seen that a full mobilisation of base moment has been achieved at this point, with a maximum value of $\tilde{M}_{\theta,b} \approx 4$, representing approximately 10 % of the applied overturning moment at the mudline. Stress paths also reveal significantly increased passive earth pressure at the toe at EPC5 which is providing a substantial amount of lateral soil reaction. Interestingly, the magnitudes of observed mobilised active earth pressures on the rear of the monopile do not appear as close to full mobilisation as the passive cases, despite the large deformation that has taken place.

The above observations illustrate the progressive development of a number of additional soil resistances that are not considered in current design methodologies. Before interrogating these further, the following section will first concentrate on the observed $p - y$ curve behaviour, since this has been most well documented in previous literature.

4.4.3 Critique of $p - y$ response

As mentioned, it was Reese and Van Impe (2001) who stated that the accurate representation of $p - y$ curve behaviour is the most important factor for the accurate prediction of laterally loaded pile performance. That said, it is widely accepted that current DNV GL (2016) recommended $p - y$ design curves are not suitable for rigid monopile behaviour despite being extensively used in practice. This therefore raises questions over any monopile design following these recommendations. Many alternatives have since been proposed across literature which are now compared and critiqued against experimental $p - y$ observations.

Dimensionless experimental $p - y$ relationships at the exact depths of EPC sensor locations are presented in Figure 4.13. In this format these represent the average trans-

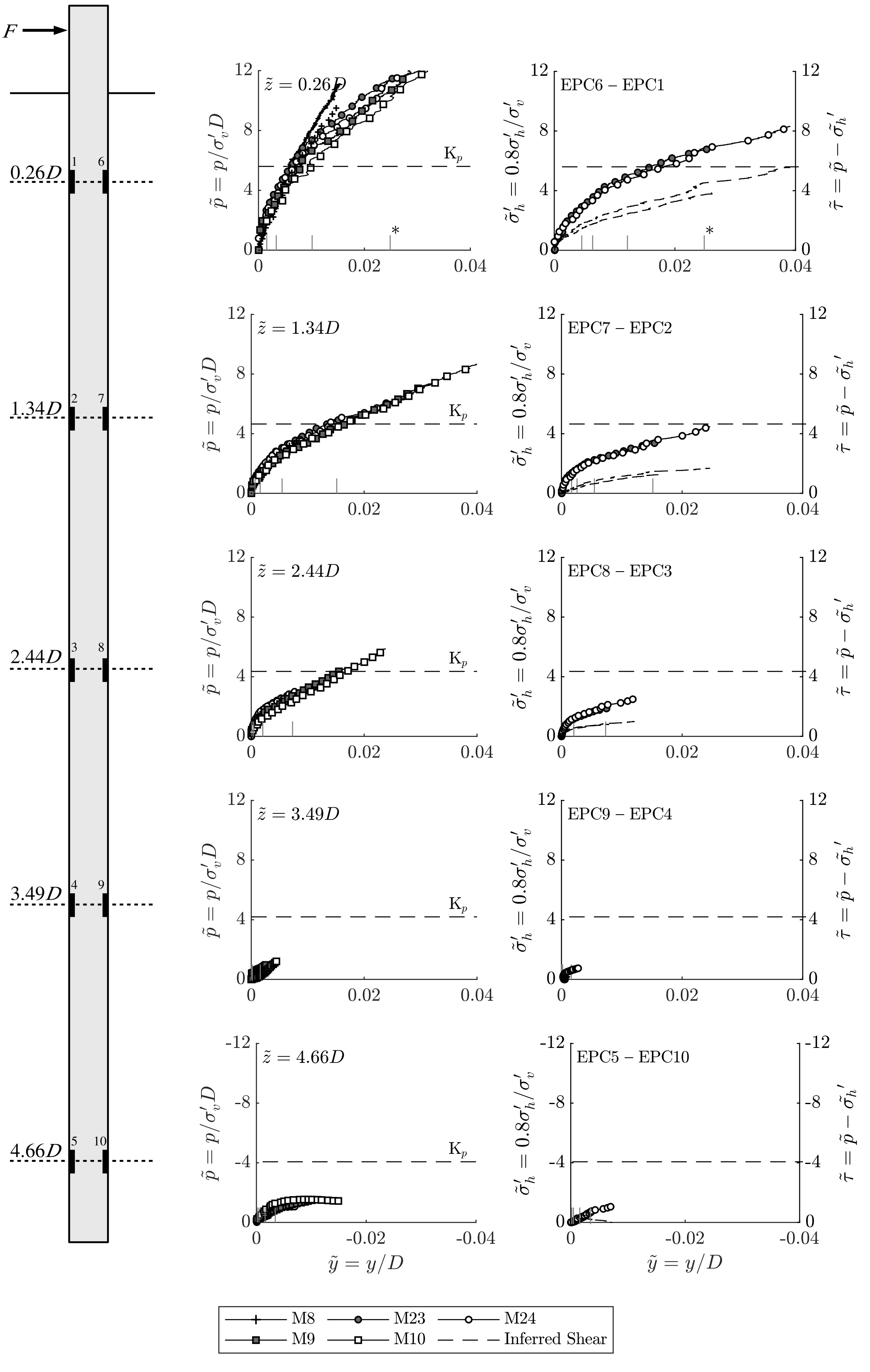

Figure 4.13: Normalised soil reaction with depth: (left tiles) calculated p – y curve behaviour from direct strain measurements; (right tiles) difference between measured direct earth pressure in front and behind pile (markers), and calculated shear component (dashed lines), (*mudline rotations at θ = 0.1, 0.2, 0.5 & 1.0°)

lational soil reaction, in relation to the vertical overburden stress, acting around the circumference of the pile. This includes both normal and shear components. In addition to these, the difference in normalised direct EPC normal stresses at the front and rear of the pile are also presented. These are multiplied by the shape factor coefficient, $\eta = 0.8$, of Zhang et al. (2005), and therefore represent the normal component of the proposed p – y breakdown (see Equation 4.6). The ratio of normal stress component to total p – y average stress is seen to range from 60 to 80 % across the different sensors, suggesting that lateral resistance is predominantly achieved from normal reaction earth pressures rather than shear. The back-calculated shear components are also illustrated, though their magnitude is fully dependent on the accuracy of calculated p – y relationships and observed pressure readings; experimental measurements of these was not made.

***(i) Initial p – y stiffness*:** calculated initial stiffness results from prototype monopile diameters ranging from 2 to 5 m are illustrated in Figure 4.14. On first inspection, there is a clear increase in stiffness with overburden stress, as to be expected for a cohesionless material, though these are significantly less than the elastic modulus of the soil. There also appears to be no noticeable effect of pile diameter, with the results from a 2 m prototype monopile in line with those of the larger 4 and 5 m counterparts, at least within the range of observed experimental variation. The relative stiffness parameter, K_{r}, however remains quite similar across these test results which may be a larger driver in p – y stiffness response (Ashour et al., 1998).

Comparison of experimental results with proposed stiffness models from across literature illustrates the large error range across some of these recommendations, most of which significantly overestimate initial p – y stiffness – of these the DNV GL (2016 design code is particularly generous on the stiffness of the system. Closest predictions appear to come from Sørensen et al. (2010) and Klinkvort (2012). The behaviour of the alternative Kirkwood (2015) model, which proposes an immediate stiffness increase below the point of rotation, is not observed to take place in this dataset. This alteration was likely an attempt to manage the additional soil resistances from base shear and moment without actually integrating these as separate spring models.

Without wanting to propose another empirical variant of the stiffness relationship with depth since there already exists a plethora in this respect, it has therefore been decided that the linear increase model of Klinkvort (2012), where the coefficient of proportionality is an empirically derived constant multiplied by the passive earth coefficient ($\tilde{K}_{py} = BK_{\mathrm{p}}$), presents the most suitable and accessible representation. This model is also the only one from the above that has been experimentally validated

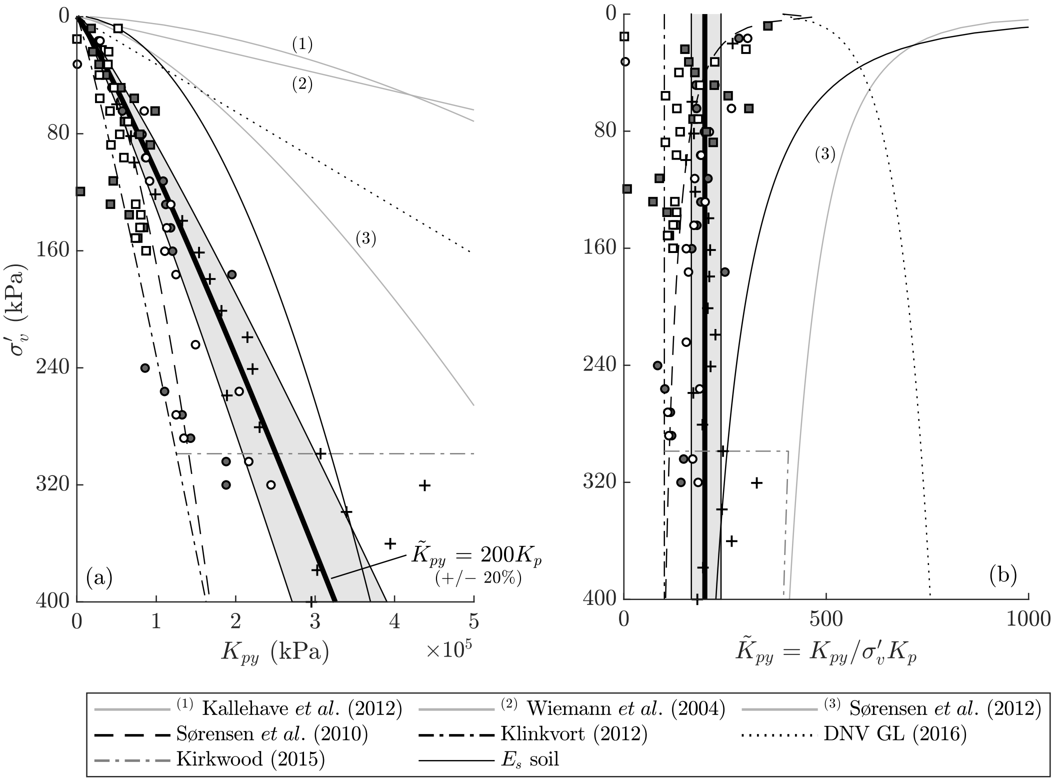

Figure 4.14: Initial stiffness of $p - y$ curves: (a) absolute stiffness; (b) dimensionless stiffness

at an appropriate stress condition. Klinkvort (2012) proposes a value of 100 for B, however results here appear to suggest a value closer to 200 as more appropriate (see Figure 4.14). The difference in B could be as a result of a number of soil and/or pile properties, of which would require considerable parametric study to fully examine.

(ii) Ultimate capacity, p_{ult}: in previous appropriate stress level experimental studies which manage to achieve ultimate $p - y$ capacity, the monopile has been modelled as a solid cylindrical member and therefore never reached plastic pile failure. This allowed complete pushover and full mobilisation of the soil capacity. In this study, the selected hollow model monopile with representative prototype bending stiffness more accurately represents the pile-soil stiffness interaction behaviour, however exhibits a significantly lower ultimate bending capacity than the solid counterpart. For this reason full mobilisation of the soil cannot be achieved since excessive applied overturning moment would lead to a plastic pile hinge close to the mudline. As a result, the direct experimental observation of p_{ult} with depth was not possible and only $p - y$ performance within the tested load range can be examined.

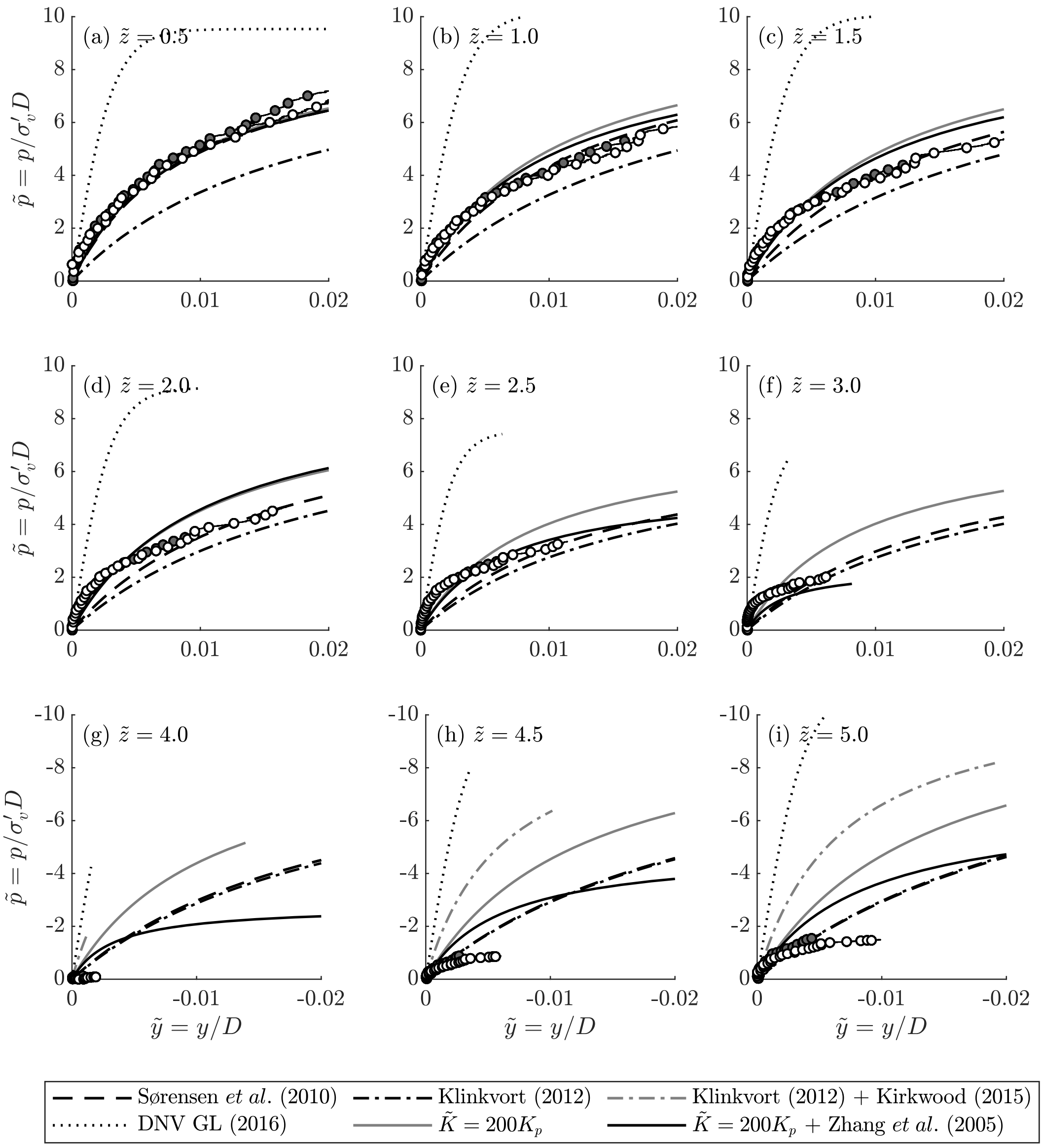

Figure 4.15: $p - y$ curve behaviour compared against literature predictions and proposed alternative (curves close to rotation point omitted for clarity)

With this in mind, Figure 4.15 presents the predicted $p - y$ curve performance from the previously outlined literature models which present favourable initial stiffness idealisations (those with particularly stiff estimations are not shown for clarity). Ultimate soil capacities are selected in line with the author's recommendations, which typically maintain the original DNV GL (2016) recommendation (see Equation 4.4), with only Klinkvort (2012) adopting a variant on this. In addition to these, $p - y$ curves formulated from the derived initial stiffnesses from this current study ($\tilde{K}_{py} = 200K_p$) are also included, of which two variants are presented: one having a magnitude of p_{ult}

equal to original DNV GL (2016) design; the other adopting the Zhang et al. (2005) variation with depth for rigid pile design. These will take the names Mod_{DNV} and Mod_{Zha} respectively forthwith.

From Figure 4.15, it is immediately clear that the DNV GL (2016) recommendation is not acceptable, and this has been demonstrated many times across literature (Klinkvort, 2012; Kirkwood, 2015; Bayton and Black, 2016). Alongside the previously identified over prediction of initial stiffness, ultimate capacity is achieved at a considerably too low magnitude of $p - y$ spring displacement. This fundamentally means that both components of its formulation are not suitable for monopiles of this geometry. Of the remaining presented methods from literature, each show a reasonable representation of the observed behaviour, particularly when examining the $p - y$ performance after the initial underestimation of stiffness at small displacements. At the base of the pile, there is a common theme across each literature proposed model of an over-prediction of soil resistance. This is likely due to the lack of representation of base shear and moment, and therefore the deep resistance must be achieved by translational $p - y$ spring resistance only close to the base.

Of the two proposed alternative $p - y$ models, Mod_{Zha} illustrates the best performance. Of course the initial stiffness for this is directly calibrated from the test results, and therefore will no doubt have strong agreement at small displacement regardless of selected ultimate capacity. At larger displacements, however, the prediction provides a much more representative behaviour, particularly at depth and close to the point of rotation.

***(iii) Implication on monopile behaviour*:** it has been shown that an accurate representation of $p - y$ curve behaviour is possible by combining appropriately selected initial spring stiffness, taken here as $\tilde{K}_{py} = 200K_p$, with ultimate soil capacity recommendations of Zhang et al. (2005). In Figure 4.16, the implications of monopile performance modelled by the selected $p - y$ representations are further explored. At this stage, the $p - y$ curve model is the only assumed soil resistance as per traditional methods of design.

It can be seen that there is a range in performance for the predicted moment-rotation response across the different $p - y$ formulations, with all but the DNV GL (2016) alternative models under-predicting initial stiffness and ultimate capacity. Focussing purely on the proposed combined model Mod_{Zha}, which has been shown to offer the most representative $p - y$ behaviour with depth, this actually presents a very poor representation of global pile behaviour. Internal bending moment and shear also reveal poor prediction. The explanation for this must be due to the absence of additional lateral soil resistance models, beyond the traditional $p-y$ curves alone, which have been experimentally seen to present significant contributions to lateral capacity (Figure 4.9).

With the above in mind, the initial recommendation of Reese and Van Impe (2001) may no longer seem appropriate – for a rigid monopile, the accurate representation of $p-y$ curve behaviour is no longer the only important factor in the accurate prediction of laterally loaded pile performance, additional models accounting for base resistances are equally accountable. The following section examines this further.

4.5 Multi-spring soil framework

It has been observed that the rigid monopile presents a number of alternative failure mechanisms that exhibit significant soil reactions at depth to counteract the lateral deformations from deep-seated rotations and 'toe-kick' displacement. At present, DNV GL (2016) and API (2011) design code recommendations only take into consideration the lateral translational soil reaction in the form of the $p-y$ curves to manage the combination of these, and as depicted in Figure 4.16 the predicted soil-pile behaviour is greatly compromised even with the strong $p-y$ model. The following section

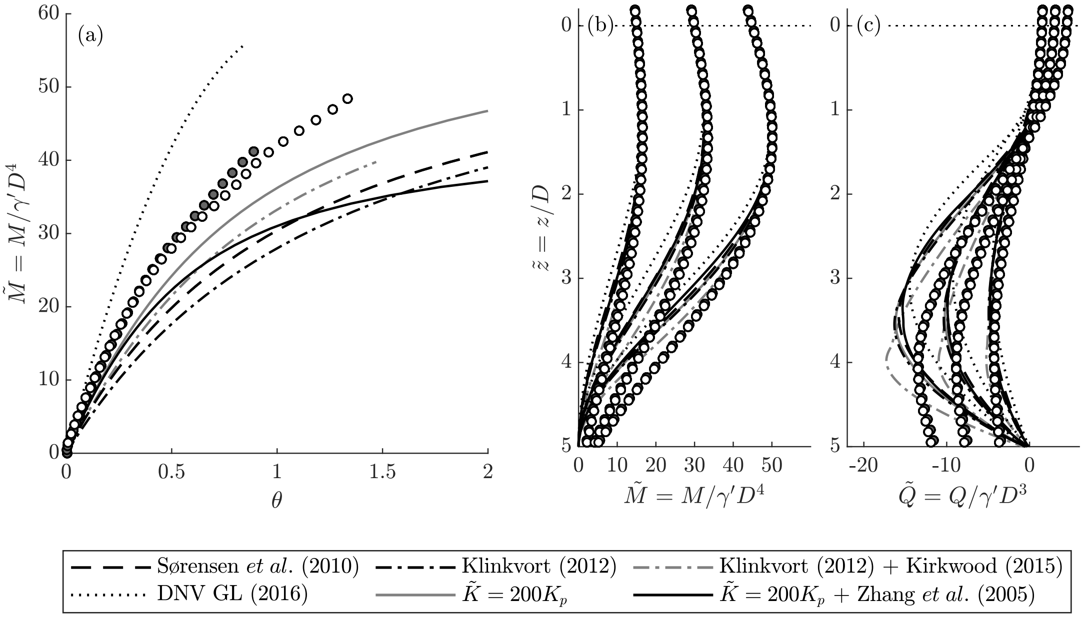

Figure 4.16: Monopile behaviour compared against literature predictions: (a) moment-rotation response; (b) bending moment with depth; (c) shear force with depth

outlines a proposed alternative multi-spring framework, specific to the monopile, which incorporates a number of additional resistances at depth which have been evidenced in experimental results.

4.5.1 Analytical model development

Here, analytically derived additional spring models for base shear, $Q_{\tau,b}$, base moment, $M_{\theta,b}$, and side shear moment, $M_{\theta,s}$, are presented. For each of these, a non-linear equation is selected and takes the form of:

$$A = B \Bigg/ \left(\frac{1}{K} + \frac{B}{A_{ult}} \right) \tag{4.11}$$

where A and B represent the variables of interest for representation, *e.g.* moment or shear for A against rotation or deflection for B. K represents the respective initial stiffnesses of the non-linear curve. This expression allows for good control of stiffness and ultimate capacity for an accurate description of non-linear behaviour. It has been widely adopted for the representation of non-linear behaviour across many soil applications (Kondner, 1963; Georgiadis et al., 1992; Klinkvort and Hededal, 2014).

Where possible, dimensionless properties of the spring model framework have been made against pile diameter, D, and effective overburden pressure, $\sigma'_v = \gamma' z$, to allow for transferability across different geometries and stress conditions. Additionally, for each case, initial spring stiffness has been formulated with respect to the calculated elastic modulus of the soil, E_{s}, at the location of interest, allowing ease of translation from standard laboratory element test results (shear box or triaxial) or on-site measurements (*e.g.* CPT or pressuremeter). Where these are unavailable, the value of elastic modulus of a material can be taken as $2(1+\nu)G_0$ where ν is the Poisson's ratio, adopting a value here of 0.3 for a fine sand, and G_0 the initial shear modulus. In Randolph et al. (1994), an estimation for G_0 is made based on the mean effective stress, p', and the relative density, R_{d}, at that location, such that:

$$E_s = 2(1+\nu) \times 400 p_a \exp(0.7 R_d) \left(\frac{p'}{p_a} \right)^{0.5} \tag{4.12}$$

where p_{a} is the atmospheric pressure taking a value of 100 kPa. Using this elastic modulus, an analytical approximation of the stress - strain response ($\sigma = E_s \epsilon$) is defined for each individual spring alternative based on the specific mechanism geometry.

(i) Base shear, $Q_{\tau,b}$**:** the maximum shear at the pile base is derived as the sum of the shear capacity associated with both the vertical stress from the soil column within the pile, $\sigma_{v,s}$, assuming zero plug, and from the mass of the foundation, tower and turbine combined, $\sigma_{v,p}$. From these, shear stress is calculated based on angle of friction between the two materials – for the base soil-soil interface, the angle of friction is taken as ϕ'_{peak}, whereas for the pile-soil interface takes an angle of δ equal to $0.7\phi'_{peak}$ (for a smooth steel, *c.f.* Randolph et al., 1994). Following the work of Bolton (1986), peak angle of friction, ϕ'_{peak}, is defined by relative density and mean effective stress to account for sand dilation behaviour at different overburden stresses. Equation 4.13 presents the ultimate base shear capacity which is also illustrated graphically in Figure 4.17.

$$Q_{\tau,b} = A_p \sigma_p \tan\delta + A_s \sigma_s \tan\phi'_{peak} \tag{4.13}$$

where A_{p} and A_{s} are the areas of the pile base and internal soil column respectively. This can be expressed in terms of diameter only, where D_{i} represents the inner diameter ($D_i = D_o - 2t$), for an unplugged pile.

$$Q_{\tau,b} = \frac{\pi}{4}\Big(D^2\sigma_p \tan\delta + D_i^2(\sigma_s \tan\phi'_{peak} - \sigma_p \tan\delta)\Big) \tag{4.14}$$

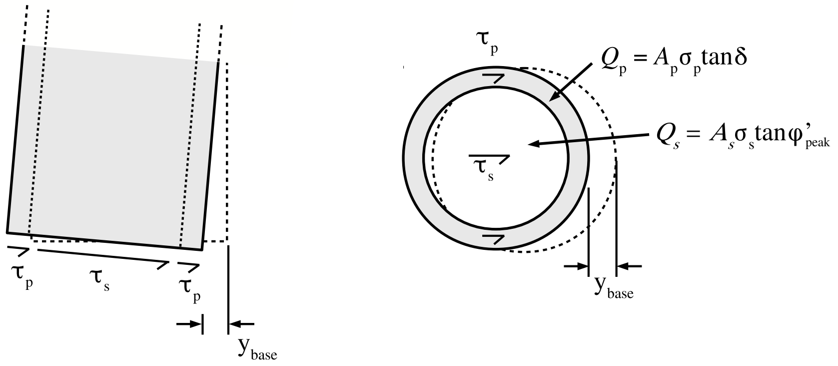

(a) (b)

Figure 4.17: Schematic illustration of base shear analytical approximation: (a) side elevation; (b) base section

The initial stiffness of the base shear spring, which is defined as the ratio between base shear force and base deflection ($K_{\tau,b} = Q_{\tau,b}/y_{base}$) is based on the elastic modulus of the soil at this depth and geometric aspects of the mechanism. Firstly an average base shear equivalent strain and stress are to be defined as follows:

$$\epsilon_{\tau,b} = y_{base}/D \qquad \text{and;} \qquad \tau_{\tau,b} = \sigma'_{ave}\tan\phi \tag{4.15}$$

where σ'_{ave} is the average stress over the full pile base area taking into account pile and soil column components. The classical stress - strain relationship, $\tau_{\tau,b} = E_s\epsilon_{\tau,b}$, can be used to connect the two such that the base deflection can be written as:

$$y_{base} = \sigma'_{ave} \tan \phi'_{peak} D / E_s \tag{4.16}$$

As mentioned, the base shear framework spring stiffness is defined as the ratio between base shear force and deflection and is therefore formulated as:

$$K_{\tau,b} = \left(\sigma'_{ave} \tan \phi'_{peak} \pi D^2/4\right) / \left(\sigma'_{ave} \tan \phi'_{peak} D / E_s\right) \tag{4.17}$$

giving:

$$K_{\tau,b} = \frac{\pi}{4} E_s D \tag{4.18}$$

A graphical depiction of the analytical proposal is presented in Figure 4.18 alongside the superimposed experimental observations.

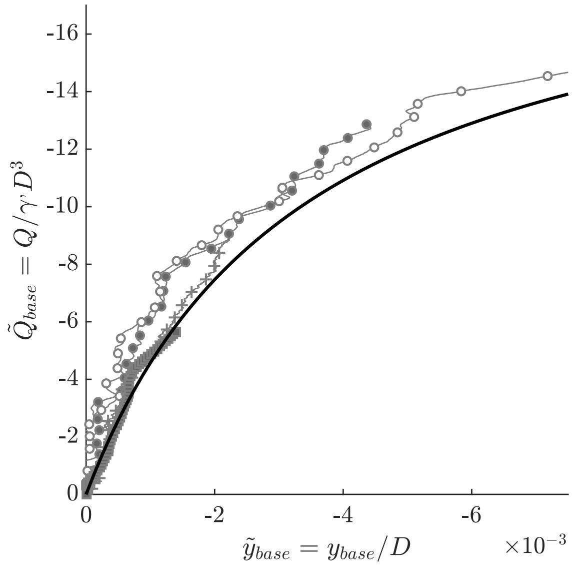

Figure 4.18: Analytical prediction of shear at base

(ii) Base moment, $M_{\theta,b}$**:** the calculation of the base moment resistance assumes base pile rotation about an origin point taken at one edge of the pile rim (see point o in Figure 4.19). This provides simplification to a complex stress distribution which is likely to see an origin point of rotation at a varying position between the pile edge and centre.

The philosophy behind the base moment ultimate capacity is the assumption of full mobilisation of ultimate bearing resistance on the pile rim, assuming no soil plug, as it penetrates into the soil with increasing rotation. After subtracting the proportion of bearing stress accounted for by the self-weight of the pile, the remaining bearing resistance is taken to vary linearly from zero at the origin of rotation to maximum at the opposing edge. The resistive bearing moment is then calculated as the integral of bearing stress around the base multiplied by its lever arm between the centre of area and the origin point 'o'. The magnitude of the selected bearing capacity factor is taken to be half that of the remaining traditional end bearing pile ($N_q^*/2$), since it is assumed that the pile base rotation drives only one 'bulb' failure surface propagating from the base of the pile (depicted in Figure 4.19). The maximum bearing moment is therefore calculated as follows:

$$M_{\theta,b} \approx \frac{\pi}{16} N_q^* \big(D^2 - D_i^2\big) \gamma' z \times \frac{2D}{3} \tag{4.19}$$

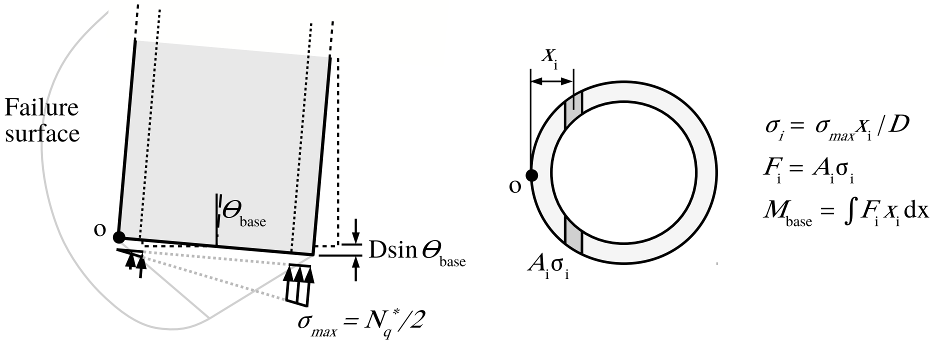

(a) (b)

Figure 4.19: Schematic illustration of base moment analytical approximation: (a) side elevation; (b) base section

Derivation of base moment spring stiffness involves the appropriate conversion of base rotation to an equivalent strain for input into the classical stress - strain approximation. Since the model is idealised as a bearing resistance scenario, the associated strain is therefore taken as the ratio of average base vertical displacement and a defined zone of influence, nD, below the base of the pile. Average base strain and stress are therefore calculated as:

$$\epsilon_{\theta,b} = \big(D \sin\theta_{base}\big)\big/ nD \approx \theta_{base}/n \qquad \text{and} \qquad \sigma_{\theta,b} = 12 M_{\theta,b} \big/ \pi D^3 \tag{4.20}$$

where θ_{base} is taken in radians. The value of the influence factor n typically ranges from 0.7 to $4.0D$ (Yang, 2006) for full bearing resistance and depends on the initial soil state. Base moment model spring stiffness is calculated as the ratio between base moment and rotation ($K_{\theta,b} = M_{\theta,b}/\theta_{base}$). Following the same methodology for the base shear, the relationships in Equation 4.20 are combined with the an idealised stress - strain representation of $\sigma_{\theta,b} = E_s\epsilon_{\theta,b}$, to give an estimation for base rotation as:

$$\theta_{base} = \frac{12n}{\pi} M_{\theta,b} \big/ E_s D^3 \tag{4.21}$$

which leads to a representation of initial stiffness of:

$$K_{\theta,b} = \frac{\pi}{12n} E_s D^3 \tag{4.22}$$

Figure 4.20 presents the proposed model performance against superimposed experimental observations. The value for n is proposed to take a value of 1.0 based on observations from finite element analyses of rigid monopile geometries.

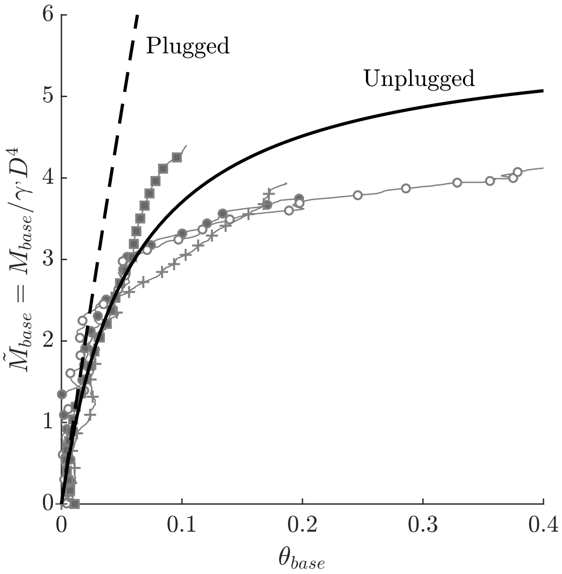

Figure 4.20: Analytical prediction of moment at base

***(iii)* Side shear moment, $M_{\theta,s}$:** as the diameter of the monopile increases, any rotation that takes place about the pile centreline induces substantially large vertical displacements at the pile-soil interface which will mobilise shear resistance across the pile diameter. The vertical shear stresses are ultimately governed by the horizontal normal stress that is acting on the pile at that location, be it a passive or active state, or a point in between, for the front or rear of the translating pile respectively. The side shear moment is then calculated by integrating the shear stress over the area it acts multiplied by its lever arm, taken here as the half pile diameter.

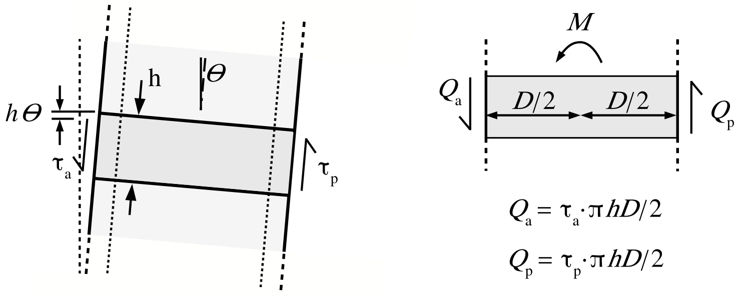

(a) (b)

Figure 4.21: Schematic illustration of side shear moment analytical approximation: (a) side elevation; (b) individual discretised element

The following presents the fundamental side shear moment which acts over a finite discretised length of pile, h:

$$M_{\theta,s} = \tau_a \frac{\pi h D}{2} \cdot \frac{D}{2} + \tau_p \frac{\pi h D}{2} \cdot \frac{D}{2} \tag{4.23}$$

$$M_{\theta,s} = \Big(\eta K_a \gamma' z \tan\delta \frac{\pi h D}{2} + \eta K_p \gamma' z \tan\delta \frac{\pi h D}{2}\Big)\frac{D}{2} \tag{4.24}$$

where η is taken as the normal stress reduction factor to account for pile circularity (Zhang et al., 2005). The reduced formulation is as follows:

$$M_{\theta,s} = \frac{\pi}{4}\big(K_a + K_p\big)\eta\gamma' z \tan\delta \; hD^2 \tag{4.25}$$

Calculation of side shear moment spring initial stiffness takes a similar direction as the base moment. An equivalent shear strain parameter associated with vertical displacement induced by pile rotation is first derived, which takes the form:

$$\epsilon_{\theta,s} = h\theta/h \approx \theta \qquad \text{and;} \qquad \tau_{\theta,s} = K\eta\sigma'_v \tan\delta \tag{4.26}$$

Side shear moment spring stiffness is calculated as the ratio between side shear moment and rotation ($K_{\theta,s} = M_{\theta,s}/\theta$), and can therefore be deduced as:

$$K_{\theta,s} = \frac{\pi}{4} E_s D^2 \tag{4.27}$$

It was not possible to experimentally measure the magnitude of side shear moment applied to the pile and therefore no direct validation is made for this case.

***(iv) Alternative p – y curves*:** based on the observations made in Figure 4.15 and accompanying analyses outlined previously, it has been decided that the Mod_{Zha}

model provides the best representation of the $p - y$ curve behaviour across the full depth of the monopile and will therefore be adopted forthwith in this model. Figure 4.22 presents the schematic representation of Zhang et al. (2005) ultimate soil reaction distribution with depth. Initial $p - y$ spring stiffness has previously been discussed and has been chosen to take the value of $200K_p\gamma'z$, with p_{ult} following recommendations of Zhang et al. (2005).

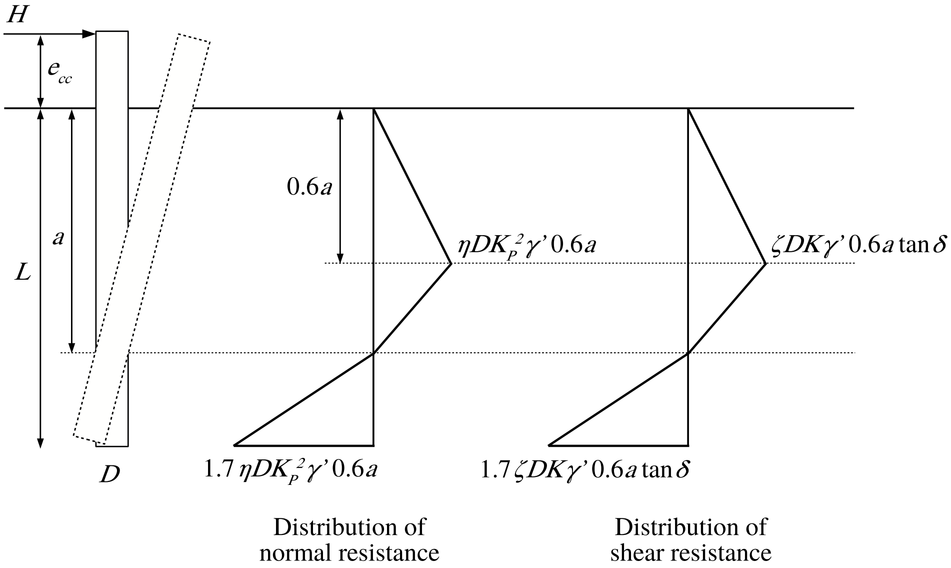

Figure 4.22: Distribution of normal and shear resistance according to Zhang et al. (2005)

A summary of the final individual spring model formulations for both ultimate capacity and initial spring stiffness are presented in Table 4.1 below. As a matter of interest, Figure 4.23 also illustrates the analytical cumulative individual spring component resistance for a typical monopile geometry alongside that of a traditional slender scenario. It can be seen that after the translational horizontal resistance ($p - y$ curves), the majority of additional resistance is derived from base shear. The slender pile presents little additional resistances.

4.5.2 Validation

The proposed multi-spring model is now validated against observed physical model experimental data which represent three different prototype monopile scenarios; two of which present K_{r} values ranging from 52 – 73 and therefore show a rigid response; one presenting a much larger K_{r} value of 587 and therefore shows much more flexible

Table 4.1: Final multi-spring model ultimate capacity and spring stiffness formulations

Model spring [Dimensions]	Ultimate capacity	Initial stiffness
Base shear [F]: $Q_{\tau,b} = f\big(K_{\tau,b}, y_{base}\big)$	$\frac{\pi}{4}\Big(D^2\sigma_p \tan\delta + D_i^2[\sigma_s \tan\phi'_{peak} - \sigma_p \tan\delta]\Big)$	$\frac{\pi}{4}E_s D$
Base moment [FL]: $M_{\theta,b} = f\big(K_{\theta,b}, \theta_{base}\big)$	$\frac{\pi}{24}N_q\big(D^2 - D_i^2\big)\gamma' z D$	$\frac{\pi}{12}E_s D^3$
Side shear moment [FL/L]: $M_{\theta,s} = f\big(K_{\theta,s}, \theta\big)$	$\frac{\pi}{4}\big(K_a + K_p\big)\eta\gamma' z \tan\delta\, hD^2$	$\frac{\pi}{4}E_s D^2$
p – y curve [F/L]: $p = f\big(K_{py}, y\big)$	$\big(\eta K_p^2 + \zeta K \tan\delta\big)\gamma' z D$ (1)	$200 K_p \gamma' z$ (2)

(1) Zhang et al., (2005)

(2) Variation on Klinkvort (2012)

behaviour. Results are presented in Figure 4.24 alongside traditional DNV GL (2016) estimations (dashed lines) for information.

As seen, the multi-spring model presents a more accurate prediction of monopile behaviour, not just in terms of global moment-rotation response, but also across the bending, shear and deflection observed with depth in comparison to the previously presented alternative models across literature, which only consider p – y curve resistance. In Figures 4.24(i) & (ii), where the monopile can be considered rigid, the model is able to capture base moment and shear resistance well and this provides additional resistance to the applied overturning moment, thus bringing previously low global moment-rotation predictions in Figure 4.16 in line with observed behaviour. The DNV code consistently illustrates a poor representation.

With regards the flexible monopile behaviour in Figure 4.24(iii), the proposed model again performs well. As to be expected for flexible lateral pile behaviour, zero bending and shear are seen at the base in the experimental results and this is reflected in the model prediction. The additional spring mechanisms are not mobilised and therefore do not provide any additional resistance. Incidentally, the DNV GL (2016) design p – y curve only formulation also performs admirably for this flexible scenario. This is due to its fundamental empirical derivation being based on piles closer to this pile-soil stiffness range.

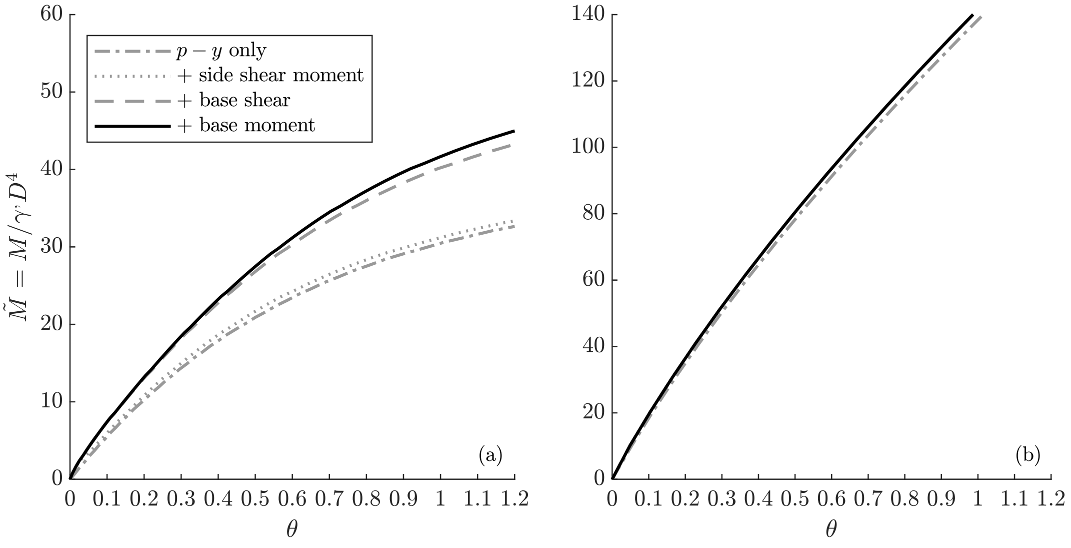

Figure 4.23: Individual spring component lateral resistance: (a) D_p = 5 m, L/D = 5; (b) D_p = 2 m, L/D = 50

4.5.3 Prediction of future monopile behaviour

It has been seen that the proposed multi-spring model presents favourable predictions for monopile behaviour at representative geometries and relative stiffnesses. It is now of interest to evaluate model performance upon extrapolation to much larger, stiffer monopiles that may be deployed in the future. With experimental and field data at this scale not available, results from FE estimations must be adopted for comparison. One such large diameter monopile is numerically modelled in initial PISA project literature (Byrne et al., 2015). Here, the 'short' monopile has a diameter of 10 m and is embedded to a depth of 20 m in dense, fully saturated sand, presenting a K_r value of just 3, *i.e.* very rigid. The authors also present a numerical prediction for a 'long' pile, alongside DNV GL (2016) design predictions for both pile scenarios, which allows for a confident calibration of soil input parameters to be deployed (since these are not stipulated in the literature) in the multi-spring model formulation (taken here to be γ' = 10 kPa and ϕ' = 38°).

Overall there is a strong agreement of predicted behaviour from the multi-spring approach and FE estimations. It would appear, however, that the proposed model shows signs of over-predicting the initial stiffness of the moment-rotation behaviour, whilst under-predicting the ultimate resistance. This is evidenced across both scenarios and may be due to a combination of a number of factors that remain unclear without local soil-pile information from validation data to compare against.

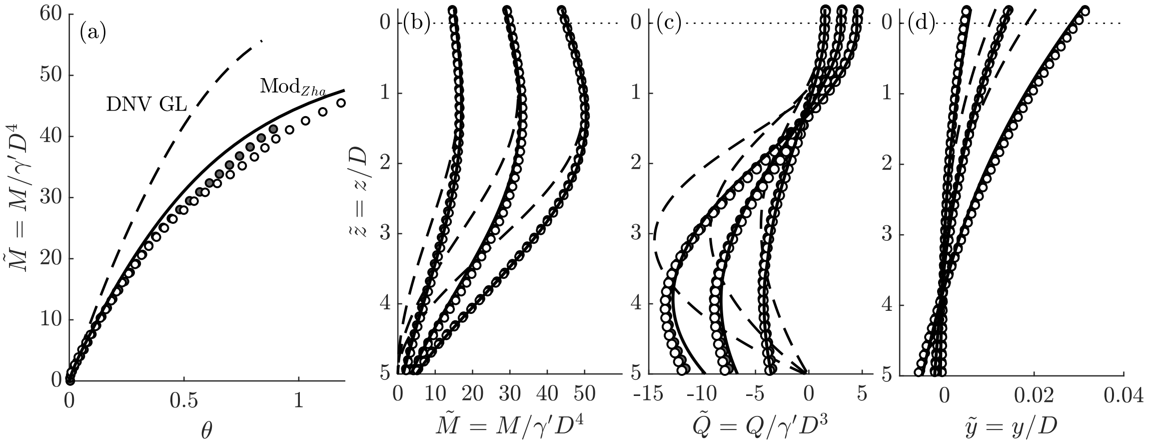

(i) Tests M23 & M34 (D_p = 4 m, $L/D = 5$, $K_\mathrm{r} = 52$)

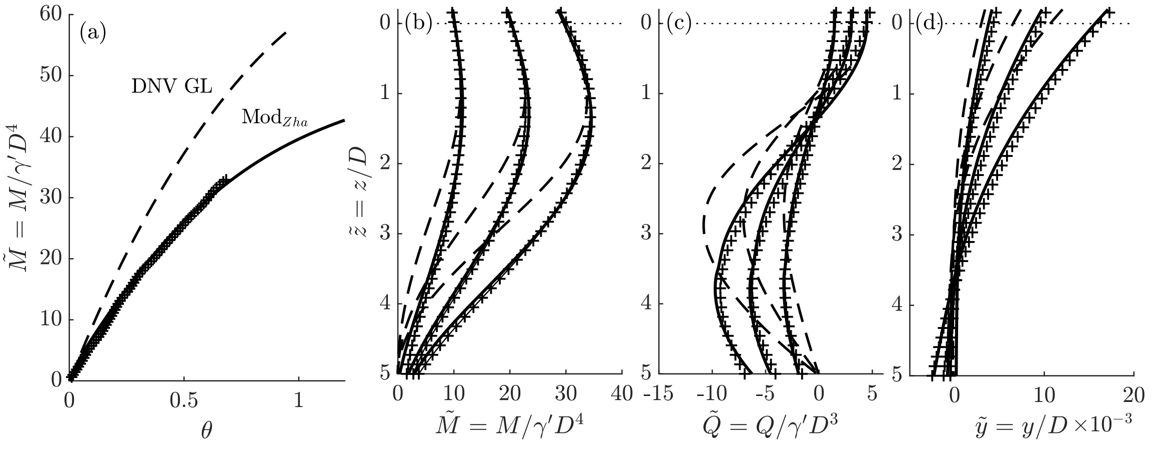

(ii) Test M8 (D_p = 5 m, $L/D = 5$, $K_\mathrm{r} = 73$)

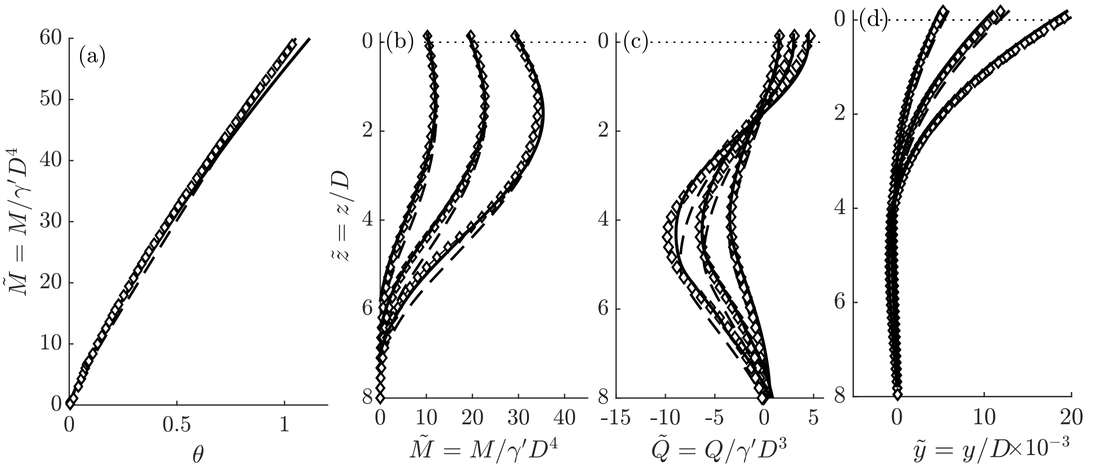

(iii) Tests M6 (D_p = 5 m, $L/D = 8$, $K_\mathrm{r} = 587$)

Figure 4.24: Comparison of monopile behaviour with proposed multi spring model: (a) moment-rotation; (b) bending moment; (c) shear force; (d) deflection

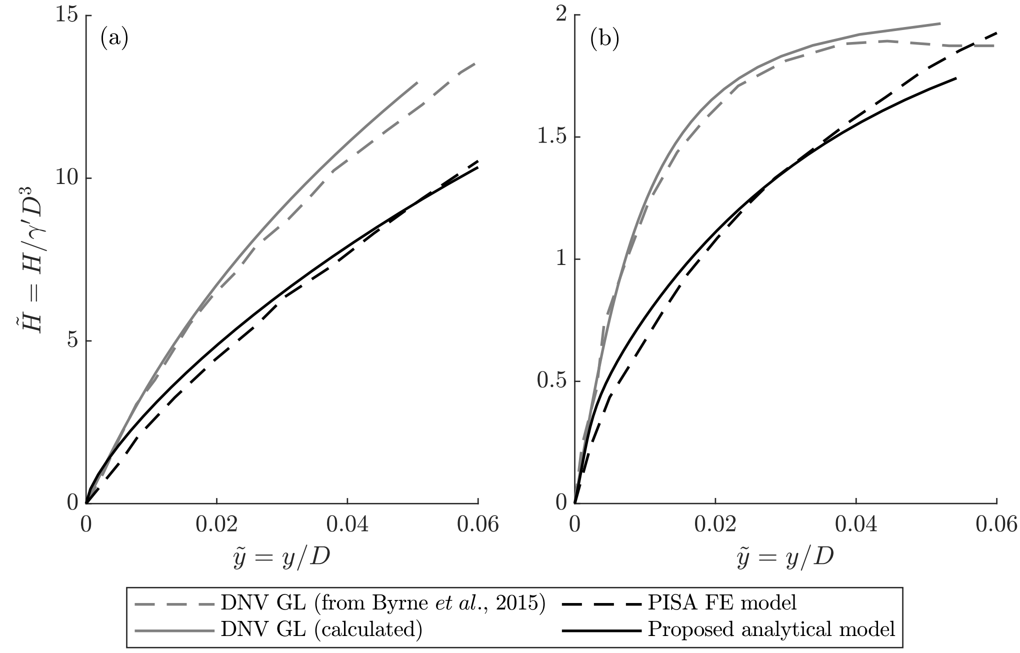

Figure 4.25: Comparison of proposed analytical model with PISA FE predictions: (a) 'long' pile ($D_\mathrm{p} = 10$ m, $L = 60$ m, $K_\mathrm{r} \approx 400$); (b) 'short' pile ($D_\mathrm{p} = 10$ m, $L = 20$ m, $K_\mathrm{r} \approx 3$)

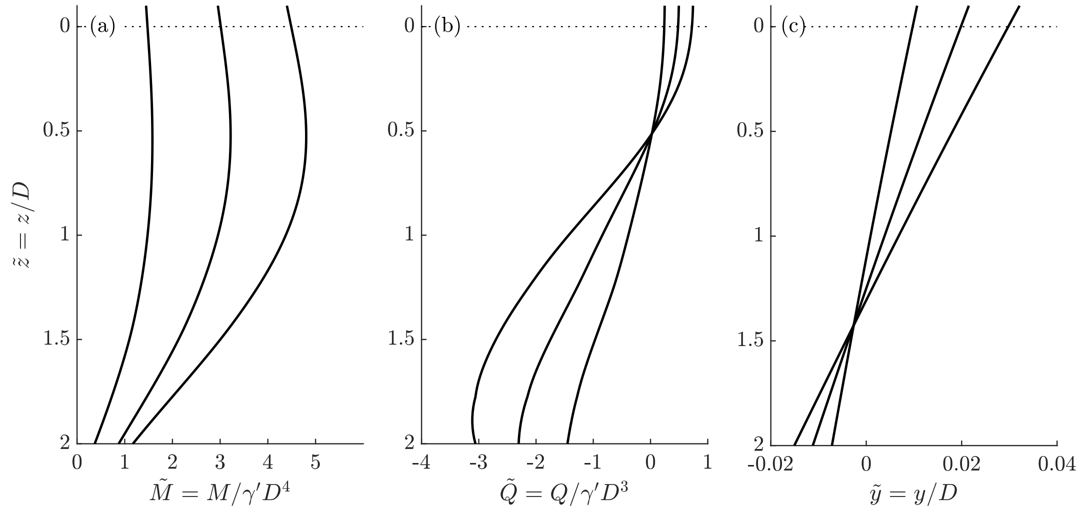

Figure 4.26: Predicted 'short' monopile behaviour ($D_\mathrm{p} = 10$ m, $L = 20$ m, $K_\mathrm{r} \approx 3$): (a) bending moment; (b) shear force; (c) deflection

To offer insight into the possible internal bending and shear mechanisms taking place for these very rigid structures, predicted pile-soil interaction behaviour is also presented in Figure 4.26. It can be seen that there is significant base moment, up to 25 % of the applied overturning moment, as well as very large base shear resistances. The deflected shape presents a near perfectly rigid response. These predictions will of course require experimental validation, and to obtain these will require a substantially large test facility (be it in a centrifuge environment or otherwise) to develop the necessary stress conditions, and equally distant boundary conditions.

4.6 Concluding remarks from monotonic behaviour

In this chapter, observations from monotonic pushover tests have been presented. In depth analysis of the failure of a monopile foundation reveals the progressive mobilisation of soil resistance which originates from the surface and propagates to the pile toe.

1. At low magnitude loads, the majority of lateral deflection and associated soil resistance is observed close to the mudline with little to no deformation at depth. This reflects the behaviour expected from a laterally loaded flexible pile. With the increasing applied overturning moment, full passive resistance close to the surface is achieved and additional soil resistance is developed from depth in the form of base shear and moment as the toe of the pile begins to ‘kick’. At high magnitudes of load, soil is fully mobilised across all shallow depths and considerable rotation at the base is observed resulting in large passive resistance developed here.

2. Comparison of observed experimental $p-y$ curve behaviour with DNV GL (2016) design code and outlined alternatives from across literature reveals inaccuracies in current methodologies, both in terms of initial stiffness and ultimate capacity approximations. It has been proposed here that a $p-y$ model combining the observations of Klinkvort (2012) and Zhang et al. (2005) show the best representation of behaviour with depth, particularly close to the point of rotation and at the toe. That being said, despite a strong portrayal at a $p-y$ level, lateral capacity of a rigid monopile is still underestimated meaning the traditional design philosophy of $p-y$ spring only is no longer valid. Additional lateral soil resistance must be accounted for in model formulation for the base shear and moment mechanisms.

3. An alternative multi-spring model has therefore been outlined which takes into consideration base shear and moment components, as well as a representation

for side-shear with pile rotation. Comparison with observed results over a pile-soil relative stiffness range of 53 to 587 (which represents both rigid and flexible behaviours) reveals a strong predictive capacity, not just at a global moment-rotation level, but also pile moment and shear behaviour with depth. It is the recommendation that this multi-spring approach should be adopted for all monopile design which present any rigid behavioural traits.

4. It is to be noted that a small number of experimental nuances need to be considered whilst evaluating these conclusions. Firstly the inherent centrifuge under- and over-stress conditions present across the depth of the sample mean that stiffness and ultimate capacity may be compromised. This may result in an under-prediction of pile initial stiffness response since it is in the soil close to the surface that lateral resistance is first gained. On the flip side, the pile ultimate capacity may be over-predicted as strength gained from base mobilisation mechanisms may be over-predicted.

5. Cyclic Lateral Behaviour

5.1 Statement of intent

Aspects of cyclic monopile behaviour are now explored. In this chapter, a comprehensive review of current design philosophies and cyclic accumulation models from across literature is first outlined. Initial analysis of physical model experimental results focus on the global monopile cyclic behaviour with the aim of verifying previously observed trends and proposed models. More representative varying load packages are also applied to understand the monopile behaviour beyond traditional constant cyclic loading. Through the use of local instrumentation beneath the mudline, observations of internal soil stress and stiffness changes are analysed to rationalise the global phenomena observed. Finally, the formulation of a new cyclic design chart accumulation model for the prediction of accumulated monopile rotation subject to both constant and varying load is also outlined.

5.2 Background

The cyclic behaviour of a monopile is complex. Over the course of the working lifetime of a wind turbine structure, the foundation is subjected to 10's of millions of load cycles of varying direction and magnitude (Byrne and Houlsby, 2006; Houlsby, 2016), with resulting implications on pile performance that need to be considered. In current DNV GL (2016) design code recommendations, the specification for managing the degradation effects associated with cyclic loading is to simply apply a one-off reduction to the empirical adjustment factor, A (see Equation 4.5), such that $A_{\text{cyc}} = 0.9$ along the full depth of the pile, irrespective of the number and nature of the cyclic loading. This results in a reduction to the $p - y$ curve ultimate capacity in the upper surfaces of the soil. This has been shown to be an important misrepresentation of cyclic behaviour (LeBlanc et al., 2010b; Kirkwood and Haigh, 2014; Zhu et al., 2014).

In an attempt to address this limitation, early research by Little and Briaud (1988), proposed a cycle count based degradation parameter to be directly applied to the displacement component of the individual $p - y$ curves. This allowed a cycle by cycle alteration of $p - y$ curve performance and therefore a more realistic representation. Long and Vanneste (1994) later improved this degradation parameter to incorporate the individuality of the pile setup and loading characteristic, such that:

$$p_N = p_1 N^{(\beta-1)t} \tag{5.1}$$

$$y_N = y_1 N^{\beta t} \tag{5.2}$$

where β takes the value of 0.6 and t is a function of cyclic load ratio, installation method and soil density. It was proposed here that one-way loading was the most onerous condition for soil degradation. Lin and Liao (1999) outlined a similar strain based method with a logarithmic strain evolution and cyclic degradation parameters incorporating pile embedment length and stiffness as well as those mentioned above.

More recent research has since focused on the pile cyclic behaviour at a global level with the aim of developing empirical models for the prediction of pile head accumulated displacement (or rotation) and system stiffness changes. These models clearly demonstrate significant accumulation of pile head rotation upon each cycle as well as increases to pile-soil interaction stiffness and changes to global structure natural frequency, all of which are dependent of the characteristic of the applied cyclic load (LeBlanc et al., 2010b; Abadie et al., 2018; Kirkwood, 2015; Truong et al., 2018). None of these are currently taken into consideration in cyclic lateral pile design. With the maximum diameter of the monopile ever increasing, the boundaries of performance are constantly being pushed and with this, the requirement for an accurate predictive tool of monopile performance throughout its design life has never been greater. This new motivation has given rise to a constantly evolving body of research examining the different challenges surrounding the cyclic lateral response of large-diameter monopiles. The following paragraphs detail a selection of key themes from across literature.

5.2.1 Load characteristic definition

It is worth noting here from the outset that the chosen definition of the cyclic load characteristic to be used throughout this chapter follows that outlined in LeBlanc et al. (2010b), where the two independent cyclic load constants are defined as follows:

- $\zeta_{\mathrm{b}} = M_{\mathrm{max}}/M_{\mathrm{Ed}}$ – the ratio between the maximum applied moment and the moment capacity of the pile-soil system; and
- $\zeta_{\mathrm{c}} = M_{\mathrm{min}}/M_{\mathrm{max}}$ – the ratio between the minimum and maximum applied moments.

These two constants can express any form of cyclic load, as illustrated by Figure 5.1.

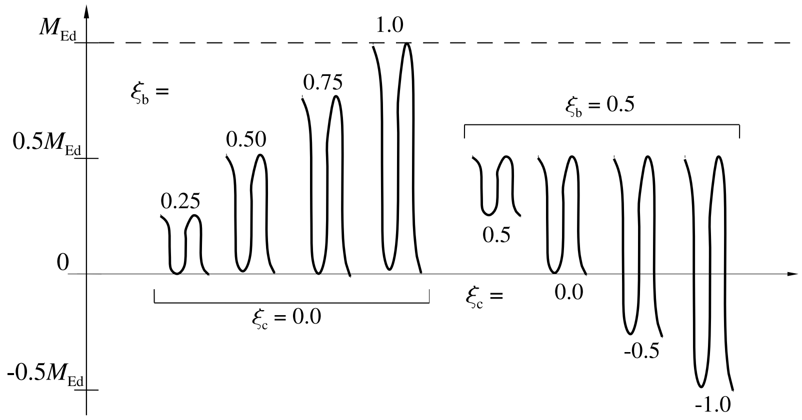

Figure 5.1: Cyclic load characteristics defined in terms of ζ_b and ζ_c (*c.f.* LeBlanc et al., 2010b)

The definition of pile-soil moment capacity, M_{Ed}, is found to vary across literature, with some authors selecting the load magnitude at a perceived monopile ultimate failure, or more often at a chosen magnitude of pile-head displacement or rotation (*e.g.* at $y = 0.1D$). In practice, the selection of this value is at the discretion of the researcher since this simply defines the baseline of the load magnitude ratio across the test matrix. It is when comparing tests across literature that a degree of consistency is required.

5.2.2 Existing cyclic experimental database

The earliest cyclic datasets were developed with the O&G industry in mind (Little and Briaud, 1988; Verdure et al., 2003; Rosquoët et al., 2007) and as such the piles exhibited particularly large K_{r} values, thus presenting flexible failure mechanisms and significant bending close to the surface. It is likely that only the soil in this region experienced cyclic degradation, and is the reason early model recommendations only consider alterations to soil resistance here (compared to the static response). Given the deep seated rotational failure mechanisms associated with the monopiles deployed today, the observations from early datasets are unlikely to be directly transferable.

Motivated by the requirement for new long term cyclic lateral load datasets on large-diameter monopiles, numerous physical model experiments have since been conducted and are adopted in the calibration process of proposed empirical accumulation models. Small scale cyclic model testing at $1g$ has been carried out on the laboratory floor (for example LeBlanc et al., 2010b; Peralta and Achmus, 2010; Cuéllar, 2011), as well as *in situ* at a field test site (Li et al., 2017) and in large soil tanks (Chen et al., 2015). These provide a relatively simple experimental setup and operational environment, and as such upwards of 10^6 load cycles have been applied at this stress scale. Concerns are raised, however, over the implications of high sand dilatancy and reduced soil stiffness on the model pile performance at the low experimental overburden stresses (see Bolton, 1986 for example). Of course, important trends can still be identified from these studies, such as the most onerous load characteristics or the effects of load direction variation, however uncertainty remains over the quantifiable nature of these results. In this respect, the execution of centrifuge experiments conducted at Ng (for example Klinkvort, 2012; Kirkwood, 2015; Truong et al., 2018), have allowed for the correct representation of overburden stresses and have captured the most representative *in situ* stress state changes without moving to an actual prototype monopile scale environment.

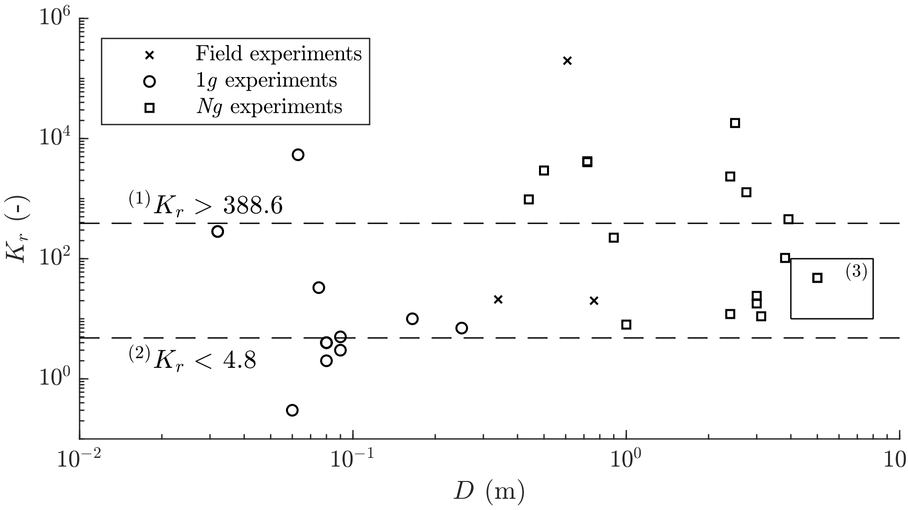

Figure 5.2: Available cyclic datasets and their respective pile geometry. N.B. $^{(1)}$Perfectly flexible, $^{(2)}$perfectly rigid, $^{(3)}$prototype geometrical range (D = 4–8m)

By way of presenting a complete database of publicly available cyclic lateral load datasets alongside their respective pile geometries, Figure 5.2 illustrates the relatively few studies present within the geometrical and stress state range of interest (marked solid box area$^{(3)}$). Today's monopiles are both rigid in pile-soil stiffness behaviour and large in diameter and therefore experimental datasets need to reflect this for confidence in the model calibration process.

5.2.3 Cyclic accumulation models

Based on observations from physical model tests, cyclic displacement accumulation models have been founded on both logarithmic (*e.g.* Lin and Liao, 1999; Rosquoët et al., 2007; Li et al., 2017; Chen et al., 2015) and power (*e.g.* Little and Briaud, 1988; Long and Vanneste, 1994; LeBlanc et al., 2010b; Klinkvort, 2012; Truong et al., 2018) function relationships. Table 5.1 presents a selection of accumulation model choices across literature alongside experimental stress level, model pile geometries and maximum applied cyclic count used in the model calibration process.

Table 5.1: Cyclic accumulation models

Power law formulation:	$y_N/y_1 = N^\alpha$				
Author(s)	Scale	D (m)	K_r (-)	N_max	α
LeBlanc et al. (2010b)	1g	0.08	4.4	10000	0.02–0.25
Zhu et al. (2016)	Ng	2.5	>1x10^4	3000	0.05–0.16
Truong et al. (2018)	Ng	2.75–3.92	10 − 454	50-1500	0.05–0.20
Klinkvort (2012)	Ng	3.0	18	10000	0.04–0.20
Kirkwood (2015)	Ng	3.8	103	60000	0.05–0.38
Logarithmic law formulation:	$y_N/y_1 = 1 + \beta \ln N$				
Author(s)	Scale	D (m)	K_r (-)	N_max	β
Lin & Liao (1999)	Field	0.3–1.42	500->1x10^5	100	0.02–0.24
Li et al. (2015)	Field	0.34	21	5000	0.125
Peralta & Achmus (2010)	1g	0.06	0.3	10000	0.21
Chen et al. (2015)	1g	0.165	10	10000	0.005–0.02
Rosquoët et al. (2007)	Ng	0.72	>1x10^3	40	0.04–0.09
Li et al. (2010)	Ng	3.1	11	1000	0.17–0.25

Although not fully conclusive, it would appear from Table 5.1 that a power relationship is the prevailing model selection based on the physical experiments conducted at more representative monopile geometries and stress conditions. This is in agreement with the recommendation of Peralta and Achmus (2010), where a logarithmic relationship for flexible piles, and a power fit for rigid piles are suggested to be most appropriate. For the majority of cyclic experimental datasets, the upper bound of maximum cycle count was limited to an order of magnitude of around 10^3 with very limited data extending beyond this. The confidence in the model accumulation performance at very high number of cycles is therefore greatly compromised. Indeed, Abadie et al. (2018) observe an over prediction of accumulated rotation at high cycles for their power relationship model in relation to experimental data (Figure 5.3a), and in the one available very high cyclic count dataset ($\mathrm{N} > 10^6$) of Cuéllar et al. (2009), a distinct stabilisation of cyclic displacement amplitude (defined as the difference between maximum and minimum displacement for each cycle) is observed after approximately 10^5 cycles (Figure 5.3b). The authors are able to relate this to an observed stabilisation in soil flow movement at the surface (further information on this is presented in Section 5.2.5).

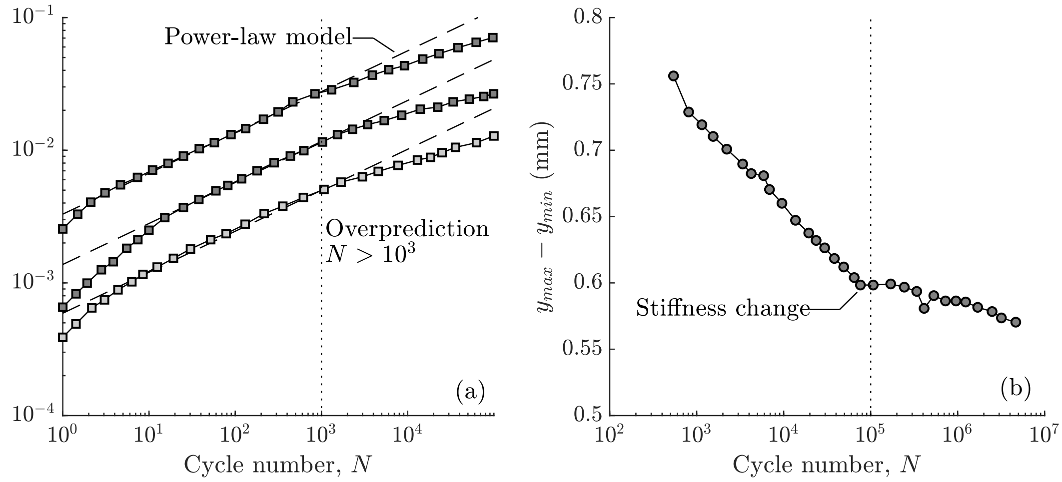

Figure 5.3: Previous dataset behaviour at very high cycles; (a) accumulated rotation overprediction (Abadie et al., 2018); (b) cyclic amplitude trend change (Cuéllar et al., 2009)

It can also be seen in Table 5.1 that a range of magnitudes for the cyclic accumulation constants, α and β, adopted in both the power and logarithmic relationships respectively, have been outlined across literature. In the case of the power law, the magnitude of α is seen to have a range from 0.02 to 0.38, where β ranges from 0.005 to 0.25 for the logarithmic law. Much like with the aforementioned $p - y$ degradation models, the value of α and β across literature has been shown to be dependent on a number of experimental characteristics:

$$\alpha, \beta = f(\zeta_b, \zeta_c, D, R_d) \tag{5.3}$$

Klinkvort (2012), Kirkwood (2015) and LeBlanc et al. (2010b) all observe increases in rate of cyclic accumulation with an increase in load ratio parameter ζ_b. Although the effect is not so prominent in Truong et al. (2018) who proposing cyclic load ratio (ζ_c) and sand density the more critical drivers in the rate of cyclic accumulation. Recent

FEM simulations performed by Luo et al. (2018) also suggest additional diameter effects on the rate of cyclic accumulation, with the magnitude of α proportional to the pile diameter.

With regards to the cyclic load parameter ζ_c, which characterises the cyclic load, clear discrepancy can be observed between experiments conducted at $1g$ and those at a prototype representative stress level. At $1g$ (LeBlanc et al., 2010b; Abadie et al., 2018), it is evident that the most onerous load case occurs when $\zeta_c < 0$, with peak accumulation at $\zeta_c \approx$ -0.6, with the authors observing up to twice the total rotation for this load case compared to a one-way scenario. This is in contrast to the centrifuge tests (Klinkvort, 2012; Kirkwood, 2015; Truong et al., 2018) where the maxima appears to be centered at $\zeta_c \approx 0$. This difference may be attributed to the lack of overburden stress that is present in a $1g$ experiment. Here any redistribution of sand that occurs during the positive load phase cannot generate the 'locked-in' stresses close to the pile that a centrifuge counterpart is able to. These stresses subsequently provide additional stiffness which reduces pile movement on the return negative load phase.

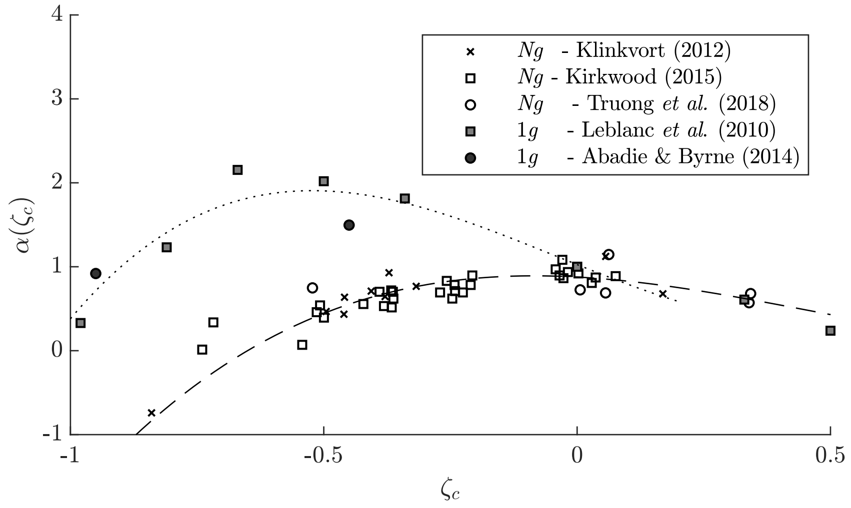

Figure 5.4: Empirical parameter $\alpha(\zeta_c)$ from previous literature; dashed (- -) and dotted ($\cdots$) trend lines represent centrifuge and $1g$ tests relationships respectively

5.2.4 Varying load magnitude

The above developments in predictive accumulation models are derived from and validated against experiments with constant load magnitude throughout. In reality, loading on an offshore monopile is constantly changing in magnitude, eccentricity and direction over its entire lifetime and these need to be taken in consideration for the confident prediction of monopile long-term performance. Firstly, the effects of multi-directional loading have been studied by several authors (Su et al., 2014; Rudolph et al., 2014; Nanda et al., 2017; Richards et al., 2018). Whilst these offer valuable insights into pile behaviour under these load scenarios, and demonstrate the potential for significant increases in pile head displacement with direction variation, there still remain considerable questions regarding the long-term effects of load in a simple single plane, and therefore focus here remains in this respect.

When it comes to long-term superposition of varying load, very limited physical model experimental datasets are available across literature. Any load variation that has been considered has exclusively focused on the global pile behaviour subject to the successive application of packages of constant load (LeBlanc et al., 2010a; Abadie et al., 2018; Li et al., 2017; Truong et al., 2018), which either increase or decrease with consecutive packages. As a general observation from these, the load package with the largest magnitude appears to have the largest contribution to the pile deformation.

Exploring more closely the effects of load sequencing, both LeBlanc et al. (2010a) and Abadie et al. (2018) observe little difference in the magnitude of ultimate accumulated permanent rotation, provided equal number of each load package is applied across the full time history. For a load regime following a sequence of 10^4×A→100×B→10×C, a difference in ultimate accumulated permanent rotation of just 1.4% was found in comparison to a load sequence of 10×C→1000×B→10^4×A (see Figure 5.5).

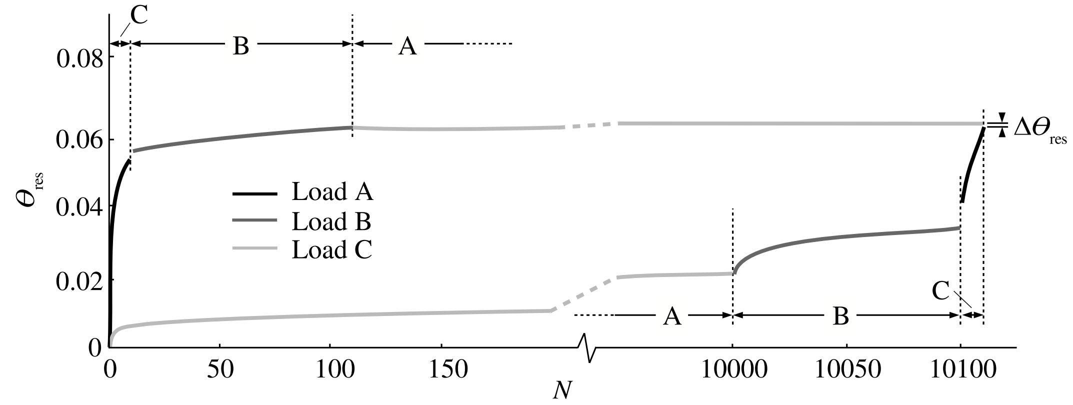

Figure 5.5: Permanent pile head rotation for both increasing and decreasing multi-amplitude cyclic load sequences (LeBlanc et al., 2010a)

Given the nature of loading in the offshore environment, it is unknown as to which order the applied varying magnitude load packages will arrive, which makes the prediction of accumulated pile head displacement (or rotation) difficult. One method is to adopt the Miner's rule (1948). This cumulative damage model was first introduced into soil mechanics by Stewart (1986) for the prediction of incurred strain in cyclic triaxial laboratory tests. It has since successfully been adopted by Lin and Liao (1999) to evaluate the flexible pile strain accumulation for successive cyclic lateral load packages of different magnitudes, though in this case validation was made with just 50 cycles of applied load. Figure 5.6a presents the simplicity of the predictive model formulation.

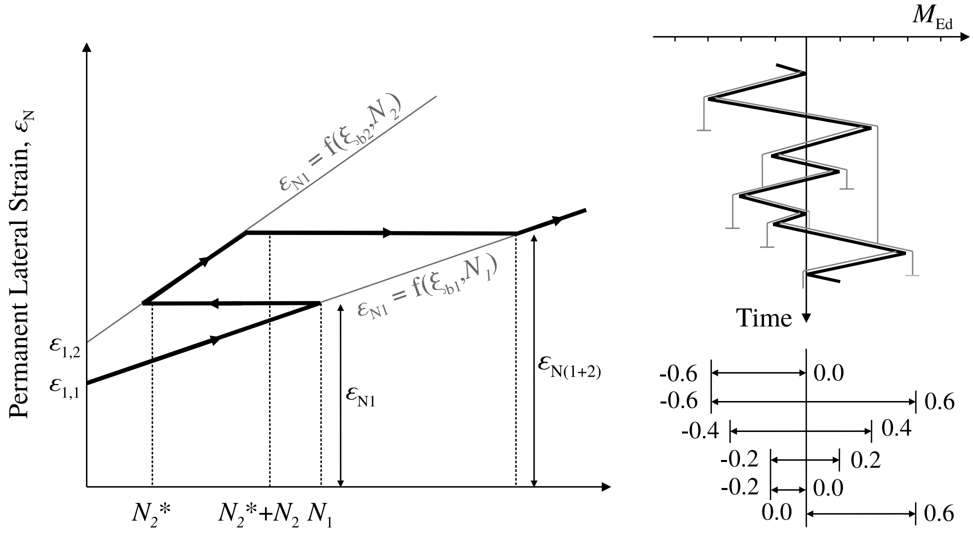

(a) (b)

Figure 5.6: (a) Application of the Miner's rule (c.f. Lin and Liao, 1999); (b) Extended rainflow-counting method based on the procedure by Rychlik (1987)

Recent experimental studies of much greater cyclic counts (LeBlanc et al., 2010a; Li et al., 2017; Truong et al., 2018) illustrate the effectiveness of the Miner's rule, when coupled with the author's own individual accumulation model. Across these, reasonable comparisons were found for most of the one-way loading tests, however the Miner's rule was found to struggle for a two-way loading counterpart.

To date, physical modelling experiments have only considered the superposition of load sequences with constant load per package. Of course, in reality the load magnitude is seemingly randomly changing with cycles and the monopile behaviour subject to this loading regime is unclear. It has been proposed that by applying the more complex rainflow-counting method outlined by Rychlik (1987) (see Figure 5.6b), a random cyclic load time-series can be decomposed into a set of fully closed hysteresis loop load reversals defined in terms of ζ_b and ζ_c. Here, the load history is compared to the flow of water down a series of pagoda roofs, where individual rainflows are assumed to successively begin at the inside of each strain peak. The rainflow path is followed down each of the pagoda roofs, with specifics of successive flow path intersections dictating which rainflow cyclic stresses are to be counted or not. Individual load cycles can then be related to individual empirical accumulation parameters (α or β) and can be inputted into an accumulation pile rotation model. This method has, however, only been hypothesised and is not validated against any experimental evidence.

5.2.5 Cyclic stiffness degradation

The rationale of monopile load–deflection (or equally moment–rotation) stiffness response can be represented as either absolute stiffness, k_{abs}, or secant stiffness, k, for a cyclic loading event. The secant stiffness is typically more widely of interest since this describes the soil-pile behaviour upon each cycle, and therefore the actual state the soil is currently in. This can be used to calculate important design aspects such as load dampening and system natural frequency.

It is well established in literature (Rosquoët et al., 2007; LeBlanc et al., 2010b; Klinkvort, 2012; Bienen et al., 2012; Kirkwood, 2015) that the secant stiffness of monopiles founded in both dense and loose sand increases upon the application of cyclic lateral loads (in both $1g$ and Ng). Authors are also in agreement that a logarithmic relationship, as per Equation 5.4, best describes this evolution with cycles.

$$\frac{k_{N,\theta}}{k_{1,\theta}} = 1 + \kappa_\theta \ln N \tag{5.4}$$

where κ_θ is an empirically derived constant to describe the rate of stiffness evolution. According to literature κ_θ is dependent on the load magnitude and characteristic (LeBlanc et al., 2010b; Klinkvort, 2012; Kirkwood, 2015). A higher relative density is also seen to give rise to faster stiffness increase with cycles (Chen et al., 2015).

$$\kappa_\theta = f(\zeta_b, \zeta_c, R_d) \tag{5.5}$$

Much like for the accumulation of rotation, there are conflicting observations on the rate of stiffness increase, with respect to the load characteristic, between the results obtained at $1g$ and those at a representative stress level. At $1g$ with LeBlanc et al. (2010b), two-way loading ($\zeta_c < 0$) is shown to generate the slowest rate of stiffness increase, which is reflected in the greatest accumulated rotation here. In stark contrast, Klinkvort (2012) observe at Ng two-way loading to generate the fastest rate of stiffness increase. The rationale for this has previously been hypothesised due to the 'locked-in' stresses that develop with sand redistribution under load which can only develop at higher overburden stresses.

One observation that has been documented by both Kirkwood (2015) and Truong et al. (2018) that indicates the potential ‘locked-in’ stresses is the residual bending moments that remain upon pile unload (Figure 5.7a). Since no external load is applied at this time, it would imply that the ‘locked-in’ bending is a result of an increase in residual horizontal stress in the soil adjacent to the pile due to sand redistribution. The underlying result being an increase in overall foundation stiffness. In much longer cyclic experiments at $1g$, Cuéllar (2011) found coloured surface sand to migrate towards the pile and form a convection flow cell in the upper regions adjacent to the pile (see Figure 5.7b). Observed densification of the soil within this cell leads to an increase in stiffness with number of lateral load cycles. Incidentally, the largest applied loads generated the largest convective cell which would imply greater sand densification and therefore may provide an explanation for the fastest rate of stiffness increase for this load characteristic.

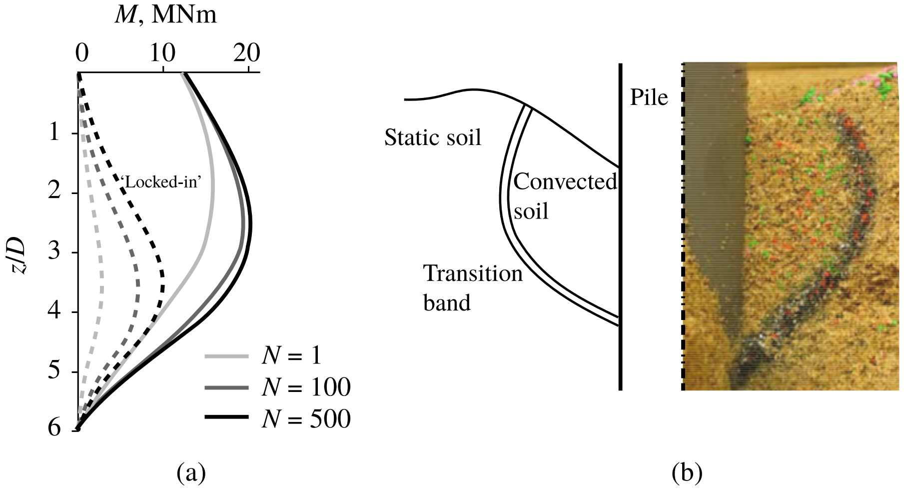

Figure 5.7: (a) ‘Locked-in’ bending moments (dashed lines) developing on unload during cyclic load regime (Truong et al., 2018); (b) Proposed convective flow cell adjacent to pile (Cuéllar, 2011)

Finally, Kirkwood (2015) hypothesised that with successive load packages of increasing magnitude, the rate of stiffness increase for a subsequent load package should be less than if the preceding package had not been applied. This change of stiffness rate evolution depends on the ratio of load magnitudes between the successive load packages ($\zeta_{\mathrm{b,N-1}}/\zeta_{\mathrm{b,N}}$), as well as the number of applied cycles. The proposed empirical reduction parameter is applied to the originally defined κ in Equation 5.4. Several nuances exist with this proposal, such as its breakdown at low cyclic counts and its inability to manage successive load packages of reducing load magnitude.

5.3 SLS aims and objectives

The review of previous cyclic literature has outlined a number of experimental studies where applied loads have varied in both cyclic magnitude and characteristic across the test matrix. Within these studies, attempts to independently characterise pile rotation accumulation and stiffness behaviour based on either ζ_{b} or ζ_{c} have been made, without great attention being placed on one parameter or the other in solidarity.

The complex local soil mechanics phenomena that take place under cyclic loading are not well examined or understood for the simpler one-way loading case, and this complexity is only elevated for a two-way scenario. A decision has therefore been made to focus on one-way loading alone with the aim of addressing a number of the uncertainties that remain in this respect. Specific objectives of the experimental programme strive towards the better understanding of both global pile and local soil behaviour and are outlined below:

1. increase the order of magnitude of maximum cyclic count at prototype stress levels, over a wider range of representative load magnitudes (both serviceability and fatigue limit state magnitudes), to explore the confidence levels in previously outlined accumulation model formulations;
2. observe the global pile-soil behavioural response when subjected to cyclic regimes of varying magnitude which are more representative to typical random storm conditions, and validate the suitability of damage accumulation models;
3. greater understand monopile stiffness changes with cycles through the direct measurement of ‘locked-in’ stresses on the monopile;
4. develop a new design chart cyclic accumulation model to allow for the prompt prediction of accumulated rotations at the mudline subject to packages of both constant and varying load magnitude.

5.4 Global monopile cyclic response

This section will focus on the experimental observed global behaviour of the monopile foundation subject to cyclic lateral loads – this meaning the external observations that can be made at the mudline and above. Accumulated pile head rotations and global system stiffness changes are both explored. These are compared with observed trends from across previous literature. Any accumulation model that is presented, however, is empirical in nature and explores trends in behaviour based on load magnitude ratios and cyclic counts. The local pile-soil interaction will be explored later in this chapter (Section 5.7) in an attempt to piece together the changes in internal soil stress and stiffness with global observations.

In total, 15 individually prepared cyclic lateral load tests were performed in the centrifuge; 7 of these on a model pile with a prototype diameter of 5m and 8 with a prototype diameter of 4m. The individual test cycle count ranged from 14 cycles, to explore the very large strain accumulations for high-magnitude unsymmetrical loading (C37), to 10^5 cycles to observe the ratcheting associated with a low magnitude fatigue load scenario (C35). Selection of applied load package magnitudes in between these minimum and maximum extremes was made to optimise the potential for observing changes in monopile accumulation behaviour with load level increase. Figure 5.8a presents a typical time history of applied moment and observed rotation at the mudline.

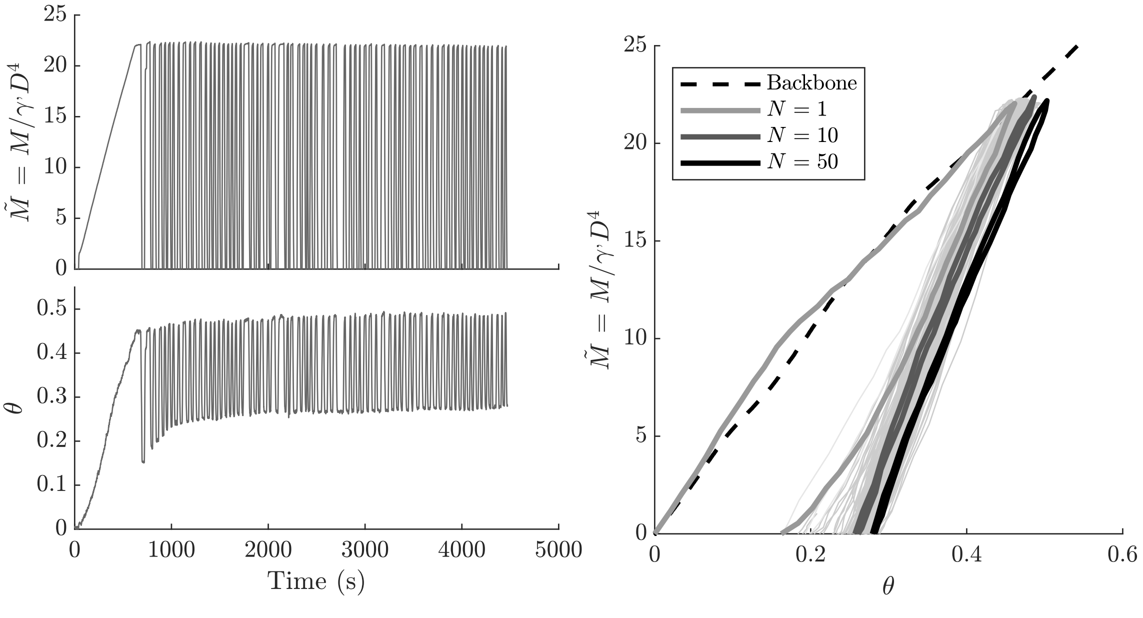

(a) (b)

Figure 5.8: Test no. C31: (a) example time history of applied load and pile head rotation; (b) observed moment-rotation response

5.4.1 Definition of global behaviour

Throughout literature, a variety of definitions for global pile load (applied force or overturning moment), deformation (pile head displacement or rotation) and stiffness (any combination of the previous) have been presented which can make it difficult for direct qualitative comparison. This thesis will present all global behaviour in terms of applied normalised overturning about the mudline ($\tilde{M}$), resulting rotation at the pile head (θ) and dimensionless secant stiffness being the relationship between the two ($\tilde{k}_\theta$ = $\tilde{M}/\theta$). Schematic representation of these global definitions are presented below.

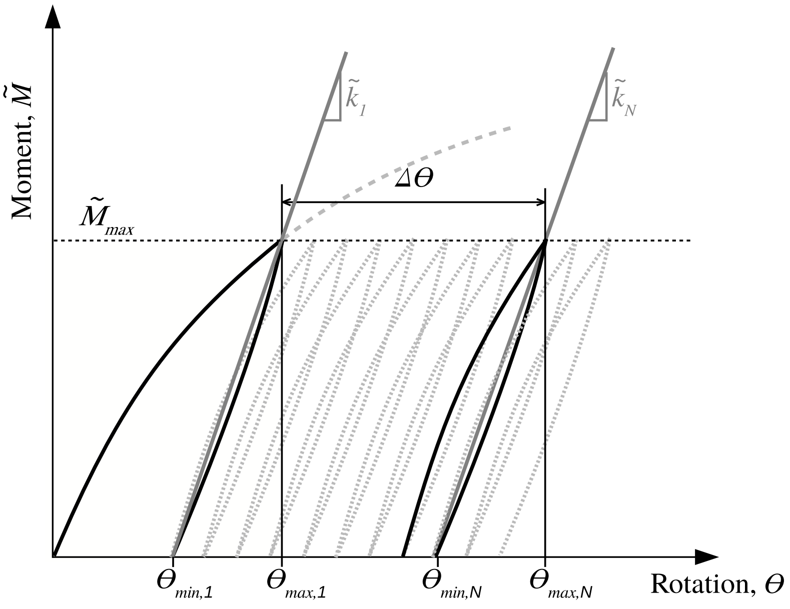

Figure 5.9: Definition of global behaviour parameters (θ_{max} rotation on maximum load, θ_{min} permanent rotation on unload)

The calculation of load magnitude ratio, ζ_{b}, requires the definition of M_{Ed} which provides the baseline for all applied moments. In this case it has been decided to be taken at the point of mudline rotation at the serviceability limit since this is most applicable to design. It is the recommendation of the DNV GL design code (*c.f.* Section 7.6.2.7) that a serviceability permanent rotation, θ_{min}, of 0.5° at the mudline should not be exceeded. Taking into the account the possible 0.25° of pile installation error, the allowable permanent serviceability rotation should therefore actually be reduced to 0.25°. This would require $M_{\mathrm{Ed,SLS}}$ to be defined at a load magnitude that induces 0.25° rotation upon unload. With this in mind, the values of $\tilde{M}$ = 32.7 and 35.3 for model piles MP1 and MP2 respectively are determined from the backbone response presented in Section 4.4.

5.4.2 Pile head rotation

By way of illustration of the accumulation of mudline rotation subject to cyclic lateral load, Figure 5.8b displays a typical global normalised moment-rotation response for a constant cyclic load package. Selected cycles are highlighted to emphasise the evolution of foundation secant stiffness and rotation with cycle number. Unlike previous literature, the following section will examine both maximum, θ_{max}, and permanent, θ_{min}, rotation on load and unload respectively. For the constant load experiments θ_{max} and θ_{min} at each cycle were found by means of the aforementioned user-defined *peakfinder* script (see Section 3.4.7). Figure 5.10 presents their respective absolute evolution with cycles where it is clear a larger load induces greater accumulated rotation.

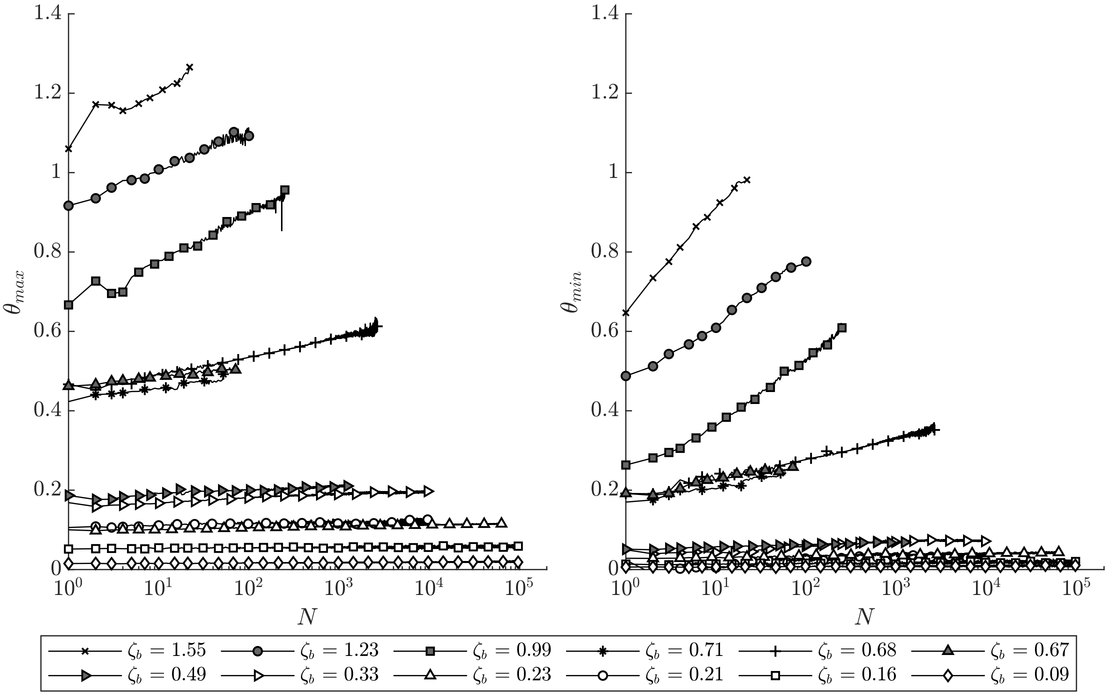

Figure 5.10: Evolution of maximum rotation, θ_{max}, and permanent rotation, θ_{min}, with cycles

In the development of previously published accumulation models, maximum pile head rotation has typically been described by one of two normalisation methods. Firstly, the ratio between the absolute rotation at N cycles and the rotation observed after one cycle, *i.e.* $\theta_{\text{max,N}}/\theta_{\text{max,1}}$ (*e.g.* Klinkvort, 2012; Truong et al., 2018), and secondly, in terms of the accumulation of rotation that occurs after the first cycle, *i.e.* $(\theta_{\text{max,N+1}}-\theta_{\text{max,1}})/\theta_{\text{max,1}}$ (*e.g.* LeBlanc et al., 2010b; Abadie et al., 2018). Both methods have their advantages; with the former providing clearer observations of the rotation accumulation at low cyclic counts, whereas with the latter the more subtle, very long-term ratcheting behaviour becomes more apparent.

Figure 5.11 presents the results from across all constant load cyclic experiments for both normalisation methods and in both a log–log and semi–log graphical representation. A straight line data trend in either log–log or semi–log would point towards a power or logarithmic accumulation model, respectively, being the most suitable representation which has been of debate across literature. From Figures 5.11a & b it is unclear as to a preferred choice, with both log–log and semi–log appearing to present straight line trends and least squares fit values reflect this. On the other hand, the inspection of Figures 5.11c & d illustrates a distinct variation in long-term behaviour for higher ratios of ζ_{b} compared with lower ratios. For a value of $\zeta_{\mathrm{b}} > \sim 0.50$, the accumulated rotation appears to follow a power law ($\frac{\Delta\theta_{\mathrm{max}}}{\theta_{\mathrm{max},1}} = N^{\alpha_{\mathrm{max}}}$) with reasonable accuracy (Fig. 5.11c). However when $\zeta_{\mathrm{b}} < \sim 0.50$, there is a distinct change in accumulation trend whereby the logarithmic law ($\frac{\Delta\theta_{\mathrm{max}}}{\theta_{\mathrm{max},1}} = 1 + \beta_{\mathrm{max}} \ln N$) presents the most suitable model representation (Fig. 5.11d). A dashed line of transition is marked across for information. Incidentally, Luo et al. (2018) found a similar trend shift at $\zeta_{\mathrm{b}} \approx 0.56$ in their numerical simulation study, however no reasoning was given for this selected separation point.

On a practical note, this would mean that the selection of a power law function to predict accumulated rotation at low design cyclic loads would overestimate accumulated rotation, whereas a logarithmic trend for high design cyclic loads would underestimate the accumulated rotation.

Comparing this observation with the previously analysed progressive monotonic failure behaviour (Section 4.4) reveals a link between trend selection and observed failure mechanism. At low applied overturning moment, it has been seen that monotonic behaviour illustrates a more flexible pile response, with proportionally greater pile bending. For the low load ratio cyclic tests ($\zeta_{\mathrm{b}} < \sim 0.50$), the logarithmic law presents the best representation which reflects the recommendation of Peralta and Achmus (2010) who stipulate a logarithmic trend for flexible piles. On the other hand, at higher magnitudes of overturning moment the monotonic behaviour of the pile was seen to be rigid, and for high load cyclic tests ($\zeta_{\mathrm{b}} > \sim 0.50$), these exemplify a power law accumulation. Peralta and Achmus' recommendation for rigid pile accumulation is also a power law. In addition, LeBlanc et al. (2010b) do state that their proposed power law is less suitable for the lower magnitude loads.

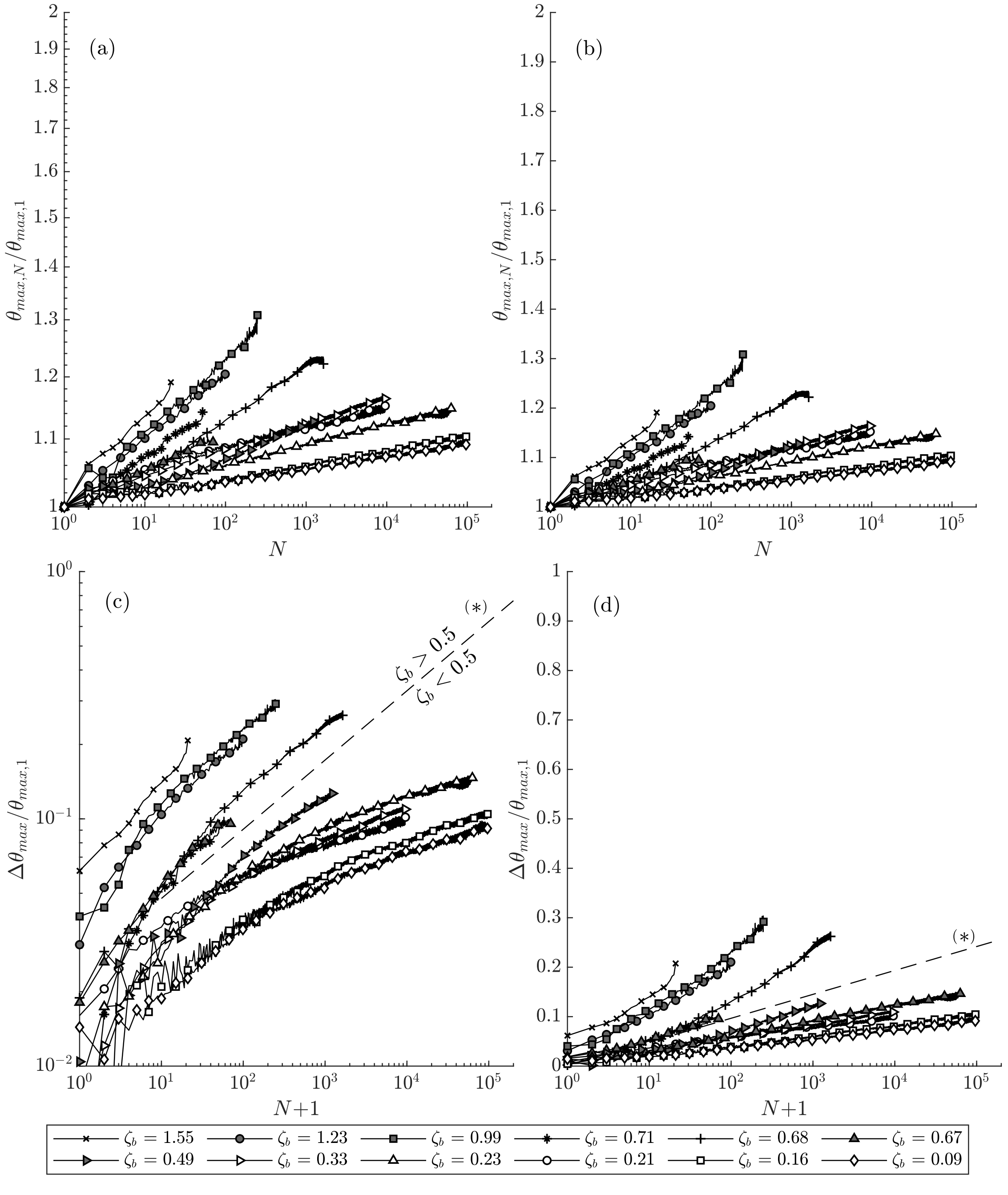

Figure 5.11: Normalised maximum rotation at the mudline, $\theta_{\max,N}/\theta_{\max,1}$, expressed in (a) log–log form; (b) semi–log form. Normalisation accumulated maximum rotation post first cycle, $\Delta\theta_{\max}/\theta_{\max,1}$, expressed in (c) log–log form; (d) semi–log form. $^{(*)}$ line of trend transition

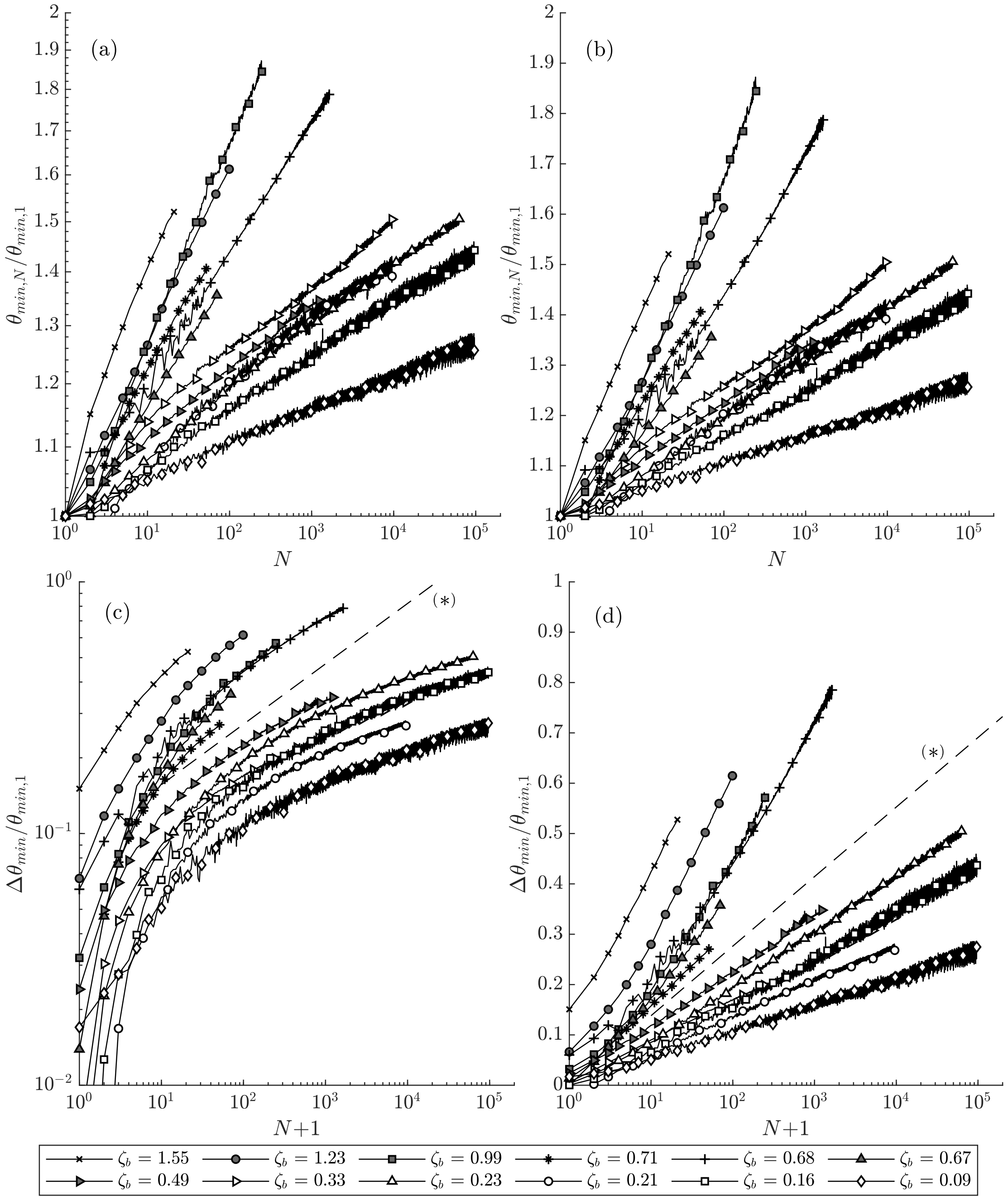

Figure 5.12: Accumulated residual rotation at the mudline, $\theta_{\mathrm{min,N}}/\theta_{\mathrm{min,1}}$, expressed in (a) log–log relationship; (b) semi–log relationship. Change in maximum rotation post first cycle, $\Delta\theta_{\mathrm{min}}/\theta_{\mathrm{max,1}}$: (c) log–log relationship; (d) semi–log relationship. $^{(*)}$ line of trend transition

The same process of normalisation is now repeated for the permanent rotation, θ_{min}, which remains upon unload of the pile. Figure 5.12 presents the cyclic accumulation in both log–log and semi–log form, of which the previously outlined observations from maximum rotation results are again seen here. Comparison of Figures 5.11 and 5.12 also reveals a much faster rate of accumulated rotation on unload in comparison to on load. This can be attributed to the progressive stiffness changes and soil redistribution that takes place as the load is removed from the pile.

Across Figures 5.11 & 5.12, no matter the graphical form choice, it is clearly shown that the rate of cyclic maximum rotation accumulation increases with ζ_{b}, which agrees with many physical model results across literature (*e.g.* Klinkvort, 2012; Kirkwood, 2015; Chen et al., 2015). There is also clear long-term ratcheting which continues to evolve throughout the full duration of this test series (up to maximum cycle count of 10^5). Figures 5.13a & b present the relationships of ζ_{b} against the accumulation coefficient for the logarithmic and power trend respectively.

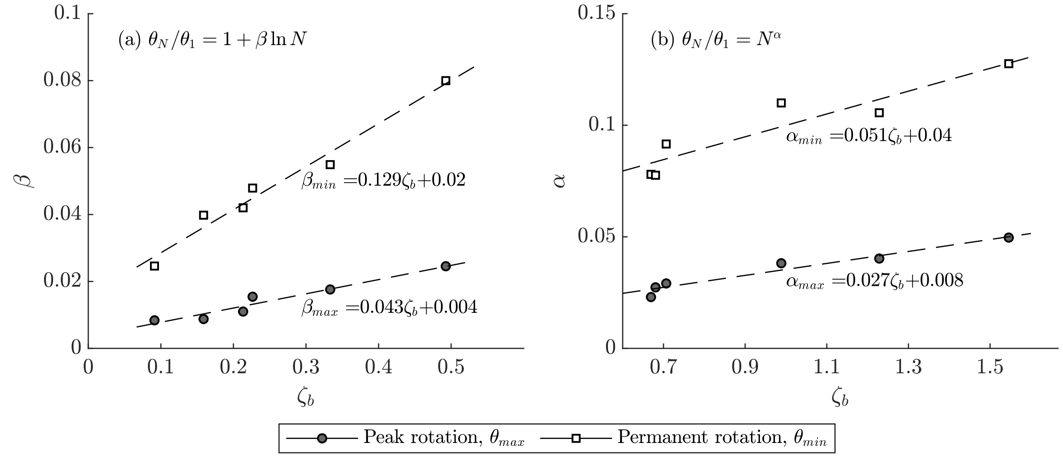

Figure 5.13: Variation of (a) β with $\zeta_{\mathrm{b}} < 0.5$; and (b) α with $\zeta_{\mathrm{b}} > 0.5$

5.4.3 Cyclic stiffness

It has been well documented that there is a progressive increase in secant stiffness with number of applied cycles over a range of sand densities and stress levels (LeBlanc et al., 2010b; Klinkvort, 2012; Kirkwood, 2015). The results from this study, presented in Figure 5.14, reflect the findings from this previous research. For a higher magnitude load, the absolute value of $\tilde{k}_\theta$ is lower (Figure 5.14a) which reflects the greater plastic deformation expected. Comparison of stiffness ratio between the Nth and first cycles (Figure 5.14b) reveals a faster accumulation for greater ζ_b.

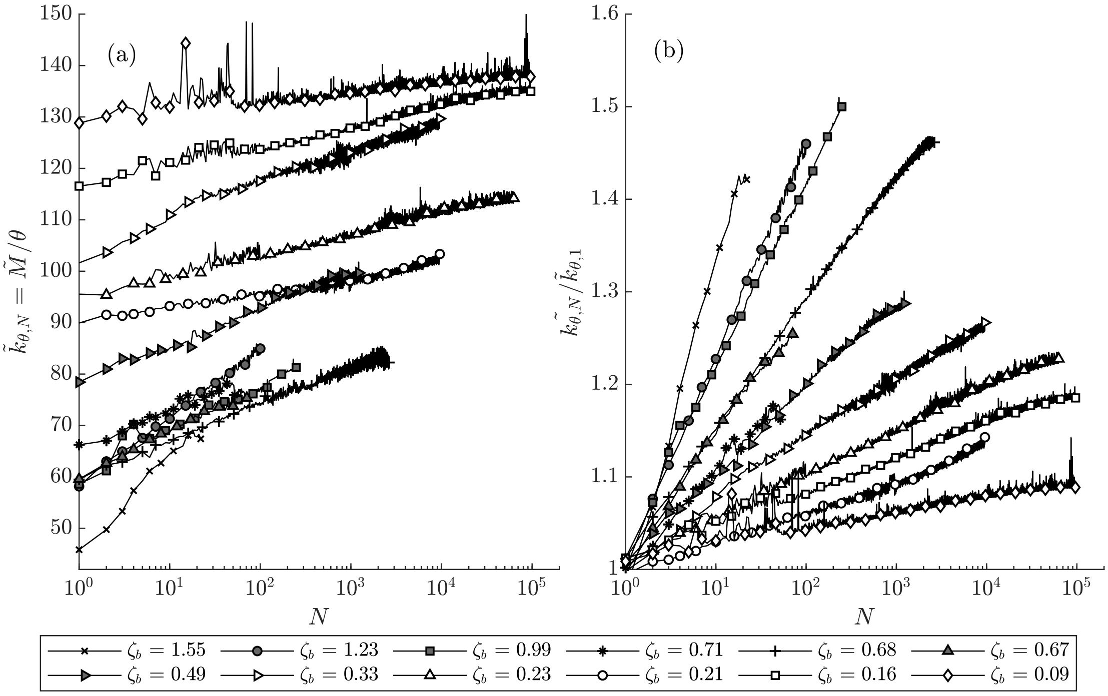

Figure 5.14: Evolution of (a) dimensionless secant stiffness, $\tilde{k}_{\theta,N}$; (b) normalised secant stiffness, $\tilde{k}_{\theta,N}/\tilde{k}_{\theta,1}$

Figure 5.15 shows the rate of stiffness increase, κ_θ, with the applied load ratio, ζ_b, where κ_θ is the logarithmic coefficient relating $\tilde{k}_{\theta,N}$ and $\tilde{k}_{\theta,1}$. A clear proportional relationship is seen which agrees with observations from previous literature (Klinkvort, 2012).

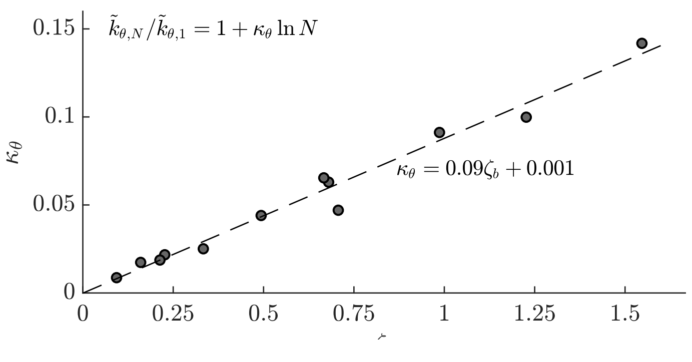

Figure 5.15: Variation of κ_θ with ζ_b

5.4.4 Varying load behaviour

A series of experiments were subsequently performed to observe the implications of varying the load magnitude across a number of load packages. Load packages of purely increasing, increasing and decreasing as well as 'random' sequencing were applied across several tests. From these, it was possible to verify a number of previously outlined superposition methods across literature.

(*i*) *The Miner's rule*: as previously mentioned, the Miner's rule has performed well in both $1g$ and Ng stress conditions (LeBlanc et al., 2010a; Truong et al., 2018) for the prediction of rotation accumulation from successive low cyclic count increasing load packages in a one-way scenario. The maximum cycle count, limited to just 3000 over three separate packages, makes it difficult however to have confidence in the long-term capacity of this method without further validation. To address this, a number of long-term cyclic experiments with different varying loading configurations were performed here – maximum total cycle counts ranged from 35,000 to 150,000 across two to eight different load packages of both low and high magnitudes (tests C34-C36, C43 & C44). Figures 5.16 and 5.17 present the results from two of these, which illustrate a number of interesting observations, outlined below.

Firstly, the experimental interaction behaviour that takes place between successive load packages is shown to be dependent on the nature and cycle count of the previous loading history applied. Figures 5.16c and 5.17c present the permanent rotation with cycles from tests C36 & C43, where it can be seen for relatively low magnitude loads for a preceding package, the behaviour of the subsequent load package appears to be unaffected by the previous loading. This is evidenced by an immediate increase in rotation as well as an onset of new increased rate of accumulation upon the application of the first load cycle. Similar behaviour is also seen in tests C34 & C35 whereby 100,000 cycles of low amplitude cyclic loads were followed by a further 50,000 cycles at higher loads with no apparent effect from the previous load.

When the load magnitude of the preceding package becomes sufficiently large, the accumulated rotation that has developed interacts with that of the subsequent load package. At the points marked by an asterisk (*) in Figures 5.16c and 5.17c, it can be seen that the initial rate of rotation accumulation is substantially reduced until a distinct number of load cycles has been applied. The new accumulation regime only then begins when the number of applied cycles equates to the predicted accumulated trend for that load magnitude, had no previous load history been applied (represented by the dotted lines).

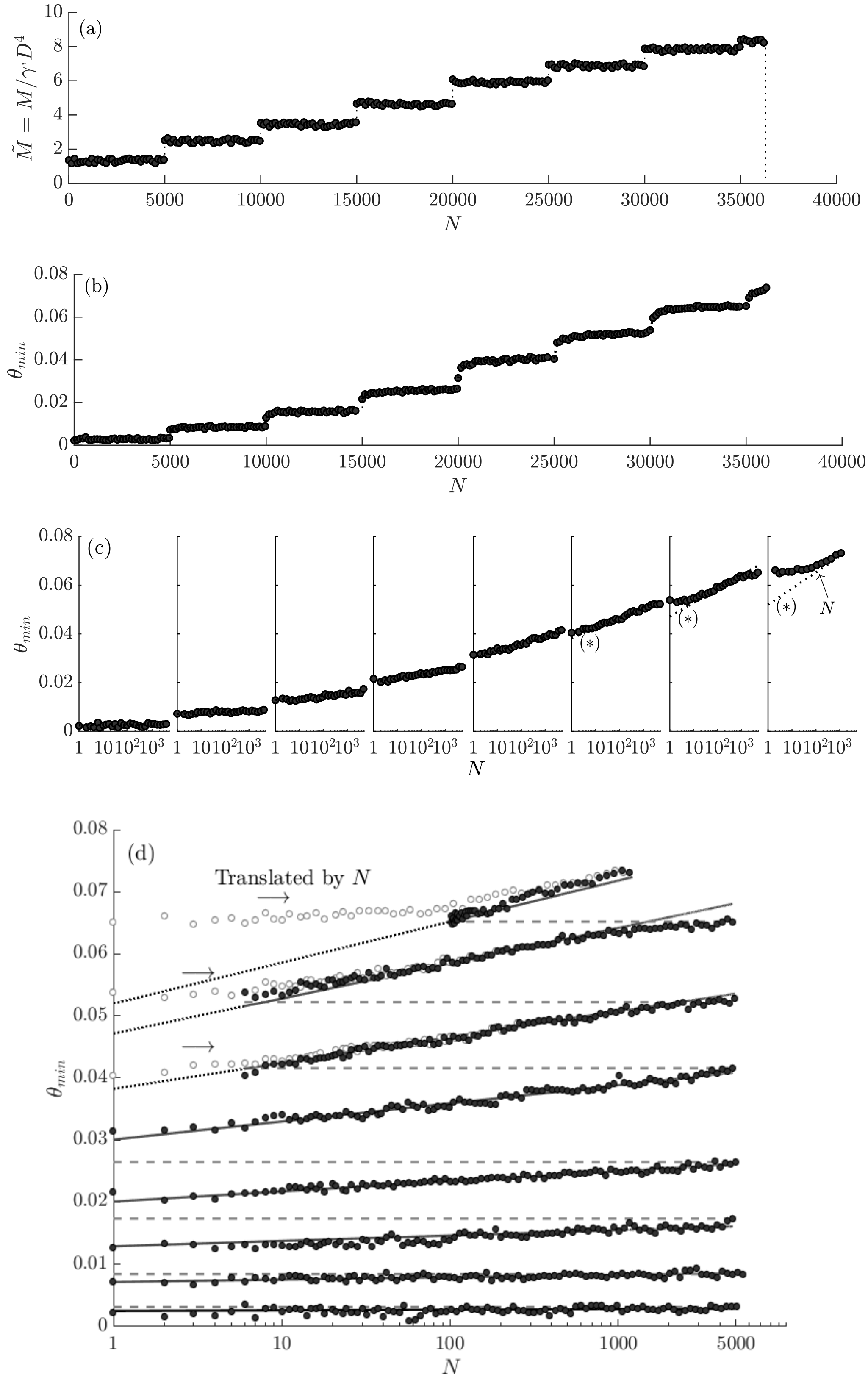

Figure 5.16: Sequence of load packages of increasing load magnitude (C36): (a) applied load; (b)/(c) observed permanent rotation; (d) comparison of measured and predicted accumulation based on the Miner's rule

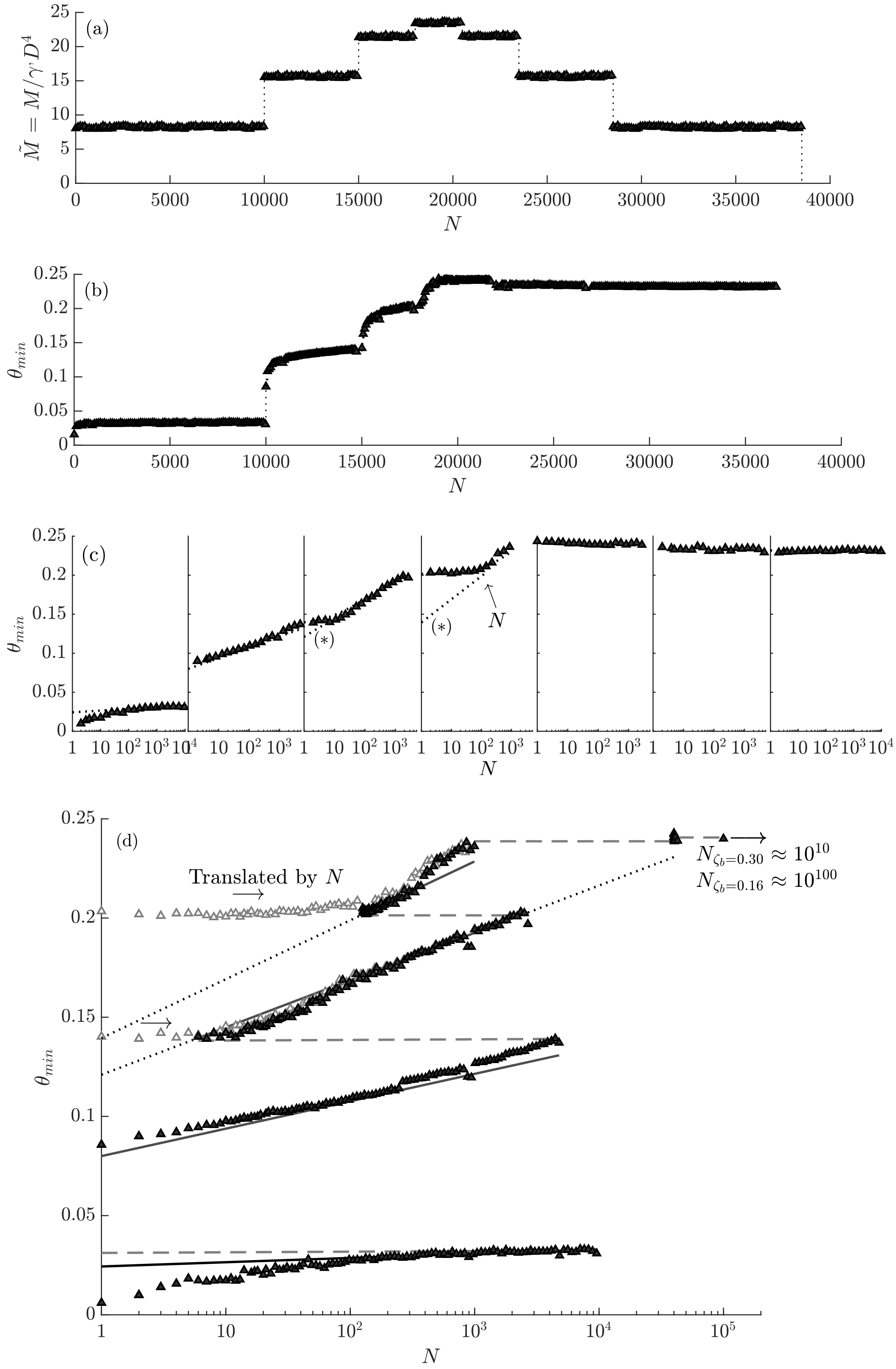

Figure 5.17: Sequence of load packages of increasing and decreasing load magnitude (C43): (a) applied load; (b)/(c) observed permanent rotation; (d) comparison of measured and predicted accumulation based on the Miner's rule

As a recap, the Miner's rule couples previously identified empirical accumulation models (derived in Section 5.4.2) with linear cumulative damage interaction. What this means here for the monopile case is that upon the completion of one full cyclic package of constant load magnitude, the value of permanent rotation is then back-traced until an intersection with the next load package accumulation trend is made. If there is no intersection before $N = 1$, Miner's rule dictates that the previous package has no effect on the subsequent one. For the case where the back-traced line does intersect the new prediction trend, the new cyclic count accumulates forthwith with the baseline cycle number defined at this point of intersection. This cycle number can also be calculated mathematically as below (expressed here for the logarithmic trend).

$$N_b = \exp\left(\frac{1}{\beta_b}\left[\frac{\theta_{1,a}}{\theta_{1,b}}\left(1+\beta_a \ln N_a\right)\right]\right) \tag{5.6}$$

where N_{b} is the equivalent cycle number for a new cyclic package with load ratio ζ_b after a load package of N_{a} cycles with load ratio ζ_a. β is taken from Figure 5.13.

Experimental results are presented in conjunction with the Miner's rule predictions in Figures 5.16d and 5.17d. Good agreement is seen proving the validity of the linear superposition theory. For the load case where no interaction between successive loading is predicted, the observed absolute value of experimental rotation for the first cycle from the succeeding package is noticeably greater than the returning back-traced line. The rate of accumulation for the new load is also greater. Both of these experimental observations illustrate zero interaction between the two load packages. Where the Miner's rule does predict interactional effects, it can be seen that by manually translating the observed experimental rotation by the number of cycles equal to N (marked in Figures 5.16c & 5.17c) allows for a strong comparison of predicted and observed results.

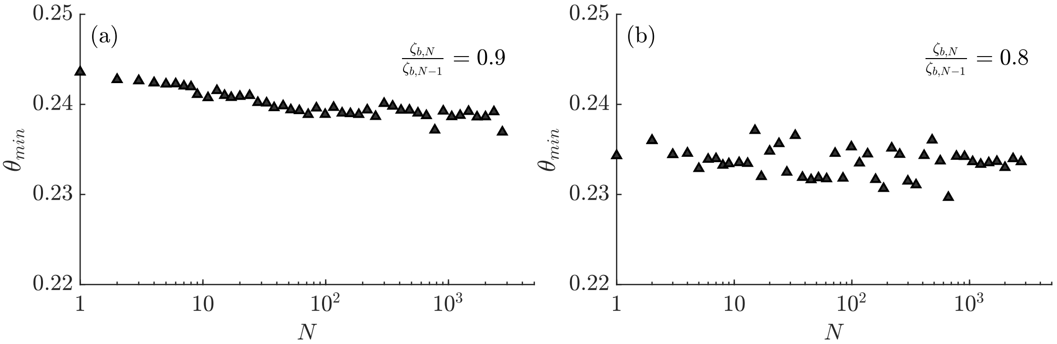

Figure 5.18: Monopile rotation restoration observed upon application of a following lower magnitude load package (test C43): (a) load package 5; (b) load package 6

It can be said that for the successively increasing magnitude cyclic load packages, the Miner's rule illustrates very good performance. There is, however, one experimental observation that this method fails to capture. Upon the application of a subsequent load package of lower magnitude than previous, there is evidence of a minor reduction in permanent rotation with applied cycles (see Figure 5.18). This phenomenon has also been observed by Abadie et al. (2018). Albeit a very modest rotation correction, the Miner's rule has no manner to deal with this, since the cumulative damage approach assumes no restorative behaviour. The internal soil mechanical behaviour at these moments are later explored in Section 5.7.2, in an attempt to rationalise this behaviour.

***(ii) Rainflow count method*:** attention is now turned to a more complex loading regime (test C44). Following an initial 10,000 cycles of low magnitude cyclic load, approximately 1000 cycles of what has the appearance of random load magnitude was applied in an attempt to simulate a typical storm response. This was then followed by another 10,000 cycles of low magnitude load. Applied cycles and observed permanent rotations of the storm load section are presented in Figures 5.20a & b. Upon first inspection it is clear that large loads dominate the accumulation of permanent rotation. Low magnitude loads present only minor increases, of which become progressively less prominent as the magnitude of permanent rotation increases.

A cycle-by-cycle Miner's decomposition theoretically has the ability to predict the magnitude of final permanent accumulated rotation for a random cyclic load sequence. Each cycle, or small cyclic package of the same load magnitude, has its own individual load characteristic and can be accounted for by way of an equivalent cyclic position in the linear cumulative damage model space depending on the magnitude of permanent rotation the monopile is experiencing at that time. This, however, becomes very untidy and difficult to follow given the number of switches from low and high load across the cyclic regime (as evidenced in Figure 5.21a), and is particularly complex with load reversals.

The proposed extended rainflow count method provides a much simpler alternative where the random loading can be broken down into packages of individual load magnitude, which can subsequently be applied in an accumulation model formulation. In this study, only one-way loading with $\zeta_{\mathrm{c}} = 0$ has been considered, and therefore the hysteresis loop closes after each cycle, meaning each cycle is counted for in the rainflow count. Given the indifference in the magnitude of final permanent accumulated rotation regardless of load sequencing (proven in LeBlanc et al., 2010a; Abadie et al., 2018), the permanent accumulated rotation associated with random load packages can be analysed by way of the Miner's rule with progressively increasing magnitude load packages. This approach assumes no restorative behaviour associated with subsequent load cycles of lower magnitude, and therefore can be considered conservative in nature. With this in mind, Figure 5.19 illustrates the total load sequence dissected into defined load magnitudes and corresponding cycle counts.

It is to be reiterated that this exercise has only been performed for a one-way loading scenario; in reality a wide range of load directions and combinations are to be expected. These obviously significantly increase the complexity of the rainflow count.

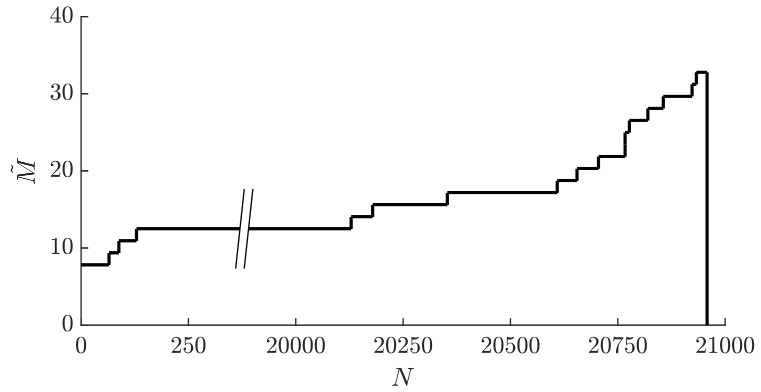

Figure 5.19: Dissection of random load sequence (Figure 5.20a) by extended rainflow count method (test C44)

Figure 5.21b presents the result from the decomposed rainflow count approximation in Miner's form. It can be seen that the final estimated permanent rotation provides a reasonable comparison with the experimental result. The minor over prediction points towards the conservative nature of this method.

***(iii) The Masing rules*:** the two original and two extended Masing rules (Masing, 1926; Pyke, 1979) have previously modelled small-strain elemental soil behaviour subject to symmetrical cyclic loading with success (Puzrin and Shiran, 2000). The laws have also translated with reasonable accuracy to the prediction of monopile foundation degradation, again under symmetrical loading, *i.e.* ζ_c = -1, (Kelly et al., 2006; Abadie, 2015). In these cases, due to the nature of the load, long term cycling has resulted in a kinematic hardening response and therefore rotation convergence after a number of cycles which allows for the success of the Masing application. When it comes to asymmetrical loading regimes, *i.e.* ζ_c > -1, results from a selection of tests explored here present some observations that both conform and conflict with Masing behaviour.

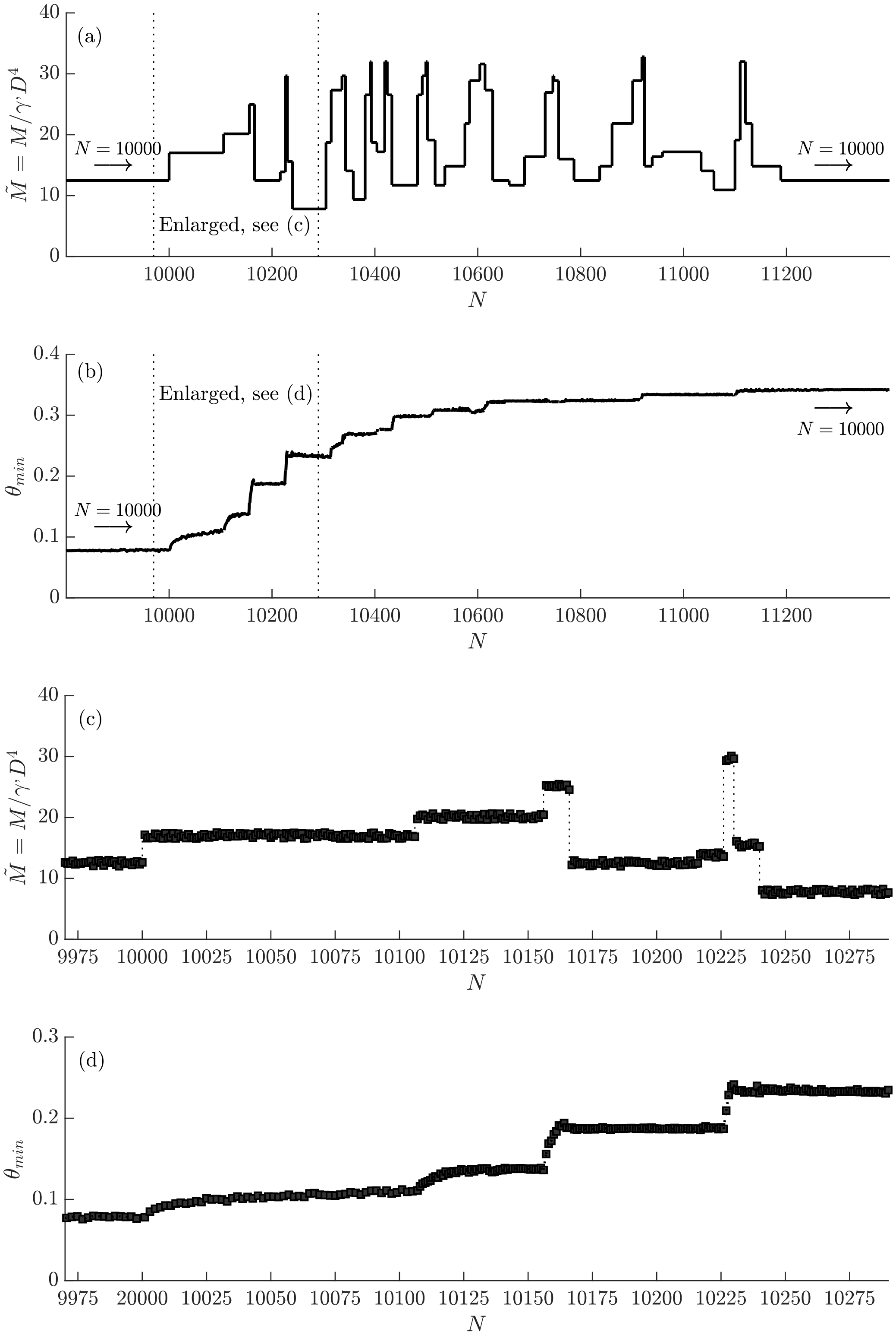

Figure 5.20: Sequence of random load packages (C44): (a) total applied load; (b) total observed permanent rotation; (c) enlarged area applied load; (d) enlarged area observed permanent rotation

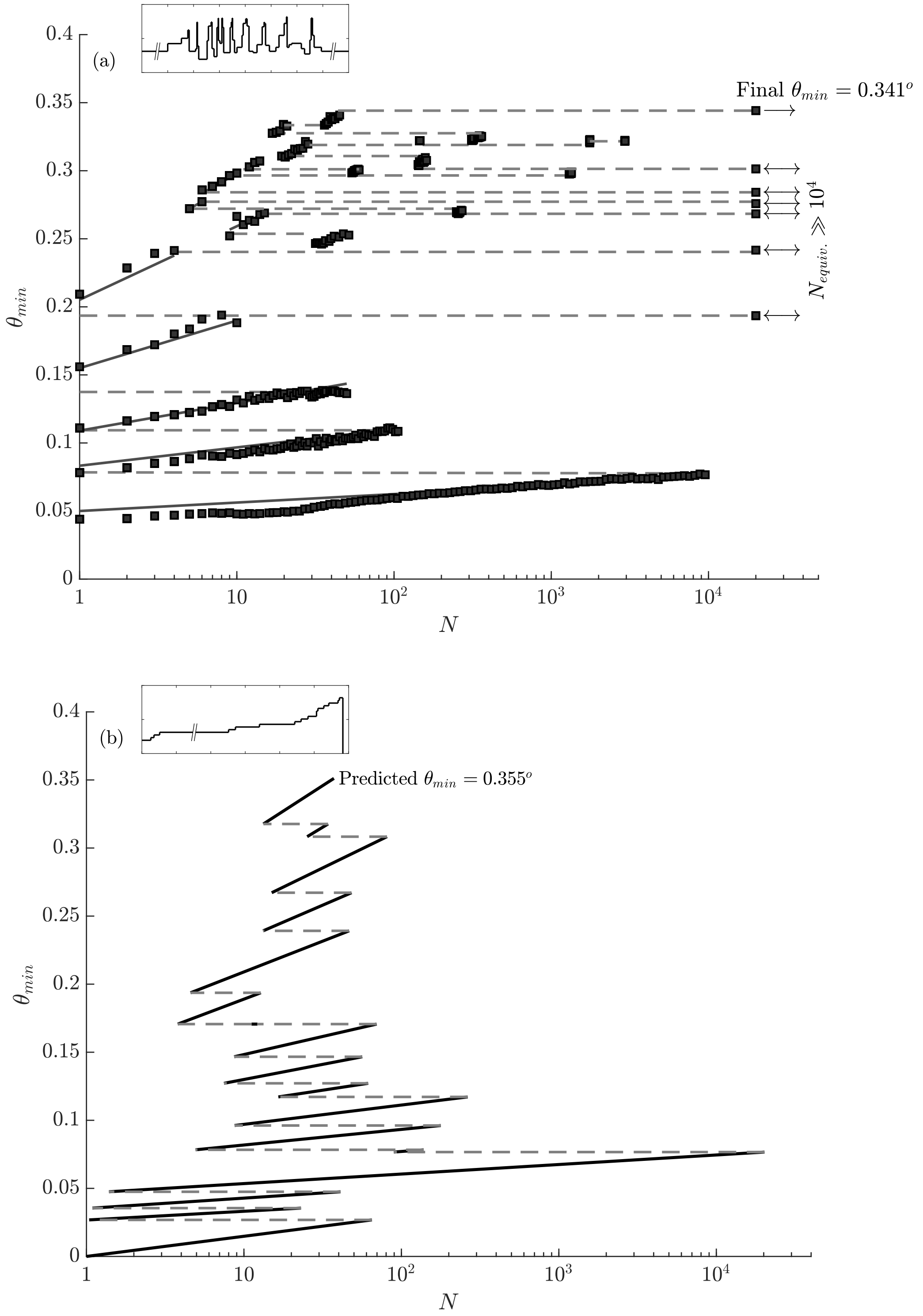

Figure 5.21: Sequence of random load packages (C44): (a) comparison of measured and predicted accumulation based on the Miner's rule for individual load packages; (b) predicted accumulation after load package grouping

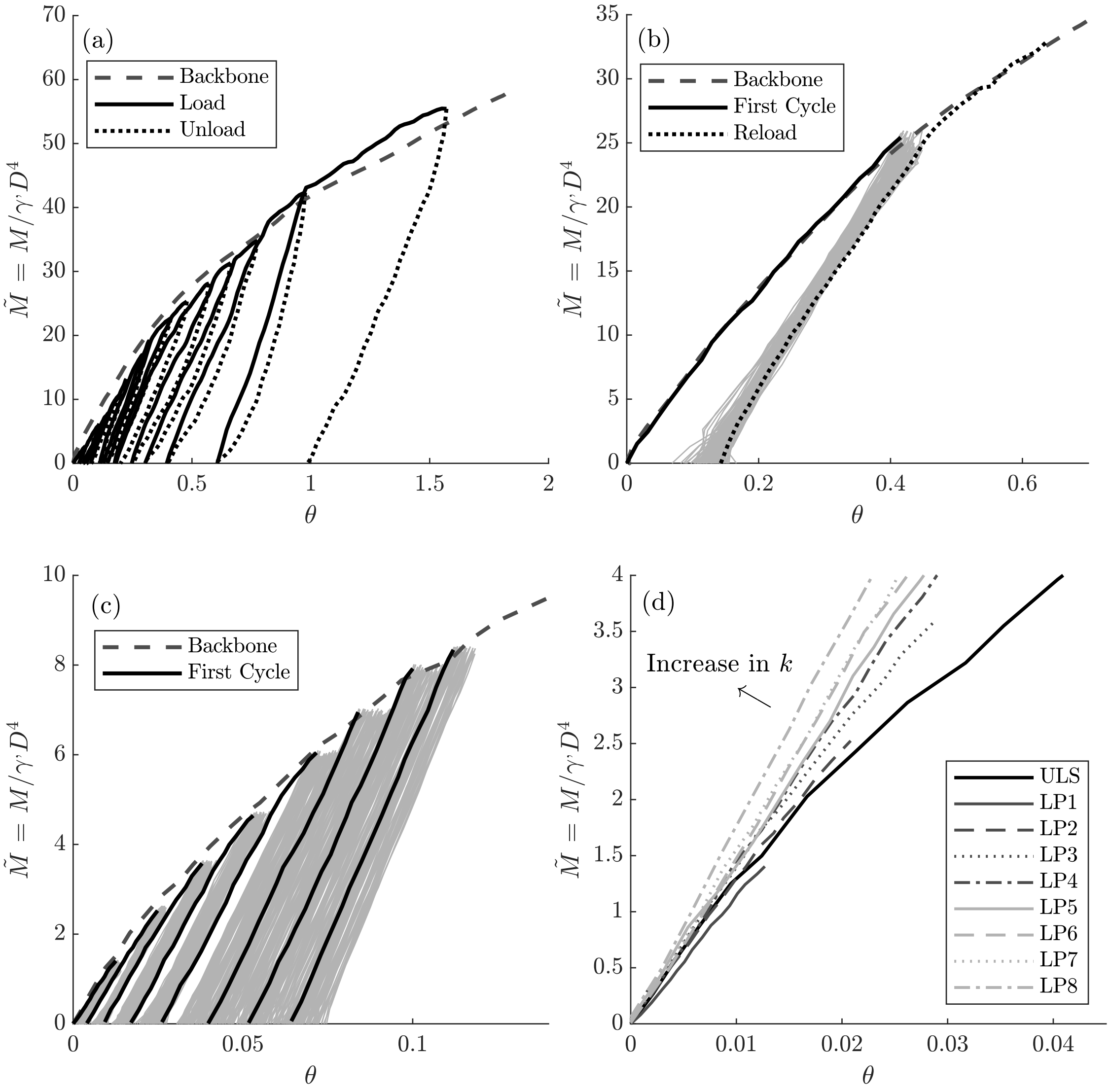

Figure 5.22: One-way loading $\tilde{M}$–θ response: (a) single cycle increasing load magnitude (C37); (b) multi-cycle response followed by monotonic push (C42); (c) a series of multi-cycle increasing in load magnitude (C36); (d) enlargement of initial stiffness of first load cycle of each package

In a series of increasing magnitude single load cycles where racheting behaviour is not observed (Figure 5.22a), the second original and first extended Masing rule's are satisfied, these being: (*i*) the initial secant stiffness of the reload curve follows that of the original backbone curve; and (*ii*) after an unload-reload curve rejoins the backbone curve, any further loading continues along this backbone curve. The latter is also evidenced across the long-term loading tests (Figure 5.22b & c). When applying long-term asymmetrical cyclic loading which do demonstrate ratcheting effects, it is revealed that the second original Masing rule is no longer valid. With each cycle, progressive stiffness increases and deformation mean that reload curves no longer follow the behaviour of original backbone response, even for the first load cycle of a new greater magnitude hysteretic load package. An enlargement of the initial portion of the first cycle response in Figure 5.22d clearly shows the increase in stiffness upon the initialisation of a new hysteresis loop and this stiffness continues to evolve throughout the entire loading sequence.

The Hyperplastic Accelerated Ratcheting Model (HARM) outlined in Abadie (2015) attempts to combine ratcheting with original Masing laws by introducing the ability to accumulate plastic deformation (*i.e.* permanent rotation) for an asymmetric applied cyclic load. Whilst providing good comparisons with observed experimental tests, the model requires a significant number of input parameters, some of which are empirically derived. The complexity of the model in comparison with existing empirical relationships potentially negate its effectiveness for long-term cyclic packages, however its ability to predict more complex loading behaviour, which simpler models cannot manage, is a distinct advantage.

5.5 Serviceability cyclic accumulation design chart

Through the experimental cyclic dataset, global empirical trends have been identified which are able to predict with a good level of accuracy the accumulation of rotation at the mudline for a monopile foundation of the experimental geometry tested, subject to asymmetrical one-way loading. It has also been seen that the Miner's rule for damage accumulation is an effective initial design tool for predicting the interaction behavioural effects of cyclic load packages of varying load magnitude.

As useful as the Miner's rule is, it can, however, be a time-consuming process to reach the final predicted accumulated rotation, particularly for a cyclic sequence of many different magnitude load packages where many mathematical formulations of each load package are required. In light of this, a new design tool is proposed here which will significantly accelerate this process. The proposed method is based on the Norwegian Geotechnical Institute (NGI) cyclic degradation approach where contours of monopile rotation are located in a load–cycle number three dimensional (3D) space ($\zeta_b - \zeta_c - N$). From here, the user is able to simply examine the contour diagram, trace the load history and read off the accumulated rotation for any cyclic sequence. The following sections outline the model philosophy, its formulation and finally a validation against a number of varying magnitude load packages experimental results.

5.5.1 NGI cyclic degradation model

The Norwegian Geotechnical Institute (NGI) cyclic degradation approach is a powerful tool used in cyclic design of geotechnical structures (Andersen, 2009, 2015). It was originally proposed for the evaluation of undrained cyclic loading conditions in order to evaluate the cyclic soil strength and pore pressure development, which was subsequently used in bearing capacity and serviceability calculations for a number of offshore applications (Sturm et al., 2012). The model has since been translated to many other applications including the cyclic loading from traffic and earthquakes, for example (Sturm et al., 2012). The 3D contour models are based on cyclic element laboratory tests, both triaxial and direct simple shear, and can be applied to sands, silts and clays alike. The capability of the NGI approach is such that any stress and cyclic state (defined in terms of average and cyclic shear stresses, τ_{ave} and τ_{cyc}) in a cyclic laboratory test can be related to a single point in the 3D strain space (N, γ_{ave}, γ_{cyc}).

An example original cyclic stress-strain contour plot is presented in Figure 5.23a. For further information on the fundamentals of the NGI cyclic accumulation approach, Andersen (2009) presents a comprehensive history of its development and outlines a number of example applications. Figure 5.23b illustrates one of these examples for a simple eccentrically loaded shallow footing design problem, with the potential failure surfaces in the soil beneath and their predicted respective element level stress-strain behaviour shown.

Whilst the initial application of the NGI degradation model is aimed towards the soil at an element level (individual shear strain degradation under both direct shear and triaxial loading) which can be applied in traditional analytical design, the fundamental philosophy does not solely lie here. The shear strain experienced at an element scale can be replaced with a global characteristic of a monopile foundation, and therefore can be equally used as a global predictive design tool. Instead of expressing contours of failure in terms of shear strain, γ, these can simply be replaced with contours of monopile rotation, θ. In order to keep in line with DNV GL (2016) serviceability limit state design recommendations, these contours are expressed in terms of permanent rotation at the mudline, where a threshold criteria can be set at $\theta_{\mathrm{Ed,SLS}} = 0.25^{\circ}$. Figure 5.24a presents a schematic representation of the 3D model space with the three dimensions being ζ_b, for load ratio, ζ_c, for load characteristic (see Section 5.2.1 for definition of these) and N, for number of applied cycles.

At this stage, the initial model presented here only considers one 'slice' of the 3D space (Figure 5.24b) – this being for cyclic load sequences with characteristic $\zeta_c = 0$, *i.e.* one-way asymmetrical loading – and the following model development and validation reflects this. As previously identified with the Miner's damage accumulation model, the proposed cyclic contour formulation also does not account for cyclic restoration associated with the application of a subsequent lower magnitude cyclic load packages. Incorporating this would add much undesired complexity to the model application, potentially negating its practicality. With this is mind, the model will inherently be on the conservative side for predicted permanent accumulated rotations where load reduction is evidenced. By tracing back along the contour line, the effect of permanent rotation reduction with subsequent applied load packages of lower magnitude could be accounted for. However, given the very small magnitude of this effect, it has not been explored further here.

5.5.2 Accumulation model development

The development of the contour model is relatively straightforward provided cyclic rotation experimental results (or empirical predictive trends) are available for the specific design case. Here, the full range of constant load experimental results outlined

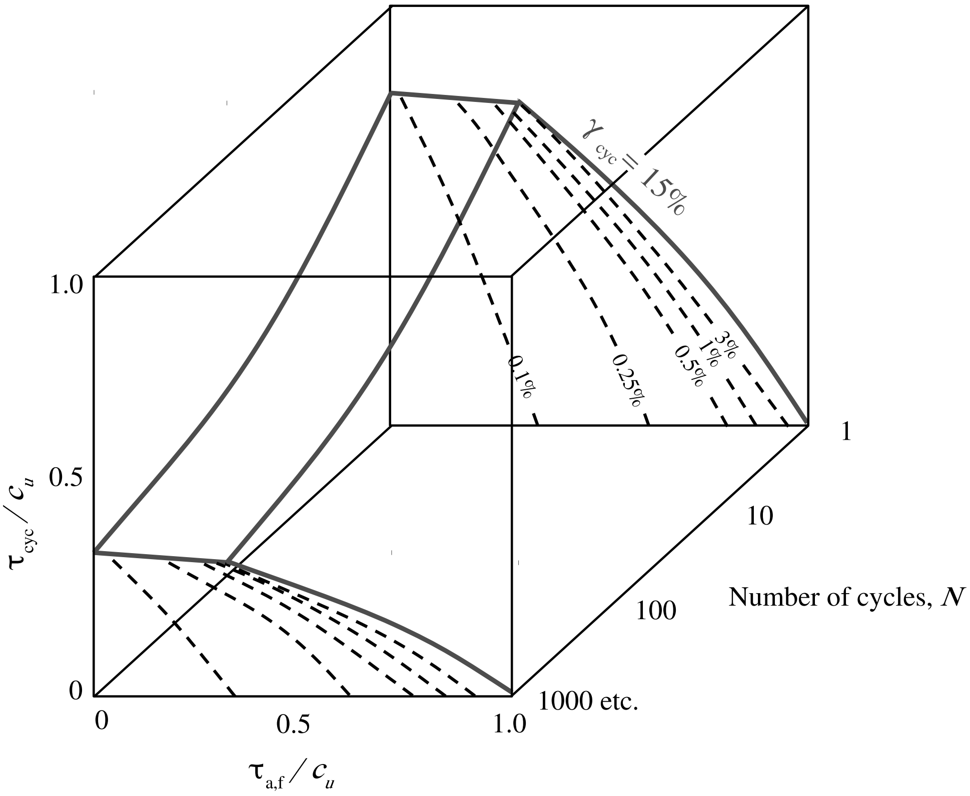

(a)

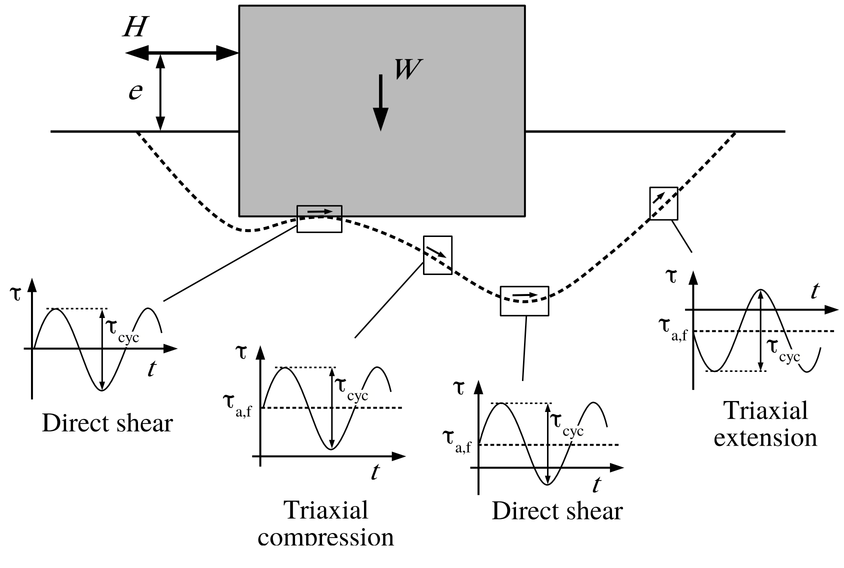

(b)

Figure 5.23: (a) Original contour diagram expressing shear strains developed with cycles of cyclic shear stress (Andersen, 2009); (b) example application of NGI model for offshore shallow footing

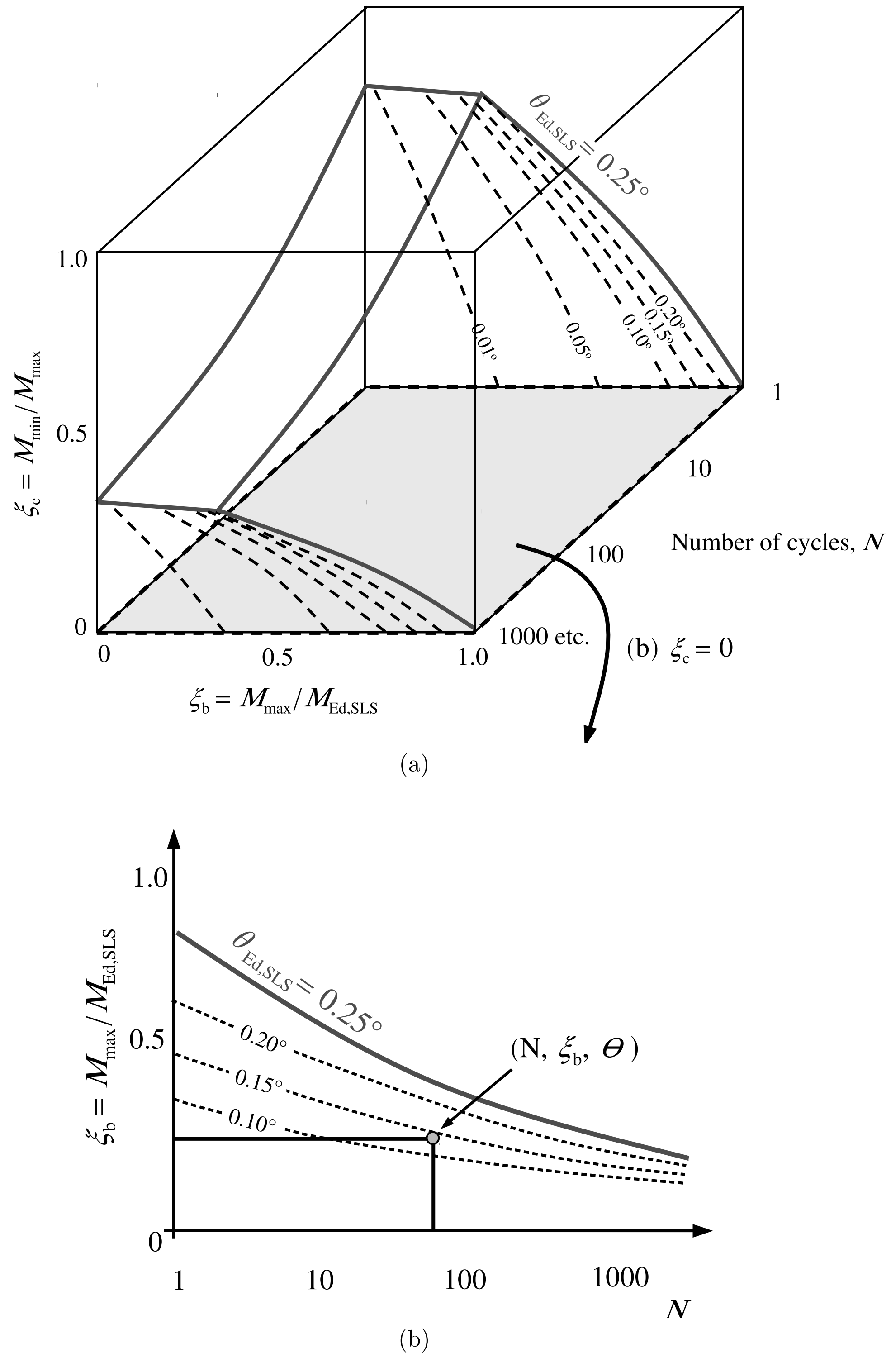

(a)

(b)

Figure 5.24: (a) Proposed model application expressing monopile mudline rotation developed with cycles of cyclic load; (b) one 2D slice of contour plot at $\zeta_c = 0$

within this thesis are to be used to populate the cyclic degradation contour diagram. Given that interest at this stage is only aimed towards the load characteristic case of $\zeta_c = 0$, a 2D slice of the 3D model will exclusively be presented forthwith, with the x axis representing the number of applied cycles, N and the y axis, the applied cyclic load ratio, ζ_b. The model formulation process is outlined below, with the positioning of experimental results within the 3D space illustrated in Figure 5.25.

1. the position of cyclic load ratio, ζ_b, is identified on the y axis associated with each individual experimental result;
2. a line representing the progression of the cyclic load package is traced directly across the 2D space until the final number of applied cycles is reached;
3. positions along this line are populated with the observed permanent mudline rotation at the associated number of applied cycles;
4. the process is repeated for experimental test results of different load ratio to fully populate the 3D space;
5. contours of rotation are now positioned across the full load – cycle count space.

Whilst the above formation is aimed towards constant magnitude cyclic load packages, rotation behaviour from monotonic experiments can also be used in the model population provided full unload history is recorded. These provide a baseline at an abscissa location $N = 1$. Moreover, the results recorded from test C37 are particularly useful since many separate individual load cycles of increasing magnitude are applied and allowed to fully unload, presenting a number of baseline locations on the y axis for several magnitudes of ζ_b at $N = 1$.

Once populated, individual contours of rotation can be traced by hand across the 2D slice, or for more accuracy are recommended to be modelled using graphical software to allow for the interpolation between all points in the complete matrix made up of load ratio, cycle number and associated magnitudes of rotation. Here, the MATLAB *contour* function was deployed with the input matrix dataset as outlined above. Figure 5.26 presents the final fully populated predictive contour model.

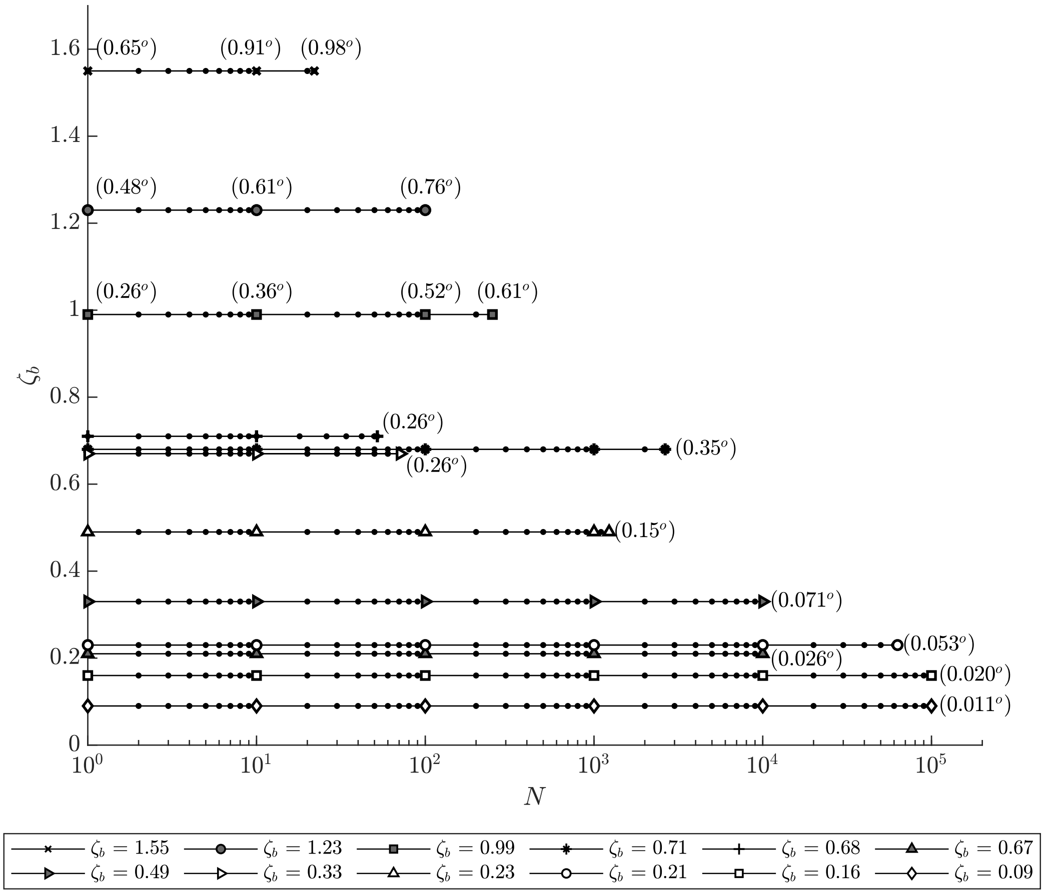

Figure 5.25: Positioning of cyclic experimental results in 2D space ($\zeta_b - N$)

5.5.3 Model application

In principle, the application of the contour model is straightforward. It can be used to predict the permanent mudline rotation for any given cyclic load ratio and number of cycles. As an example of its ease, for a monopile subject to a cyclic load package of load ratio $\zeta_b = 0.5$ and cycle count N = 10,000, a line is simply traced from $\zeta_b = 0.5$ on the ordinate axis and the contour magnitude is read-off at the coordinate point (N = 10,000, $\zeta_b = 0.5$). This gives a permanent rotation of 0.21°. The contour space can also be used to stipulate lifetime serviceability limit state load ratios, determined as the applied cyclic load ratio which will never reach $\theta_{\text{min,SLS}} = 0.25^{\text{o}}$ over the complete lifetime of the foundation. For this monopile case, a monopile subject to 10^7 load cycles at a load ratio of $\zeta_b \approx 0.40$ is predicted to never reach the SLS failure criteria. It is worth noting that the results from this contour diagram are only validated for the experimental setup used in this study and are likely to differ for monopiles of different diameter, embedment ratio and sand relative density.

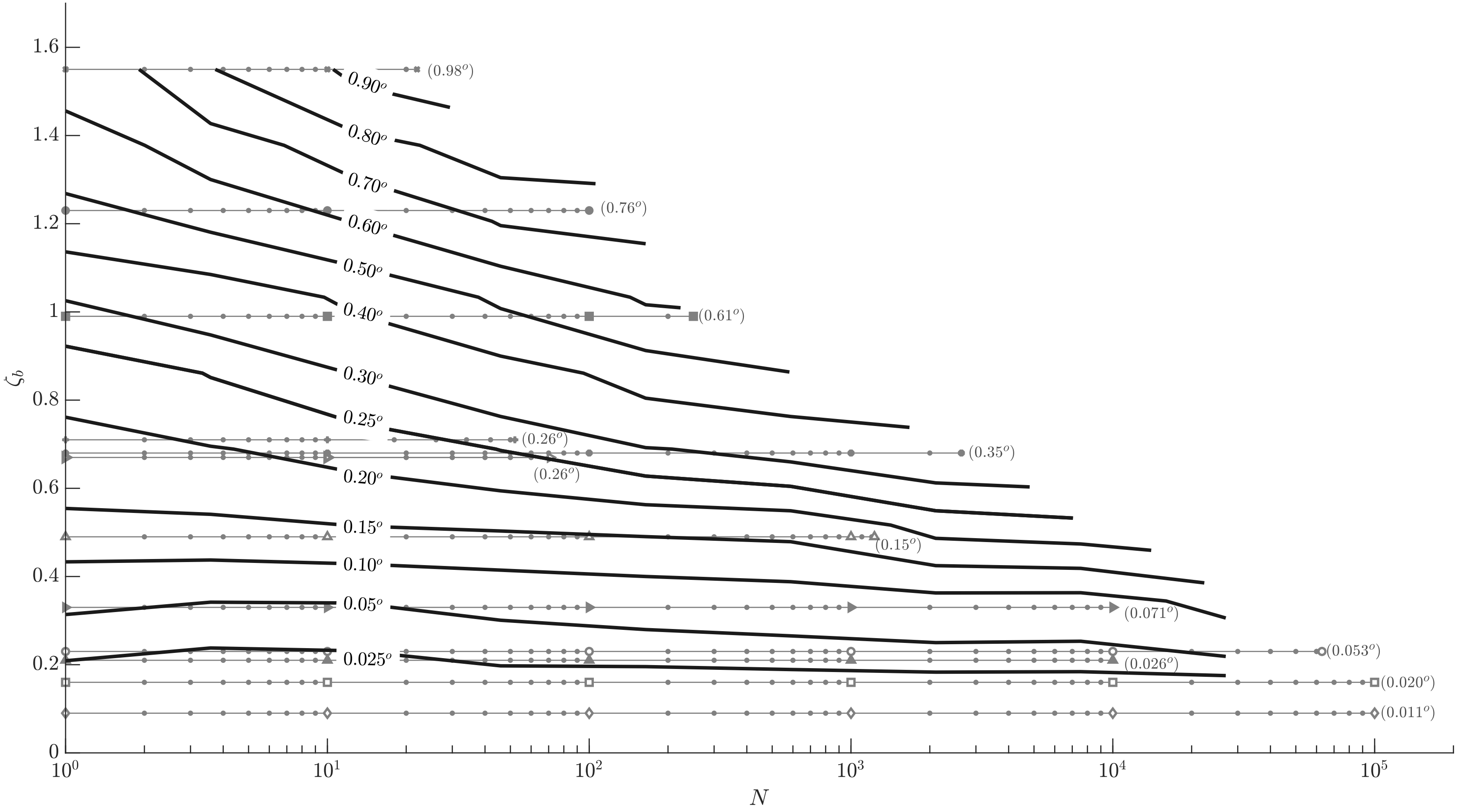

Figure 5.26: Final cyclic accumulation contour diagram at $\zeta_c = 0$. Individual results from cyclic experiments are overlaid alongside final recorded permanent rotations

5.5.4 Model performance under varying load

The true potential and advantage of the cyclic contour degradation model arises when wanting to analyse a load sequence with many different load magnitudes and cycle numbers. This resembles the expected loading case for a prototype monopile scenario where load magnitudes and eccentricities are highly variable throughout the lifetime of the foundation.

In practice, the individual load packages of the complete load sequence are first sorted (by means of the previously outlined rainfall count method or similar) and ordered into separate load magnitudes alongside their respective number of applied cycles. From here, the first sorted load package is traced from the starting point at $[N = 1, \zeta_{b,1}]$, to an end position equal to the complete number of applied cycles for this individual load magnitude package. A value of the rotation contour associated with this location in the $\zeta_b - N$ space is determined and used as temporary memory state parameter that takes into consideration the effects of the complete cyclic loading history. The corresponding number of equivalent applied load cycles for the subsequent applied load package is then determined by tracing along this rotation contour until the ordinate value of the new load ratio is reached. The process is repeated for the full sorted load sequence.

If when tracing along the rotation contour line the ordinate position of the subsequent load package magnitude is not reached before $N = 1$, the new load package cycle count simply restarts from $N^* = 1$. This reflects the philosophy adopted in the Miner's cumulative damage approach and signifies that the previous loading has no future effect on the rotation behaviour of the subsequent load package. Figure 5.27a illustrates a schematic example of this non-interaction case. For the case where tracing along the rotation contour does intersect with the subsequent load package ζ_b ordinate position before reaching $N = 1$, the subsequent load package number of cycles is added onto this intersection equivalent cycle count (marked as N^*) and the number of cycles is traced until $N^*{+}N_2$ is reached. This methodology is illustrated in Figure 5.27b.

5.5.5 Model validation

To validate the model performance, three varying load experimental test results are presented in this format. The predictions of the two simpler load sequences from tests C36 and C43 are first traced on Figures 5.28 & 5.29. Observed magnitude of rotations at the final load cycle of each load package are also superimposed on these and coincide well with the predicted contour line locations.

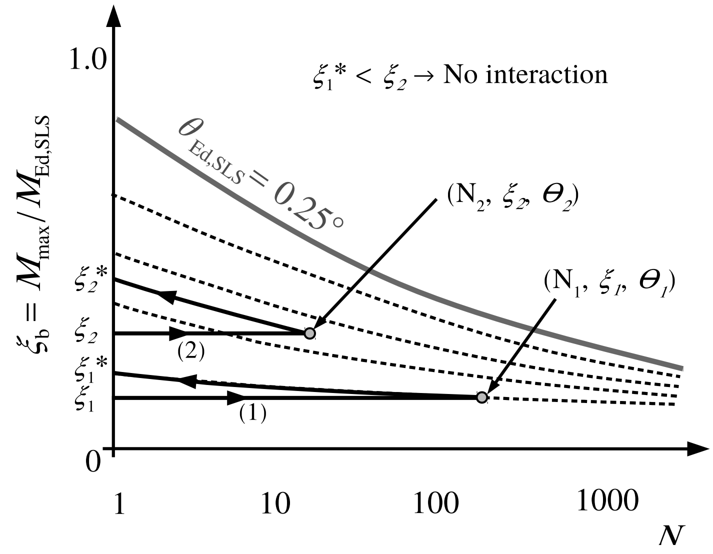

(a)

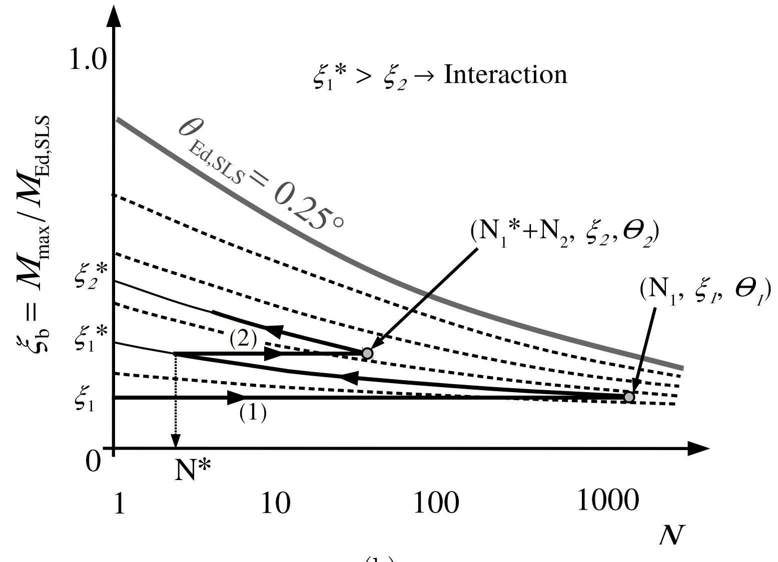

(b)

Figure 5.27: Schematic illustration of (a) non-interaction of successive load packages; (b) interaction of successive load packages

For each load sequence presented in Figures 5.28 & 5.29, it can be seen that both non-interaction and interaction of rotation behaviour is observed between successive load packages. For test C36, the first four packages (LP) of load are shown to have zero impact on the subsequent rotation behaviour. It is only when LP 5 is reached that this has implications on subsequent LP 6, 7, 8 and 9. In test C43, given the higher magnitude applied loads, the observed interaction effects are greater. As an example, the implication of LP 3 on the rotation behaviour of LP 4 is such that it is equivalent to 110 cycles of load (N_4^*) with magnitude LP4 having already been applied before the start of this new load package. The 1000 actual applied load cycles of LP 4 are then added to N_4^* to give an equivalent applied cycle count of 1110 cycles. This inherently presents a greater accumulated permanent rotation than if no load history had be applied. During the reducing load phase of the load sequence, the value of rotation is simply traced down the contour to the ordinate location of the lower magnitude LP 5 and the equivalent cycle number associated with this load package is very large ($N_5^* \approx 30000$). The additional 3000 load cycles therefore presents little to no noticeable increase to the predicted permanent of rotation. In fact, as previously identified, observed experimental results see a degree of rotation restoration for this load reduction; this is not captured in the contour model formulation.

The more complex random load sequence from test C44 is now traced on to Figure 5.30. The load sequence has again been decomposed into the individual cyclic load packages by the rainflow count method as per Figure 5.19 in Section 5.4.4. It is clear that interaction behaviour takes place immediately from the first load package and continues throughout the full decomposed load sequence. Observed experimental rotation at the end of the entire load package is superimposed and shows a strong correspondence with the predictive contour lines.

From Figure 5.30 it can be hypothesised that the rotation behaviour of the entire loading history of test C44, made up for more than 21000 load cycles of many packages of load of varying magnitude and cycle count, can be simulated by an equivalent 17 cycles of the final applied load package, with load ratio $\zeta_b = 0.93$. This would significantly accelerate the monopile detailed design phase, where only the behaviour from this substantially reduced number of cycles would require further numerical modelling. This proposed design philosophy will need to be carefully validated for the monopile case through additional tailored experimental tests.

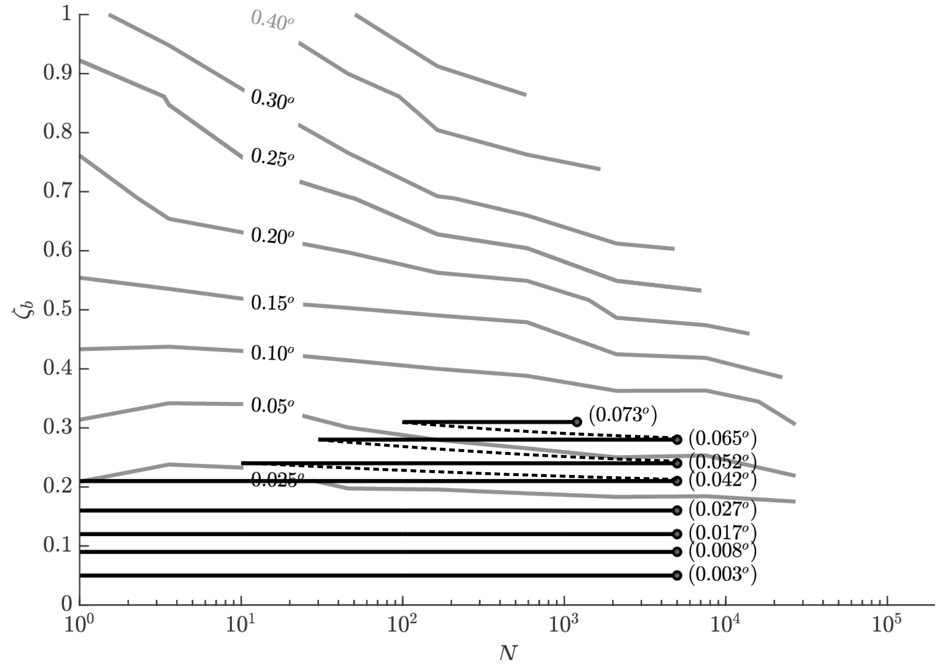

Figure 5.28: Cyclic accumulation contour diagram application for test C36. Values in brackets at crossed markers represent observed experimental results

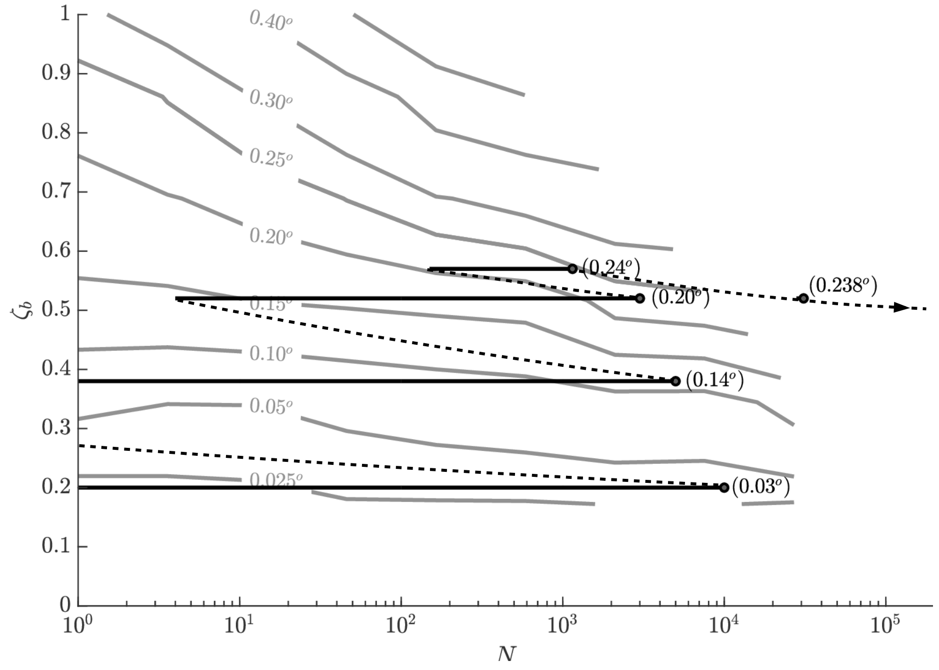

Figure 5.29: Cyclic accumulation contour diagram application for test C43. Values in brackets at crossed markers represent observed experimental results

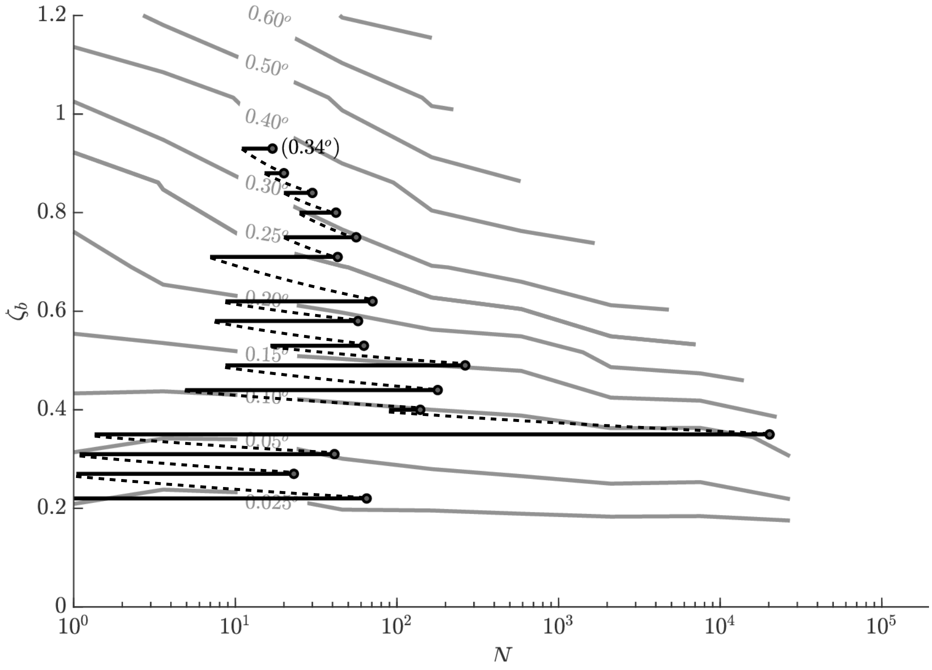

Figure 5.30: Cyclic accumulation contour diagram application for test C44. Values in brackets at crossed markers represent observed experimental results

5.6 Concluding remarks from global behaviour

In this section, an overview of the global monopile response subject to numerous one-way asymmetrical loading regimes has been presented. The key findings have provided verification of a number of previously outlined observations, accumulation models and superposition techniques from across literature. A new contour-based rotation accumulation design model has also been outlined. A summary of the key concluding remarks from a global perspective are outlined below:

1. long-term cyclic load experiments over a magnitude of 10^5 cycles prove that progressive accumulation of rotation and stiffness continues to evolve (ratcheting) for the entire duration of this cyclic regime;

2. empirically derived power- and logarithmic-law trends are shown to be best predictors for the rate of accumulated rotation for high and low constant cyclic load respectively. A transition in model trend occurs in the region of $\zeta_{\mathrm{b}} \approx 0.5$, which ultimately dictates the long-term model prediction performance. Incidentally this load magnitude coincides with previously identified flexible to rigid behavioural transition outlined in the monotonic analysis;

3. the Miner's rule can effectively predict the accumulated permanent rotation of varying magnitude cyclic loading scenarios. The extended rainflow count method is also shown to be a powerful tool to dissect a random storm load sequence into a series of individual packages, which can then be implemented into a Miner's rule estimation with success;

4. evidence of a small degree of rotation restoration is seen upon the application of a subsequent load of lower magnitude. Current cumulative damage models do not account for this behaviour;

5. a new contour-based accumulation model has been proposed which allows for the accelerated prediction of accumulated permanent rotation at the mudline. Decomposed cyclic load histories can be traced across the three-dimensional ζ_b – ζ_c – N space to swiftly predict the magnitude of accumulated rotation.

The identification of these global behaviour trends are useful from a design perspective since empirical accumulation models can be directly implemented in the prediction of pile response. Through the implementation of a small number of strategically designed physical model experiments, a full design contour plot can be drawn up and estimations of permanent rotation can be made for any load scenario. It is now of interest to explore inside the soil to connect these observations made with soil-pile interactional behaviour beneath the mudline.

5.7 Local pile-soil cyclic interaction

In the previous section, several global cyclic trends have been identified with the observations made agreeing with many previous literature findings, providing confidence in their nature. Across this literature, however, little experimental evidence is available that examines the fundamental changes in soil mechanical behaviour that is taking place beneath the mudline within the proximity of the pile. In a similar fashion to the monotonic response, observations from strain measurements, which can be directly used to calculate bending moment, as well as direct horizontal pressure outputs from EPC sensors are now pieced together in an attempt to rationalise some of the observed global trends.

5.7.1 Constant load sequence

The constant load cyclic sequences are first analysed. As a brief summary of the global trends, it has been seen that larger applied cyclic loads present faster accumulations of rotations with empirical power-law accumulation models presenting the most suitable model prediction. Low magnitude applied cyclic loads show long-term ratcheting which continues throughout the load sequence with accumulation best described with a logarithmic trend. For all tests, global stiffness was seen to progressively increase with the application of cycles. Analysis of localised soil-pile observations may reveal important information to explain these changes across the test matrix.

***(i) Pile bending moment*:** direct observation of pile bending moment provides the simplest tool of analysis to gain an understanding of the pile-soil interaction behaviour with cycles. It has been shown in literature (Kirkwood, 2015; Truong et al., 2018) that after a number of applied cycles, there is a degree of 'locked-in' internal pile bending moment, which is likely due to a combination of sand redistribution and localised changes in void ratio that occurs during the loading sequence (Cuéllar, 2011). Previous literature datasets have typically concentrated on presenting the locked-in bending of two-way cyclic loading.

From this experimental study, Figure 5.31 presents the bending moment with depth from both a high magnitude load (test C38) and low magnitude load (test C35) cyclic scenario as a ratio of the applied overturning moment at the mudline. The selection of these two load cases for presentation is due to the distinct differences in accumulation behaviour at high and low load at a global level. These show the aforementioned locked-in bending increase with number of applied cycles. Incidentally, the magnitude of maximum bending with depth upon load does not appear to change considerably

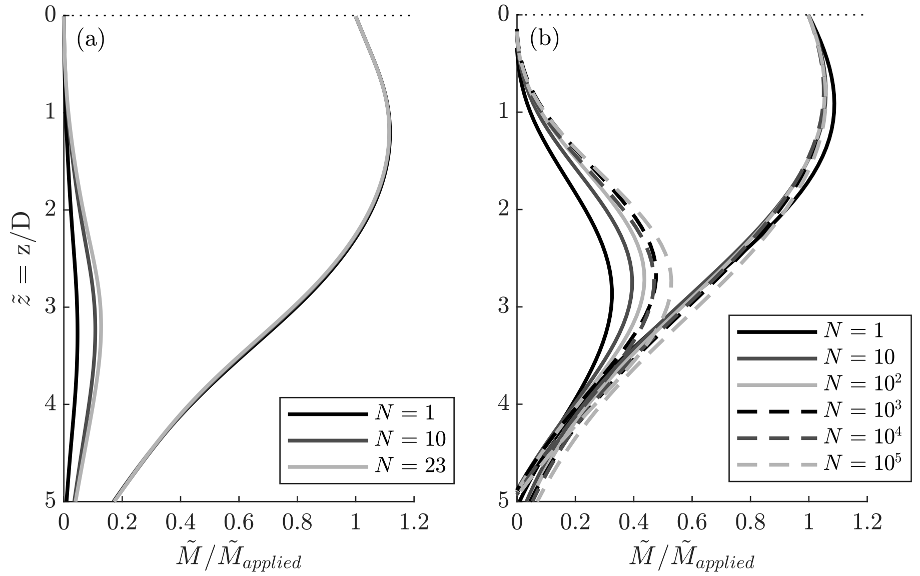

Figure 5.31: Locked-in bending moment progression as a ratio of applied overturning moment at the mudline: (a) test C38 ($\zeta_b = 1.55$); (b) test C35 ($\zeta_b = 0.09$)

across the full test matrix.

It is immediately clear from Figure 5.31 that for a larger applied overturning moment, the ratio of locked-in bending in relation to the applied moment is significant less than that for the smaller overturning moment. For the case of $\zeta_b = 1.55$, locked-in bending is of the order 10% of the applied moment, whereas for $\zeta_b = 0.09$, this is significantly greater at 50%. The location of this locked-in bending maximum is also deeper for the higher applied moment, pointing towards deeper locked-in stress distributions. The above observations are evidenced across the full test matrix with locked-in bending accumulation trends presented in Figure 5.32a.

The observed difference in locked-in bending ratio behaviour across the range of load ratios tested may be explained by the nature of the failure mechanism that is taking place at that cyclic load magnitude. In Section 4.4.2 for the monotonic pushover behaviour, it has been shown that for relatively low magnitudes of applied overturning moment, the monopile has a tendency to behave in a more flexible manner, this meaning proportionally greater pile bending as opposed to a full body rotation for the input work done. This will result in proportionally greater elastic recovery potential in comparison to applied bending as it unloaded. This recovery on unload is prevented due to the redistribution and inflow of sand particles close to the surface behind the translating pile, the result of which is locked-in internal bending owing to the new soil-structure interaction regime established. Incidentally, in a suite of monotonic tests,

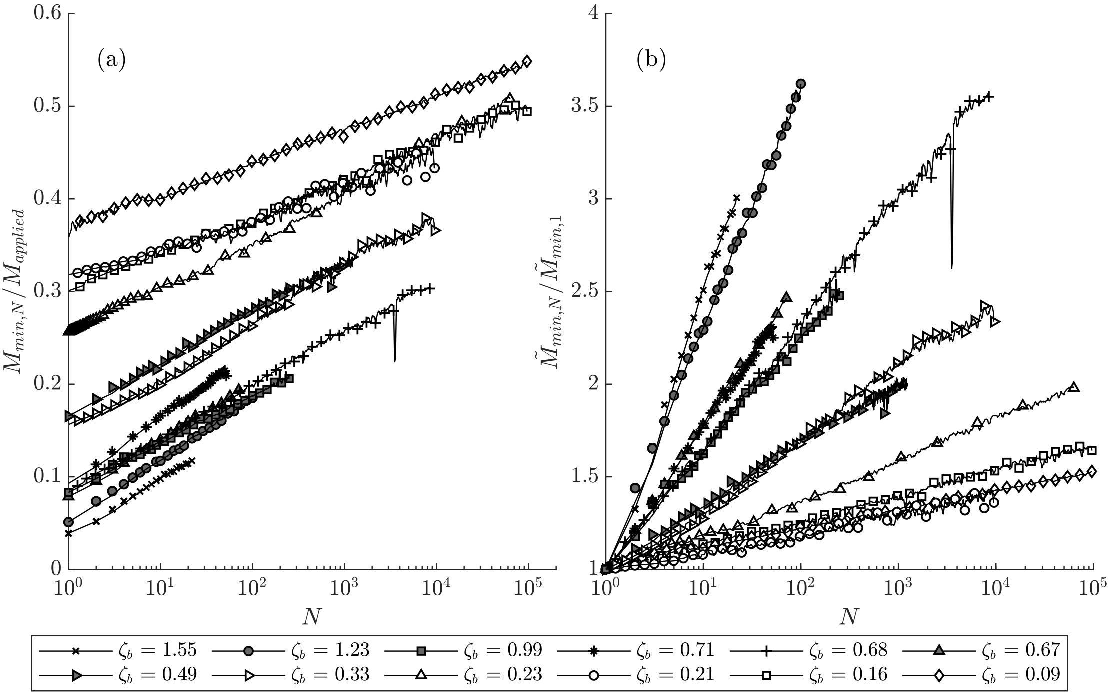

Figure 5.32: Locked-in bending moment progression: (a) as a ratio of cyclic applied overturning moment; (b) as a ratio of locked-in moment after first cycle

Bayton and Black (2016) also observed a significantly greater ratio of locked-in bending on unload for a flexible pile geometry in comparison to a rigid pile counterpart.

For the larger applied overturning moments, the monopile presents a much more rigid, rotational mechanism and therefore illustrates proportionally less bending for the input work done. With this, a proportionally lower amount of elastic recovery is available on unload, and despite the inherently greater sand redistribution that takes place, a reduction in relative locked-in bending is shown. In the aforementioned study of Bayton and Black (2016), the rigid pile geometry presented considerably lower relative locked-in bending on unload, which directly reflects these observations. Figure 5.33 outlines the variation of locked-in bending after the first cycle as a ratio of the applied overturning moment at the mudline with the changing value of load ratio, ζ_b.

In Figure 5.32b, the progression of cyclic locked-in bending moment is now introduced in terms of a ratio between residual bending present after the N^{th} and first cycles (*i.e.* $\tilde{M}_{min,N}/\tilde{M}_{min,1}$). When presented in this format, it can be seen that as the value of ζ_b increases, this produces a faster rate of increase of locked-in bending moment with Figure 5.34 presenting the direct relationship between ζ_b and χ, defined as the rate of locked-in bending moment accumulation:

$$\frac{\tilde{M}_{min,N}}{\tilde{M}_{min,1}} = 1 + \chi \ln N \tag{5.7}$$

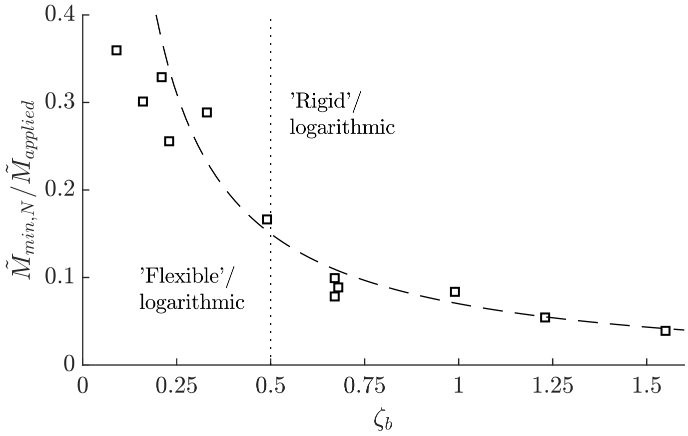

Figure 5.33: Variation of $\tilde{M}_{min,N}/\tilde{M}_{applied}$ with ζ_b

A distinct comparison can be drawn between the locked-in bending moment behaviour observed here and the accumulation of global pile secant stiffness presented earlier in Figure 5.14. As previously seen, the rate of secant stiffness accumulation also increases proportionally to the applied load ratio, indicating that the magnitude of locked-in bending relative to the current applied load is directly influential on the global monopile stiffness response.

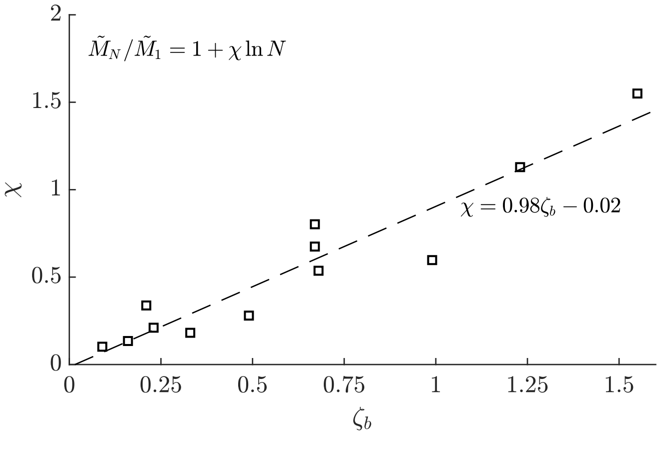

Figure 5.34: Variation of χ with ζ_b

***(ii)* Local soil stress:** attention is now turned to the local horizontal soil stress behaviour in the proximity of the monopile of which can be directly deduced from individual EPC sensor readings. Previous attempts have been made by Kirkwood (2015) to quantify this stress distribution with cycles using a Tekscan pressure sensor sheet wrapped around the circumference of the pile, however the sensor accuracy with depth and repeatability is not so strong rendering it difficult to identify consistent trends.

EPC sensor results here are presented for both in front and behind the loaded pile to demonstrate the active and passive components of the cyclic horizontal stress behaviour. Figures 5.35 & 5.38 present the direct pressure readings from selected cycles for both load and unload phases of high and low magnitude constant cyclic load packages. Within these figures, dotted lines illustrate the K_o condition, *i.e.* the theoretical stress state the soil is under before the start of cyclic loading. Stress path analyses are also presented in Figures 5.36 & 5.39 for the first and last cycles of both the high and low load sequences to illustrate localised stress changes during the full individual cycle hysteretic loop. In addition, recorded time-lapse images of the surface movements are presented in Figures 5.37 & 5.40.

(a) *High magnitude applied cyclic load* – firstly, for the high load magnitude cyclic sequence (Figure 5.35), large passive pressures are immediately seen with cycle 1 at sensor readings in front of the pile close to the mudline as well as at the rear of the pile close to the base. This illustrates the rotation and the 'toe-kick' behaviour that has previously been identified for large applied loads. In conjunction with these, the pressure reduction to the rear of the pile illustrates the active stress state that develops here on load. With this there is the potential for sand to redistribute as it prevents a gap from forming behind the advancing pile in response to the reduction in horizontal stress, of which will be explained in more detail later. On unload, the high passive pressures in front of the pile close to the mudline are seen to return to close to the K_o stress condition allowing a small amount of sand grain redistribution on the front side also. The increased horizontal stress condition, however, remains locked with depth after the first cycle.

    Stress path analyses provide complimentary evidence of the locked-in stress history during the cycle with depth. For the first load cycle (Figure 5.36a), it can be seen that the large passive resistive stresses behind the pile close to the base are developed immediately and these remain throughout the full cycle history – there is no stress state reversal and very little change in stress magnitude upon unload.

A similar observation is made for the active stress condition on the opposite side of the pile, which always presents a stress lower than the theoretical K_{o} state. With any shear mobilisation of a dense sand, it can be expected that a degree of expansion takes place due to dilation. If the overburden stress is sufficiently large, for example at substantial depths along the monopile, this expansion will contribute to an increase in normal stress acting at the interface of the shearing zone, and will ultimately provide additional resistance for the translating pile. Once the increased localised normal stress has developed, unless there is a global load reversal which gives rise to substantial reverse stress relief, it will remain locked-in on unload and throughout future loading. This is exemplified across all tests.

Close to the mudline surface, a very large increase in horizontal stress in front of the pile is seen upon loading. This exceeds predicted full passive resistance and therefore can be assumed to have been fully mobilised beyond a critical state condition. This will of course result in large dilation potential. When the load is removed, however, passive horizontal stresses at this location are, unlike at depth, completely dissipated to the original K_{o} condition with no residual stress remaining on unload. This must be as a result of the low overburden stress condition here and therefore any dilation that occurs is unlikely to induce increases in normal stress and will present changes in the surface topology in front of the pile.

With the progressive application of cycles, interesting changes to the stress distribution are observed across the cyclic history. At depth, there is a very minor increase in passive stress at the rear of the pile after the first cycle with this magnitude appearing to stabilise both on load and unload after the applied 22 cycles. In fact for the final applied load cycle, the stress path reveals no noticeable change in passive stress magnitude despite a full load-unload cycle (Figure 5.36b) – here the stress behaviour is fully locked-in – and must significantly contribute to the global stiffness response, since this in effect is acting close to an encastre support at the base

Close to the surface, a reduction in the observed maximum horizontal passive stress in front of the pile with cycles is seen to take place. This illustrates a loss of soil strength here from the repetitive high applied stress beyond critical state causing the initially dense sand to dilate and become looser (since overburden stress at shallow depth is low, there is no potential for these to lock-in). The observations here are in agreement with early DNV GL (2016) adjustment factors as well as literature models (Little and Briaud, 1988; Long and Vanneste, 1994) which do indeed recommend ultimate strength reduction with applied cycles. This reducing behaviour is, however, restricted to the surface. With the progressive reduction in resistance close to the surface, this inherently necessitates greater horizontal stress derivation from deeper along the pile to resist the applied cyclic overturning moment, which is evidenced across the dataset with a progressive shift of maximum horizontal stress with depth.

Finally, in addition to the locked-in stresses that develop at depth on unload, horizontal stresses also build-up close to the mudline at a depth of around $z/D \approx 1$ at the rear of the pile. Unlike the deeper locked-in stresses, these are not generated from dilation induced increases in confining stress, since the stress path here on load is reducing from the original K_o to an active state and therefore little dilation will actually take place. In addition, the overburden stresses are minimal so the lock-in potential is small. In this case, explanation is likely due to the redistribution of sand grains that is taking place in this region. As the horizontal stress behind the advancing pile reduces, the sand will have the tendency to move in the direction of the pile so as to prevent the formation of a gap. Upon unload of the pile, the new additional soil behind the pile will prevent the elastic recovery potential of the monopile as it is unloaded causing passive stress to develop behind the pile. It is seen in the stress path that with each load and unload cycle, there is a constant switch from locked-in passive stress to near zero stress, which stimulates continual redistribution of sand on every cycle. The time-lapse images in Figure 5.37 illustrate a small progressive movement of sand towards the pile with applied high magnitude cyclic loads (here test C39 is presented as only 22 load cycles were applied for C38 and therefore did not show noticeable movement). Cuéllar (2011) proposed that this generated into an eventual convective sand flow pattern beneath the mudline in the vicinity of the pile.

(b) *Low magnitude applied cyclic load*: for the case of a low magnitude, high cycle count experimental scenario (Figure 5.38), the distribution of soil stress with depth reflects the mechanism that it is experiencing for this lower level load. On the application of load, there is no horizontal stress increase at the toe, demonstrating that rotation is not taking place. Horizontal passive stress at the front of the pile close to the surface does, however, remain substantially large on load and reduces quickly to the initial K_o condition with depth. This illustrates that the majority of lateral strength is derived from the upper portions of soil, which is synonymous of a flexible type failure mechanism.

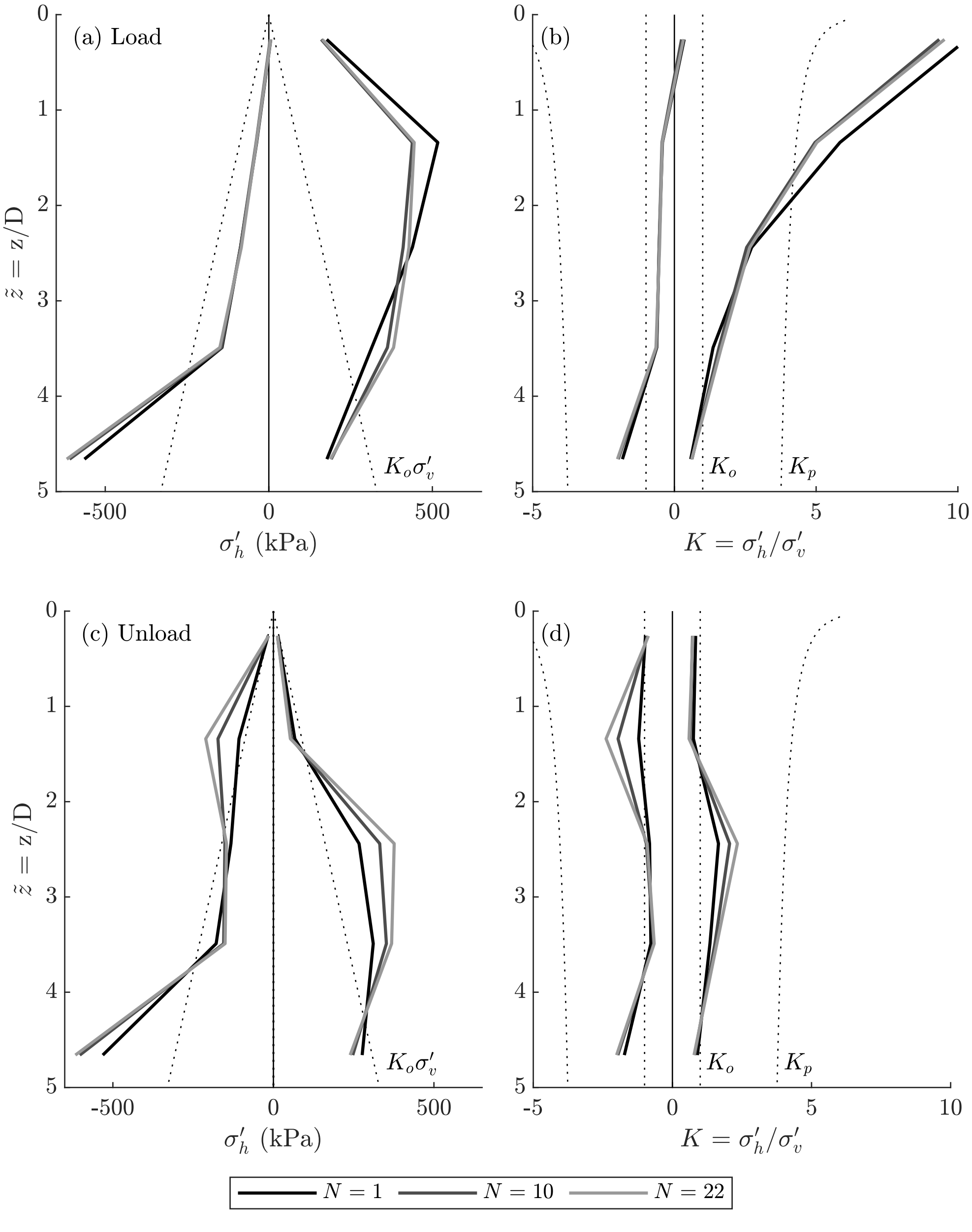

Figure 5.35: Horizontal soil stress variation with cycles (Test C38 – $\zeta_b = 1.55$): absolute magnitude on (a) load; (c) unload; dimensionless magntiude on (b) load; (d) unload

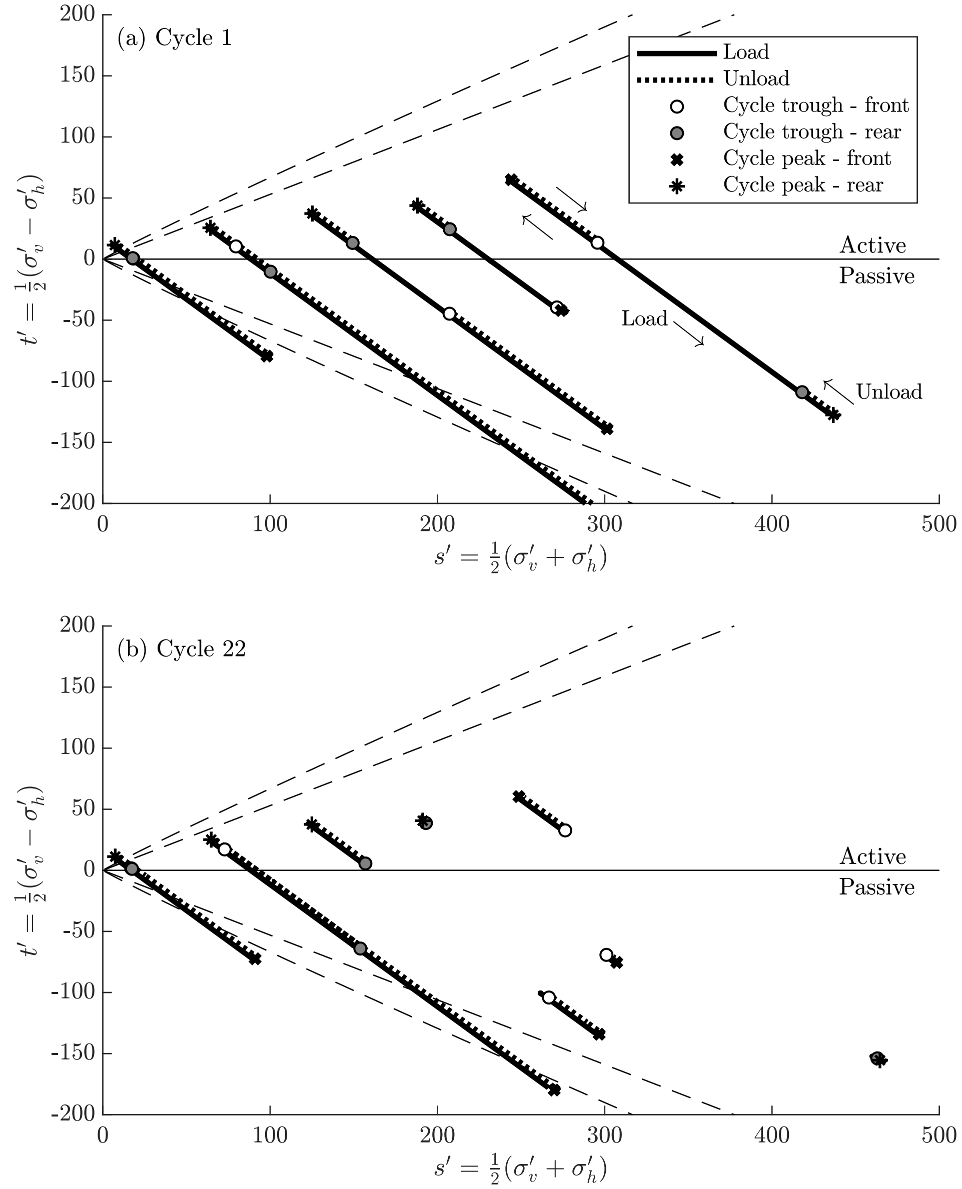

Figure 5.36: Stress path analysis for (a) first; and (b) last applied cycle (Test C38 – $\zeta_b = 1.55$)

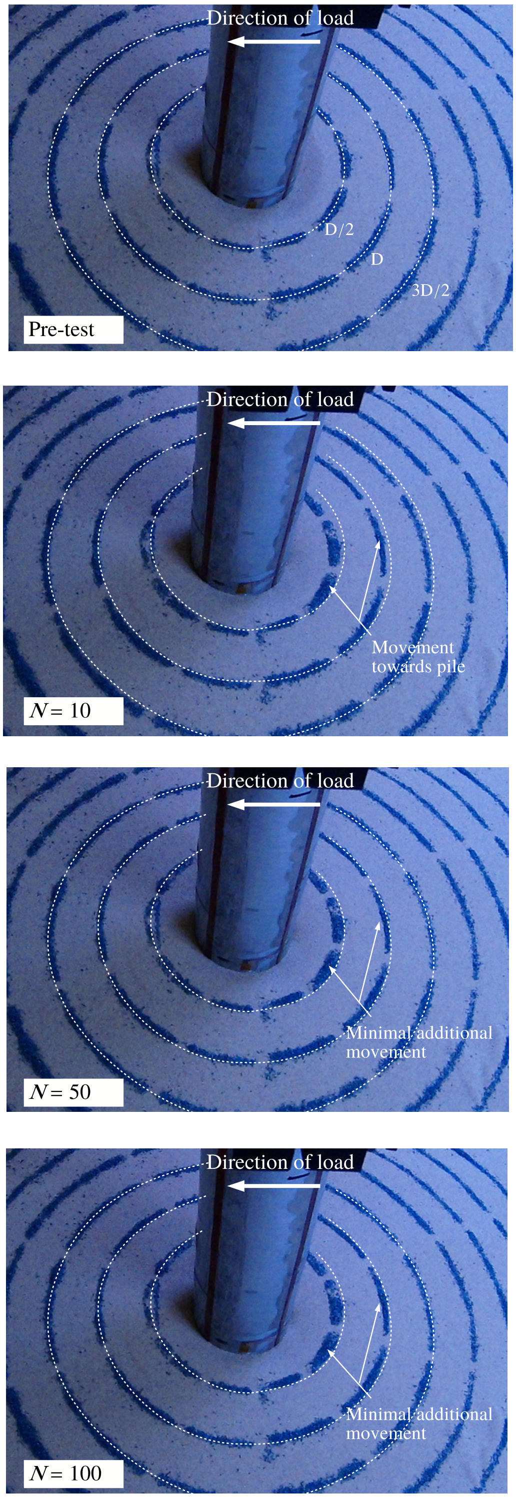

Figure 5.37: Surface sand movement with applied cycles on high magnitude cyclic load experiment (test C39 – $\zeta_b = 1.23$)

Stress path analyses with depth for the first applied cycle (Figure 5.39a) reveal the same underlying trends, with a proportionally large amount of mobilisation close to the surface, with next to zero at the base.

After the application of thousands of load cycles at this low load magnitude, a differing behavioural pattern presents itself in comparison to the high load scenario. Whereas for the high load case a reduction in maximum horizontal stress with applied load cycles close to the surface was apparent, here with each cyclic decade gain, the horizontal stress on load at the front of the pile constantly increases. Differences are also seen on unload where with the high load case, relatively large locked-in stresses at depth in comparison to the surface were experienced; these are not seen for a low magnitude load case since little to no sand mobilisation takes place at depth. This results in no potential for sand dilation and associated increases in normal stress, which can therefore not be locked-in on unload. This has implications on global stiffness behaviour.

Close to the surface, relatively large locked-in stresses develop at the rear of the pile. This stress lock-in is more progressive and builds up over many thousands of cycles and can be explained by the sand redistribution phenomena that is taking place behind the pile. As previously seen, these stresses also develop at the rear of the pile for the high load magnitude case, however at a noticeably deeper location. An explanation for this may be due to the pile translation at the surface being inherently much larger with each cycle for the high load and therefore allowing greater sand movement to fill the deeper forming gap behind the advancing pile. The migrating sand 'falling' into this deeper gap formation will therefore present resistance to the recovering pile at a greater depth – this is seen at approximately $z/D \approx 1$ (Figure 5.35). With regards the low magnitude case, the amount of pile translation at the surface on load is not as large and therefore any sand migration towards the pile will fill a relatively shallower potential forming gap. This will present resistance to pile recovery at this shallower depth, in the region of $z/D \approx 0.25$ for test C35. Incidentally, Cuéllar (2011) also observed a shallower, narrower sand convective flow pattern for lower magnitude applied overturning moments.

Figure 5.40 presents the time-lapse images for the progressive migration of sand towards the monopile (here test C33 is presented due to data recording issues for the lower load magnitude cases; it is expected that surface sand behaviour is very similar for the other low magnitude load cases). After 60,000 applied load cycles, considerable surface movement has taken place within the zone of influence, which extends to almost $2D$ from the outer diameter of the monopile.

> Examination of the stress path behaviour at the front of the pile for the final applied cycle (Figure 5.39b) reveals the similar trend as for the high load case, with a switch from passive to original stress condition with each full cycle loop. At the rear, however, the passive locked-in stress state that has built-up with cycles remains present throughout the entirety of load cycle – this meaning that a residual horizontal stress to the rear of the pile is present both on unload (as to be expected since this prevents elastic pile recovery), but also on load. The latter would indicate that the additional stress developed from the progressive sand redistribution becomes so great that the magnitude of applied load is not large enough to allow sufficient pile translation and an associated reduction in horizontal stress behind the advancing pile to fully remove these on load.

The underlying trends presented for each of high and low magnitude applied cyclic load cases are echoed across the full test matrix depending on the applied load ratio. To illustrate these, variation in the observed horizontal stress outputs with applied cycles, across the test matrix of model piles instrumented with EPC sensors, is presented in Figures 5.41 & 5.42. Specific interest in the sensor outputs from close to the surface and to the pile toe are made since these appear to reveal the most important trends for cyclic stress variation which can be attributed to observed global trends. It can be seen that for the two lower load magnitude cases ($\zeta_b = 0.21$ & 0.33), these demonstrate the large unload stress build-up close to the surface at the rear of the pile (Figure 5.41d), with no change in stress at depth. The remaining larger load magnitude test results present increasingly greater stress at the base with each larger applied load, with little stress lock-in on unload close to the surface. The progression of locked-in stress with cycles at the base across each test is also evident.

It is worth noting here briefly that the above observations are for a no scour protection scenario and therefore present idealised surface movements and stress behaviours close to surface. In reality, with the dumping of large volumes of rock armour protection, additional overburden stress will be introduced which may allow greater lock-in potential for the stresses developed on load and unload close to the original surface. This will inherently affect the progression of global stiffness and rotation. Experimental modelling of this will be required to fully understand the potential implications in cyclic design with scour protection.

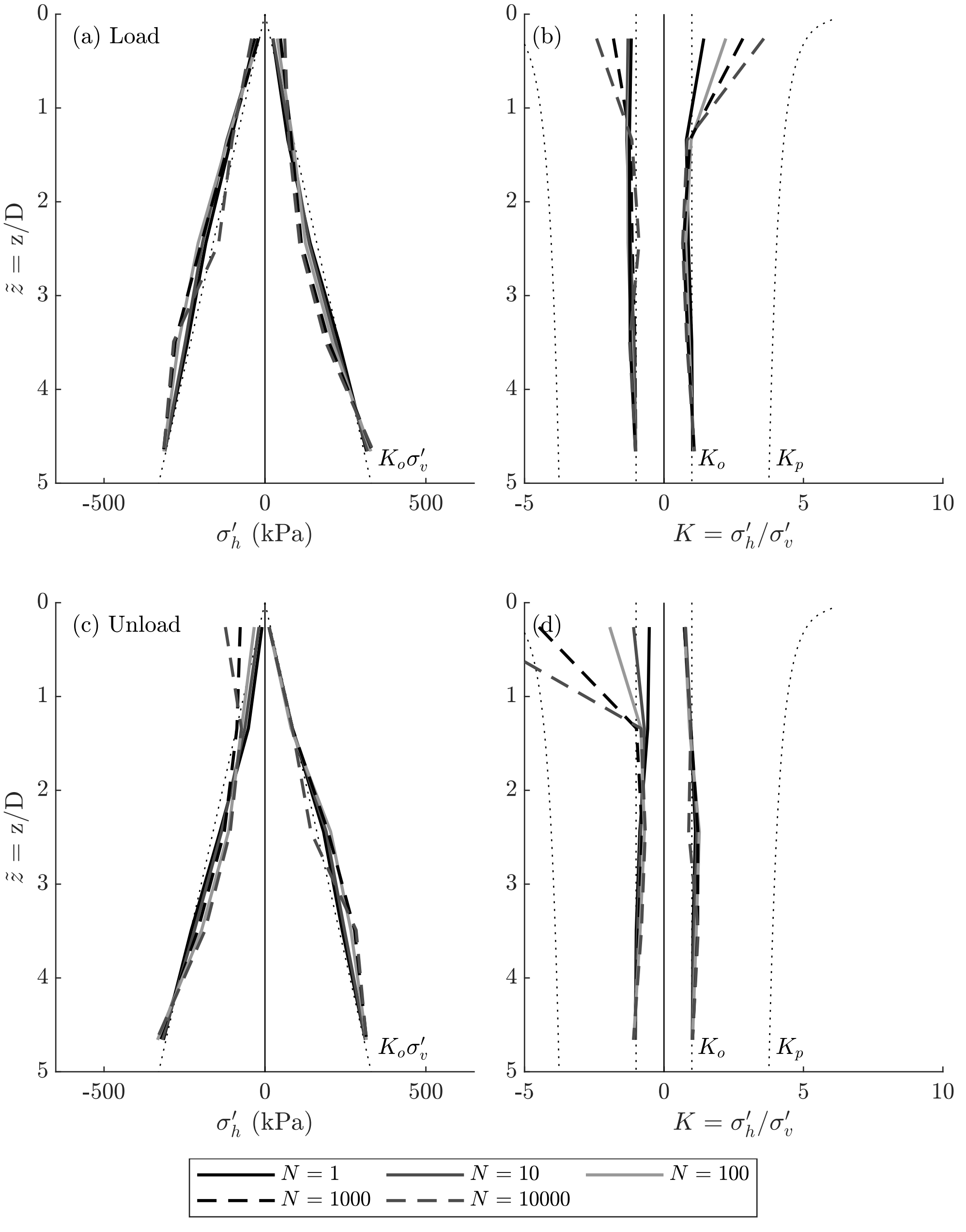

Figure 5.38: Horizontal soil stress variation with cycles (Test C44 – $\zeta_b = 0.33$): absolute magnitude on (a) load; (c) unload; dimensionless magntiude on (b) load; (d) unload

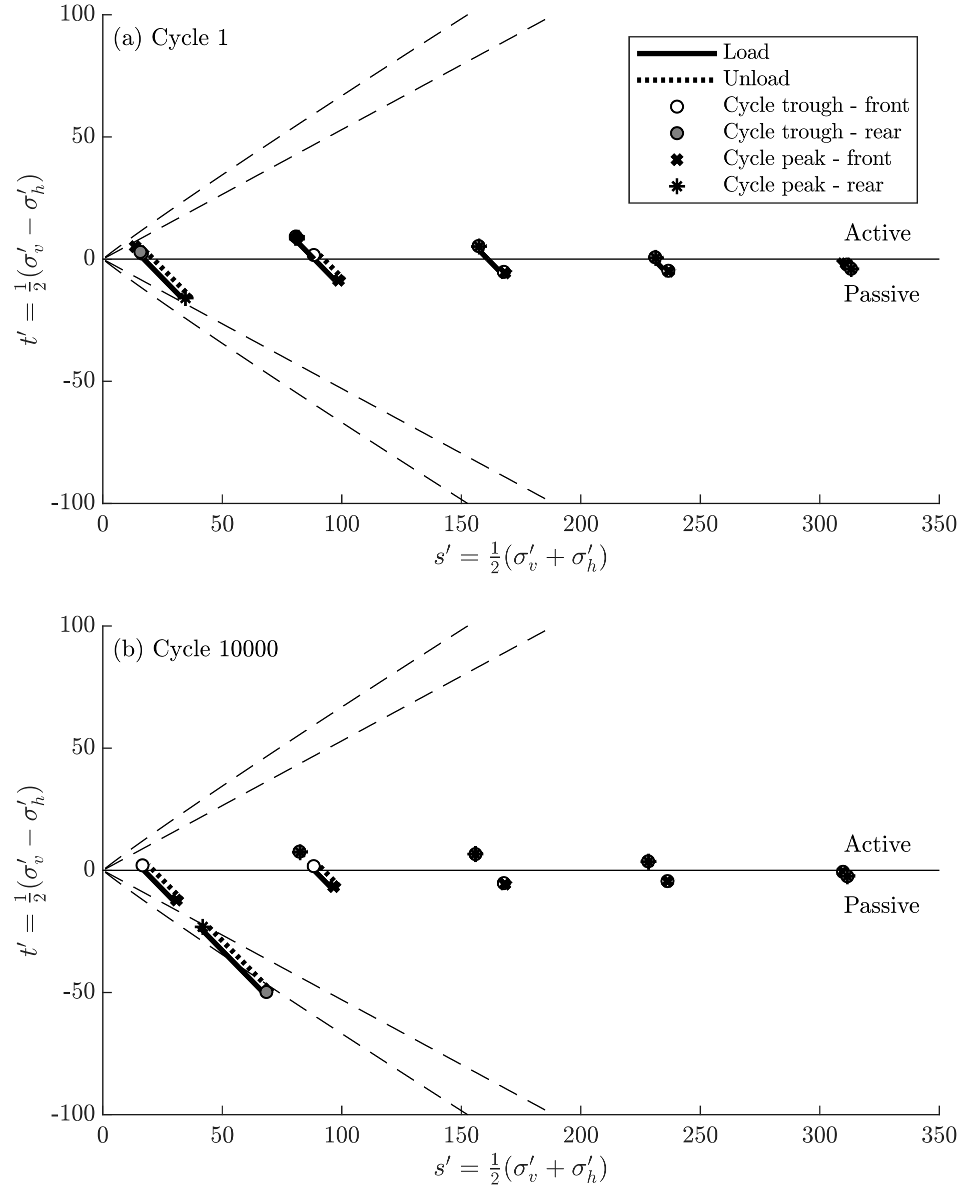

Figure 5.39: Stress path analysis for (a) first; and (b) last applied cycle (Test C44 – $\zeta_b = 0.33$)

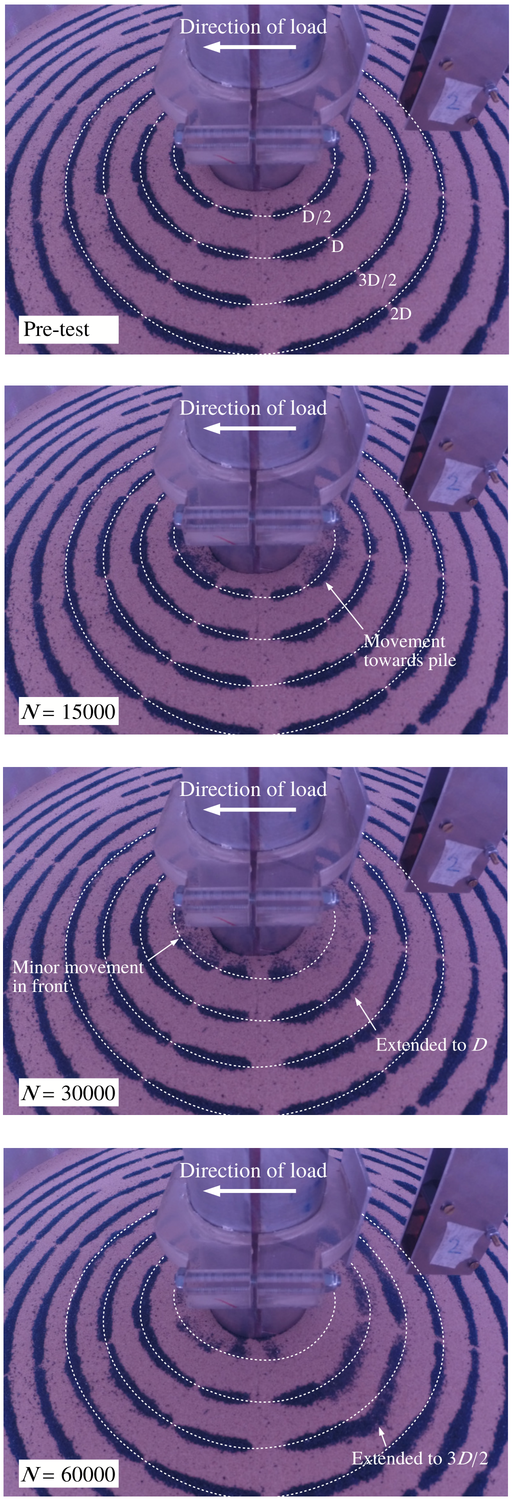

Figure 5.40: Surface sand movement with applied cycles on low magnitude experiment (test C33 – $\zeta_b = 0.23$)

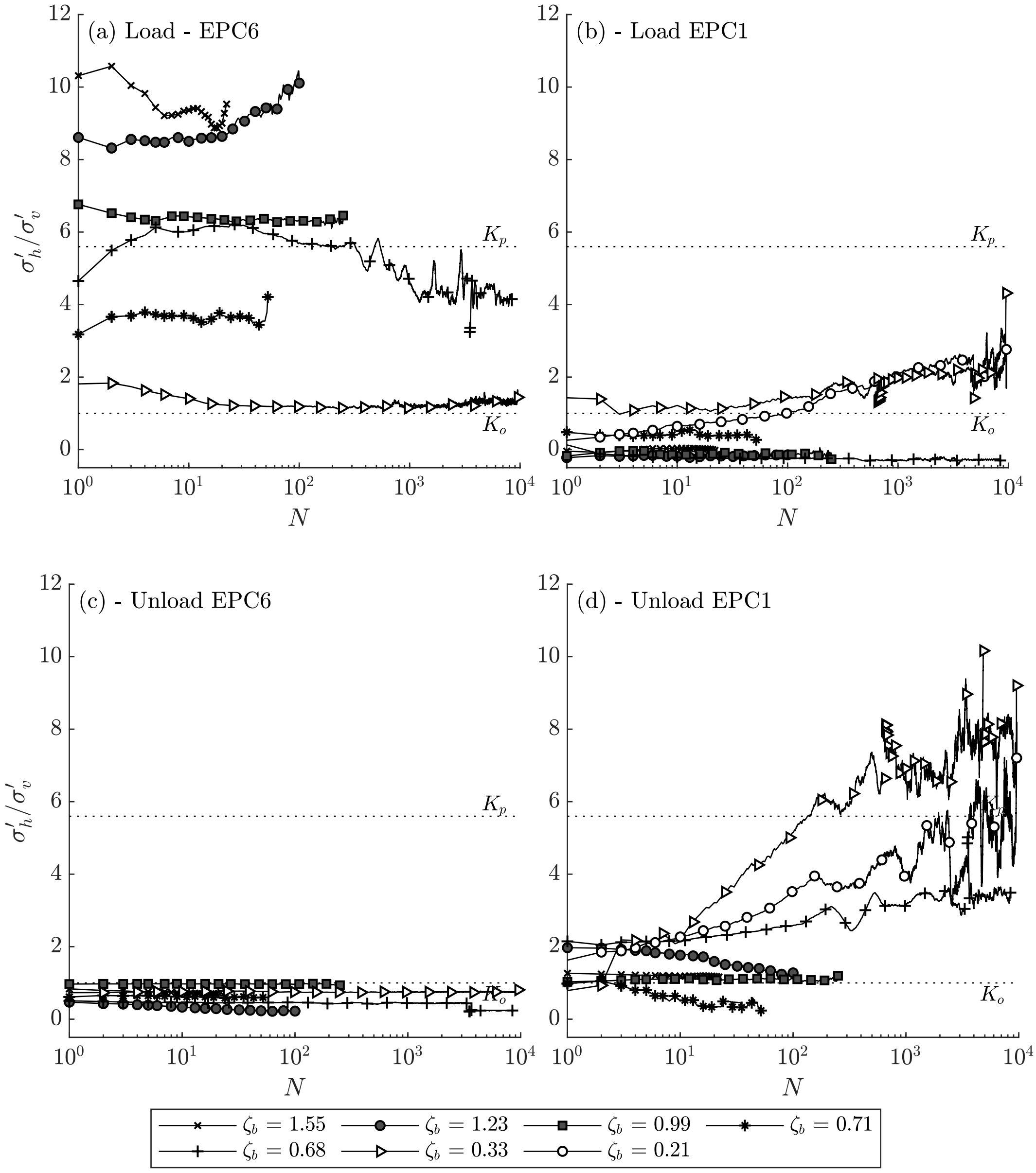

Figure 5.41: Horizontal stress variation close to soil surface. *N.B.* EPC6 in front of pile, EPC1 at rear of pile

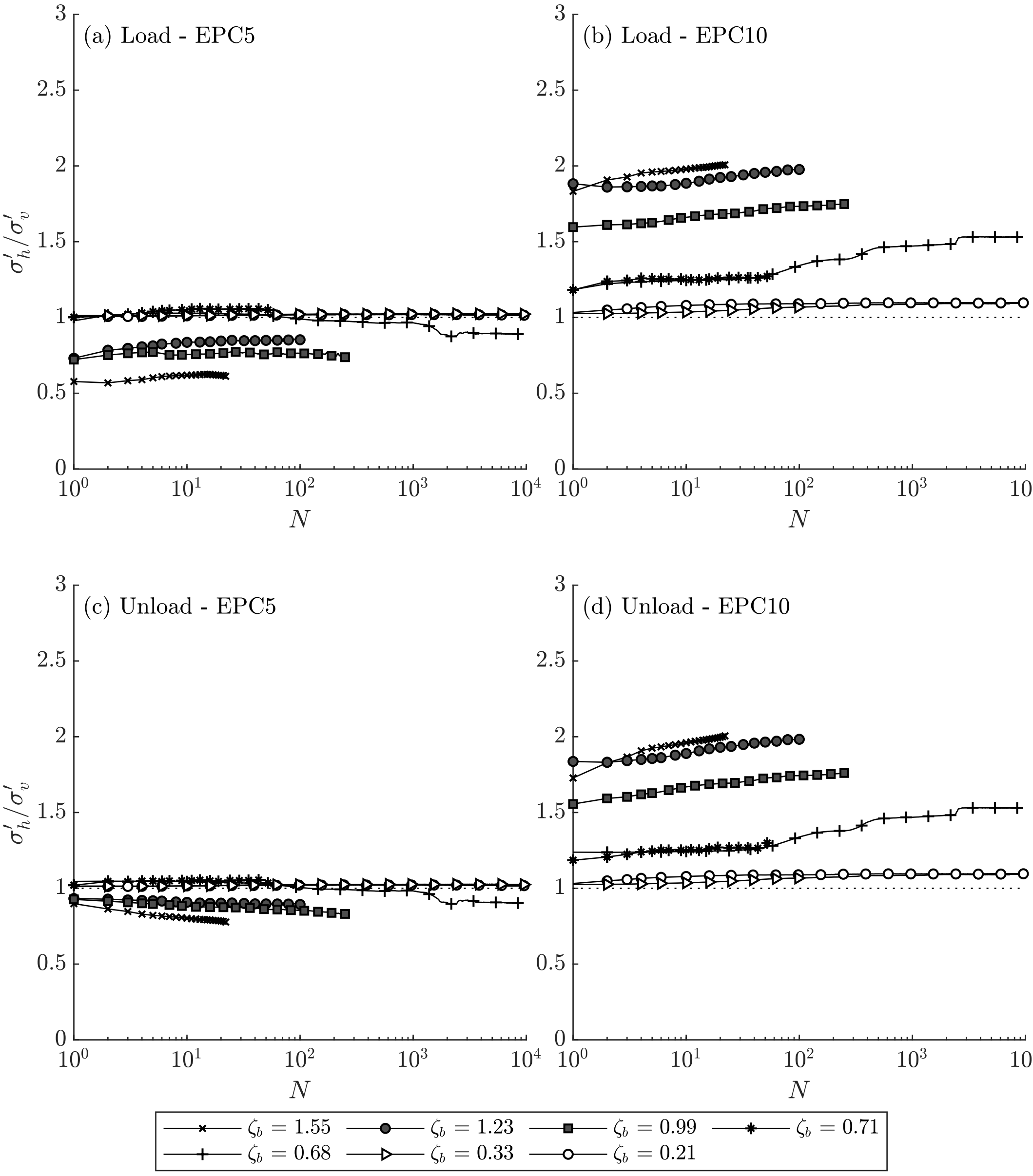

Figure 5.42: Horizontal stress variation close to pile toe. *N.B.* EPC10 in front of pile, EPC5 at rear of pile

***(iii) Connection with global behaviour*:** local pile-soil interaction behaviour has been presented and some interesting stress state changes have been identified across the range of load ratios applied in the test matrix. Here, connection between local and global observations is summarised, with the cyclic experiments again separated into two distinct behaviours associated with high and low magnitude applied cyclic loads.

(a) *High magnitude applied cyclic load* – from a global monopile point of view, significant accumulated rotations are experienced for high magnitude applied overturning moments, with the accumulation trend best described using a power-law model. The rate of foundation stiffness accumulation is also greatest for the high magnitude load case which coincides with the faster rate of locked-in bending moment increase for these high loads. The observed stress distributions upon load present significant passive resistive stresses both in front of the pile close to the surface and at the rear at the base, thus demonstrating a rigid failure mechanism. According to Peralta and Achmus (2010), the power-law progression for global accumulated deformations is most suitable for rigid pile geometries and the results here reflect this.

    It has been shown that with cycles of high magnitude load, the horizontal passive stresses in front of the pile close to the surface progressively reduce resulting in the additional resistance to be derived from deeper along the monopile. In order to develop sufficient strain at depth to mobilise these deeper horizontal stresses, progressively larger rotations at the mudline are required, leading to a fast accumulation of pile head rotation. On the flip side, with the mobilisation of larger horizontal stresses at greater depths with each cycle, there is a greater potential for stress lock-in given the associated greater overburden stresses at these deeper locations. This will contribute to the faster observed global foundation stiffness increase as the greater locked-in stresses development. Figure 5.43 presents a schematic summary of the behaviour seen on load and unload for one individual cycle.

(b) *Low magnitude applied cyclic load* – this cyclic load scenario presents significantly less rotation than higher load counterparts and these accumulate at much slower rates, best described using a logarithmic-law trend. The monopile does not, however, stop experiencing long-term ratcheting and continues to increase in global foundation stiffness throughout the entire load history, albeit at a slower rate relative to the observed stiffness after the first cycle.

    Locally, horizontal stress outputs reveal little to no change close to the pile base, with the majority of horizontal stress resistance achieved close to the sur-

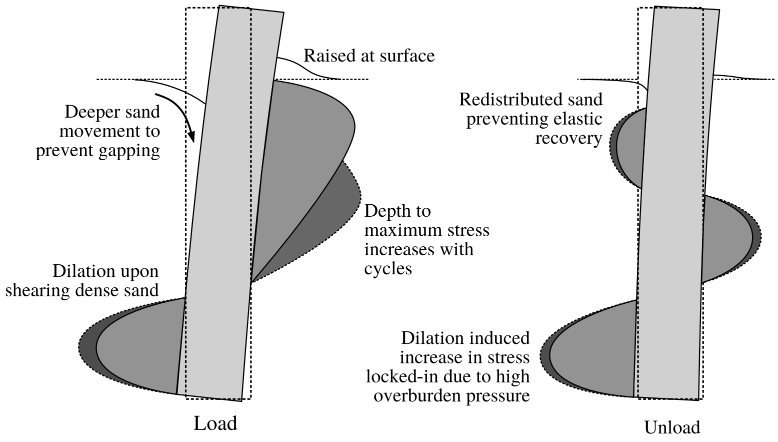

Figure 5.43: Schematic illustration of stress distribution with high magnitude cyclic load-unload

face. This is illustrative of a flexible failure mechanism and the global rotation logarithmic accumulation trend reflects this (it was Peralta and Achmus (2010) who proposed logarithmic progression of global rotation accumulation for flexible piles). In contrast to the high load case, the magnitude of horizontal stress close to the surface progressively increases with each applied load cycle which can be attributed to either increased soil stiffness or increased pile deformation, both of which will mobilise greater resistive stress. Here, this is likely to be a combination of both, with additional stiffness gained from observed sand redistribution close to the surface and increased strain from the progressive increase in monopile rotation.

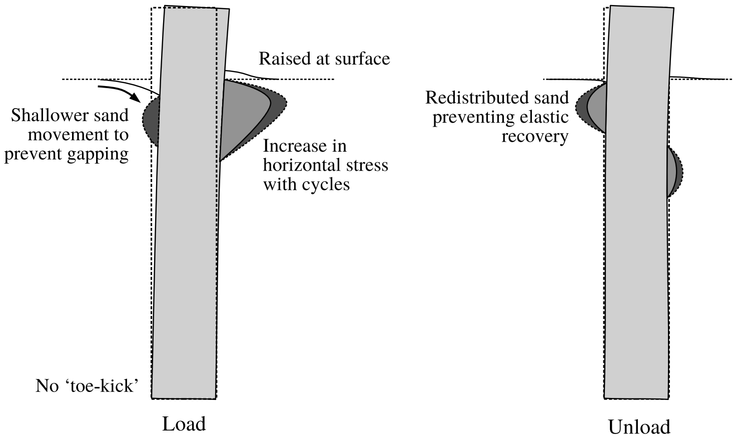

Figure 5.44: Schematic illustration of stress distribution with low magnitude cyclic load-unload

Given that only the soil close to the surface is mobilised, any stiffness increase in the global foundation response must be due to changes in the sand in this region. It has been seen that despite a relatively low applied load, there is still substantial sand redistribution behind the pile as it prevents a gap formation behind the advancing pile. Upon unload, the elastic recovery potential of the monopile, which is proportionally larger for the flexible type mechanism, is prevented due to the presence of this redistributed sand and therefore additional horizontal stresses and subsequent internal pile moments are developed with cycles. For this low load case, the reduced rate of global foundation stiffness accumulation can be related to the reduced rate of bending moment accumulation. Given the deeper, locked-in stresses are not developed for this case, the stiffness changes are dominated by the surface sand movements rather than deep dilation induced normal stress increases and due to the relatively slower rate of sand redistribution at lower loads, these generate at a slower rate.

5.7.2 Varying load sequence

For the experimental scenarios of cyclic varying load magnitude, it has previously been seen that interaction of global rotation accumulation behaviour takes place between successive load packages, the degree of which is dependent on the number and nature of the respective applied load cycles. The previously identified rainflow cyclic count method coupled with the proposed contour based rotation accumulation model appear to perform well for the prediction of this global behaviour. Local soil-pile interaction is now examined for a number of more complex varying applied load sequences with the aim of rationalising these against global observations. Internal bending and local horizontal soil stress measurements (where available) are again analysed from three separate cases, these being: (*i*) progressively increasing, (*ii*) progressively decreasing, and (*iii*) random cyclic loading.

***(i) Increasing load package*:** the packages of progressively increasing load magnitude are first analysed (test C36, and first half of test C43). As a reminder of the cyclic load profiles, Figures 5.16a & 5.17a present the load histories for these respectively.

Firstly, the bending moment profiles with depth on load and unload from the final applied cycle of each individual increasing magnitude load package are presented in Figures 5.45 & 5.46. On first inspection, it can be seen that for each increase in applied cyclic load, the absolute magnitude of locked-in bending moment increases accordingly. The magnitude of base moment also increases with each successive load package signifying the translation from a flexible to rigid mechanism of failure. Dividing these by the applied overturning moment at the mudline for each respective package sees the lower magnitude applied loads presenting a higher ratio of locked-in moment. The collective observations each agree with the previously identified trends from the analysed constant magnitude loading (see Section 5.7.1).

In addition to changes in absolute magnitude and relative bending profiles, it can also be seen across Figures 5.45 & 5.46 that with the increased magnitude cyclic load, the depth to the maximum locked-in moment increases in parallel. This depth change is subtle within the individual experiments, however becomes clearer when comparing across the wider range of applied load magnitudes between tests C36 and C43. For test C36, applied overturning moment increases from $\zeta_b = 0.05$ to 0.25 over 7 LP, with a depth to maximum locked-in moment presenting itself at values of $z/D < 3$. In test C43 on the other hand, the monopile is subject to greater loads with ζ_b increasing from 0.23 to 0.63 over 4 load packages, with the respective depths to maxima $z/D > 3$. This depth change can be attributed to changes in localised locked-in stress behaviour. As

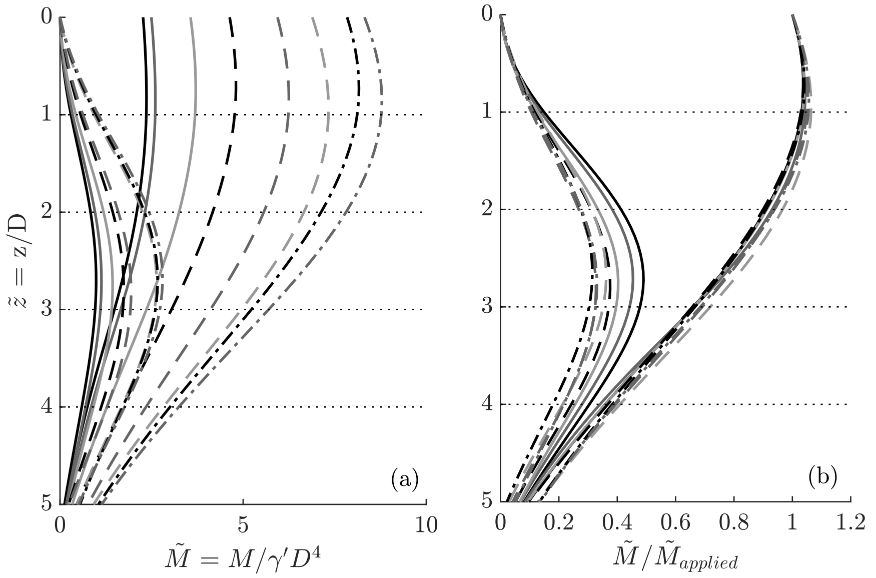

Figure 5.45: Bending moment profile on load and unload for progressively increasing load magnitude packages (test C36): (a) dimensionless magnitudes; (b) as a ratio of applied overturning moment at the mudline

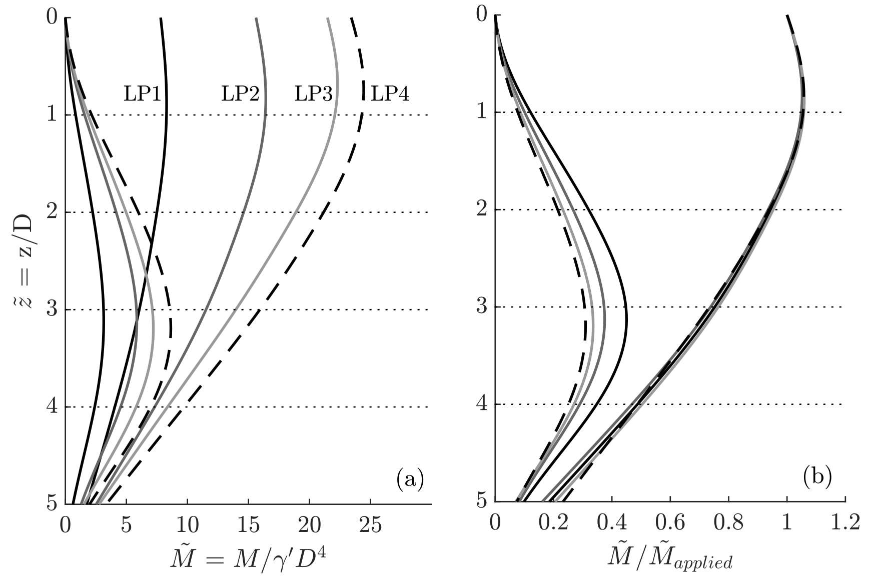

Figure 5.46: Bending moment profile on load and unload for progressively increasing load magnitude packages (first half of test C43): (a) dimensionless magnitudes; (b) as a ratio of applied overturning moment at the mudline

a reminder, it has been seen for the constant load experiments, higher applied cyclic loads mobilise soil at greater depths and therefore present deeper locked-in stresses, most notably close to the pile base. The observed progression of stress distribution with depth for increasing load cycles specific to test C43 are presented later in this section.

Global monopile rotation interaction has been seen to take place between successive load packages during the increasing portion of test C43. This is evidenced between LP 2 & LP 3, and LP 3 & LP 4 where the rate of rotation accumulation upon application of the new LP is delayed until a finite number of load cycles has been applied. At a global level, this cycle number has been predicted with reasonable accuracy by the Miner's rule as well as the proposed contour accumulation model, where tracing along the contour of currently experienced permanent rotation will reach the equivalent cycle number N^*, at the point of intersection with the new applied load ratio. Essentially, the parameter N^* combines the effects of the complete previous load history into an equivalent number of applied cycles of the new load magnitude. For test C43, N^* takes a value of approximately 6 and 110 respectively. The new established rotation accumulation can then be predicted forthwith using empirical accumulation trends, with the input cycle count for these equal to $(N_i^* + N_{i+1})$.

In order for the observed interactional effects at a global scale to unfold, localised changes in the sand behaviour must take place such that either an immediate variation in bending moment response or stress distribution occurs at the cycle number, N^*, or a particular stress or convective flow threshold is reached by N^* cycles, to allow the faster rotation accumulation to take place. It is likely that any individual experimental observations in pile bending or soil stress changes, coupled with sand redistribution in the proximity of the pile, are subtle and it is the sum of their combined effect that leads to the more noticeable rotation change at a global scale. Nonetheless, local behaviour is now analysed and any variations in and around the load cycles of interest are noted with potential hypotheses for these outlined.

The progressive change in bending moment across the complete increasing load sequence is presented in Figure 5.47. Four points of interest with depth are considered – these being one close to the surface, two at mid depth and one close to the pile toe – with these depths coinciding with the locations of selected EPC sensors. Dotted lines, representing the transition cycle number at the point of rotation interaction, N^*, are superimposed for information.

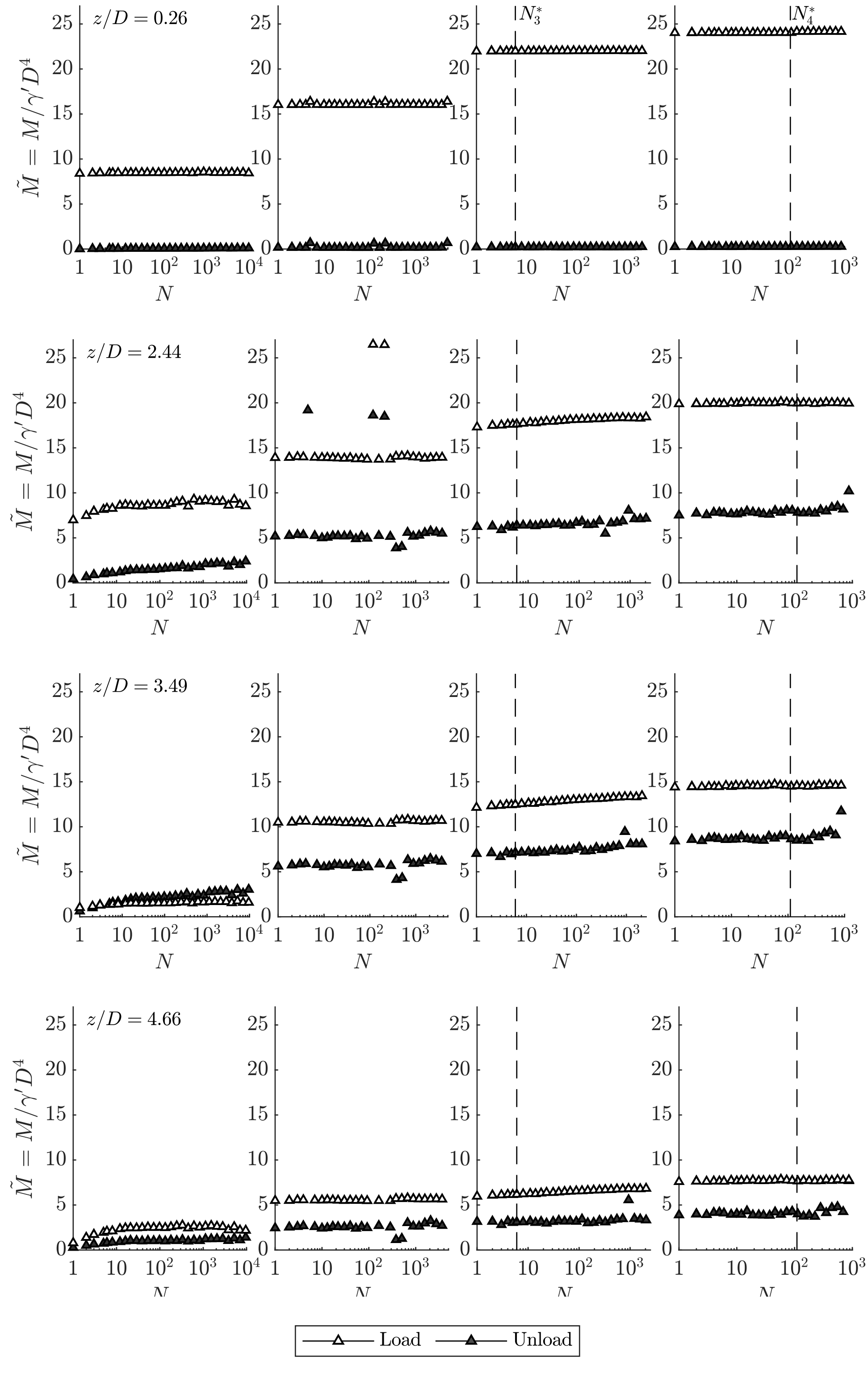

Figure 5.47: Bending moment variation at four locations of interest for load package of increasing magnitude (test C43 – LP 1, 2, 3 & 4)

From Figure 5.47 it can be seen that at shallow depths, the bending moment on load is large and presents a very near constant magnitude across the all the cycles, directly reflecting the constant applied overturning moment at the mudline for each individual increasing load package. Upon unload, there is also next to zero locked-in bending observed and therefore zero elastic recovery potential energy is stored within the monopile at this shallow depth.

With depth, the bending moment behaviour is seen to be no longer constant across each load package, despite the constant applied overturning moment at the mudline, signifying that changes within the soil are taking place with cycles. Firstly, for the initial two packages of load, monopile bending on load progressively increases with cycles immediately from the start of the load package. This increased pile bending directly leads to greater rotation at the mudline and can be attributed to a reduction in sand strength close to the surface leading to greater lateral resistance being derived from depth. This is analogous to an increase in effective lever arm associated with the applied load. Similar increases in locked-in bending with cycles are also seen on unload which is to be expected due to the higher overburden stresses at the greater depths locking-in the greater moments experienced on load.

Turning attention to the latter two load packages, of which experience a degree of rotation interaction due to the load history, a subtle interaction between the bending moment behaviour is also evidenced. It can be seen that the final locked-in bending developed at the end of the preceding package has a very similar magnitude to that at the start of the new package – a behavioural trait that is directly comparable to the observed global level at these transitions which sees minimal change in permanent rotation despite the onset of new greater magnitude load. This continuation of locked-in bending magnitude between successive interactive load packages becomes clearer with increased depth – at $z/D = 3.49$ & 4.66 there is almost no difference in bending on unload from the final applied cycle of the previous package and the first applied cycle of the new package. This demonstrates the interactional effect of a progressive build-up of locked-in bending on future monopile behaviour, and must lead to interaction at a global rotation level.

Observations of any particular behavioural changes that occur in and around the point of N^* are now examined. Prior to this transition point, it can be seen that the magnitude of bending moment on unload appears relatively unchanged from the previous package and remains of relatively constant magnitude until reaching N^* cycles. It is to be noted that the bending moment experienced upon loading does show immediate increase in line with increased applied overturning moment. Upon reaching N^*

cycles, locked-in moment begins to show increased magnitude signifying greater mobilisation of adjacent soil and greater stored energy. It is unclear, however, from the direct observations of these as to the rationale for this distinct transition point, though they appear to go directly hand-in-hand with the permanent rotation behaviour.

From the observed local pile bending behaviour, evidence is inconclusive as to the specific rationale for the transition cycle number associated with the onset of additional locked-in bending, N^*; this appears to be simply a consequential effect of the new rate of pile rotation accumulation, or vice versa. Contextualising the monopile as a whole, however, it could be hypothesised that potential changes in the input energy transfer mechanism to the soil-pile system actually provide the stimulus for the new rotation accumulation rate. Having seen that up to N^* cycles there is no increase in locked-in bending, and therefore no increase in stored potential energy, and knowing that there is no increase in permanent rotation on unload and therefore no work-done in the plastic deformation of sand, any non-recoverable energy throughout the load cycle must be transferred directly into the soil in a different way. This could be the redistribution of the organisation of sand close to the surface, without noticeably altering the pile deformation or bending behaviour, in terms of the initiation of a new sand flow regime, or removal of a previously formed regime. Cuéllar (2011) does indeed observe a deeper and wider convective sand flow regime for larger applied loads and it is perhaps the initiation of this that assumes the additional input energy until N^* cycles is reached.

Once the new flow regime is sufficiently developed, future input energy from applied loading results in the reinitialisation of plastic pile deformation and build-up of potential energy within the monopile itself in the form of greater locked-in moments. Without dissecting the model before, during and after the observed N^* cycles, it is impossible to actually verify this change in sand flow regime using traditional opaque sand models. Time lapse images of the surface movements may reveal subtle changes however these were taken at a rate of 1 frame every 30s and therefore the possible mechanisms before and after N^* are very difficult to trace (*N.B.* 6 and 110 cycles are applied in approximately 1 and 20 seconds respectively and therefore cycle by cycle behavioural changes would not have been captured in the frame rate). A transparent alternative sand medium coupled with laser PIV tracing may provide clarity on this phenomenon since the tracking of individual particles with each load could be possible (see Black and Take 2015, for example of transparent soil application).

The horizontal stress distributions with depth from the individual EPC sensor outputs are now presented in Figure 5.48 for the first and final applied cycles of these

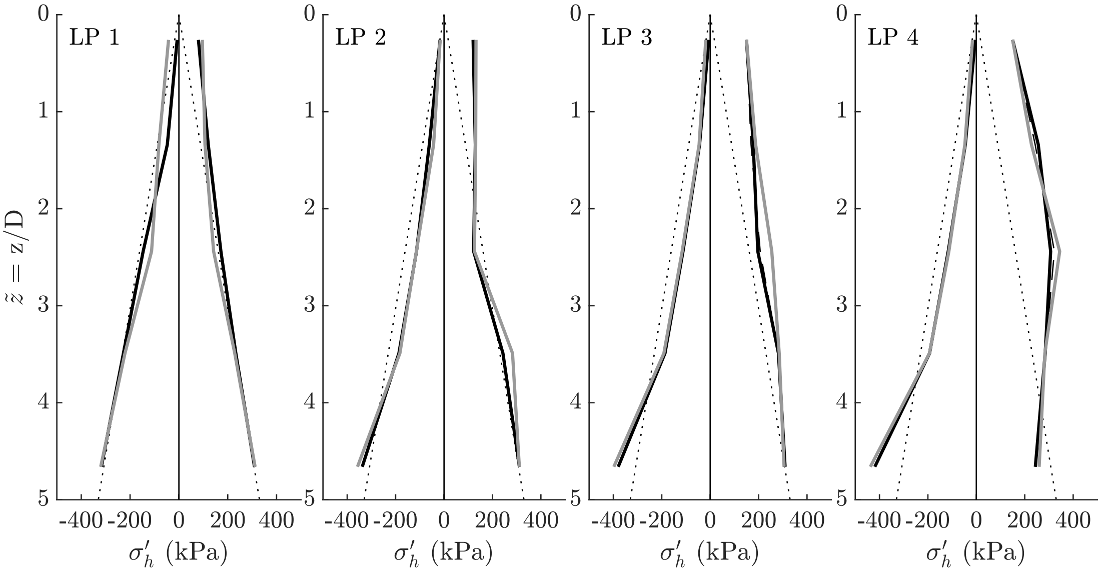

(a) Load

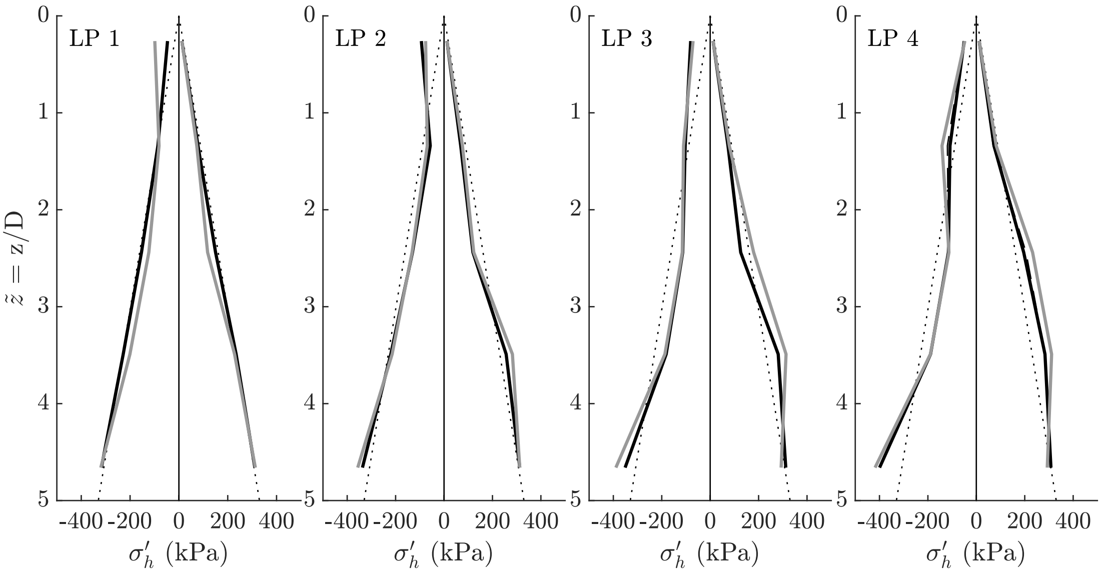

(b) Unload

Figure 5.48: Horizontal locked-in stress distribution on (a) load; and (b) unload for load package of increasing magnitude (test C43 – LP 1, 2, 3 & 4)

load packages. As the magnitudes of the applied load packages progressively increase, it can be seen that the mechanism of pile failure changes reflecting observations made previously – LP 1 is of low load magnitude and therefore only experiences mobilisation close to the surface; whereas LP 2 onwards see the onset of full-body rotation and therefore increased passive horizontal stresses at the rear of the pile at the toe are mobilised. Interestingly, the locked-in stresses to the rear of the monopile directly at the surface present a larger magnitude for the smaller applied load, and this progressively reduces with the subsequent larger load packages. Its position also deepens which can be attributed to a deeper redistribution of sand as the gapping potential behind the advancing pile also deepens. As previously hypothesised, the delay in initialisation of the new load magnitude accumulation rate may be as a direct result of the establishment of this new sand redistribution regime.

As a matter of interest, horizontal stress outputs for the exact cycle numbers $N_3^* = 6$ and $N_4^* = 110$ are also presented in conjunction by way of dashed lines. These show that very little noticeable difference in stress distribution between the first and the $N^{*\text{th}}$ cycles takes place, providing evidence that input work done to the pile system is being dissipated by other redistribution mechanisms that do not significantly change the horizontal stress distribution. In an attempt to illuminate further this transition, Figures 5.49 and 5.50 present the progression of horizontal stresses at selected depths (three EPC sensors closest to the surface to observe changes to surface stress conditions; one near the base) both in front and behind the monopile over this full load history of the increasing portion for test C43.

Firstly, attention is focused on the behaviour at the front of the pile in the upper regions of sand (EPC 6, 7 & 8). Close to the surface, the recognisable trend of an increased horizontal passive stress on load for an increased applied overturning moment presents itself, with a return to original stress condition on unload. A ceiling of horizontal soil strength appears to be reached during LP 3; this is likely due to the continuous high cyclic stress condition beyond critical state causing substantial dilation at the surface and consequently lower strength. With increased depth, LP 1 and LP 2 do not present significant increase in horizontal stress since the majority of the resistance is derived from the soil closest to the surface. As for LP 3 and LP 4, given that the upper portion of sand has reached its lateral passive capacity, horizontal resistance is derived from greater depths, which sees an increase in output readings from EPC 7 and EPC 8. Interestingly, at the point of N^*, there is a noticeable shift in the horizontal stress distribution with depth – EPC 7 sees a reduction at N^* cycles, whereas at EPC 8 the stress increases from here. This shift in stress distribution with

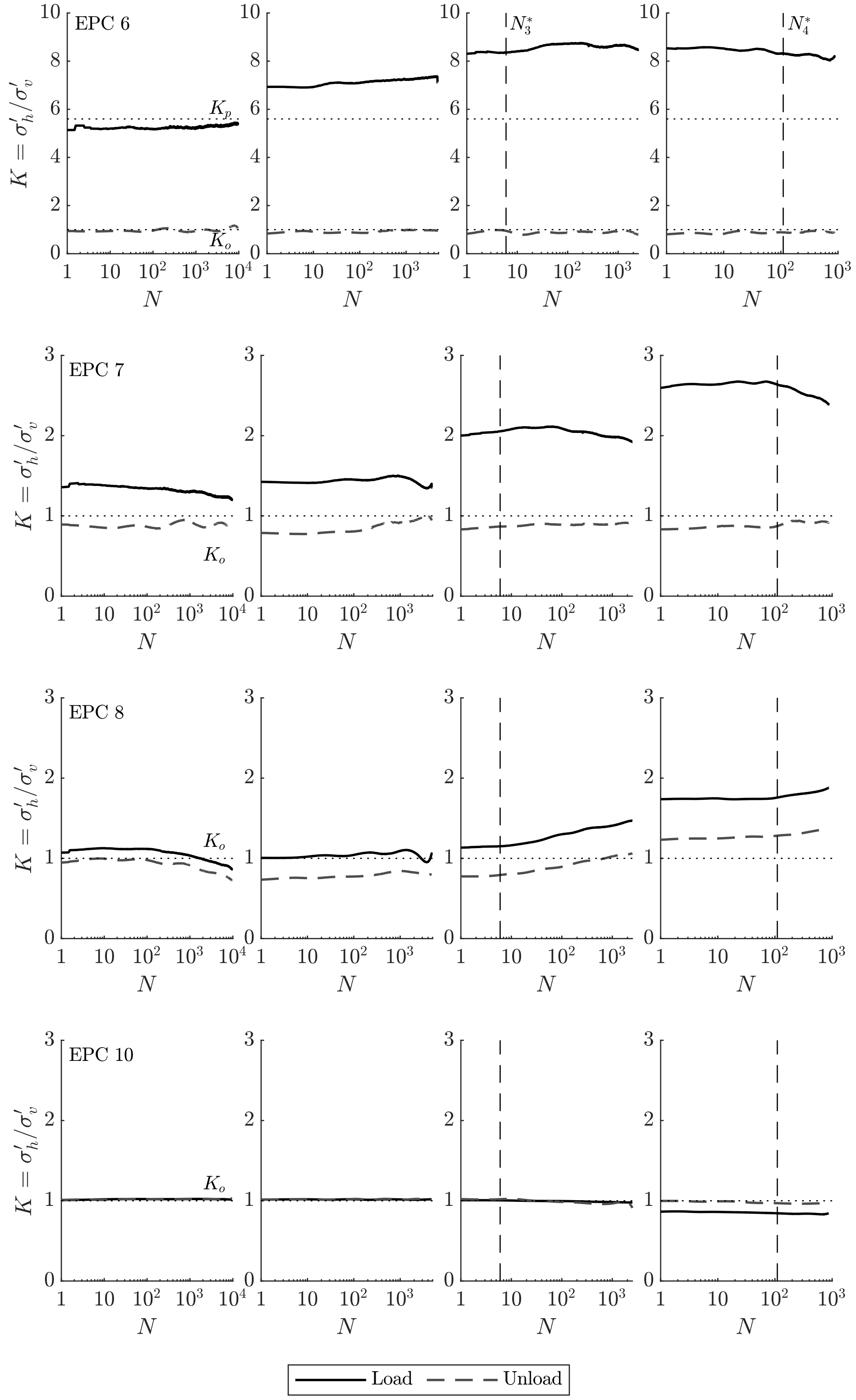

Figure 5.49: Horizontal stress variation in front of monopile at four locations of interest for load package of increasing magnitude (test C43 – LP 1, 2, 3 & 4)

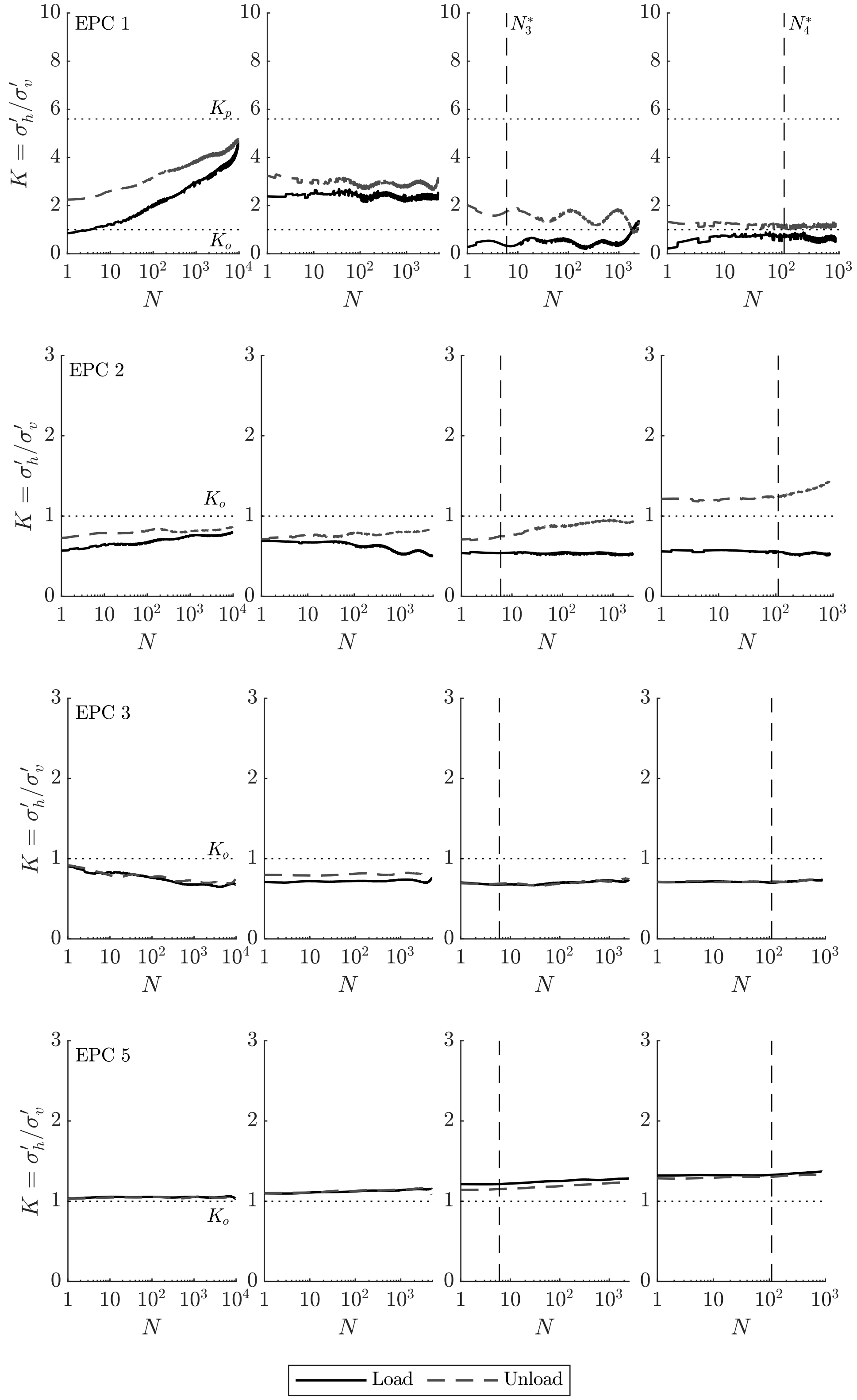

Figure 5.50: Horizontal stress variation at rear of monopile at four locations of interest for load package of increasing magnitude (test C43 – LP 1, 2, 3 & 4)

depth is in line with both the observed greater bending moment and mudline rotation that begins to present itself at the transition cycle number, N^*.

At the rear of the pile in the upper layers of sand (EPC 1, 2 & 3), interesting changes in stress behaviour are seen to take place, which may provide particular evidence to support the hypothesis of global pile rotation interaction at the transition cycle number N^*. For the low magnitude load in LP 1, a relatively large residual stress builds very close to the surface with applied cycles which remains in place even on load. This reflects previous experimental observations. The development of stress very close to the surface demonstrates the sand redistribution mechanism taking place here – a low magnitude load presents minimal gapping potential and therefore any preventative sand flow is shallow. The resulting redistributed sand is close to the surface and prevents pile elastic recovery here. Upon the application of the greater magnitude load LP 2, it can be seen that the amount of residual stress here reduces immediately with the first applied cycle and remains relatively constant forthwith. This behaviour is likely due to the new greater pile translation at the surface from the very first load cycle of higher magnitude resulting in a deeper potential gap formation. Given the already substantial redistributed sand at the rear of the pile from the previous load package, albeit at a shallower depth, this simply 'falls' into the position of the deeper vacated space from the translating pile under the new greater load. This means that the new sand interaction regime at the rear of the pile is developed almost immediately, and therefore doesn't require many cycles to build-up.

For LP 3 and LP 4, which see interactional effects from the previous load history at a global mudline rotation level, a reduction in horizontal stress behind the pile close to the surface is again seen for the increased magnitude of applied load. For these load packages, however, this stress reduction requires a greater number of cycles to dissipate than previously seen, with the cycle number before stress stabilisation appearing to coincide with the transition at N^*, illustrating that the new stress interaction regime requires stimulation over a number of cycles to develop. This requirement for additional applied cycles could be attributed to a number of mechanisms taking place behind the pile; one such being the slower redistribution of sand filling the deeper potential gap formation behind the translating pile. Since the deeper previously redistributed sand is under a greater overburden stress, it can no longer 'fall' into position as easily and therefore requires greater stimulation from several applied load cycles for it to fully stabilise. Furthermore, the reduction at EPC 1 corresponds with an increase in stress at EPC 2, signifying the deepening of the sand convective flow regime. These observations can be related to the aforementioned hypothesis which stipulates that the initialisation of the new soil-pile convective sand flow regime is the main driver in delaying the onset of the new accumulation regime. Once the new convective flow regime has been established, then all the previously seen mechanisms associated with cyclic loading recommence.

Close to the pile base, evidence of a pile rotation mechanism is clear from LP 2 onwards, given the increase in passive resistive stress seen at EPC 5 at the rear. The magnitude of horizontal stress with cycles here appears to show only very minor changes occurring at N^* which are coincidental of the sand behaviour changes occurring closer to the surface resulting in the increase in rotation.

***(ii) Decreasing load package*:** the local behaviour of the series of progressively decreasing magnitude load packages is now analysed. The experimental results presented are from the second half of test C43. The total increasing-decreasing load history of test C43 provides a more realistic, but still of sufficient simplicity to allow observation of trends in comparison to the constant load magnitude sequences.

Firstly, observing the bending moment profiles with depth for the four decreasing load packages sees the very noticeable locked-in bending remain, particularly at depth, immediately from the largest magnitude load of LP 4 to the end of the load package of lowest magnitude LP 7 (Figure 5.51a). As a matter of interest, if the bending profiles on decreasing load are directly compared with those on increasing load (Figure 5.46a), of which are subjected to the same respective applied overturning moments (*i.e.* in reflection), a very distinct difference in bending magnitude and shape is seen, both on load and unload. The profiles on the application of load present a significantly greater magnitude of moment close the base, so much so that the bending profile for LP 7 continues to show increasing magnitude until a depth of $z/D \approx 3$, which illustrates that the locked-in stress distribution developed at the pile-sand interface at depth is the dominate driver in the pile bending shape and therefore has major implications on global stiffness behaviour. On unload, the bending profile appears to remain a very similar absolute magnitude across each of the decreasing load packages. The relative potential elastic recovery energy stored in the monopile becomes relatively large at the final applied load package.

The ratio of bending magnitude in comparison to the magnitude of applied overturning moment at the mudline is also presented in Figure 5.51b and illustrates a progressively very large developing locked-in bending magnitude ratio for the reducing load packages – as an example, the maximum locked-in bending for LP 7 is of the order of 100 % of the applied overturning moment.

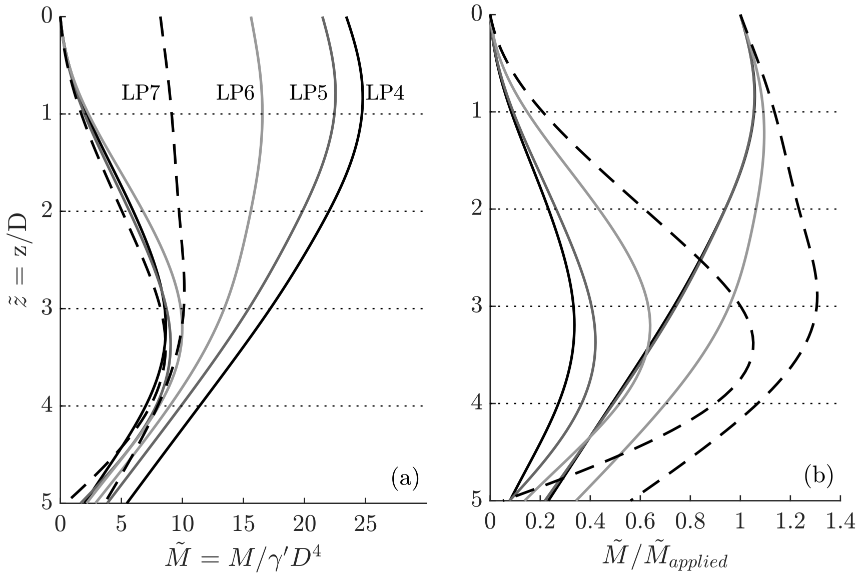

Figure 5.51: Bending moment profile on load and unload for progressively decreasing load magnitude packages (second half of test C43): (a) dimensionless magnitudes; (b) as a ratio of applied overturning moment at the mudline

In addition to the bending moment profile shape with depth, its magnitude at selected locations along the monopile depth is again presented for the full load history across each of the decreasing load packages (Figure 5.52). The high relative magnitude of locked-in bending is very clear and much more pronounced at depth. At $z/D = 0.26$ there is almost no locked-in bending, however from $z/D = 2.44$ and deeper the large bending on unload is seen to remain from LP 4 to the end of LP 7. On closer inspection, it can be seen from Figure 5.52 that there is in fact a very minor reduction in locked-in bending across the applied cycles in the successive load packages of lower magnitude. This can be related to the minor rotation restoration seen at a global level.

The same underlying trends are observed in the horizontal pressure distributions with depth, presented for the first and final applied load cycles of each load package of the decreasing portion of test C43 in Figure 5.53. Upon the application of load, a reduction in passive horizontal pressure at the front of the pile is seen close to the surface for each reducing load package, with the depth of influence also reducing with each successive load. The locked-in pressures to the pile front at mid-depth, however, remain despite the lower magnitude loads likely not influencing at this depth and therefore these provide additional lateral stiffness. At the rear of the pile, the reduction in pressure to a near active state is equally seen across all load packages.

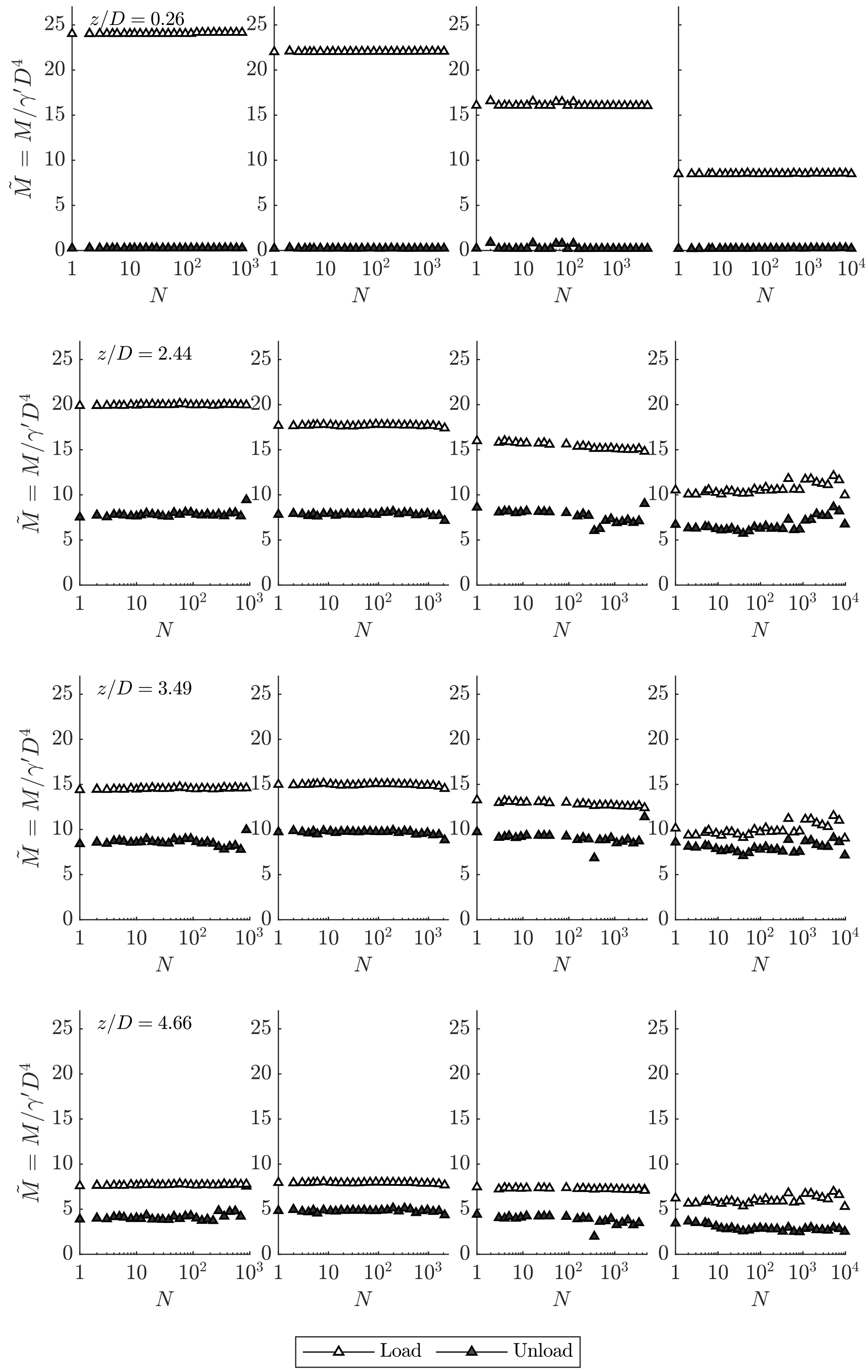

Figure 5.52: Bending moment variation at four locations of interest for load package of increasing magnitude (test C43 – LP 1, 2, 3 & 4)

Interestingly for LP 7, it can be seen that a build-up of pressure on load behind the pile at a shallow depth appears to recommence again, having previously been seen for low magnitude loading. At depth, the large passive horizontal pressure at the base remains throughout the full decreasing sequence, despite this not being mobilised at the very low magnitude load of LP 7.

On the unload phase, the stress distribution profile at depth remains very similar throughout, illustrating that the high overburden pressures are locking-in the previously developed stresses and these are not relieved despite the subsequent lower magnitude loading. It is likely that a high magnitude load reversal is the only way to remove these, as large opposing deformation at the base is required. Close to the surface, however, it can be seen that as the load magnitude decreases, there is a noticeable reinitialisation of the shallow locked-in stress behind the loaded pile. It formation from the greater pile translation. On decreasing load, it can be seen here that the deeper locked-in stresses (at $z/D \approx 1.0$) associated with the large convective flow regime remain, however additional stress also begins to redevelop at shallow depth (at $z/D < 1.0$). This suggests that the local redistribution regime at this shallow depth is redeveloping, which can be attributed to the new low magnitude load presenting a new shallow potential gap formation of which is being refilled by new surface sand. For previously larger applied load packages (LP 4, 5 & 6), this shallow depth would have not seen sand build-up due to deeper sand movements dominating sand redistribution.

Figures 5.54 and 5.55 present the progression of horizontal stresses at the front and rear of the monopile respectively at the selected locations over the course of the full history. Very little variation close to the pile base for EPC 5 & 10 is seen, proving that the stresses locked-in due to the high overburden pressure will always remain after the highest applied load unless a greater load is applied or a load reversal is applied of sufficient magnitude to mobilise an opposing rotational failure mechanism. Close to the surface, the reduction in passive resistive stress at the front is seen for the progressively reducing load packages. The interesting stress behaviour to the pile rear close to the surface presents itself clearly for the low magnitude load packages (LP 6 & 7). The progressive increase in locked-in stress at EPC 1 is seen as the load reduces, demonstrating the reinitialising of a shallow sand redistribution mechanism. The deeper locked-in stresses at EPC 2 for the previously greater load packages remains.

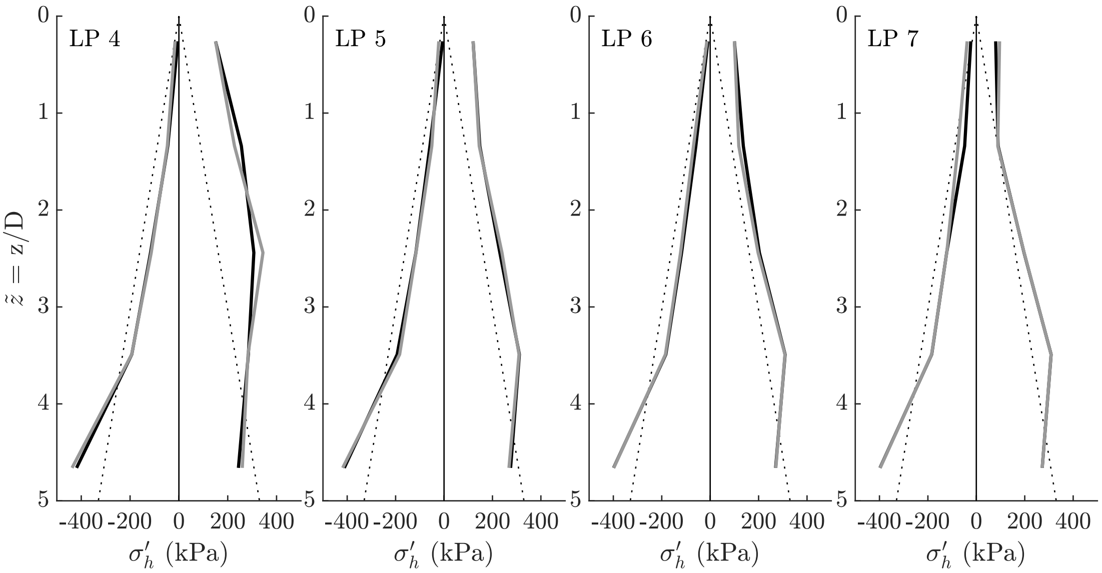

(a) Load

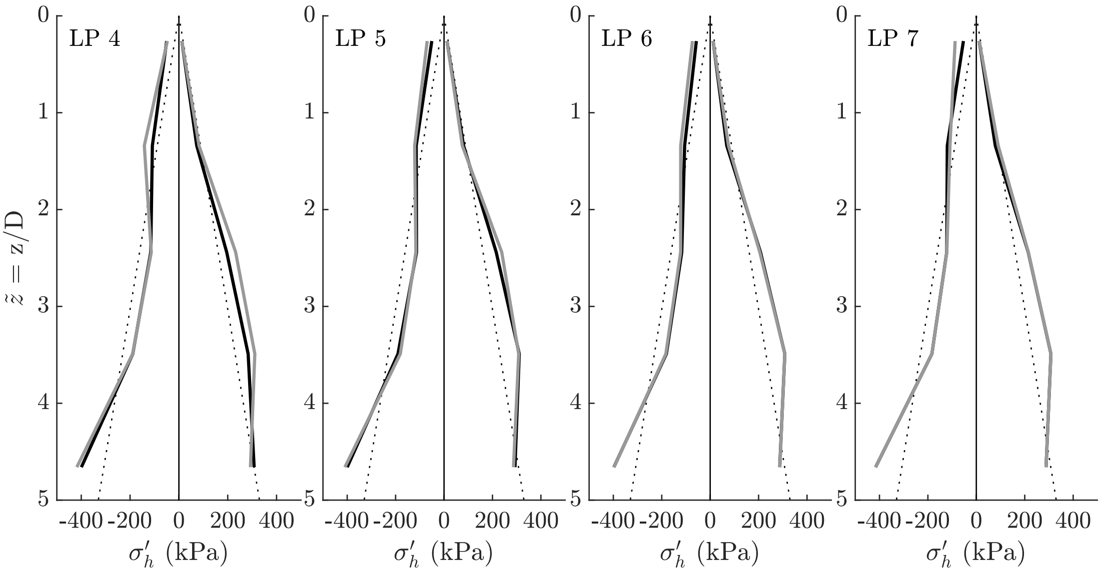

(b) Unload

Figure 5.53: Horizontal locked-in stress distribution on (a) load; and (b) unload for load package of decreasing magnitude (test C43 – LP 4, 5, 6 & 7)

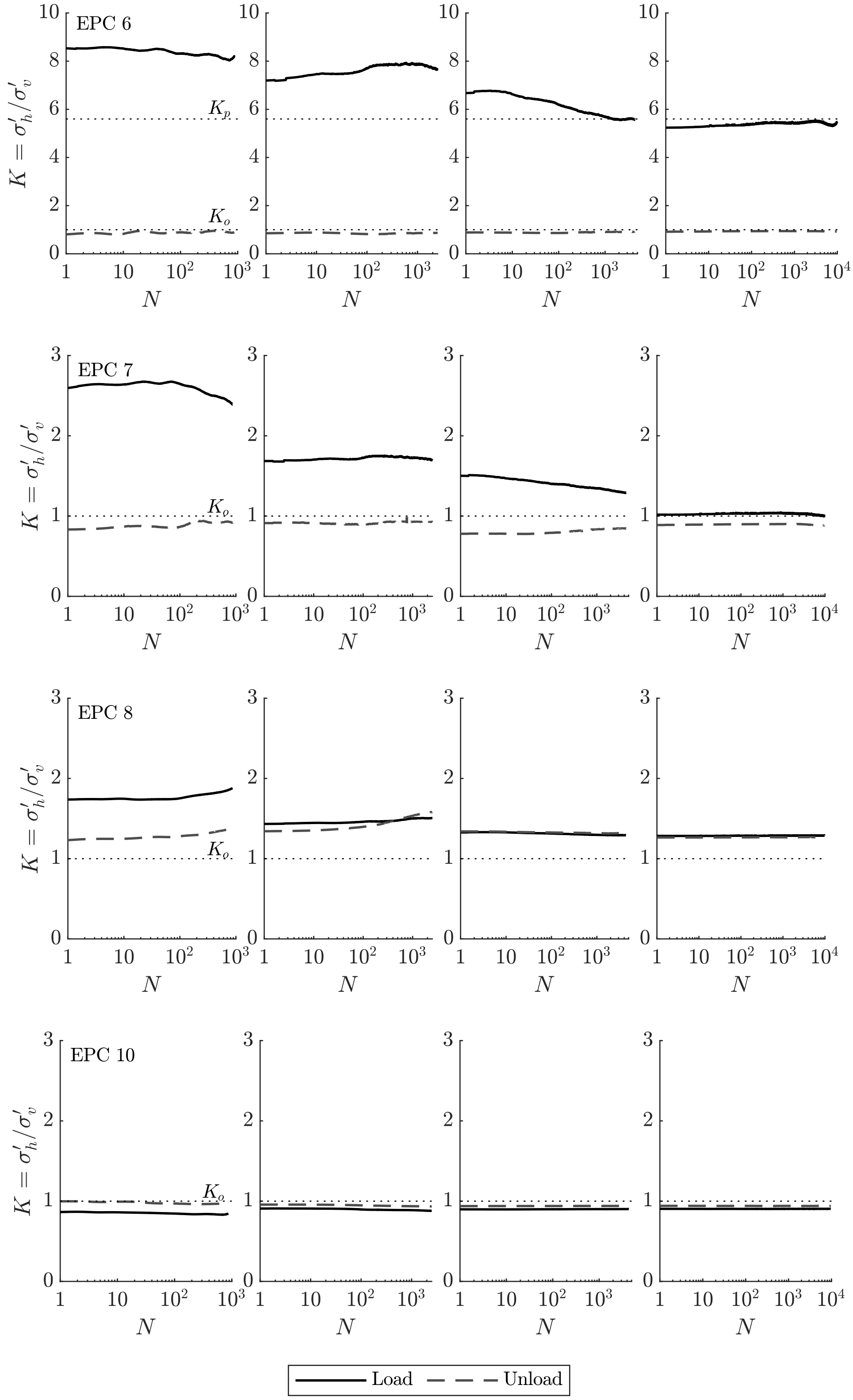

Figure 5.54: Horizontal stress variation in front of monopile at four locations of interest for load package of decreasing magnitude (test C43 – LP 4, 5, 6 & 7)

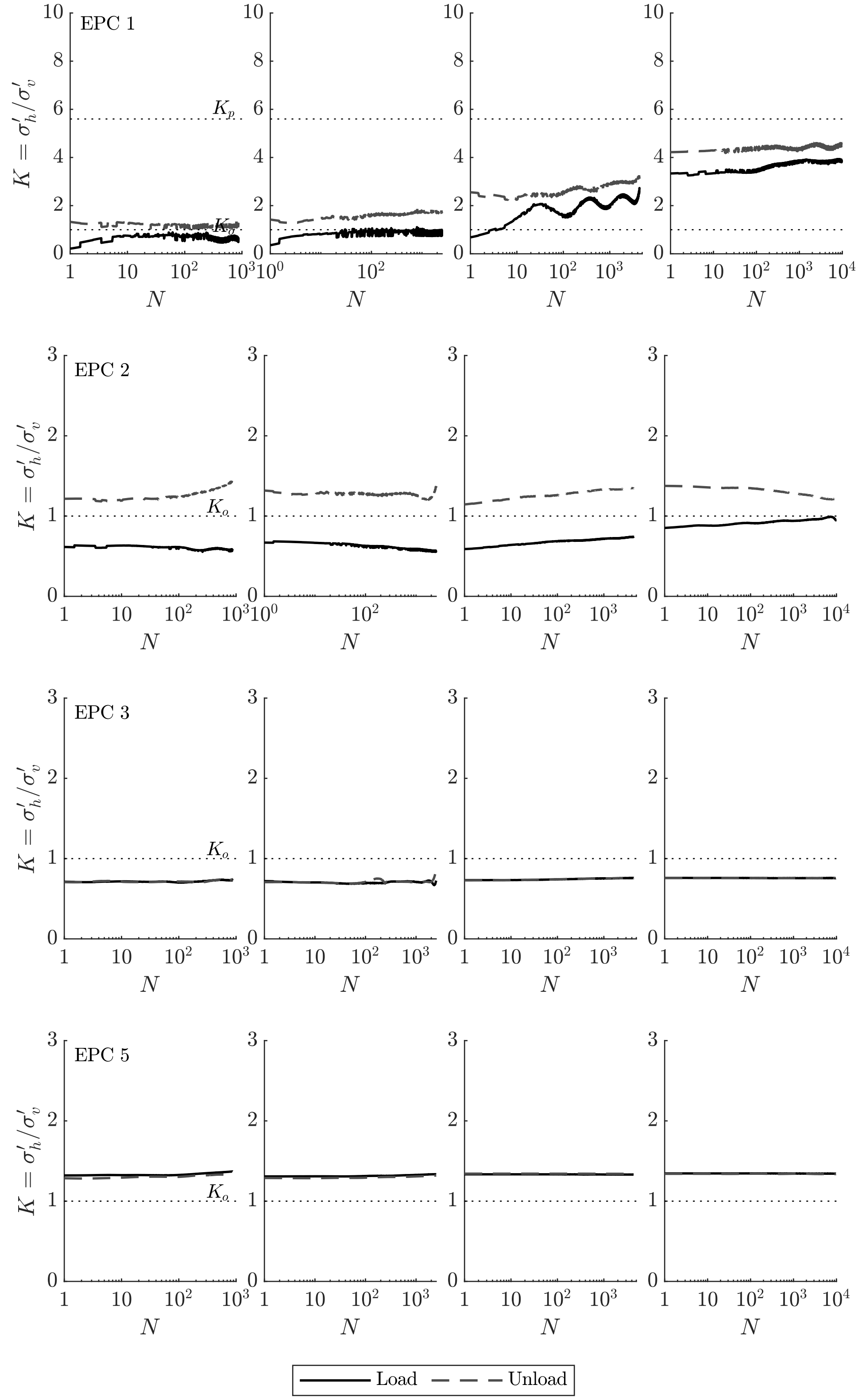

Figure 5.55: Horizontal stress variation at rear of monopile at four locations of interest for load package of decreasing magnitude (test C43 – LP 4, 5, 6 & 7)

***(iii) Random load package*:** finally, local pile-soil interaction behaviour for the random load sequence (test C44) is analysed. Figure 5.56a presents the applied load history of the random section of interest of the load sequence. As a reminder, 10,000 cycles of low magnitude load were also applied both before and after this random load sequence.

The variation of bending moment at the four depths of interest ($z/D = 0.26$, 2.44, 3.49 & 4.66) along the monopile across the full random load history is first presented in Figure 5.56b. It can immediately be seen that after the initial 10,000 applied load cycles, a degree of locked-in bending moment has already developed with depth (except at $z/D = 0.26$ which sees minimal locked-in bending over the entire load history). After the passing of the full random load sequence, which sees a small number of very high, and a large number of low applied overturning moments, it is evident that the magnitude of locked-in bending has increased – percentage increases of 4, 27, 39 and 48 % are seen for the four depths of interest respectively, showing that the greatest lock-in potential is at the base, where the overburden pressures are greatest.

Observing the progression of bending moment with depth across the full cyclic history, a number of observations can be made. Firstly, much like the global rotation, the bending behaviour is dominated by the small number of high magnitude applied loads. Interestingly, with these high magnitude loads there appears to be a more pronounced dampening effect with depth upon loading; this meaning that close to the surface, a large fluctuation between the bending maxima and minima is seen upon the application of each applied maximum and minimum load right the way through the full random load sequence. Close to the base these observed peaks and troughs are not so pronounced and become even less prominent with the progression of the random load package. This is likely due to the progressive increase in relatively larger locked-in stresses with applied cycles, in comparison to the observed moment on load at this depth.

Likewise, the locked-in moments on unload are seen to progressively increase with the number of applied cycles, and it would appear that the small number of high magnitude loads again present the largest increases in locked-in bending. It is also apparent that after the application of these low cycle count, high magnitude loads a degree of locked-in bending reduction is evidenced during the subsequently lower magnitude loading portions of the random package. They do not, however, return to the same magnitude as before and therefore the gradual build-up of bending is seen across the full random load sequence. This relatively rapid reduction, which seems to

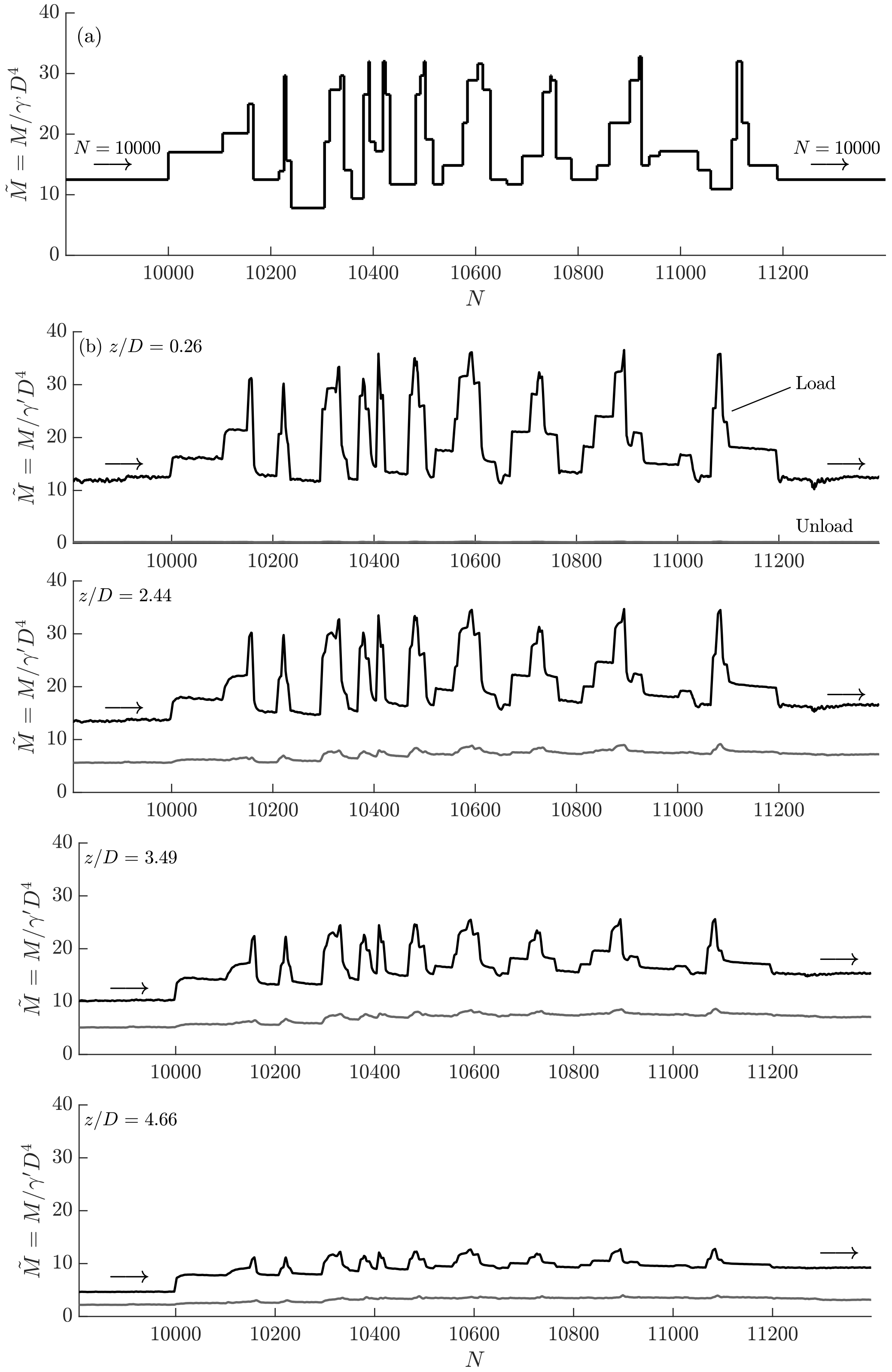

Figure 5.56: Cyclic progression of bending moment on load and unload with random load sequence (test C44): (a) applied load; (b) observed bending moment at selected depths

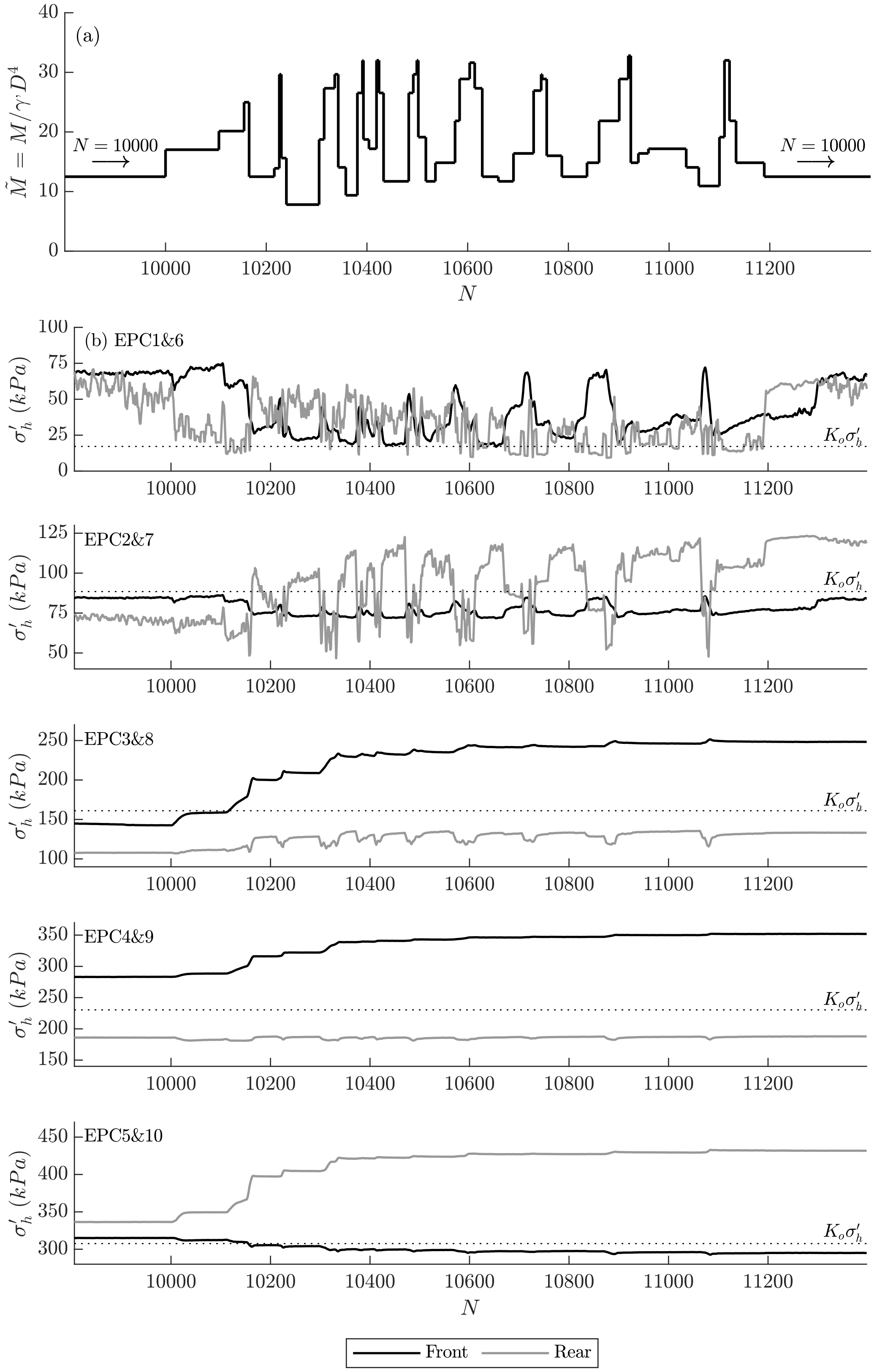

Figure 5.57: Cyclic progression of locked-in stress horizontal stress on unload with random load magnitude packages (test C44): (a) applied load; (b) horizontal stresses at EPC locations

take place over the course of less than 10 cycles, is not observed to the same degree in the longer term decreasing loading regime. One potential reason for this is due to the new deeper redistributed sand regime having not established in the small number of applied high load cycles and therefore when a lower load is reapplied, the pile-soil interaction close to the surface resumes close to its original behaviour.

Figure 5.58 presents the bending profiles with depth, both on load and unload, for the individual cycles both immediately before the first applied load of the random package, and immediately after the last applied load, and therefore illustrates the implications of a particularly large 'storm' event on pile performance. The increase in locked-in bending that has developed over the load event is evident, particularly at depth. In addition, the location of this maximum also deepens. The particularly large increase in locked-in bending over the course of the random sequence has predominantly developed due to only a small number of high magnitude loads within this period. The larger than previous bending moment upon load results in a much stiffer load-deformation response for the subsequent 10,000 cycles and this has implications on the global behaviour where these cycles do not see any noticeable increases in pile rotation at the mudline.

Finally, observations from the output horizontal stress EPC sensors on pile unload are presented in Figure 5.57. Note the changing y axis scale across each EPC location with depth to maximise the resolution of the observed effects of the random load package.

Moving from top to bottom, first of all it can be seen that close to the surface (EPC 1 & 6), there is considerable stress fluctuation which directly follows the specific load magnitude of each applied cycle. At this shallow depth, the stress behavioural trend is similar both in front and to the rear of the pile, where the amount of locked-in stress is dominated by the current load magnitude. Ultimately, locked-in stress here is dictated by the amount and depth of sand redistribution that is taking place – the lower the load, the shallower gapping potential behind the pile and therefore redistributed sand moves to a shallower depth, resulting in shallower locked-in stress and increased output from EPC 1. Equally, the higher loads lead to essentially deeper locked-in stresses and therefore lower output from EPC 1, coupled with greater output at EPC 2. The above is evidenced throughout the stress history – build-up of locked-in stress is apparent after a period of many low magnitude load cycles, however these are immediately broken down on the application of just one single high magnitude load, whose likely cause is the redistributed sand 'falling' to a deeper location behind the pile.

Moving down the pile (EPC 2 & 7), the fluctuation effect associated with each individual cycle is dampened. To the rear, troughs in stress magnitude are only seen at the instances of particularly high applied load, and the locked-in stress in general shows a progressive increase across the full load sequence. This provides evidence for the continuous increase in average stress due to redistribution of sand to this depth, which is driven by each higher magnitude applied load redistributing the gathered sand at shallower depths. At the front of the pile, stress magnitude sees periodic increases at instances of higher applied load, although no locked-in stress with load history is evident.

At EPC 3 & 8, the locked-in stresses are no longer dominated by a cycle-by-cycle variation and their progressive development over the course of the random load package is clearer. It can be said that at this depth the larger overburden pressures prevent dissipation of the accumulating stress and therefore any induced stress increases develop on the application of a particularly high magnitude load remain for the rest of the load sequence. Finally, at depth (EPC 4, 5, 9 & 10), the only noticeable changes in locked-in stresses arise upon the application of very large magnitude applied overturning moments since these induce rotational failure mechanisms and mobilise passive resistance at the rear of the pile at the toe. The few high magnitude applied loads at the beginning of the sequence provide the most dominant changes to locked-in behaviour at these depths and any subsequent low magnitude loading does not present any stress change adjustment. In fact, it appears that only 5 or 6 individual packages of high loading (made up of two or three separate individual loads) are required to develop the majority of the locked-in stress for the entire load history at these depths.

Much like the bending behaviour, Figure 5.59 presents the locked-in horizontal stress distribution profiles on unload for the same cycles of interest pre and post the random ‘storm’ load sequence. Before the random package, there is little horizontal residual stress increase at depth with a relatively large observed residual stress at the pile close to the surface. Once the loading has passed, the rear of the pile at the base shows a substantial increase in residual horizontal stress given the large mobilisation from high magnitude loads. The front also illustrates locked-in stresses at mid-depth which will inherently increase the stiffness of the future, post-storm low magnitude loading.

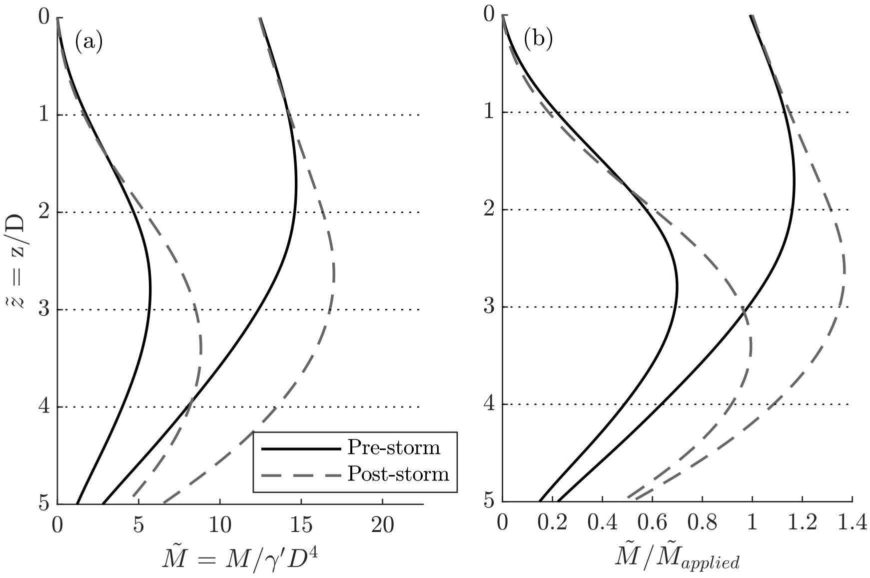

Figure 5.58: Bending moment profile pre- and post-storm event (test C44): (a) dimensionless magnitudes; (b) as a ratio of applied overturning moment at the mudline

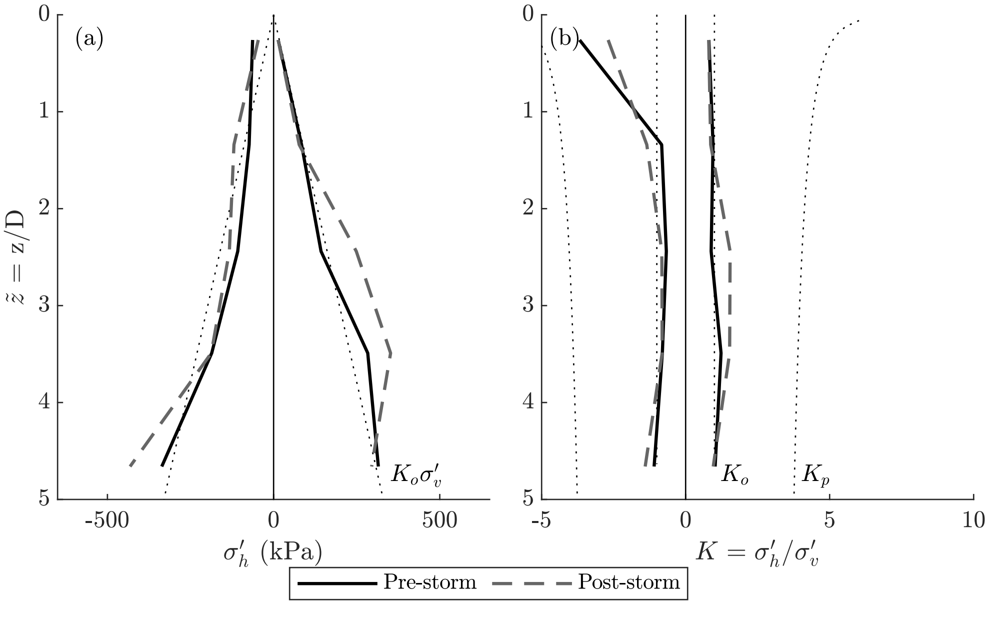

Figure 5.59: Horizontal soil stress variation pre- and post-storm event (test C44): (a) absolute magnitude; (b) dimensionless magnitude

5.8 Concluding remarks from local behaviour

Observations from local monopile bending moment and direct horizontal stress measurements have been made in an attempt to rationalise the previously identified global trends. The key findings from both constant and varying load packages are outlined below:

1. locked-in bending moment on unload is seen to progressively increase throughout the cyclic loading and its rate of accumulation can be described logarithmically for the constant load sequences. The maximum observed locked-in bending as a ratio of the applied overturning moment at the mudline sees a much larger ratio $\tilde{M}_{min}/\tilde{M}_{applied}$ for lower magnitude loading, which can be attributed to the proportionally more flexible nature of the failure mechanism and the proportionally greater prevented elastic recovery. In addition, comparing the accumulated bending at the N^{th} applied cycle with that after the first sees a significantly faster rate of accumulation for the larger applied loads;

2. local horizontal stress measurements with depth provide evidence of the change in failure mechanisms experienced across the load range of applied cyclic packages. For high magnitude cyclic loading, substantial passive stress is seen to develop at depth which remains with the full load history; this is due to the large overburden pressures at these depths preventing dissipation of built up stresses and therefore has substantial implications on global stiffness response. For low magnitude cyclic loading, stress increase on unload is only evidenced very close to the mudline, which can be attributed to surface sand migration and redistribution filling the potential gapping behind the advancing pile;

3. varying magnitude load sequences see subtle interactions between successive load packages at a local scale with the cycle count for local behavioural changes coinciding the cycle count for global rotation changes. Progressively increasing magnitude load packages see the previously large accumulated bending moments at depth interacting with the accumulation of bending moment of the subsequent package. The level of interaction is such that no variation in locked-in bending is seen at the onset of the new higher magnitude loading regime, reflecting the global rotation behaviour at this transition point. Upon reaching N^* cycles, the point of new rotation accumulation, the locked-in bending accumulation also recommences. For decreasing load packages, deep locked-in moments remain with each progressively lower magnitude load package, providing substantial increases in system stiffness;

4. differences in sand redistribution behaviour close to the surface appear to provide

the stimulus for the onset of the new rotation accumulation rate between two interacting load packages. It has been hypothesised that a new, deeper and wider sand redistribution regime associated with higher magnitude loading needs to be fully initialised before the input work done with each load cycle can be subsequently transferred to further plastic deformation and storage as potential energy in the form of locked-in bending. Horizontal stress measurements at the rear of the pile close to the surface see a progressive reduction and deepening of locked-in stress, directly associated to the deeper location of the redistributed sand. At the point of N^* cycles, a stabilisation of stress measurements in these regions relatively close to the surface is seen which suggests the new regime has fully established;

5. for a random load sequence representing a ‘storm’ scenario, it is evident that the low number, high magnitude applied cyclic loads dominate the progression of pile bending and horizontal stress accumulation, particularly at depth. Close to the surface, stress measurements appear to directly follow the load magnitude of the individual applied cycles, with high magnitude loads removing previously built-up stresses very close to the surface. The horizontal stress to the rear of the pile progressively deepens as a result of the deeper potential gapping associated with each high magnitude load.

6. Conclusion

The offshore wind industry is expanding at an increasingly rapid rate. Larger diameter turbines are now being deployed in deeper waters further from the shoreline, with these presenting new challenges for geotechnical engineers – the foundation is subject to much greater magnitude cyclic lateral loads from both stronger winds and waves, resulting in greater overturning moments at the mudline.

At present, the monopile remains the foundation of choice, thanks to a number of reasons including its simplicity, suitability to mass-production and historic success. With larger applied loads, this drives the requirement for larger pile diameters and wall thicknesses, and consequently increased pile-soil stiffnesses, each of which gives rise to changes in failure mechanics in comparison to traditional offshore O&G pile foundations.

Current design methodologies for laterally loaded monopiles set out in DNV GL (2016) and API (2011) design codes follow the Winkler-on-a-beam design philosophy, with the characteristics of associated non-linear springs, also known as $p - y$ springs, calibrated against a series of experimental results on small diameter, slender piles (Murchison and O'Neill, 1984). Concerns are raised surrounding the model translation to today's much larger diameter monopiles, particularly with regards the $p - y$ curve method's initial stiffness and ultimate resistance, and the overall design method's ability to take into consideration the additional failure mechanisms associated with more rigid pile geometries. The performance of the monopile subject to cyclic lateral loading is also not well captured in current design, with a blanket reduction factor applied to the $p - y$ curve ultimate resistance, regardless of the number and nature of the cyclic load. It has been shown across literature that this does not provide an accurate representation of the actual monopile behaviour (Klinkvort, 2012; Byrne et al., 2015; Bayton and Black, 2016).

The work carried out in this thesis has attempted to clarify a number of these concerns through the physical modelling of both monotonic and cyclic lateral loading scenarios. Centrifuge modelling has allowed for the accurate representation of field scale stress conditions and therefore provided greater confidence in the soil-pile stiffness response, which is so critical in serviceability design. The major findings from this research are summarised in the following sections, which can be separated into individual categories of ultimate limit state monotonic behaviour, and serviceability limit state cyclic behaviour both under constant and varying load magnitude.

6.1 Monotonic loading

An in-depth analysis of monopile ultimate failure has been performed for a typical prototype geometry (D = 4-5 m, $L/D = 5$). The gradual application of overturning moment revealed the progressive mobilisation of soil resistance originating from the soil surface, and gradually propagating to the pile toe with increasing load.

Complex instrumentation located on the extremity of the model pile has allowed for the capture of interesting soil-pile interactive behaviour which revealed changes in monopile behaviour with depth and increasing load. Firstly, at low magnitude load, pile lateral deformation and soil mobilisation was restricted to the regions close to the mudline, with little to no change at depth. This was representative behaviour of a flexible pile failure mechanism. As the applied load increased, ultimate passive resistance close to the surface was reached and therefore additional resistance was derived from depth along the pile, plus the onset of base 'toe-kick' and the associated base shear and moment resistances. This demonstrated the transition to a rigid, rotational failure mechanism. Upon reaching the high magnitude load, the soil was fully mobilised across all shallow depths and considerable rotation at the base was observed resulting in large base shear and moment components.

Traditional DNV GL (2016) design recommendation $p - y$ curves, as well as a number of proposed alternatives, have been compared against the experimental observed $p - y$ behaviour. Initial stiffness of the DNV GL (2016) showed significantly greater values than experimental results which led to a complete overprediction of pile performance. These observations supported the findings of Sørensen et al. (2010), Klinkvort (2012) and Kirkwood (2015). Of the proposed alternatives, it has been shown that a combination of an adjusted initial stiffness recommendation of Klinkvort (2012) coupled with the ultimate lateral resistance of Zhang et al. (2005) showed the best representation of $p - y$ behaviour, particularly close to the point of rotation and at the toe, where others showed over-predictions in both stiffness and strength.

Despite the good representation at a $p - y$ level, the complete global behaviour of the rigid monopile, however, was still poorly predicted both in terms of moment-rotation response and bending moment and shear profiles with depth. It was therefore proposed that the implementation of additional soil-pile mechanisms, observed experimentally as base shear and moment, were necessary to provide the additional soil resistance within the spring model. With this in mind, an alternative analytical multi-spring model framework has therefore been outlined and validated against experimental results.

Analytical spring models for base shear, base moment and side shear moment have been derived and the individual spring performance has been made against experimental observations and showed good comparisons within the geometric range tested (except side shear moment which has not been directly measured experimentally). Introducing these into a user defined finite difference approximation design tool (coupled with previously identified best represented $p - y$ curves) showed strong predictions against global experimental monopile behaviour, not just at a moment-rotation level, but also in terms of pile moment and shear profiles with depth.

6.2 Constant cyclic loading

Following the performance and analysis of monotonic ultimate limit state behaviour, a comprehensive test matrix of cyclic experiments was subsequently undertaken. In this current research, concentration was made on one-way loading (*i.e.* $\zeta_c = 0$). Cyclic experimental load ratios ranged from low cycle counts at high magnitude ($\zeta_b = 1.55$) to hundreds of thousands of cycles at low magnitude ($\zeta_b = 0.09$). In short, high magnitude cyclic loads presented the largest rotations with fastest rates of rotation accumulation, and low magnitude loads showed continuous ratcheting of rotation which continued to increase across the full length of the applied loads.

Experimental observations from direct pressure measurements revealed different soil-pile interaction behaviours, which reflected the monotonic behaviour at these load magnitudes, depending on the applied load ratio. For high magnitude cyclic loads, a rigid, rotational cyclic behaviour was observed, with significant mobilisation of the sand close to the base. These were seen to remain locked-in from the very first cycle and remain across the full cycle count. Low magnitude loads presented little to no mobilisation at depth with only the upper layers presenting a build-up of locked-in stress, attributed to sand redistribution. Comparing these with observations at a global rotation level, rotation accumulation for high magnitude load was shown to be best represented using a power-law trend ($\theta_N/\theta_1 = N^{\alpha}$). This was in agreement with Peralta and Achmus (2010) who recommended power-law trends for rigid pile geometries. At a transition point in load ratio of approximately $\zeta_b \approx 0.5$, rotation accumulation prediction appeared to be better represented using a logarithmic-law trend ($\theta_N/\theta_1 = 1 + \beta \ln N$). It was at $\zeta_b < 0.5$ in the monotonic behaviour that the observed flexible mechanisms became more prominent, which reflects the recommendation of Peralta and Achmus (2010) where the logarithmic-law trend is recommended.

Local soil-pile interaction behaviour was captured with strain measurements and earth pressure cell (EPC) sensors. Locked-in bending moment on unload was seen to progressively increase throughout the cyclic load sequence, with the maximum observed locked-in bending as a ratio of the applied overturning moment clear for the low magnitude applied loads. This was as a result of the proportionally more flexible behaviour of the monopile at low magnitude loads and therefore the elastic recovery potential, which was prevented due to sand redistribution filling a potential gap behind the advancing pile, was also proportionally greater. Presenting the accumulated locked-in bending after N cycles as a ratio of that observed after the first cycle showed a faster rate of accumulation for the larger applied loads.

Furthermore, global pile moment-rotation stiffness accumulation rate was shown to be best represented by a logarithmic-law trend. The stiffness after N cycles in relation to the first cycle showed a greater rate of stiffness accumulation for higher magnitude loads, which was directly related to the accumulation of locked-in bending moments within the pile.

6.3 Varying cyclic loading

To conclude the experimental test matrix, a series of varying load magnitude cyclic experiments was performed, of which included progressively increasing, increasing and decreasing, and random 'storm' equivalent load packages.

Observed global experimental rotation behaviour was shown to be accurately predicted using the Miner's rule cumulative damage approach. The interaction of rotation between successive load packages revealed a threshold number of applied cycles which needed to be reached before the onset of further rotation accumulation for the subsequent load package of higher magnitude. At a local pile-soil interaction level, interaction was also observed with the locked-in bending moment between successive load packages. In the cases where no global rotation interaction was seen, locked-in bending immediately increased after the application of the first cycle of the new load package. However, where rotation interaction did take place, the magnitude of locked-in bending remained constant with the application of the new higher load magnitude load package, illustrating that the build-up of locked-in moment throughout the previous package was sufficiently large to interact with the subsequent package. This clearly had implications on mudline rotation behaviour. Incidentally, at the transition cycle number for the onset of further rotation accumulation, locked-in bending was also seen to increase once again.

It was not clear from measured bending moments as to the rationale for the onset cycle number of further pile rotation accumulation, since the accumulation of bending magnitude with depth appeared to take place instantaneously and simultaneously with the accumulation of rotation. No noticeable indication of a threshold moment breach was apparent. Observations from local horizontal stress measurements close to the surface, however, revealed potential evidence of changes in sand redistribution behaviour which could provide explanation for this onset delay. For low magnitude loads, locked-in stress was seen to develop very close to the surface, which was as a result of sand redistribution filling a potential shallow gap formation behind the advancing pile. With cycles, this was proposed to develop in a convective flow regime (Cuéllar, 2011) which required input energy to maintain. Upon the application of a new higher magnitude load package, it has been hypothesised that the new deeper and wider sand redistribution regime which followed was required to be fully initialised before any further input energy could be transferred to plastic deformation and subsequent rotation accumulation. At the point of reinitialisation of rotation accumulation, stabilisation in horizontal stress measurements were seen, which points towards a new fully established sand redistribution mechanism.

Finally, for the random load package, representative of a 'storm' scenario, it has shown that the few high magnitude applied cycles dominated the accumulation of permanent rotation and the progression of locked-in bending and horizontal stress accumulation alike.

6.4 Design recommendations

***(i) Monotonic ultimate limit state design*:** it is the recommendation that any laterally loaded pile that exhibits rigid failure characteristics must include in the model representation additional resistance accounting for base resistance mechanisms. Failure to include these will result in a misrepresentation of the pile behaviour, and will likely result in an under-prediction of monopile performance, even if the correct selection of $p - y$ curve behaviour is made. Incidentally, using the DNV GL (2016) design code will result in a significant over-prediction of pile performance for rigid cases. For more flexible pile cases, it has been seen that the DNV GL (2016) design performs much more admirably and therefore can still be deployed for these. The proposed model alternative also performs well for this case also, given that the base model springs are not mobilised.

***(ii) Cyclic serviceability limit state design*:** empirical trends have been identified for the prediction of rotation accumulation of the cyclically lateral loaded pile. For high applied magnitude cyclic loads, a power-law representation is most appropriate for the accurate prediction; whereas for low magnitude cyclic loads, a logarithmic-law representation illustrates a better performance. This is due to the respective rigid and flexible natures of the cyclic failure mechanisms. From a design point of view this is important since adopting a power-law for the prediction of low magnitude cyclic load behaviour will inherently over-predict rotations; likewise a logarithmic-law deployed for high magnitude cyclic load prediction will inherently under-predict rotations.

Within this work, a new contour accumulation model has been proposed and is recommended to be adopted in initial design of monopile cyclic rotation accumulation. The contour-based approach significantly accelerates the prediction of accumulated permanent rotation at the mudline and is particularly useful for predicting the pile performance of decomposed random 'storm' cyclic load packages, since the load history can simply be traced across the three-dimensional load-cycle space.

From an industry point of view, there is major concern over monopile performance under the lifetime serviceability limit state. The results from this experimental study provide further insight into this aspect of monopile behaviour and further the database of cyclic results.

6.5 Recommendations for future work

The conclusions drawn from this study have added to the understanding of monopile behaviour when subject to both monotonic and cyclic loading scenarios. That being said, there still remain numerous challenges surrounding monopile design that are beyond the scope of this current PhD research. A summary of a key selection of these are listed below:

1. it is expected that the monopile diameter will continue to increase over the coming years (Kallehave et al., 2015). In this experimental test matrix, the maximum prototype equivalent diameter tested was 5 metres, with this being the maximum diameter also used in the validation of the proposed multi-spring model alternative (with actual physical model results). Incidentally, the proposed model was also seen to perform well against FEM predictions for larger diameter, reduced embedment pile scenarios, however results from physical model experiments would provide much greater confidence in the model functionality. Model diameters of up to 10 m in diameter at representative field scale stresses are likely to require testing to stay in-line with industry outlook. If these were to be completed in a centrifuge environment, a sufficiently large test strong box would be required to ensure boundary effects did not influence the pile behaviour.

Equally so, a sufficiently large actuation system would be required to provide a large enough force to induce full mobilisation of the surrounding soil;

2. in terms of cyclic loading, observations of the behavioural response for larger diameter monopiles would also be very useful to validate the global trends identified here;

3. hypotheses have been proposed in this work regarding the potential mechanisms of redistributed sand upon the application of load packages of differing load magnitude which show interactive behaviour. Here, it is predicted that the initialisation of new soil flow regimes in the vicinity of the pile is one of the main drivers for the delay in further rotation accumulation between successive interactive load packages. One method of verifying these would be to dissect the model at various different load cycles before and after the transition cycle for reinitialisation of rotation accumulation. This would, however, require many individual tests to be prepared and tested with the exact same methodology and each test stopped at various different cycle numbers to allow this sand particle tracking. This would not be recommended as it is likely the preparation variation from test to test would be greater than the potential sand movements occurring at the onset of a new rotation accumulation regime. In this case, an alternative transparent sand medium (see Black and Take (2015) for previous example application) could allow for the exact tracking of analogous sand particles with each applied cycle and therefore may illuminate the sand redistribution behaviour;

4. finally, in a brief study by Klinkvort and Page (2014) a laterally loaded large diameter monopile is modelled numerically in dense sand conditions with three different input scenarios of sand permeability representative of: a fully drained, a fully undrained and an expected drainage condition. It was seen that the fully undrained case presented a larger lateral capacity in comparison to the fully drained condition. Interestingly the representative sand permeability case also showed an increase in resistance in comparison to the fully drained case suggested a build-up of pore pressure. Experimental observations of this is yet to be seen (Kirkwood, 2015; Chen et al., 2015), however it is possible that sufficiently large pile diameters, which represent potential future installations, have not yet been modelled. The greater flow dissipation path for these may allow for the build up of pore pressure and given the dense sand nature, associated dilation would result in greater sand resistance.

7. References

Matlab, 2018. TheMathworks, Natick, MA, USA.

C.N. Abadie. *Cyclic Lateral Loading of Monopile Foundations in Cohesionless Soils*. PhD thesis, University of Oxford, 2015.

C.N. Abadie, B.W. Byrne, and G. Houlsby. Rigid pile response to cyclic lateral loading: laboratory tests. *Géotechnique*, 2018.

M. Achmus, Y.S. Kuo, and K. Abdel-Rahman. Behavior of monopile foundations under cyclic lateral load. *Computers and Geotechnics*, 36(5):725–735, 2009.

M. Alizadeh and M.T. Davisson. Lateral load tests on piles - Arkansas River project. *Journal of the Soil Mechanics and Foundations Division*, 96(5):1583–1604, 1970.

American Pertroleum Institute. RP 2GEO Geotechnical and Foundation Design Considerations. 2011.

K.H. Andersen. Bearing capacity under cyclic loading — offshore, along the coast, and on land. The 21st Bjerrum Lecture presented in Oslo, 23 November 2007. *Canadian Geotechnical Journal*, 46(5):513–535, 2009.

K.H. Andersen. Cyclic soil parameters for offshore foundation design. the 3rd mcclelland lecture. In *Frontiers in Offshore Geotechnics III*, pages 5–82, 2015.

M. Ashour, G. Norris, and P. Pilling. Lateral Loading of a Pile in Layered Soil Using the Strain Wedge Model. *Journal of Geotechnical and Geoenvironmental Engineering*, 124(4):303–315, 1998.

J.H. Atkinson. Non-linear soil stiffness in routine design. *Géotechnique*, 50(5):487–508, 2009.

S.M Bayton and J.A. Black. The effect of soil density on offshore wind turbine monopile foundation performance. In *Proceedings of the 3rd European Conference on Physical Modelling in Geotechnics*, 2016.

A. Betz. Wind-Energie und ihre Ausnutzung durch Windmühlen. 1926.

W. Beuckelaers, H.J. Burd, G.T. Houlsby, B.W. Byron, and R.A. McAdam. Data analysis for the PISA Project, 2017.

S. Bhattacharya. Challenges in Design of Foundations for Offshore Wind Turbines. *Engineering & Technology Reference*, pages 1–9, 2014.

B. Bienen, J. Dührkop, J. Grabe, M.F. Randolph, and D.J. White. Response of piles with wings to monotonic and cyclic lateral loading in sand. *Journal of Geotechnical and Geoenvironmental Engineering*, 138(3):364–375, 2012.

B. Bienen, R.T. Klinkvort, C.D. O'Loughlin, F. Zhu, and B.W. Byrne. Suction caissons in dense sand, part I: installation, limiting capacity and drainage. *Géotechnique*, 68 (11):937–952, 2018a.

B. Bienen, R.T. Klinkvort, C.D. O'Loughlin, F. Zhu, and B.W. Byrne. Suction caissons in dense sand, part II: vertical cyclic loading into tension. *Géotechnique*, 68(11):953–967, 2018b.

J.A. Black and W.A. Take. Quantification of optical clarity of transparent soil using the modulation transfer function. *Geotechnical Testing Journal*, 38(5), 2015.

J.A. Black, N. Baker, and A. Ainsworth. Establishing a 50g-ton geotechnical centrifuge at the university of sheffield. In *Proceedings of the 8th International Conference on Physical Modelling in Geotechnics, 14-18 Jan 2014, Perth, Australia*, 2014.

M.D. Bolton. The strength and dilatancy of sands. *Géotechnique*, 36(1):65–78, 1986.

J.L. Briaud and T.D. Smith. Using the pressuremeter curve to design laterally loaded piles. In *Offshore Technology Conference, Houston, USA*, 1983.

J. Brinch Hansen. *A general formula for bearing capacity.* 1961.

British Antarctic Survey. *Ice cores and climate change.* 2014.

K.T. Brødbæk, M. Møller, S.P.H. Sørensen, and A.H. Augustesen. Review of p-y relationships in cohesionless soil. *DCE Technical report No.57*, (57):Aalborg University, 2009.

B.B. Broms. Lateral resistance of piles in cohesionless soils. *Journal of the Soil Mechanics and Foundations Division*, pages 123–156, 1964.

BSI. Maritime Structures - Part 1: Code of practice for general criteria. Technical report, 2000.

M. Budhu and T.G. Davies. Analysis of laterally loaded piles in soft clay. *Journal of geotechnical engineering*, 114(1), 1988.

T. Burton, D. Sharpe, N. Jenkins, and E. Bossanyi. *Wind Energy Handbook*. John Wiley & Sons Ltd, 2001.

BVG Associates. *Guide to an offshore wind farm*, 2019. Published on behalf of The Crown Estate and the Offshore Renewable Energy Catapult.

B.W. Byrne and G.T. Houlsby. Foundations for offshore wind turbines. *Philosophical Transactions of the Royal Society A: Mathematical, Physical and Engineering Sciences*, 361(1813):2909–2930, 2003.

B.W. Byrne and G.T. Houlsby. Assessing Novel Foundation Options for Offshore Wind Turbines. Technical report, 2006.

B.W. Byrne and G.T. Houlsby. Helical piles: An innovative foundation design option for offshore wind turbines. *Philosophical Transactions of the Royal Society A: Mathematical, Physical and Engineering Sciences*, 373(2035), 2015. doi: 10.1098/rsta.2014.0081.

B.W. Byrne, R. McAdam, H.J. Burd, G.T. Houlsby, C.M. Martin, L. Zdravkovi, D.M.G. Taborda, D.M. Potts, R.J. Jardine, M. Sideri, F.C. Schroeder, K. Gavin, P. Doherty, D. Igoe, A. Muir Wood, D. Kallehave, and J.S. Gretlund. New design methods for large diameter piles under lateral loading for offshore wind applications. In *Frontiers in Offshore Geotechnics III*, pages 705–710, 2015.

Carbon Brief. Analysis: UK renewables generate more electricity than fossil fuels for first time, 2019. URL `https://www.carbonbrief.org/analysis-uk-renewables-generate-more-electricity-than-fossil-fuels-for-first-time`.

D. Carrington. Drifting off the coast of portugal, the frontrunner in the global race for floating windfarms, 2015. URL `http://www.theguardian.com/environment/2014/jun/23/drifting-off-the-coast-of-portugal-the-frontrunner-in-the-global-race-for-floating-`
[Online; accessed 11-March-2015].

D.P. Carter. *A non-linear soil model for predicting lateral pile response*. PhD thesis, University of Auckland, 1984.

J.P. Carter and F.H. Kulhawy. Analysis and design of drilled shaft foundations socketed into rock. *Report EL-5918, Electric Power Research Institute, Palo Alto, CA*, 1988.

R.P. Chen, B. Zhu, Y.X. Sun, and W.D. Guo. Lateral cyclic pile - soil interaction studies on a rigid model monopile. *Geotechnical Engineering*, 168(GE2):120–130, 2015.

C.J.F. Clausen, P.M. Aas, and K. Karlsrud. Bearing capacity of driven piles in clay, the NGI approach. In *Frontiers in Offshore Geotechnics*, 2005.

O.J. Cotter, B.W. Byrne, and G.T. Houlsby. Installation of suction caissons for offshore renewable energy structures. In *Frontiers in Offshore Geotechnics II*, pages 569–574, 2010.

P. Cuéllar. *Pile Foundations for Offshore Wind Turbines: Numerical and Experimental Investigations on the Behaviour under Short- Term and Long-Term Cyclic Loading.* PhD thesis, 2011.

P. Cuéllar, M. Baeler, and W. Rücker. Ratcheting convective cells of sand grains around offshore piles under cyclic lateral loads. *Granular Matter*, 11(6):379–390, 2009.

H.L. Davidson. Laterally Loaded Drilled Pier Research. Volume 1: Design Methodology. Technical report, 1982.

Department for Business Enterprise and Regulatory Reform (BERR). Atlas of uk marine renewable energy resources: A strategic environmental assessment report. 2008.

Department of Energy and Climate Change (DECC). *The UK low carbon transition plan: national strategy for climate and energy.* 2009.

DNV GL. DNV GL-ST-0126 : Support structures for wind turbines. Technical report, 2016.

R. Dobry, M. O'Rourke, J.M. Roesset, and E. Vicente. Stiffness and damping of single piles. *Journal of the Geotechnical Engineering Division*, 108:439–459, 1982.

D.J. Douglas and E.H. Davis. The movement of buried footings due to moment and horizontal load and the movement of anchor plates. 14(2):115–132, 1964.

G. J. Dyson and M. F. Randolph. Monotonic Lateral Loading of Soil in Calcareous Sand. *Journal of Geotechnical and Geoenvironmental Engineering*, 127(4):346–352, 2001.

European Commission. The Paris Protocol - a blueprint for tackling global climate change beyond 2020, 2015.

C.C. Fan and J.H. Long. Assessment of existing methods for predicting soil response of laterally loaded piles in sand. *Computers and Geotechnics*, 32(4):274–289, 2005.

K. Fleming, A. Weltman, M.F. Randolph, and K. Elson. *Piling engineering.* Taylor & Francis, third edition, 2009.

J. Garnier, C. Gaudin, S.M. Springman, P.J. Culligan, D. Goodings, D. Konig, B. Kutter, R. Phillips, M.F. Randolph, and L. Thorel. Catalogue of scaling laws and similitude questions in geotechnical centrifuge modelling. *International Journal of Physical Modelling in Geotechnics*, 3:01–23, 2007.

M. Georgiadis, C. Anagnostopoulos, and S. Saflekou. Centrifugal testing of laterally loaded piles in sand. *Canadian Geotechnical Journal*, 29(2):208–216, 1992.

M.W. Gui, M.D. Bolton, J. Garnier, J.F. Corte, G. Bagge, J. Laue, and R. Renzi. Guidelines for cone penetration tests in sand. In *Proceedings of the International Centrifuge Conference 1998, Tokyo*, pages 155–160, 1998.

A. Haiderali, B. Lau, S. Haigh, and S. Madabhushi. Lateral response of monopiles using centrifuge testing and finite element analysis. In *Physical Modelling in Geotechnics*, pages 743–749, 2014.

S K Haigh. Foundations for offshore wind turbines. In *Physical Modelling in Geotechnics*, pages 153–159, 2014. doi: 10.1098/rsta.2003.1286.

L. Hamre, S. Feizi Khankandi, P. J. Strom, and C. Athanasiu. Lateral behaviour of large diameter monopiles at Sheringham ShoalWind Farm. In *Frontiers in Offshore Geotechnics II*, pages 575–580, 2011.

K. Hasselmann, T.P. Barnett, E. Bouws, H. Carlson, D.E. Cartwright, K. Enke, J.A. Ewing, H. Gienapp, D.E. Hasselmann, P. Kruseman, A. Meerburg, P. Muller, D.J. Olbers, K. Richter, W. Sell, and H. Walden. Measurements of Wind-Wave Growth and Swell Decay during the Joint North Sea Wave Project (JONSWAP). Technical report, 1973.

K.H. Head. *Manual of soil laboratory testing: volume 3 effective stress tests.* Pentech Press Limited, London, 1986.

M. Hetenyi. Beams on elastic foundations: theory with applications in the field of civil and mechanical engineering. University of Michigan Press, 1946.

G.T. Houlsby. How the dilatancy of soils affects their behaviour. In *10th European Conference on Soil Mechanics and Foundation Engineering, Florence, Italy, 28th May 1991*, 1991.

G.T. Houlsby. Interactions in offshore foundation design. *Géotechnique*, 66(10):791–825, 2016.

G.T. Houlsby, R.B. Kelly, J. Huxtable, and B.W. Byrne. Field trials of suction caissons in clay for offshore wind turbine foundations. *Géotechnique*, 55(4):287–296, 2005.

J.R. Hutchison. Shear coefficients for timoshenko beam theory. *Journal of applied mechanics*, pages 87–92.

International Renewable Energy Agency (IRENA). Offshore innovation widens renewable energy options Opportunities , challenges and the vital. 2018.

R.J. Jardine and F.C. Chow. *New design methods for offshore piles.* Marine Technology Directorate Ltd, London, 1996.

R.J. Jardine, F.C. Chow, R. Overy, and J. Standing. *ICP design methods for driven piles in sands and clays.* Thomas Telford Publishing, London, 2005.

D. Kallehave, C. LeBlanc Thilsted, and M.A. Liingaard. Modification of the API p – y formulation of initial stiffness of sand. In *Proceedings of the 7th International Conference in Offshore Site Investigation and Geotechnics, London*, 2012.

D. Kallehave, B.W. Byrne, C. LeBlanc Thilsted, and K.K. Mikkelsen. Optimization of monopiles for offshore wind turbines. *Philosophical Transactions of the Royal Society A: Mathematical, Physical and Engineering Sciences*, 373(2035), 2015.

R.B. Kelly, G.T. Houlsby, and B.W. Byrne. A comparison of field and laboratory tests of caisson foundations in sand and clay. *Géotechnique*, 56(9):617–626, 2006.

P. Kirkwood. *Cyclic lateral loading of monopile foundations in sand.* PhD thesis, 2015.

P. Kirkwood and S. Haigh. Centrifuge testing of monopiles subject to cyclic lateral loading. In *Proceedings of the International Conference in Physical Modelling in Geotechnics*, number 1989, pages 827–831, 2014.

R.T. Klinkvort. *Centrifuge modelling of drained lateral pile - soil response.* PhD thesis, Technical University of Denmark, 2012.

R.T. Klinkvort and O. Hededal. Effect of load eccentricity and stress level on monopile support for offshore wind turbines. *Canadian Geotechnical Journal*, 51(9):966–974, 2014.

R.T. Klinkvort and A.M. Page. Diameter effect on the lateral response of monopiles in sand supporting offshore wind turbines. In *Numerical Methods in Geotechnical Engineering*, pages 1267–1272, 2014.

R.T. Klinkvort, B. Bienen, S. Fan, J. Black, S. Bayton, L. Thorel, G.S.P. Blanc, M. Madabhushi, S. Haigh, T. Broad, A. Zania, V. Askarinejad, Q. Li, D.S. Kim, and S. Park. Centrifuge modelling considerations of lateral loaded monopiles in sand. *Géotechnique*, under review.

R.L. Kondner. Hyperbolic stress-strain response; cohesive soils. *Journal of the Soil Mechanics and Foundations Division*, 89:115–143, 1963.

F.H. Kulhawy. Drilled shaft foundations. *Foundation Engineering Handbook*, 1991.

C. LeBlanc. *Design of Offshore Wind Turbine Support Structures: Selected topics in the field of geotechnical engineering.* PhD thesis, University of Oxford, 2009.

C. LeBlanc, B.W. Byrne, and G.T. Houlsby. Response of stiff piles to random two-way lateral loading. *Géotechnique*, 60(9):715–721, 2010a.

C. LeBlanc, G.T. Houlsby, and B.W. Byrne. Response of stiff piles in sand to long-term cyclic lateral loading. *Géotechnique*, 60(2):79–90, 2010b.

B.M. Lehane, J. Schneider, and X. Xu. Development of the UWA-05 Design Method for Open and Closed Ended Driven Piles in Siliceous Sand. In *Geo-Denver 2007*, 2007.

K. Lesny and J. Wiemann. Design aspects of monopiles in German offshore wind farms. In *Proceedings of the International Symposium on Frontiers in Offshore Geotechnics*, 2005.

W. Li, D. Igoe, and K. Gavin. Field tests to investigate the cyclic response of monopiles in sand. *Proceedings of the ICE - Geotechnical Engineering*, 168(5):407–421, 2015.

W. Li, B. Zhu, and M. Yang. Static Response of Monopile to Lateral Load in Overconsolidated Dense Sand. *Journal of Geotechnical and Geoenvironmental Engineering*, 143(7), 2017.

Z. Li, S.K. Haigh, and M.D. Bolton. Centrifuge modelling of mono-pile under cyclic lateral loads. In *Proceedings of the 7th International Conference on Physical Modelling in Geotechnics*, pages 965–970, 2010.

S.S. Lin and J.C. Liao. Permanent strains of plies in sand due to cyclic lateral loads. *Journal of Geotechnical and Geoenvironmental Engineering*, 125(9):798–802, 1999.

L.F. Ling. *Back analysis of lateral load test on piles.* PhD thesis, University of Auckland, 1988.

R.L. Little and J.L. Briaud. Full scale cyclic lateral load tests on six single piles in sand (No. TAMU-RR-5640). Technical report, 1988.

J.H. Long and G. Vanneste. Lateral Deflection of Shaft , m m Qualitative Discussion of Cyclic Behavior The behavior of a vertical pile subjected to repetitive lateral loads depends. 120(1):225–244, 1994.

R. Luo, M. Yang, and W. Li. Numerical study of diameter effect on accumulated deformation of laterally loaded monopiles in sand Numerical study of diameter effect on accumulated deformation of laterally loaded monopiles in sand. *European Journal of Environmental and Civil Engineering*, pages 1–13, 2018.

G. Madabhushi. *Centrifuge Modelling for Civil Engineers.* CRC Press, 2014.

G. Masing. Eiganspannungen und verfestigung beim messing. In *Proceedings for the 2nd International Congress of Applied Mechanics*, 1926.

B. McClelland. Soil modulus for laterally loaded piles. *Journal of the Soil Mechanics and Foundations Division*, 82(4):1–22, 1956.

G.G. Meyerhof and V.V.R.N. Sastry. Bearing Capacity of Rigid Piles Under Eccentric and Inclined Loads. *Canadian Geotechnical Journal*, 22(1):267–276, 1985.

G.G. Meyerhof, S.K. Mathur, and A.J. Valsangkar. Lateral resistance and deflection of rigid walls and piles in layered soils. *Canadian Geotechnical Journal*, 18(2):159–170, 1981.

M.A. Miner. Cumulative damage in fatigue. *Journal of applied mechanics*, 12(3): 159–164, 1948.

A. Mitchell. On submarine foundations; particularly the screw pile and moorings. *Minutes of the Proceedings of the ICE*, 7:108–132, 1848.

J.R. Morison, J.W. Johnson, and S.A. Schaaf. The force exerted by surface waves on piles. *Journal of Petroleum Technology*, 2, 1950.

J.M. Murchison and M.W. O'Neill. Evaluation of p - y relationships in cohesionless soils. In *Analysis and Design of Pile Foundations. Proceedings of a Symposium in Conjunction with the ASCE National Convention*, pages 174 – 191, 1984.

S. Nanda, I. Arthur, V. Sivakumar, S. Donohue, A. Bradshaw, R. Keltai, K. Gavin, P. MacKinnon, P. Rankin, and D. Glynn. Monopiles subjected to uni- and multi-lateral cyclic loading. *Proceedings of the Institution of Civil Engineers - Geotechnical Engineering*, 170(3):246–258, 2017.

National Aeronautics and Space Administration (NASA). Global Land-Ocean Temperature Index, 2018. URL `https://climate.nasa.gov/vital-signs/global-temperature/`. [Online; accessed 14-Dec-2018].

Offshore Wind Journal. Asia's 100-gw offshore wind potential could replace 350m tonnes of coal generation. `https://www.owjonline.com/news/view,` `asias-100gw-offshore-wind-potential-could-replace-350m-tonnes-of-coal-generation_54077.htm/`, 2018.

J. Oswald, M. Raine, and H. Ashraf-Ball. Will British weather provide reliable electricity? *Energy Policy*, 36(8):3212–3225, 2008.

O.A.L. Paramor, K.A. Allen, M. Aanesen, C. Armstrong, T. Hegland, W. Le Quesne, G.J. Piet, G.J. Raakaer, S. Roger, R. van Hal, L.J.W. van Hoof, H.M.J. van Overzee, and C.L.J. Frid. MEFEPO North Sea Atlas. *University of Liverpool*, 2009.

P. Peralta and M. Achmus. An experimental investigation of piles in sand subjected to lateral cyclic loads. In *Physical Modelling in Geotechnics*, pages 985–990, 2010.

H.G. Poulos. Behaviour of laterally loaded piles: I- single piles. *Journal of the Soil Mechanics and Foundations Division*, 97(5):711–731, 1971.

H.G. Poulos and T.S. Hull. The role of analytical geomechanics in foundation engineering. In *Foundation Engineering: current principles and practices*, 1989.

Y.V.S.N. Prasad and T.R. Chari. Lateral capacity of model rigid piles in cohesionless soils. *Soils and Foundations*, 39(2):21–29, 1999.

A.M. Puzrin and A. Shiran. Effects of the constitutive relationship on seismic response of soils. Part I. Constitutive modeling of cyclic behavior of soils. *Soil dynamics and Earthquake Engineering*, 19(5):305–318, 2000.

R. Pyke. Nonlinear soil models for irregular cyclic loadings. *Journal of the Geotechnical Engineering Division*, 105(GT6):715–726, 1979.

M.F. Randolph, R. Dolwin, and R. Beck. Design of driven piles in sand. *Géotechnique*, 44(3):427–448, 1994.

W. Rankine. On the stability of loose earth. In *Philosophical Transactions of the Royal Society of London (1776-1886)*, volume 147, pages 9–27, 1857.

L. Reese and H. Matlock. Nondimensional solutions for laterally loaded piles with soil modulus assumed proportional to depth. In *Proceedings of the 8th Texas Conference on Soil Mechanics and Foundation Engineering, Austin, Texas*, pages 1–41, 1956.

L. Reese and W.F. Van Impe. *Single piles and pile groups under lateral loading.* Balkema, Rotterdam, 2001.

L.C. Reese, W.R. Cox, and F.D. Koop. Analysis of laterally loaded piles in sand. In *Civil Engineering Hall of Fame*, 1974.

D. Remaud, J. Garnier, and R. Frank. Laterally loaded piles in dense sand: Group effects. In *International Conference Centrifuge, Tokyo, Japan, 23-25 September*, pages 533–538, 1998.

Renewable UK. Wind Energy Statistics, 2019. URL `https://www.renewableuk.com/page/UKWEDhome`.

Renewables Advisory Board. Value breakdown for the offshore wind sector. pages 1–20, 2010.

I. Richards, B.W. Byrne, and G.T. Houlsby. Physical modelling of monopile foundations under variable cyclic lateral loading. In *Proceedings of the 9th International Conference on Physical Modelling in Geotechnics*, pages 737–742, 2018.

S. Rosbjerg and H. Gravesen. OWA Offshore wind farm foundations, UK Round 3 design basis version 1. 2009.

F. Rosquoët, L. Thorel, J. Garnier, and Y. Canepa. Lateral Cyclic Loading of Sand-Installed Piles. *Soils and Foundations*, 47(5):821–832, 2007.

F. Rosquoët, L. Thorel, J. Garnier, and M. Khemakhem. P-y curves on model piles: Uncertainty identification. In *Physical Modelling in Geotechnics*, pages 997–1002, 2010.

C. Rudolph, J. Grabe, and B. Bienen. Response of monopiles under cyclic lateral loading with a varying loading direction. In *Physical Modelling in Geotechnics*, number 2008, pages 453–458, 2014.

I. Rychlik. A new definition of the rainflow cycle counting method. *International Journal of Fatigue*, 9(2):119–121, 1987.

J.A. Schneider and M. Senders. Foundation Design: A Comparison of Oil and Gas Platforms with Offshore Wind Turbines. *Marine Technology Society Journal*, 44(1): 32–51, 2010.

T.D. Smith. Pile horizontal soil modulus values. *Journal of Geotechnical Engineering*, 113(9), 1987.

Statista. Number of offshore rigs worldwide 2018 by region, 2018. URL `https://www.statista.com/statistics/279100/number-of-offshore-rigs-worldwide-by-region/`. [Online; accessed 19-March-2019].

H.E. Stewart. Permanent strains from cyclic variable-amplitude loadings. *Journal of Geotechnical Engineering*, 112(6):646–660, 1986.

H. Sturm, K.H. Andersen, T. Langford, and M. Saue. An introduction to the NGI cyclic accumulation approach in the foundation design of OWTs. In *12th Baltic Sea Geotechnical Conference, Rostock, Germany*, 2012.

D. Su, W.L. Wu, Z.Y. Du, and W.M. Yan. Cyclic Degradation of a Multidirectionally Laterally Loaded Rigid Single Pile Model in Compacted Clay. *Journal of Geotechnical and Geoenvironmental Engineering*, 140(5), 2014.

S.P.H. Sørensen. *Soil-structure interaction for non-slender, large-diameter offshore monopiles.* PhD thesis, Aalbord University, 2012.

S.P.H. Sørensen, L.B. Ibsen, and A.H. Augustesen. Effects of diameter on initial stiffness of p – y curves for large-diameter piles in sand. In *Numerical Methods in Geotechnical Engineering*, pages 907–912, 2010.

K. Terzaghi. Evaluation of Coefficients of Subgrade Reaction. *Géotechnique*, 5(4): 297–326, 1955.

The Crown Estate. Round 3 zone appraisal and planning. Technical report, London, 2010.

S. Thomas. Geotechnical investigation of uk test sites for the foundations of offshore structures. Prepared by McClelland Limited for the Department of Energy, 1990.

S. Timoshenko. On the correction factor for shear of the differential equation for transverse vibrations of bars of uniform cross-section. In *Philosophical Magazine*, 1921.

S. Timoshenko. *History of strength of materials.* McGraw-Hill, New York, USA, 1953.

P. Truong, B.M. Lehane, V. Zania, and R.T. Klinkvort. Empirical approach based on centrifuge testing for cyclic deformations of laterally loaded piles in sand. *Géotechnique*, pages 1–32, 2018.

UK Government. Climate Change Act 2008, 2008.

UK Government. *The Clean Growth Strategy: Leading the way to a low carbon future.* 2017.

UK Met Office. *Climate change – the facts.* 2009.

University College San Diego (UCSD). The Keeling Curve, 2018. URL `https://scripps.ucsd.edu/programs/keelingcurve/`. [Online; accessed 20-July-2018].

L. Verdure, J. Garnier, and D. Levacher. Lateral cyclic loading of single piles in sand. *International Journal of Physical Modelling in Geotechnics*, 3(3):17–28, 2003.

A.B. Vesic. Beams on Elastic Subgrade and the Winkler's Hypothesis. In *Proceedings of 5th International Conference of Soil Mechanics*, volume 1, pages 845–850, 1961.

P. Vølund. Concrete is the Future for Offshore Foundations. In *Wind Engineering*, volume 29, pages 531–539, 2005.

C. West and M. Gawith. Measuring progress - preparing for climate change through the UK climate impacts programme. Technical report, UKCIP, Oxford, 2005.

J. Wiemann, K. Lesny, and W. Richwien. Evaluation of the pile diameter effects of soil-pile stiffness. In *Proceedings of the 7th German wind energy conference (DEWEK), Wiljelhshaven, Germany*, 2004.

Wind Europe. Offshore Wind in Europe: Key trends and statistics 2017, 2018. URL `https://windeurope.org/wp-content/uploads/files/about-wind/statistics/WindEurope-Annual-Offshore-Statistics-2017.pdf`.

Wind Power Offshore. Analysis: Why did RWE decide to drop Atlantic Array?, 2013. URL `https://www.windpoweroffshore.com/article/1223085/analysis-why-rwe-decide-drop-atlantic-array`.

E. Winkler. Die Lehre Von Elasticitaet Und Festigkeit. In *H. Dominicus, Prague*, volume 1, 1867.

J. Yang. Influence zone for end bearing of piles in sand. *Journal of Geotechnical and Geoenvironmental Engineering*, 132(9), 2006.

L. Zdravkovic, D.M.G. Taborda, D.M. Potts, R.J. Jardine, M. Sideri, F.C. Schroeder, B.W. Byrne, R. McAdam, H.J. Burd, G.T. Houlsby, C.M. Martin, K. Gavin, P. Doherty, D. Igoe, A. Muir Wood, D. Kallehave, and J. Skov Gretlund. Numerical modelling of large diameter piles under lateral loading for offshore wind applications. In *Frontiers in Offshore Geotechnics III*, pages 759–764, 2015.

L. Zhang, F. Silva, and R. Grismala. Ultimate Lateral Resistance to Piles in Cohesionless Soils. 131:78–83, 2005.

B. Zhu, Y.X. Sun, R.P. Chen, and Y. Chen. Model tests on offshore monopile subjected to lateral monotonic and cyclic loading. In *Physical Modelling in Geotechnics*, pages 553–559, 2014.

B. Zhu, T. Li, G. Xiong, and J.C. Liu. Centrifuge model tests on laterally loaded piles in sand. *International Journal of Physical Modelling in Geotechnics*, 16(4):160–172, 2016.